

NORTHWESTERN UNIVERSITY

Application of Cesium Dihydrogen Phosphate in Intermediate Temperature Electrochemical Devices

A DISSERTATION

SUBMITTED TO THE GRADUATE SCHOOL

IN PARTIAL FULFILLMENT OF THE REQUIREMENTS

for the degree

DOCTOR OF PHILOSOPHY

Field of Material Science and Engineering

By

Austin Plymill

EVANSTON, ILLINOIS

March 2021

© Copyright by Austin B. Plymill 2021

All Rights Reserved

Abstract

Electrochemical cell devices are increasingly being sought for energy conversion and storage applications due to their high efficiencies and their potential for operating free of greenhouse gas (GHG) emissions. Solid Acid Electrochemical Cells (SAECs), which most commonly employ CsH_2PO_4 (CDP) as the electrolyte component, are uniquely suited to meet the demands of these energy applications due to their operability at intermediate temperatures. Cesium dihydrogen phosphate displays high ionic conductivity at the moderate temperature of 250 °C and stability over a wide range of environments. This intermediate operating temperature gives SAECs advantages in reaction kinetics and fuel flexibility over cooler operating systems and advantages in cost, portability, and system complexity over warmer operating systems. This thesis primarily explores (i) electrocatalysis of the hydrogen oxidation reaction (HOR) in existing and novel catalyst systems, showing that SAECs are highly effective for hydrogen extraction from ammonia, and (ii) the techno-economic feasibility of using SAECs for ammonia synthesis.

First, a systematic analysis of HOR on composite electrodes in CDP-based SAECs is performed. Evaluations of HOR on the conventional catalysts, Pt and Pd, are performed in addition to analysis of the more novel Ru, Pt-Pd-Ru alloys, and metal phosphide systems. The three monometallic systems display comparable HOR activity at low oxidation potentials, while Ru is poisoned at high potentials. Introduction of small amounts of Pt and/or Pd to Ru eliminates the poisoning effect. Nickel-based phosphide catalysts show promise as active earth abundant HOR catalysts.

Next, ammonia electro-decomposition is explored. Use of either Pt or Ru alone as NH_3 electrooxidation catalysts results in poor H_2 production rates. However, integration of a Ru-based reforming catalyst layer with a Pt-based H_2 electrocatalyst layer in a hybrid cathode structure results in the production of high-purity hydrogen at an unprecedented rate, opening the potential for using ammonia as a hydrogen carrier.

Finally, a techno-economic analysis of using SAECs for ammonia synthesis is performed. This analysis shows that by leveraging cheap electricity, modular design, and distributed locations, SAECs can be market competitive with existing and possible future technologies for ammonia synthesis.

Acknowledgements

First, I would like to thank my advisor Professor Sossina Haile for having me as a part of her group and for her continual guidance. During my time here, she has shown me many of the facets of being a scientific detective and what it is like to captain a crew exploring uncharted waters. I would also like to thank Dr. Calum Chisholm who was invaluable to learn from and whose boundless optimism inspires me to believe that we can make a difference in this world. I also owe many thanks to Dr. Alex Martinson, who in many ways molded my initial graduate research experience. I will always appreciate his imbuing spirit of trying things and for introducing me to the fascinating world of surface science. I would also like to thank Professor Michael Bedzyk and Professor Christopher Wolverton who also both served on my committee and whose insights provided helpful guidance for my research. I would also like to thank Professor Simon Billinge, who helped us bring the pyentioostat project farther than I ever thought possible. From him, I learned much about bringing an open-source application through development. Thanks also to Professor Mark Werwath who taught me much on how to look towards commercializing technology, and I would not have my 5th chapter without his guidance. I would be remiss if I did not acknowledge my undergraduate research mentors who inspired me to pursue my Ph. D. in the first place. Many thanks to Professor Haixuan Xu for facilitating my embarkment into the exploration of materials phenomena. I fondly remember our meetings of wondering, hypothesizing, and discovery. Thanks also to Dr. Brenda Smith, in whose lab I found the visceral fulfillment in developing fascinating materials. Letting me also make the RGB superparamagnetic phosphors even though we only need the UV (and the red was expensive to make) showed me how fun and satisfying materials development can be.

I am grateful to my senior colleagues who have offered me support in countless ways during my graduate research career. Thanks to Dr. Dae-Kwang Lim who in many ways served as my mentor in the group. Not only did he share his expertise in electrochemistry among many areas, but also, he inspired me with his kindness and dedication. Thanks also to Dr. Timothy Davenport who always pushed me to go as far as possible when trying things out. Thanks to Dr. Chris Kucharczyk for the helpful suggestions (including my dive into the world of color palettes) he provided along the way. I want to thank Dr. Daehee Lee for all his helpful advice, wise words, and consistent encouragement. Also, thanks to Dr. Abdulmenan Hussein

for help on the interesting things we explored, I miss his happy presence! Thanks to Dr. Jill Wenderott whose kindness is immeasurable. From cat-sitting, to experimental help, to editing my dissertation, she is always there, and I aspire to be as helpful of a friend as her. I owe thanks to Dr. Ara Jo for her boundless assistance towards the end of my graduate research work, Dr. Emanuela Mastronardo for providing helpful advice on several research points, and to Dr. Sihyuk Choi for his helping hand.

My fellow graduate students have doubtlessly improved my experience within the group. The camaraderie that we had in the upstairs office helped me feel at home. Thanks to Dr. Xin Xu for all the love and laughter. Thanks to Dr. Weizi Yuan for always jumping into endeavors headfirst with me. Thanks to Dr. Ruiyun Huang for the deep conversations probing the nature of things. Thanks to Xin Qian for being there to help when I needed it. I also owe thanks to my fellow solid acid electrochemists Dr. Haemin Paik and Shobhit Pandey. Dr. Paik's dedication has helped me in many ways as a researcher and friend, and for that I am truly grateful. Thanks to Shobhit his help in our exploring of pushing the bounds of solid acid electrochemical cells and for the ponderings of the future. Thanks also to Dr. Sheel Sanghvi for the hours of troubleshooting and brainstorming. Thanks to my group cohort Xin Qian and fellow Vol Connor Carr for their help with various research challenges and support throughout. Also, thanks to Louis Wang and Elise Goldfine for the experiments they have assisted me with. Thanks to the incumbent glovebox czar, Isaac Dyer, I know Gondor is in good hands. Thanks also to Dalton Cox and Grace Xiong for the notes along the way.

Several collaborators outside of our group aided in many ways to this work. Thanks to Claudia Battistella for her help with the rotary evaporator and Aleia Bellcross for help with surface tension measurements. Thanks also for all the TEM work that Chi Zhang supported me with. Thanks to Professor Stephanie Brock and her group for providing us with the nickel phosphide catalysts. Thanks to Tirzah Abbott for the SEM and sputtering help whenever I needed it. Thanks to Rebecca Sponenburg for the ICP-OES aid and the numerous hours spent trying to dissolve various materials. Thanks also to the rest of the pytentostat team not yet mentioned including Jeremy Hitt, Michael Spencer, Sun Hwi Bang, and Yao Tong. They spent much time in this project that we became invested in, learned much along the way, and I am proud to have worked alongside them.

I would also like to acknowledge my funding sources who have made all the work here possible. This work would not have been possible without the financial support of the Advanced Research Projects Agency-Energy (ARPA-E) from the Department of Energy (DOE). I was supported by the Reliable Electricity Based on Electrochemical Systems (REBELS) and Renewable Energy to Fuels Through Utilization of Energy-Dense Liquids (REFUEL) programs for most of my experimental work. The projects and missions of the ARPA-E projects are particularly inspiring, and I am grateful to have had the opportunity to continue their mission. Additionally, I would like to thank the financial support from the JUAMI program as I was working on developing a python-based API to interface with the Arduino-based potentiostat. The democratization of knowledge and technology is a noble mission that I resonate with and I was glad to be able to aid this in whatever small ways I can.

I would not be where I am today without a host of teachers that taught me along the way, and I would like to opportunity to thank a few distinguished ones that I recall being pivotal for me. Thanks to Ms. Reeves for inspiring me to read everything I can pick up. Thanks to Mr. Green who always fielded my off-the-wall questions and dug to the bottom of them. Thanks to Ms. Finley who showed me the alchemy turning the mundane to fascination. Thanks to Coach Holman who showed me how to push myself harder than I ever thought I could. Thanks to Ms. Diehm who showed me how to have confidence in myself. Thanks to Mr. Baker for helping me take a leap of faith.

Finally, I would like to thank my friends and family who have been loving and supporting of me in my journey. Thanks to my fellow aliens and outcasts Stephen Campbell and John Carney. Our historic escapades make for bonds impossible to break, but our greatest adventures still lie before us. Thanks to my mom for always believing in me and giving me every opportunity. Thanks to my dad for inspiring me and encouraging me to pursue my dreams. Thanks to my brother for always calling me back and entertaining our goofiest of ideas. Thanks to my wife, Kayce, for always loving and supporting me. Even when times are dark, she makes every day better and I look forward to our new life together.

List of Abbreviations

AC	Alternating Current
ACIS	Alternating Current Impedance Spectroscopy
AFC	Alkali Fuel Cell
AFM	Atomic Force Microscopy
ALD	Atomic Layer Deposition
ASU	Air Separation Unit
ASR	Area Specific Resistance
BET	Brunauer–Emmett–Teller
CA	Chronoamperometry
CDP	Cesium Dihydrogen Phosphate, CsH_2PO_4
CRL	Chemical Reaction Layer
CV	Cyclic Voltammetry
CVD	Chemical Vapor Deposition
DC	Direct Current
dFLW	Distributed Finite-Length Warburg
DRIFTS	Diffuse Reflectance Infrared Fourier Transform Spectroscopy
EDS, EDX	Energy Dispersive X-ray Spectroscopy
EIS	Electrochemical Impedance Spectroscopy
EL	Electrocatalyst Layer
FCC	Face-centered Cubic
fCNT	Functionalized Carbon Nanotubes
GDL	Gas Diffusion Layer
GHG	Greenhouse Gas
GUI	Graphical User Interface
HCP	Hexagonal Close-packed
HER	Hydrogen Evolution Reaction

HOR	Hydrogen Oxidation Reaction
IPA	Isopropyl Alcohol
LHV	Lower Heating Value
LMP	Locational Marginal Price
LSV	Linear Sweep Voltammetry
MCFC	Molten Carbonate Fuel Cell
MPL	Microporous Layer
MOCVD	Metal-organic Chemical Vapor Deposition
MS	Mass Spectrometry
MWCNT	Multi-walled Carbon Nanotubes
nGr	Nano-graphite
O&M	Operations and Maintenance
OCV	Open-circuit Voltage
ORR	Oxygen Reduction Reaction
PAFC	Phosphoric Acid Fuel Cell
PEMFC	Polymer Electrolyte Membrane or Proton Exchange Membrane Fuel Cell
PGM	Platinum Group Metals
PPA	Power Purchasing Agreement
SAEC	Solid Acid Electrochemical Cell
SAFC	Solid Acid Fuel Cell
SCCM	Standard Cubic Centimeters
SEM	Scanning Electron Microscopy
SOFC	Solid Oxide Fuel Cell
TBTDET	(tert-butylimido)tris(diethylamido) tantalum
TCD	Thermal Conductivity Detector
TCL	Thermal-cracking Layer
TEM	Transmission Electron Microscopy
TGA	Thermogravimetric Analysis

TPD	Temperature Programmed Desorption
UHP	Ultra-high Purity
V	Vulcan XC-72
XPS	X-ray Photoelectron Spectroscopy
XRD	X-ray Diffraction
XRF	X-ray Fluorescence

List of Symbols

Symbol	Meaning	Common Units
A	Area	cm^2
a	Activity	Dimensionless
ASR	Area Specific Resistance	$\Omega \cdot \text{cm}^2$
B	Angular Breadth	$^\circ$
C	Capacitance	F
C	Cost	\$
c	Concentration	mol/m^3
D	Diffusion Coefficient	cm^2/s
d	Distance	m
E	Thermodynamic ideal voltage	V
E_a	Activation Energy	J
F	Faraday Constant	96,485 C/mol
f	Frequency	Hz
G, g	Gibbs Free Energy	J, J/mol
H, h	Enthalpy	J, J/mol
i	Current	mA
j	Current Density	mA/cm^2
K	Shape Factor	Unitless
k	Boltzmann's Constant	$1.38 \times 10^{-23} \text{ J/K}$
M	Mass	g
N, n	Number	Dimensionless
P	Pressure	bar, atm, Pa
Q	Charge	C
Q	Heat	J
R	Ideal Gas Constant	8.314 J/mol·K
R	Resistance	Ω
R, r	radius	m
r	Reaction Rate	Hz
S, s	Entropy	J/K, J/mol·K
S, SA	Surface Area	cm^2
S_r	Shipping Rate	\$
T	Temperature	K
t	Time	s
t	Thickness	m

U	Internal Energy	J
W	Work	J
V	Voltage	V
V	Volume	L, cm ³
Z	Impedance	Ω
0	Standard or reference state (as superscript)	
rxn	Change in a reaction (as subscript)	
s	On the surface (as subscript)	
α	CPE Ideality Constant	Dimensionless
Δ	Denotes a change in a quantity	Dimensionless
δ	Diffusion Layer Thickness	m
ε	Efficiency	Dimensionless
ε	Porosity	Dimensionless
θ	Fractional Area Coverage	Dimensionless
λ	Wavelength	nm
μ	Chemical Potential	J
σ	Warburg Coefficient	$\Omega/s^{0.5}$
τ	Tortuosity	Dimensionless
ϕ	Phase Factor	Dimensionless
ω	Angular Frequency	rad/s

Dedication

To my mother,

who built me up in everything I ever did

To my father,

who inspired me to make something of my own

To my brother,

who always wondered with me how the world could be

To my wife,

who was there with me every step of the way

Table of Contents

Chapter 1 Introduction	26
1.1 Overview	26
1.2 Electrochemical Cells	27
1.3 CsH₂PO₄ as an electrolyte	29
1.4 Catalysis	33
1.4.1 General Principle	33
1.4.2 Mechanisms of Heterogeneous Catalysis	35
1.4.3 Breaking the scaling relation	37
Chapter 2 Experimental	41
2.1 DC Electrochemical Techniques	41
2.1.1 Linear Sweep Voltammetry	41
2.1.2 Constant Potential/Current Techniques	42
2.1.3 Cyclic Voltammetry	43
2.2 AC Impedance Spectroscopy	43
2.2.1 Basic Principles	44
2.2.2 Physical Equivalent Circuit Models	45
2.3 X-ray Techniques	51
2.3.1 XRD	51
2.3.2 XRF	53
2.3.3 XPS	53
2.4 Chemical Vapor Deposition	54
2.4.1 MOCVD	54

	14
2.4.2 ALD	55
2.5 Cell Testing	56
2.5.1 Cell Fabrication	56
2.5.2 Testing Configuration	59
2.6 Adsorption Techniques.....	61
2.6.1 BET Method.....	61
2.6.2 Selective Chemisorption	63
Chapter 3 Hydrogen Electrooxidation	64
3.1 Introduction	64
3.1.1 A General Prospective	64
3.1.2 In Solid Acid Cells	66
3.2 Monometallic Systems	69
3.2.1 Platinum	69
3.2.2 Palladium.....	75
3.2.3 Ruthenium.....	79
3.3 Multimetallic Systems	87
3.3.1 Platinum-Ruthenium	88
3.3.2 Ruthenium-Palladium	93
3.3.3 Platinum-Palladium-Ruthenium.....	94
3.3.4 Platinum-Nickel	95
3.4 Metal Phosphides	97
3.4.1 Nickel Phosphide	97
3.4.2 Nickel Rhodium Phosphide.....	99

	15
3.5 Summary.....	100
Chapter 4 Ammonia Oxidation	102
4.1 Introduction.....	102
4.1.1 Ammonia Decomposition.....	103
4.1.2 Alkali Promotion of Ammonia Decomposition.....	105
4.1.3 Ammonia Electrooxidation.....	106
4.2 Ammonia Decomposition in Solid Acid Cells.....	106
4.2.1 Anode Development.....	108
4.3 Incorporating Promoters in Solid Acid Cells.....	112
4.3.1 Two-Layer Configuration.....	112
4.3.2 Investigating Phenomena in the Hybrid Cell Anode Compartment.....	118
4.4 Summary.....	128
Chapter 5 The Economic Case for Solid-Acid Ammonia Synthesis.....	130
5.1 Market	131
5.2 Logistics	134
5.3 Comparison to Hydrogen.....	136
5.4 Technoeconomic Analysis	138
5.5 Competitive Advantage.....	145
5.6 Summary.....	146
Appendix A Derivations	147
A.1 Relation Between the Free Energy of a Reaction and the Nernst Potential	147
A.2 Generalized Thermodynamic Electrochemical Potential.....	148
A.3 Overall Rate of Adsorption Reaction	150

Appendix B Calculations	151
B.1 Theoretical Maximum Catalyst Surface Area for a Given Support	151
B.2 Effect of Porosity and Tortuosity on Diffusivity	154
B.3 Thermodynamic Potential for Ammonia Decomposition System	154
B.4 Efficiency calculation for ammonia decomposition for SAEC	157
B.5 Ammonia Detection in Cathode Exhaust	157
B.6 Cost of Ammonia Transport by Truck in a Given Area by Production Volume	158
Appendix C Auxiliary Experiments	159
C.1 Ceiling for Metal Loading on CNT	159
C.2 BET Method Analysis for Supports Implemented	159
C.3 Pt/V Selective Chemisorption Experiment	161
C.4 Ru Ambient Condition Degradation	163
C.5 Probing the Oxidation State of In-house synthesized Ru	163
C.6 Ru Loading Determination by TGA	167
C.7 Optimizing C:CDP ratio on Vulcan XC-72	168
C.8 Ru/V Selective Chemisorption Experiment	169
C.9 Incorporating CsNO₃ into CDP	172
C.10 In-Operando Mass Spectrometry Tests for Ammonia Decomposition Cell	174
C.11 Investigating Different Cs Promoters and Cs as an Anion Snatcher	176
Appendix D Miscellaneous Experiments	179
D.1 ALD films for CsH₂PO₄-based Electrochemical Cells	179
D.2 Electroreduction of CO₂	185

Appendix E Software Developed.....	188
E.1 Electrochemical Impedance Fitting Program (ECIF).....	188
E.2 Pytentiostat.....	191
References.....	197

List of Figures

Figure 1.1 Schematic of a H ₂ /O ₂ fuel cell	27
Figure 1.2 Gravimetric Ragone Plot.....	29
Figure 1.3 CDP phase diagram.....	32
Figure 1.4 Catalyst free energy diagram.....	33
Figure 1.5 Relationship of catalyst parameters with the binding affinity	34
Figure 1.6 Relative oxygen chemisorption potential for the 4d metals	36
Figure 1.7 Nitrogen adsorption energy versus transition state energy and reaction turnover frequency ..	37
Figure 2.1 Linear sweep voltammetry voltage profile	42
Figure 2.2 Chronoamperometric voltage profile.....	42
Figure 2.3 Cyclic voltammetry voltage profile	43
Figure 2.4 Sinusoidal voltage perturbation and current response	44
Figure 2.5 Nyquist plot depictions for equivalent circuit elements	47
Figure 2.6 EIS data and fit for example impedance data	48
Figure 2.7 Demo of RRQ circuit with varied parameters	49
Figure 2.8 Nyquist plots of diffusion-based Warburg elements	51
Figure 2.9 Diagram of ALD system.....	55
Figure 2.10 Schematic of standard counter electrode supported electrochemical cell	58
Figure 2.11 Schematic of electrochemical testing station.....	59
Figure 2.12 BET plot with fitting constants.....	62
Figure 3.1 Electrochemical HOR measurements for Pt symmetric cell	69
Figure 3.2 XRD of 74 wt% Pt on MWCNTs produced by the NaBH ₄ reduction method.....	71
Figure 3.3 SEM and size distributions of 30% Pt/MWCNTs	72
Figure 3.4 Electrochemical HOR measurements of 74 wt% Pt/fCNT cell	73
Figure 3.5 Electrochemical HOR measurements of 74 wt% Pt/V cell	74
Figure 3.6 Electrochemical HOR measurements of commercial 20 wt% Pd/V cell.....	75
Figure 3.7 Stability tests for commercial 20 wt% Pd/C cell.....	76
Figure 3.8 Impedance and cell cross-sections of 20 wt% Pd/V symmetric cells	77

Figure 3.9 Impedance and cell cross-sections of Pd:CDP 3:7 electrode cells	78
Figure 3.10 Electrochemical HOR measurements of 61 wt% Pd/V cell	79
Figure 3.11 Non-ohmic resistances of 62 wt% Ru/fCNT-COOH cells as a function of C:CDP ratio	80
Figure 3.12 Electrochemical HOR measurements of 62 wt%Ru/fCNT C:CDP 1:3 cells with and without catalyst annealing	81
Figure 3.13 Electrochemical HOR measurements of 62 wt% Ru/fCNT cells of varying C:CDP and varying support functionalization	81
Figure 3.14 Electrochemical HOR measurements of Ru and Pt on fCNT cells in the dilute hydrogen condition as a function of water partial pressure.....	82
Figure 3.15 Electrochemical HOR analysis of 60 wt% Ru/V cell	83
Figure 3.16 Electrochemical HOR analysis of Ru and Pt on Vulcan XC-72 as a function of water partial pressure	83
Figure 3.17 Cyclic voltammetry scans under the dilute hydrogen condition of 60 wt% Ru/V cell	84
Figure 3.18 Integrating 60 wt% Ru/V cyclic voltammetry scans as a function of scan rate.....	85
Figure 3.19 Chronoamperometric voltage profiles for test in dilute hydrogen condition on a 60 wt% Ru/V cell.....	86
Figure 3.20 Magnified results of reducing and oxidizing chronoamperometric steps.....	86
Figure 3.21 Calculated Pt-Ru phase diagram	88
Figure 3.22 XRD of RuPt/V catalysts	89
Figure 3.23 TEM and EDS of Ru ₈ Pt ₂ /V catalyst.....	89
Figure 3.24 OCV reaction resistance and polarization curves under the dilute hydrogen condition for RuPt/V cells.....	90
Figure 3.25 Catalyst crystallite size before and after operation for RuPt/V as determined by XRD.....	91
Figure 3.26 Stability electrochemical HOR measurement of Ru ₈ Pt ₂ /V sample	91
Figure 3.27 HOR polarization curves for RuPt/fCNT-COOH samples.....	92
Figure 3.28 XRD of Ru ₈ Pd ₂ /V in relation to the Ru/V sample	93
Figure 3.29 HOR polarization curve of Ru ₈ Pd ₂ /V in relation to Ru, Pt, Pd, and RuPt samples.....	94
Figure 3.30 XRD of Ru ₈ Pd ₁ Pt ₁ /V sample in relation to the Ru/V sample.....	94

Figure 3.31 HOR activity in the Ru-Pt-Pd ternary system.....	95
Figure 3.32 XRD and XPS characterization of Ni@Pt/V	96
Figure 3.33 Electrochemical HOR measurements for Ni@Pt/V.....	97
Figure 3.34 XRD of Ni ₂ P before and after annealing	98
Figure 3.35 Electrochemical HOR measurements for Ni ₂ P/V	98
Figure 3.36 XRD of Ni _{1.6} Rh _{0.4} P/V	99
Figure 3.37 Electrochemical HOR measurements for Ni _{1.6} Rh _{0.4} /V	100
Figure 4.1 Free energy of ammonia decomposition as a function of temperature	106
Figure 4.2 Efficiency of ammonia decomposition as a function of voltage	107
Figure 4.3 Schematic of ammonia decomposition SAEC	107
Figure 4.4 Electrochemical ammonia decomposition measurements of 62 wt% Ru/fCNT cell	108
Figure 4.5 Polarization curves under ammonia condition of Pt and Pd-based catalyst electrodes in comparison to Ru	109
Figure 4.6 Polarization curves under ammonia condition for RuPt/fCNT electrodes.....	109
Figure 4.7 Polarization curves under ammonia condition for Ni-based catalyst electrodes	110
Figure 4.8 Electrochemical reaction resistance as a function of C:CDP ratio and polarization curves comparing fCNT-COOH vs. Vulcan XC-72 as a support	111
Figure 4.9 Polarization curves of 62 wt% Ru/fCNT under the ammonia condition as a function of support type and C:CDP ratio	111
Figure 4.10 Schematic of two-layer ammonia decomposition cell.....	112
Figure 4.11 Electrochemical measurements under dilute hydrogen and ammonia conditions for the hybrid cell	113
Figure 4.12 Determined hydrogen production rates from the cell as a function of current and voltage under the ammonia conditions	114
Figure 4.13 Comparison of polarization curves of bilayer electrode and single component electrodes under the ammonia condition.....	117
Figure 4.14 Comparison of hydrogen generation rate for the hybrid cell vs. the production rate from prior work by thermal decomposition	117

Figure 4.15 XRD patterns for stability of CDP and showing the state of the catalyst before and after being placed under humidified reducing conditions.....	118
Figure 4.16 TGA of CsNO ₃ , 60 wt% Ru/CNT, and 60 wt% Ru/CNT treated with CsNO ₃ under dry and wet reducing conditions at operating temperature.....	120
Figure 4.17 HSC calculation for CsNO ₃ stability in a range of reducing conditions.....	120
Figure 4.18 Thermodynamic CsNO ₃ -CsOH phase diagram and H ₂ O-CsOH phase diagram	121
Figure 4.19 XPS of 40 wt% Ru-nGr treated with CsNO ₃ before and after operation under the ammonia condition.....	121
Figure 4.20 XPS of tube furnace annealed 40 wt% Ru/nGr in either dry or wet ammonia conditions and promoted or unpromoted sample as well as a comparison of an as prepared unannealed sample with a sample annealed under nitrogen and a sample annealed under ammonia.....	122
Figure 4.21 Polarization curves with the as-prepared and the pre-nitrided catalysts	123
Figure 4.22 Electrochemical measurements of CsOH promoted 40 wt% Ru/nGr over a 48 hour period under constant current in the ammonia condition.....	124
Figure 4.23 XRD and TEM analysis of CRL powder after various periods of operation.....	125
Figure 4.24 In-situ XRD for the Cs-promoted 40wt% Ru/nGr sample under ammonia	126
Figure 4.25 Electrochemical measurements and XRD of RuO ₂ /V sample	127
Figure 4.26 Electrochemical ammonia measurements as a function of CRL thickness.....	128
Figure 5.1 Spatial distribution of nitrogenous fertilizer use in the US	131
Figure 5.2 Predicted levels of curtailment as a function of renewables penetration and the price of electricity at a given node in the MISO region as a function of windspeed	133
Figure 5.3 Map showing spatial distribution and scale of energy storage in the US and map showing distribution of wind power sources by capacity.....	134
Figure 5.4 Amount of ammonia transported by mode and by season	136
Figure 5.5 Schematic of ammonia synthesis SAEC	139
Figure 5.6 Ammonia synthesis SAEC workflow diagram and energy consumption breakdown	140
Figure 5.7 Unit economics for ammonia synthesis SAEC as a function of electricity price.....	141
Figure 5.8 Settlement point prices for nodes by time of day in January 2019.....	142

Figure 5.9 Cost of shipping by truck for a given fractional area of land dedicated to heavily nitrogen dependent crops based on ammonia synthesis SAEC annual production rate.....	143
Appendix Figure B.1-1 Schematic of model used for catalyst surface area.....	151
Appendix Figure B.1-2 Particle size and surface area relations.....	152
Appendix Figure B.1-3 Total possible weight fraction of catalyst loading and max surface area as a function of particle size.....	153
Appendix Figure B.2-1 Effect of porosity and tortuosity on effective diffusivity.....	154
Appendix Figure B.3-1 Nernst potential as a function of gas partial pressures at an operating temperature.....	154
Appendix Figure B.3-2 Solving for equilibrium ammonia conversion.....	156
Appendix Figure C.1-1 Non-ohmic resistance under ammonia for various Ru.MWCNT samples as a function of Ru loading	159
Appendix Figure C.2-1 BET method measurements for supports.....	161
Appendix Figure C.2-2 Incremental pore volume plots for supports	161
Appendix Figure C.3-1 Results of selective chemisorption experiments for 74 wt% Pt/V	162
Appendix Figure C.4-1 Polarization curves of HOR for 60wt% Ru/V after waiting a variable amount of days under ambient conditions	163
Appendix Figure C.5-1 XRD of 62 wt% Ru/fCNT-COOH	163
Appendix Figure C.5-2 TEM of Ru/fCNT with particle size distribution	164
Appendix Figure C.5-3 TEM image of Ru/nGr treated with CsNO ₃ after 1100 hours of operation	164
Appendix Figure C.5-4 TGA of Ru heated under air and then reduced	165
Appendix Figure C.5-5 XPS and Raman analysis of Ru/nGr treated with CsNO ₃ samples with various operating times.....	165
Appendix Figure C.5-6 XRD and TEM analysis of RuO ₂ samples.....	166
Appendix Figure C.6-1. TGA and XRD analysis of MWCNT support.....	167
Appendix Figure C.6-2 TGA analysis of Ru/fCNT-COOH support heated under air then reducing conditions.....	168

Appendix Figure C.7-1 Electrochemical measurements of Ru ₉ Pt ₁ /V cells with various C:CDP ratios...	168
Appendix Figure C.7-2 Post-operation cross-section for 60 wt% Ru/V cell	169
Appendix Figure C.8-1 Selective chemisorption for 60 wt% Ru/V.....	169
Appendix Figure C.8-2 Amount of CO adsorbed per pulse under two prereduction conditions.....	170
Appendix Figure C.8-3 CO-DRIFTS experiment for 60 wt% Ru/V	170
Appendix Figure C.8-4 TPD experiment of CO for all cycles for the 60 wt% Ru/V sample	171
Appendix Figure C.9-1 Raman and FTIR analysis of CsNO ₃ -doped CDP	172
Appendix Figure C.9-2 In-situ XRD of CsNO ₃ -doped CDP sample.....	173
Appendix Figure C.10-1 Hydrogen flow rate as determined from mass spectrometry as a function of voltage under a symmetric humidified nitrogen environment	174
Appendix Figure C.10-2 Time evolution of mass spectrometry signals of relevant gas species as a function of voltage under the ammonia condition	175
Appendix Figure C.10-3 Hydrogen flow rate as determined by MS and as implied from the current under the ammonia condition as a function of voltage.....	175
Appendix Figure C.11-1 XRD analysis of Ru/nGr with various promoters	177
Appendix Figure C.11-2 XPS of CRL powders after various periods of operation.....	177
Appendix Figure C.11-3 XPS analysis of promoted Ru/nGr samples after annealing under dry conditions, XRD analysis of CsOH-promoted samples before and after annealing under nitrogen, and XPS of nGr support and CsOH promoted Ru/nGr annealed under argon.....	178
Appendix Figure C.11-4 XRD of CsOH/V before and after anneal under nitrogen and XPS of Vulcan XC-72 support	178
Appendix Figure D.1-1 Schematic of ALD barrier implemented in SAFC cathode	179
Appendix Figure D.1-2 XPS of tantalum nitride and oxide ALD films.....	181
Appendix Figure D.1-3 XPS analysis of Ta ₂ O ₅ /Pd/MgO samples before and after wet air annealing ...	182
Appendix Figure D.1-4 Sandwich cell tests with and without tantalum oxide barrier layers	183
Appendix Figure D.1-5 Flat cell test for 1 nm barrier layer cell under fuel cell operating conditions.....	184
Appendix Figure D.1-6 XRD analysis of CDP after annealing under CO ₂	185
Appendix Figure D.2-1 Pictures of filtrate of Au/V synthesis by NaBH ₄ reduction and XRD of Au/V.....	185

Appendix Figure D.2-2 Electrochemical CO ₂ reduction test.....	186
Appendix Figure D.2-3 CO ₂ reduction test for 20 wt% Au/V catalyst.	187
Appendix Figure E.2-1 Relative read versus assigned voltage on potentiostat as a function of number averaging and rest time changing.	194
Appendix Figure E.2-2 Optimizing resolution with required time per point guidelines	194
Appendix Figure E.2-3 Pytentiostat GUI interface.....	196

List of Tables

Table 1.1 Comparison of Common Fuel Cell Types	31
Table 5.1 Annualized Metrics for SAEC Cases Considered	144
Appendix Table C.2-1 BET Analysis of Supports.....	160
Appendix Table C.3-1 Pt/V Chemisorption Calculation Details	162
Appendix Table C.8-1 Ru/V Chemisorption Calculation Details	170
Appendix Table D.1-1 Ta-based ALD films deposition parameters.....	180

Chapter 1 Introduction

Chemistry without catalysis, would be a sword without a handle, a light without brilliance, a bell without sound. - Alwin Mittasch

1.1 Overview

Solid acid electrochemical cells (SAECs) implementing CsH_2PO_4 (CDP) based electrolytes have a distinct advantage over traditional electrochemical systems in that they can operate at intermediate temperatures near 250 °C. This factor alone gives SAECs advantages in kinetics and fuel flexibility over cooler operating systems and advantages in cost and portability over warmer operating systems. Initially being demonstrated as fuel cells (SAFCs) in 2004¹, SAECs have made leaps and bounds in technological development and deployment. Utilizing their capacity to withstand rugged environments, SAECs have been developed for applications ranging from propane-to-electricity portable power units for the Army to efficient remote power for cold oil and gas drilling sites that reduces methane emissions and operating costs².

Featuring CDP as the electrolyte, the key areas for innovation in SAECs lie in opportunities to improve and tailor electrodes for reactions. Innovation in electrodes can improve cost, activity, stability, and selectivity. Furthermore, electrode investigation is key before looking at any unique reaction facilitation. This being the case, the goals of this work are to (1) improve electrodes for existing SAEC systems, (2) investigate electrodes for novel SAEC systems, and (3) understand simultaneously what drives these reactions on a fundamental level with a particular focus on catalysis.

In this chapter, an introduction to electrochemical cells as a framework for facilitating chemical reactions is presented (Section 1.2). Different types of electrochemical cells as defined by their electrolytes used are then explored with a particular focus on the unique benefits of employing CDP (Section 1.3). Finally, catalysis will be discussed both from a fundamental basis and in the context of how insights from this knowledge can aid in the design of future electrodes (Section 1.4).

1.2 Electrochemical Cells

An electrochemical cell is, in essence, a device that isolates the electronic component of a chemical reaction that involves the transfer of electrons from one molecule to another. This is performed by separating the chemical species that donates an electron from the species that accepts an electron and only providing two avenues for these species to interact. One avenue is through an insulating membrane (the electrolyte) that can conduct a chemically relevant ion while the other avenue is through an electronically conductive connection that does not intersect with the membrane and does not conduct the chemically-relevant ion. This dual-avenue setup necessitates that the course of the reaction is split into half-reactions spatially separated by the electrolyte. Ions and electrons must necessarily split and move in tandem to cross the electrolyte and complete the reaction. The part of the cell from which the electrons depart is known as the anode and the other portion when electrons are arriving is known as the cathode.

As a concrete example, let us consider a H_2/O_2 fuel cell with a proton conducting membrane (Figure 1.1). In this cell, hydrogen is supplied to the anode and oxygen (or often diluted oxygen from air) is supplied to the cathode. For the hydrogen and oxygen to react, the hydrogen molecule must lose two electrons which travel through an external circuit while the remaining protons can move through the membrane. The protons meet again with oxygen ions at the same time as the electrons arrive to form water.

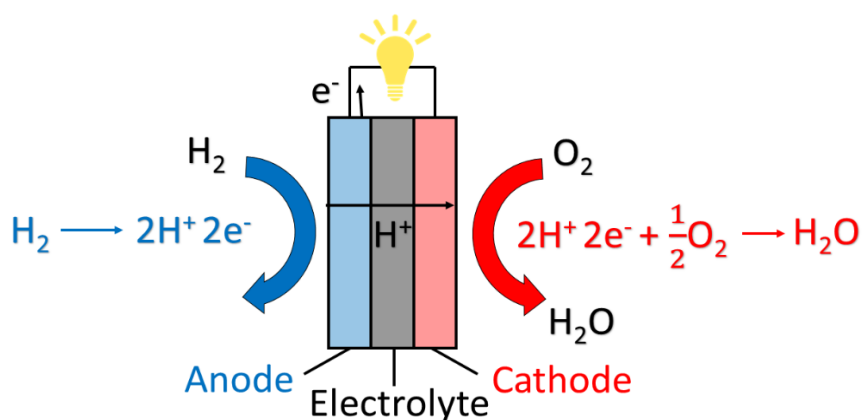


Figure 1.1 Schematic of a H_2/O_2 fuel cell with a proton conducting membrane displaying the half-reactions that take place at each electrode.

Since the H₂/O₂ reaction is spontaneous at standard conditions ($\Delta G_{rxn} = 237$ kJ/mol), an equivalent downhill electrical potential is formed (1.23 V) according to Equation 1.1 that can be used to drive electrical work, where E^0 is the standard-state reversible voltage, $\Delta \hat{g}_{rxn}^0$ is the standard-state free energy, n is the number of electrons transferred per unit reaction, and F is Faraday's constant. The relation between Gibbs Free Energy and the Nernst Potential derived in Appendix A.1.

$$E^0 = \frac{-\Delta \hat{g}_{rxn}^0}{nF} \quad (1.1)$$

Since the free energy of the reaction varies with temperature, pressure, and activity, so to the electrical potential varies with environmental conditions. This leads to the generalized form of the expression expressed in Equation 1.2, where E is the generalized thermodynamic cell voltage, $\Delta \hat{s}_{rxn}^0$ is the standard state entropy of the reaction, T is the temperature at which the reaction is carried out, T_0 is the standard-state temperature, R is the gas constant, a is the activity of a component, and v is the component coefficient. The generalized thermodynamic electric potential is derived in Appendix A.2.

$$E = E^0 + \frac{\Delta \hat{s}_{rxn}^0}{nF} (T - T_0) - \frac{RT}{nF} \ln \frac{\prod a_{products}^{v_i}}{\prod a_{reactants}^{v_i}} \quad (1.2)$$

While the current system described can draw electrical work from the free energy of water formation, it can also be used to facilitate the inverse reaction; an electric load applied can drive the splitting of water to hydrogen and oxygen. To do so, the potential must be flipped to where an oxidizing electric potential is applied on the former cathode and a reducing potential applied on the former anode. These two examples show the typical use cases of an electrochemical cell; the first described case draws electrical power from a spontaneous chemical reaction and the second utilizes electrical power to drive an otherwise unfavorable reaction. There are some other uses for electrochemical cells, such as in sensors (taking advantage of well-defined Nernst potentials formed) and gas purifiers (taking advantage of selective ion conductivity of electrolytes, but in this work the first two applications will be the most deeply considered.

It is valuable to distinguish between common types of electrochemical cells, namely between cells like the previously described fuels cells from batteries. The main distinguishing factor between these types of systems is whether they are open or closed. The H₂/O₂ fuel cell relies on a continual input of hydrogen and air for continuous operation while simultaneously exhausting water and unused reactants. This

necessarily makes the H_2/O_2 fuel cell an open system that requires inputs from and outputs to the external environment. A battery on the other hand relies on closed system electrodes that entirely contain the chemical components used. In the battery case, ions, after being transferred through the electrolyte, are stored in the opposing electrode (unless brought back to the original electrode in the case of rechargeable batteries). This being the case, the size of the electrodes determines the energy capacity for a battery.

While both designs of electrochemical are employed for energy storage, they are typically seen as complementary in their application rather than competitive. Due to their high efficiency, compactness, and power density, batteries are often sought as energy storage solutions for small to medium-sized (e.g., automobile) applications that require storage on the time scale from hours to days long storage with a lifetime on the order of years. Fuel cells, on the other hand, are sought for medium-sized (e.g., heavy-duty truck) to large scale storage for storage on the time scale from weeks to months with a lifetime on the order of decades. The Ragone plot shown in Figure 1.2 illustrates this distinction with relation to other energy storage technologies. It should be noted that additional factors can affect use cases based on the solutions currently implemented, such as the time required to load up the energy storage device, availability of sites to load from, and environmental considerations. In our specific case, CDP as an electrolyte could technically be employed in a closed battery configuration (similar to a nickel metal hydride battery), but for all practical purposes is used in open systems so further discussion herein will be limited to open systems.

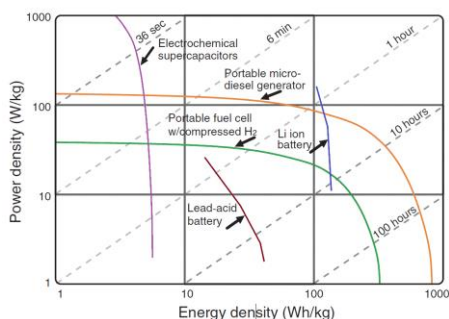


Figure 1.2 Gravimetric Ragone plot for various energy storage solutions showing tradeoff from energy and power density. Dashed lines indicate contours of constant lifetime for various power to energy density ratios. This figure was adapted from O'Hayre³ and is reprinted with permission.

1.3 CsH_2PO_4 as an electrolyte

Materials implemented for electrolytes are restrictive in their use cases, particularly regarding the temperature range in which they can be implemented. This being the case, fuel cells are typically classified by the electrolyte membrane used which is dictated by the operating temperature that can be used to

achieve sufficient ionic conductivity while the electrolyte remains stable. This leads lower temperature fuel cells to being those that transport smaller ions such as protons while higher temperature fuel cells can afford to transport bulkier ions such as oxygen. A comparison of the most common fuel cells as defined by employed electrolyte is shown in Table 1.1⁴. More detailed comparisons of fuel cell technologies are discussed in Chapter 8 of O'Hayre et al³.

Broadly speaking, fuels cells can be placed into categories of low (less than 200 °C) and high (greater than 500 °C) temperature operation. Generally, low temperature fuel cells are lacking in terms of fuel flexibility (i.e., requires high-purity hydrogen) and have slower kinetics from their lower temperature of operation. On the other hand, high temperature fuel cells are less portable, have longer ramping times, and have more expensive auxiliary components. Phosphoric Acid Fuel Cells (PAFCs) are the closest to bridging this gap, with higher fuel tolerances [1% CO tolerance as opposed to the 50 ppm CO tolerance of Polymer Electrolyte Membrane Fuel Cells (PEMFCs) and Alkaline Fuel Cells (AFC)] and operate around a modest 200 °C that is suitable for portable applications, but they suffer from a range of other issues including their use of a corrosive liquid electrolyte that volatilizes over time³.

A class of electrolyte materials known as solid acids, mitigate these challenges by operating an intermediate temperature zone. Solid acids achieve a high ionic conductivity by undergoing a phase transition to a disordered phase at elevated temperatures, which allows the oxyanion groups to almost freely reorient and thus increases the protonic conductivity by several orders of magnitude. This drastic change in conductivity has led to this phase transition being referred to as "superprotonic". Among this class of materials, CDP has emerged as a successful candidate material boasting a desirable operating temperature (240-260 °C⁵) and remarkable stability under a wide range of fuel impurities including H₂S, NH₃, CH₃OH, CH₄, C₃H₈ and CO. For comparison, CDP-based cell has shown tolerance to up to 20% CO in the fuel stream⁶.

Table 1.1 Comparison of Common Fuel Cell Types

FUEL CELL TYPE	COMMON ELECTROLYTE	OPERATING TEMPERATURE	TYPICAL STACK SIZE	ELECTRICAL EFFICIENCY (LHV)	APPLICATIONS	ADVANTAGES	CHALLENGES
Polymer electrolyte membrane (PEMFC)	Perfluorosulfonic acid	<120 °C	<1 kW–100 kW	60% direct H ₂ ; 40% reformed fuel	Backup power Portable power Distributed generation Transportation Specialty vehicles	Solid electrolyte reduces corrosion and electrolyte management problems Low temperature Quick start-up and load following	Expensive catalysts Sensitive to fuel impurities
Alkaline (AFC)	Aqueous potassium hydroxide soaked in a porous matrix, or alkaline polymer membrane	<100 °C	1–100 kW	60%	Military Space Backup power Transportation	Wider range of stable materials allows lower cost components Low temperature Quick start-up	Sensitive to CO ₂ in fuel and air Electrolyte management (aqueous) Electrolyte conductivity (polymer)
Phosphoric acid (PAFC)	Phosphoric acid soaked in a porous matrix or imbibed in a polymer membrane	150 – 200 °C	5–400 kW, 100 kW module (liquid PAFC) <10 kW (polymer membrane)	40%	Distributed generation	Suitable for CHP Increased tolerance to fuel impurities	Expensive catalysts Long start-up time Sulfur sensitivity
Molten carbonate (MCFC)	Molten lithium, sodium, and/or potassium carbonates, soaked in a porous matrix	600 – 700 °C	300 kW–3 MW, 300 kW module	50%	Electric utility Distributed generation	High efficiency Fuel flexibility Suitable for CHP Hybrid/gas turbine cycle	High temperature corrosion and breakdown of cell components Long start-up time Low power density
Solid oxide (SOFC)	Yttria stabilized zirconia	500 – 1,000 °C	1 kW–2 MW	60%	Auxiliary power Electric utility Distributed generation	High efficiency Fuel flexibility Solid electrolyte Suitable for CHP Hybrid/gas turbine cycle	High temperature corrosion and breakdown of cell components Long start-up time Limited number of shutdowns

The main consideration in stabilizing CDP for these cells is that a humid environment must be maintained as is shown in Figure 1.3⁷.

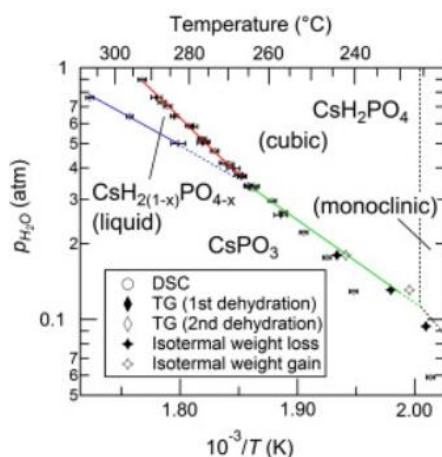


Figure 1.3 The $p_{\text{H}_2\text{O}}$ and temperature dependence on the formation of the cubic superprotonic phase for CDP⁷. Figure reproduced with permission.

Another challenge in employing CDP as an electrolyte is its chemical compatibility with candidate catalyst materials. For reasons that will be discussed in detail in Section 1.4, CDP-based electrochemical cells employ CDP in the electrode as well as in the electrolyte in a composite form with the catalyst and sometimes a support. The CDP in this situation must be in contact with the catalyst and therefore must be chemically stable with the catalyst. As Louie found in her thesis, many promising candidate catalyst materials react with CDP; this is particularly true with oxides⁸. Of note is the case with Pd which can lead to a $\sim 4x$ decrease in the ORR reaction resistance as compared to Pt, but is unstable due to CDP's reaction with Pd⁹. This has led to significant efforts to implement mechanisms to prevent this reaction without impeding electrochemical activity (e.g., ALD barriers in Appendix D.1). Barring any breakthroughs in this area (e.g., the discovery of a chemically stable mixed electronic/ionic conducting material that can be employed in SAECs or the discovery of an entirely new electrolyte material that is more universally chemically compatible), catalyst stability with CDP remains a challenge.

Compared to current state of the art, robustness and fuel flexibility are the main attractive advantages of employing SAFCs in situations which, if not for these qualities, PEMFCs might otherwise be used. With developments in improving microstructure, stability, and catalyst design SAFCs could possibly even compete in currently implemented PEMFC applications. To effectively use SAEC fuel flexibility for

broader applications or to improve the reactions for existing SAFC applications it is crucial to tailor the catalysts used for each situation. To accomplish this, it is helpful to understand the fundamental catalysis mechanism, which serves as a guide for catalyst design and will be explored in the next section.

1.4 Catalysis

1.4.1 General Principle

Catalysts are materials that increase the rate of a reaction without being consumed. This is accomplished by providing an alternative reaction path that has a lower activation energy as illustrated in Figure 1.4. This enables reactions that were otherwise kinetically blocked or prohibitively slowed. Catalysts, however, do not make the net reaction thermodynamically more favorable. When catalysts appear in the same phase as the reactants, the catalyst is termed as homogeneous, while if the catalysts and the reactants are in different phases the catalysts are termed as heterogeneous. As electrochemical reactions often occur at the interphase of a solid with either a liquid or gas reactant, we will exclusively explore the fundamentals of heterogeneous catalysis, though some materials discussed will still have the capacity to be applied to the homogeneous case.

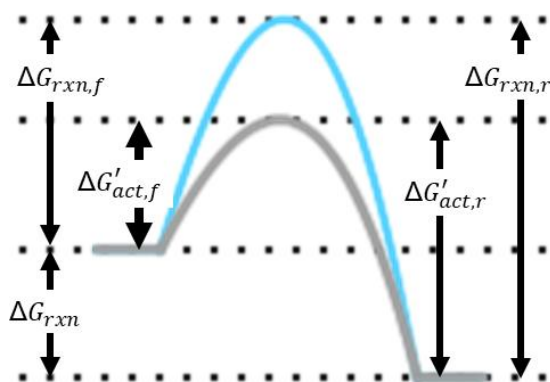


Figure 1.4 Free energy diagram for an uncatalyzed reaction (shown in blue) and the same reaction catalyzed (shown in grey). f denotes the forward reaction while r denotes the reverse reaction. This demonstrates while a catalyst lowers the activation barrier, the free energy change associated with the reaction stays the same.

In the heterogenous case, for a reaction of reactant A converting to B to be catalyzed, A must first absorb to the catalyst surface S . This can be represented by the following equation:



where k_1 denotes the rate constant for adsorption of A to S (i.e., the binding affinity), while k_2 denotes the rate constant of the conversion of A to B and the desorption of B from S . In the case of a gas phase reactant, this gives the overall reaction rate r which is dependent on the number of surface sites N_s , reactant pressure p , and fraction of the surface that is covered with the reactant θ using an extension of the Michaelis-Menten model¹⁰:

$$\frac{r}{A_s} = k_2\theta = \frac{k_2k_1p}{1+k_1p} \quad (1.4)$$

In this description, k_1 is dictated by the binding energy to which it is negatively correlated. Lower binding energies lead to a higher k_1 and thus a higher rate of absorption and a higher θ . The relationship between k_1 and θ is depicted in Figure 1.5a. Lower binding energies will increase the fractional coverage of the reactant on the catalyst in a logistic manner until the catalyst surface is fully covered.

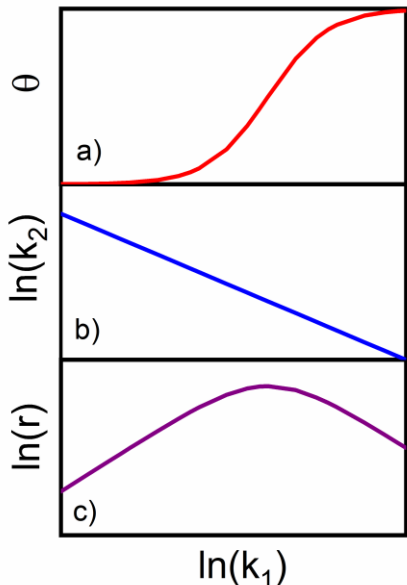


Figure 1.5 Relationship of a) fractional reactant coverage on the catalyst, b) rate of the release of the reactant, c) the overall rate of binding, conversion, and release vs. the binding affinity of the catalyst with the reactant (k_1).

Increasing the binding affinity (k_1) will lead to a higher surface coverage and will lower k_2 as desorption becomes more challenging (Figure 1.5b). Since both steps need to occur for the reaction to take place, a maximum rate of the total reaction exists with an intermediate binding affinity of the reactant to the catalyst. This makes the complete reaction capable of being defined with a unified descriptor k_1 :

$$\frac{r}{A_s} = k_2\theta = \frac{ck_1^{1-a}p}{1+k_1p} \quad (1.5)$$

where c is a constant independent of k_1 and a is the slope of the rate/equilibria relation for conversion and desorption (Figure 1.5c). This expression is derived in Appendix A.3. This concept of an optimal catalyst having a binding energy that is

neither too weak or too strong is known as Sabatier's principle. This relationship when graphed (see Figure 1.5c depiction) is known as a "volcano plot" for the characteristic inverted-V shape produced.

The main governing factors that determine catalyst effectiveness are the two previously mentioned: namely, how low is the transition state energy provided by the catalyst and how optimal is the binding affinity of the reactant to the catalyst. These factors arise from fundamental and predictable properties of prospective catalyst materials. In the next section we will explore the origins of how catalysts lower transition state energies, what governs their binding energies, and set a logical path for catalyst tunability.

1.4.2 Mechanisms of Heterogeneous Catalysis

In order to understand the key physics of heterogeneous catalysis we can look to the quantum mechanics of a molecule interacting with a surface using a one-electron description as described by Hammer and Nørskov¹¹. This one electron in the molecule will interact with the valence states of the metal surface atoms to form band(s) of states. The broad s-band is half filled (all the transition metals have one s electron in the metallic state) and the d-states form much narrower bands. The occupancy of these d-bands varies along the transition metals as they shift through the Fermi level^{11,12}.

Since d-bands are narrow, the interaction of an adsorbate state with the d-electrons of a surface often gives rise to bonding and antibonding states. The adsorbate state only broadens. The broad band limit with a single resonance is often called "weak chemisorption," whereas the split-off bonding and antibonding states is "strong chemisorption"^{11,13}.

To understand the transition from weak to strong chemisorption we can use depict what happens when a band of states is coupled to a single adsorbate level when the filling of the band is fixed. This condition leads to the center of the d-band shifting toward the Fermi level and the width of the band decreasing. The low broad band only has a single resonance, but upon shifting upward, the distinctive antibonding state appears above this band. The position of these antibonding states is above the Fermi level, so they are unoccupied. The strength of the bond is positively correlated with the number of empty antibonding states. This illustrates how a shift can occur between the two types of chemisorption. It is also noted from this from this example that another way of inducing strong chemisorption would be to shift the

bonding orbitals below the Fermi level and strong repulsion is possible if all of the antibonding orbitals are occupied when there is a large number of those states available.

This description suggests that the position and filling of the d-bands is critical to determining the bonding energy and final activation barrier. This is in fact particularly noticeable when considering that optimal catalysts for different adsorbates tend to align in columns for transition metals (e.g., Fe, Ru, Os for N₂ and Ni, Pd, Pt for H₂). For a concrete example, we can consider the oxygen chemisorption potential covariance with the d-band shift (see Figure 1.6), and the corresponding density of states (DOS) from which this arises. All of the group 10 elements have an intermediate binding energy for oxygen, while the group 11 elements are repulsive since their antibonding orbital is below the Fermi level¹¹.

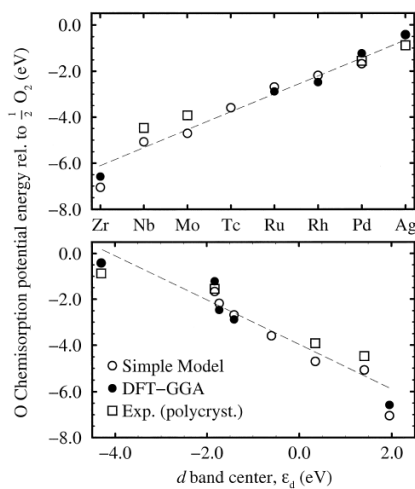


Figure 1.6 Relative oxygen chemisorption potentials across the 4d metals as a function of their d-band centers. Figure from the work of Hammer and Norskov¹¹ and is reprinted with permission.

There is also variance in transition state energies among transition metal groups due to Pauli repulsion. Due to the Pauli principle, no two electrons can be in the same state for a given molecule, so adsorbate 2p states must become orthogonal to the metal d states when they interact^{14,15}. Due to the 4d states being more extended than the 3d states and also the 5d states being more extended than the 4d states^{16,17}, there is an increase in orthogonalization energy moving down groups on the periodic table. It is also of note that cohesive energy increases along columns¹⁴.

Now understanding the origins of bonding energies, we can apply this knowledge and see how it impacts activity for a given reaction. Figure 1.7 shows the nitrogen binding energy versus activity for the

ammonia synthesis reaction¹⁸. This figure highlights something not earlier foreseen in that the transition state energy is inherently linked to the binding energy. Previously, what appeared to be two parameters that could be optimized is one factor when considering elemental composition: that is the binding energy. There are, however, other ways to impact the transition state that do not impact the binding energy and we will explore these methods in the next section.

1.4.3 Breaking the scaling relation

The first thing we can consider that breaks this scaling relation for transition metals is certain geometric effects. Some electronic effects are impacted by change in coordination too since lower coordination leads to smaller d-band widths with higher energies for metals with greater than half filled d-bands. As a simple example, we can examine the case of strain. While the chemical identity and coordination have remained the same, the only difference for the catalyst surface lies in the bond length. Tensile or compressive strains lead to either an increase or decrease in the amount of overlap between neighboring d-states and their bandwidths in tandem. D-bands will then move in energy to maintain constant filling and as a consequence will either shift the center of their d-band either up or down¹¹. This straining can be accomplished by a few methods, including by implanting ions of an inert gas in the lattice of a catalysts demonstrated by Gsell et al¹⁹. This led the catalyst to buckle and form compressive and tensile regions without changing the chemical identity or coordination of the surface. A second straining method involves depositing a thin layer of the catalyst of interest on top of another material with a different lattice constant. Pallassana and Neurock successfully showcased this technique with the deposition of Pd on Au, which made the catalyst much more active than Pd alone for the dehydrogenation of ethylene and ethyl solely by the difference of strain²⁰.

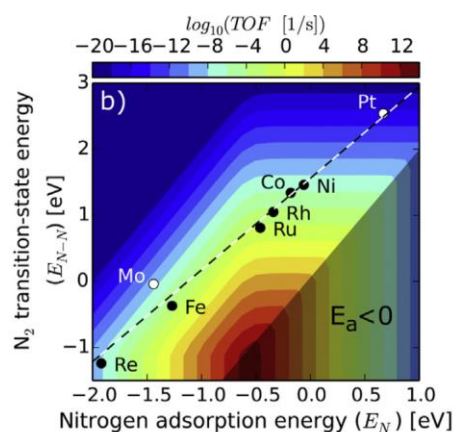


Figure 1.7 Nitrogen adsorption energy versus nitrogen transition state energies on various metals. Color here refers to the rate of the reaction in units of turnover frequency meaning times the reaction is carried out per site per second. Shaded area shows theoretical limit since the activation barrier must be greater than zero. Figure from Medford et al¹⁸. Reprinted with permission.

Facets also tend to have a significant impact both electronically and geometrically. In some simple cases the geometric and electronic effects can be isolated such as in the case of CO bonding to Pt. This is because CO undergoes atop bonding on all Pt faces, and thus experiences the same reaction geometries. The only differences arise from electronic differences, which neatly maps to d-band shifting. Geometric effects can then be determined by allowing ionic degrees of freedom for the adsorbed complex. One can then compare this with the restricted transition state case in which the geometries match and find the difference in transition state energy solely arising from geometric differences¹¹.

Variations in electronic structure increase in magnitude when considering defects such as steps, kinks, vacancies and adatoms. In some cases, there can be purely geometric differences such as the face of Ru(0001) where oxygen preferentially binds to three-fold *hcp* sites as opposed to two-fold bridge sites. Despite this, oxygen will preferentially bind to a two-fold site on a step due to the lower coordination raising the reactivity¹¹. This increased reactivity has been now broadly recognized as a general phenomenon for all heterogeneous catalysis reactions^{21,22}. This effect can be so powerful that in the case of N₂ adsorption on single crystal Ru(0001) the few present steps available completely dominate the reaction and no reactivity was measurable from the terrace^{23,24}.

A more complex pathway lies in alloying catalysts where both the electronic structure and possible bonding geometries change, while also leaving open the possibility of indirect effects (e.g., strain) if there is segregation between components. One example that takes advantage of electronic shifting is the case of dissolving a small amount of Au in Ni, which prevents carbon deposition for the dehydrogenation of methane. Since this effect is less predictable, data for d-band shifts of alloys can be found in the work of Ruban et al²⁵.

Another mechanism for breaking the scaling relations that has been quite critical historically is the addition of coadsorbates. Famous examples of this include the Haber-Bosch process for ammonia synthesis which improves the rate of reaction via the addition of alkali metal adsorbates²⁶ and the addition of sulfur to Ni catalysts for steam reforming to prevent coking²⁷. The four ways in which coadsorbates can interact with catalysts are as follows: (1) a typically repulsive interaction from the direct overlap of orbital for small distances between adsorbates, (2) indirect elastic interactions through the substrate, (3) indirect

interactions by way of the transition metal d-bands, and (4) direct electrostatic interactions. The latter two methods are quite well demonstrated in the case of nitrogen binding on ruthenium¹¹.

When a sulfur atom adsorbs onto a ruthenium three-fold site, the neighboring ruthenium atom's 4d band center shifts down. This results from the sulfur atom effectively providing extra coordination which increases the d-band width of the surface. In turn, the bonding of other adsorbates on ruthenium sites that previously reacted is weakened. This sulfur adsorption greatly increases the nitrogen transition state energy for ruthenium sites in its immediate vicinity²⁸. For alkali metal adsorbates on the other hand, the fermi level is not impacted at all, rather charge transfer from the alkali metal to the ruthenium surface induces an electrostatic effect. The induced electrostatic field from the adsorbed alkali atoms interacts with the N₂ transition state complex in a way that lowers the transition state energy. Sulfur adsorption leads to the raising the nitrogen transition state energy while alkali promoters lower it, both without changing the nitrogen adsorption energy²⁸.

Returning to the electrochemical cell context, these principles of heterogeneous catalysis still hold, with the caveat that an additional electric potential is being applied externally to promote an electron transfer reaction. Indeed, one can still generate the same volcano plots for activity based on the binding energy such as the oxygen binding energy for the oxygen reduction reaction (ORR)²⁹. In the electrochemical cell, the real uniqueness lies in that novel reactions can be stimulated to occur at temperatures and pressures at which they would otherwise not happen at. It is important to note that the presence of the electric field itself can also affect the transition state energies much like in the previously discussed cases for coadsorbates. Transition state energies can vary with other environmental changes as well (e.g., different pressures, temperatures³⁰, and even magnetic fields³¹). Nevertheless, binding energies persist as the best guiding parameter towards exploring catalysis in these systems, with the ultimate goal to enhance these catalysts through geometries, coadsorbates, and environmental conditions.

In the case of SAECs, their catalysts are also governed by surface reactions, but in a more stringent manner in that they need a path for ion/electron transport to arrive at the surface where the adsorbate will meet the metal. This leads to SAEC electrodes being composed of a catalyst dispersed on a high surface area electronically conductive support (typically carbon) mixed with the ionic conducting electrolyte. This

composite structure is intended to raise the number of active sites to yield to give as high of an activity as possible. Unfortunately, this geometry is not possible for the ORR electrode since carbon is not stable in this configuration, so alternative geometries with the catalyst being solely deposited on the electrolyte have been employed³² and are still being explored.

At low overpotentials transition state energies tend to dominate the resistance of the overall reaction for SAECs. In general, this implies that the choice of catalyst is critical for these cells. At intermediate overpotentials ohmic resistances start to dominate, though this cannot be further improved, barring the development of a superior electrolyte that operates at an intermediate temperature. At the highest overpotentials, cells can experience mass-limiting resistance, but these are typically far from operating conditions. Taken together, this information suggests that the main levers we have to pull in designing better SAECs are catalyst development and electrode geometry improvement to increase available active sites.

Chapter 2 Experimental

For if a man who has never seen fire should prove by adequate reasoning that fire burns and injures things and destroys them, his mind would not be satisfied thereby, nor would he avoid fire, until he placed his hand or some combustible substance in the fire. – Roger Bacon

2.1 DC Electrochemical Techniques

Direct current (DC) electrochemical techniques rely on unidirectional current flow setups while measuring current-voltage properties. These measurements most readily reflect their applications which will also operate in a DC manner (e.g., fuel cell operation and electrolysis), provide good continuous data with high time resolution, and are relatively simple to carry out. Experiments are carried out in either potentiostatically (potential controlled) or galvanostatically (current controlled). In steady-state conditions, these two modes of operation will yield identical results while conversely, they will differ under non steady-state conditions. We will briefly explore a few of the DC electrochemical techniques that are applied in this work.

2.1.1 Linear Sweep Voltammetry

Linear Sweep Voltammetry (LSV) is a potentiostatic technique that involves sweeping the electrical potential between two potentials (see Figure 2.1). Two important factors to involve in this measurement are the sweep direction and the sweep rate. Sweep direction refers to whether the potential is moving towards a more oxidizing or reducing condition at the working electrode. The sweep rate refers to how fast the voltage changes between applied points. The latter point is particularly important for single pass measurements as one should be assured that the measurement is done slow enough that the system is in a quasi-steady-state to be reflective of the operating characteristics of the cell.

LSV measurements are routinely carried out to measure characteristic performance quickly. When measuring fuel cell performance for instance, one readily sees the operating voltage at which peak power is obtained by examining the current-voltage relationship across the sweep range. One can also tell by the shape of the LSV current-voltage profile at which voltages, which kind of resistance are dominant across

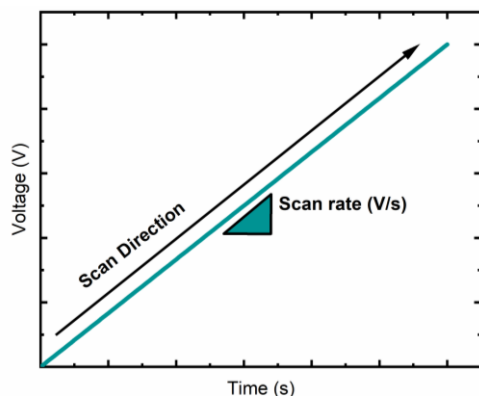


Figure 2.1 Illustrative voltage profile for a LSV measurement.

the cell. In SAECs, we are predominantly concerned with a few main sources of extra resistances which cause voltage losses called “overpotentials”. Deviations in the OCV from Equation 1.2 are typically attributed to the gas composition not being completely correct due to leaks from the cell or leaks across the cell. At low potentials, there can be high overpotentials arising from high activation barriers for chemical reactions. At intermediate potential ranges there is a linear slope region in which resistance changes as a function of ionic conduction, termed as “ohmic resistance”. At high levels of reactant consumption (and equivalently higher potentials), there becomes an additional overpotential source from not being able to transport enough mass of the reactant to the cell that the cell can convert.

2.1.2 Constant Potential/Current Techniques

Constant potential (also called chronoamperometric) and constant current techniques rely on fixing some part of the current voltage relationship to examine evolving phenomena. In other words, we take a slice of the so-called I-V curve and examine how it changes over time. For chronoamperometry, after some resting time, a square-potential wave is applied across the cell (see Figure 2.2) while in the constant current

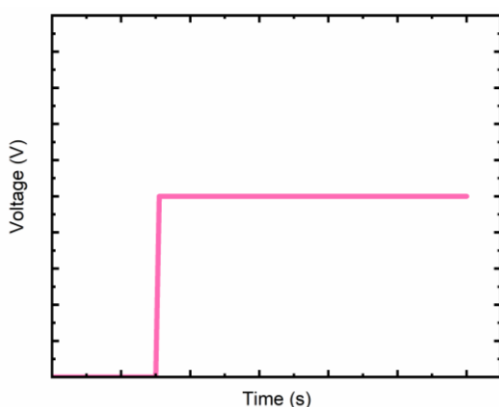


Figure 2.2 Illustrative voltage profile of a chronoamperometric measurement.

technique, just a current is maintained after some resting period.

These techniques are often applied in two situations involving the time domain. On one hand, it is often employed to examine things that happen on a fast timescale and can be used to measure things like diffusion. On the other hand, it is also used to examine long term operating performance of a given cell. This can be in a case such as a cell being held at the

potential where peak power density is achieved, and then monitoring any increases in overpotential overtime.

2.1.3 Cyclic Voltammetry

Cyclic Voltammetry (CV) is a potentiostatic technique that involves sweeping between two voltage limits that are approached with opposite sweeping directions (see

Figure 2.3 for an example CV waveform). CV measurements are often carried out as more detailed versions of LSV measurements. For one, the CV scan gives more information about the complete redox system since it scans in both

oxidizing and reducing directions. This also shows the reversibility of a redox couple. Like in LSV measurements, the measurements can be scan rate dependent if the reaction of interest is evolving at a rate slower than the implemented scan rate.

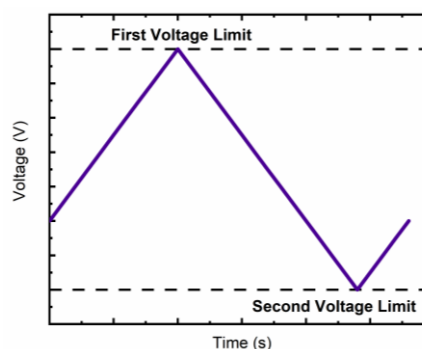


Figure 2.3 Illustrative voltage profile of a cyclic voltammetry measurement.

CV measurements can also be used to determine in situ catalyst activity if enough is known about the system of interest. This is accomplished by supplying a cathode with an inert gas and the anode with hydrogen and sweeping up to an oxidizing potential. In this range there should be a peak associated with hydrogen adsorption to the catalyst. The x-axis on a cyclic voltammogram can be converted to the time domain when the scan rate is known. Integrating the hydrogen adsorption peak with current versus time gives the total charge associated with hydrogen adsorption. This can then give the active surface area if the charge per area is known.

2.2 AC Impedance Spectroscopy

DC techniques are useful for providing a general picture of fuel cell performance, often the results are difficult to deconvolute to determine the main factors governing losses accurately. An alternating current

(AC) based technique known as electrochemical impedance spectroscopy (EIS) is the most widely used technique to address this deconvolution challenge.

2.2.1 Basic Principles

Impedance measures the effective resistance to an alternating current. This makes impedance sensitive to time and frequency dependent phenomena, unlike DC current based techniques. Whereby Ohm's law defines resistance R as the ratio between voltage V and current i , impedance Z makes this law time t dependent:

$$Z = \frac{V(t)}{i(t)} \quad (2.1)$$

Impedance measurements are typically made by applying a small sinusoidal voltage waveform:

$$V(t) = V_0 \cos(\omega t) \quad (2.2)$$

that produces a current response:

$$i(t) = i_0 \cos(\omega t - \phi) \quad (2.3)$$

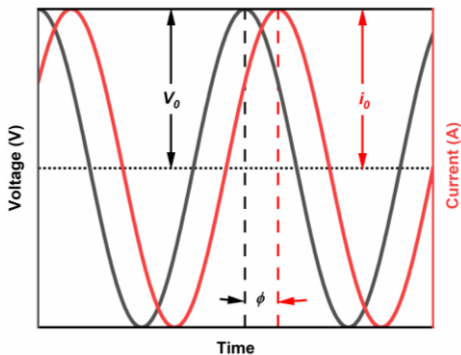


Figure 2.4 Sinusoidal voltage perturbation with resulting current response.

Where $V(t)$ and $i(t)$ are the voltage and current at time t , V_0 and i_0 are the voltage and current amplitudes, ω is the radial frequency (i.e., frequency f multiplied by 2π), and ϕ is the phase shift. The voltage perturbation is kept to a small amplitude so as to keep the response approximately linear. A visual representation of this voltage perturbation and the time-lagged current response is depicted in Figure 2.4.

By applying this waveform, this makes the sinusoidal impedance response of the system as:

$$Z = \frac{V_0 \cos(\omega t)}{i_0 \cos(\omega t - \phi)} = Z_0 \frac{\cos(\omega t)}{\cos(\omega t - \phi)} \quad (2.4)$$

We can simplify this expression by complexifying it into terms of real and imaginary components:

$$Z = \frac{V_0 e^{j\omega t}}{i_0 e^{j\omega t - j\phi}} = Z_0 e^{j\phi} = Z_0 (\cos \phi + j \sin \phi) \quad (2.5)$$

so that now the impedance can be expressed in terms of the impedance magnitude Z_0 and the phase shift, or in terms of a real component ($Z_{real} = Z' = Z_0 \cos \phi$) and an imaginary component ($Z_{imag} = Z'' = Z_0 j \sin \phi$). In these expressions j is represent the imaginary number ($j = \sqrt{-1}$) since i is typically used for the current here.

For EIS, we typically plot data in terms of the real and the imaginary components of impedance in what is known as a Nyquist Plot. In this plot, the x-axis has the real component of the impedance and the y-axis has the negative of the imaginary component. This allows for a detailed summary of the general impedance behavior of a system over many orders of magnitude in frequency. An alternative depiction of the data is through Bode Plots which more easily show how effects change over frequency. The Bode Magnitude Plot shows the magnitude of the overall impedance as a function of frequency and the Bode Phase Plot shows the phase shift as a function of frequency.

2.2.2 Physical Equivalent Circuit Models

The physical processes that occur within electrochemical cells can be modeled using circuit elements. Groups of resistors and capacitors can effectively model the behavior of ohmic conduction, reaction kinetics and mass transport. This leads us to call such circuit-based depictions of electrochemical cell impedance spectrums “equivalent circuit models”. Provided one can determine a good equivalent circuit model, physical processes and properties can be extracted from. Here, we will investigate the components to build up good equivalent circuit models for EIS.

Ohmic conduction is simple to model as this behavior is modeled just by a resistor:

$$Z_{Ohmic} = R_{Ohmic} \quad (2.6)$$

Showing that there is only a real response in the impedance. So, if we consider the Nyquist representation of this, we will see a single point on the real axis as an effective model for ohmic conduction, as is depicted in Figure 2.5a.

We need to also introduce the model for a capacitor, as there are significant charge separation events that will occur across the reaction interface over the course of an electrochemical reaction. The

impedance response of a capacitor is fully imaginary. The equation relating current and voltage for a capacitor with capacitance C is:

$$i = C \frac{dV}{dt} \quad (2.7)$$

When adding a sinusoidal waveform, this gives a current response of:

$$i(t) = C \frac{d(V_0 e^{j\omega t})}{dt} = C(j\omega) V_0 e^{j\omega t} \quad (2.8)$$

which gives an impedance shown in Figure 2.5b. and by the equation:

$$Z_C = \frac{V_0 e^{j\omega t}}{C(j\omega) V_0 e^{j\omega t}} = \frac{1}{Cj\omega} \quad (2.9)$$

For electrochemical cells, it is often the case that the capacitive element might deviate from an ideal capacitor due to several factors such as a distribution of capacitance, distribution of reaction rates, roughness, or non-uniform current distribution. A more general form that encompasses these non—ideal features is an element known as a constant phase element C_α . This element deviates from the capacitance by a factor of α , where α is a number between 0 and 1 with 1 being a perfect capacitor. This is shown in Figure 2.5c and given by³³:

$$Z_\alpha = \frac{1}{C(j\omega)^\alpha} \quad (2.10)$$

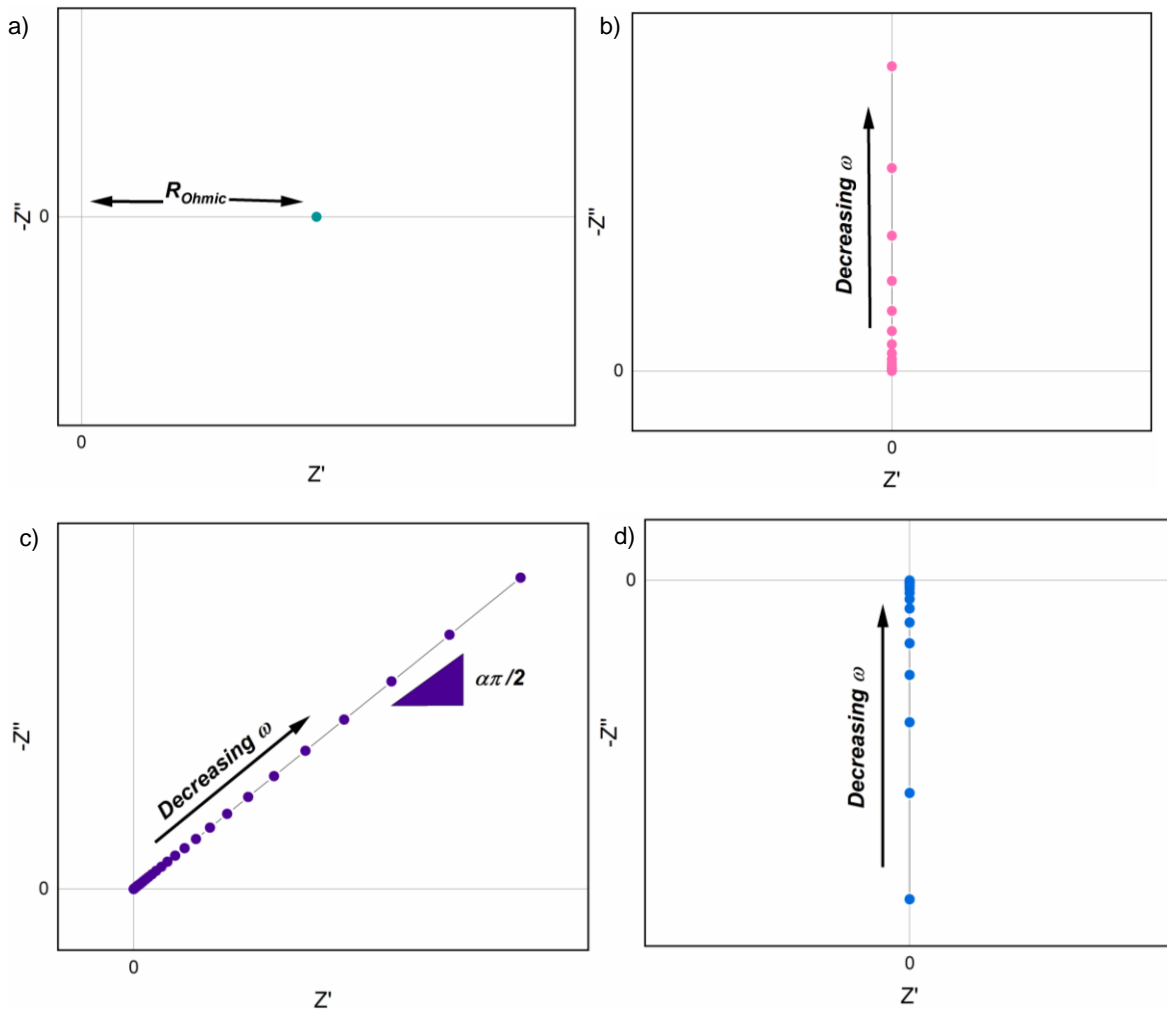


Figure 2.5 Nyquist plot depictions of the following equivalent circuit elements: a) resistor, b) capacitor, c) constant phase element, d) inductor.

A final relevant elementary circuit element is the inductor. This mostly matters for the experimental setup since wires leading to and from the testing apparatus can induce some level of inductance in the measurement. The impedance response for an inductor with inductance L is shown in Figure 2.5d and given by:

$$Z_L = j\omega L \quad (2.11)$$

Often, the processes in an electrochemical cell are a combination of these equivalent circuit elements. If they are represented by elements in series, the impedance components can be just added together normally. If the elements are in parallel, then the components are added reciprocally.

The most common equivalent circuit that occurs for an electrochemical reaction is a resistor and a constant phase element in parallel. The reason why for this can be understood when thinking about the physical steps happening. Charge accumulation on the surface of the reaction site during electrochemical reaction causing a capacitive element to form. This charge accumulation effect is not uniform across the surface, so the capacitive element is a constant phase element. The reaction kinetics, on the other hand, are entirely represented by a resistor and is directly related to the activity of the electrochemical reaction.

This leads to many impedance measurements in the early regions of the polarization curve to be defined by an ohmic resistance in series with some number of RQ elements affiliated with electrochemical reactions. An example of EIS data from an electrochemical cell that is fit with an RRQRQ circuit using an in-house built Python program called ECIF³⁴ is shown in Figure 2.6.

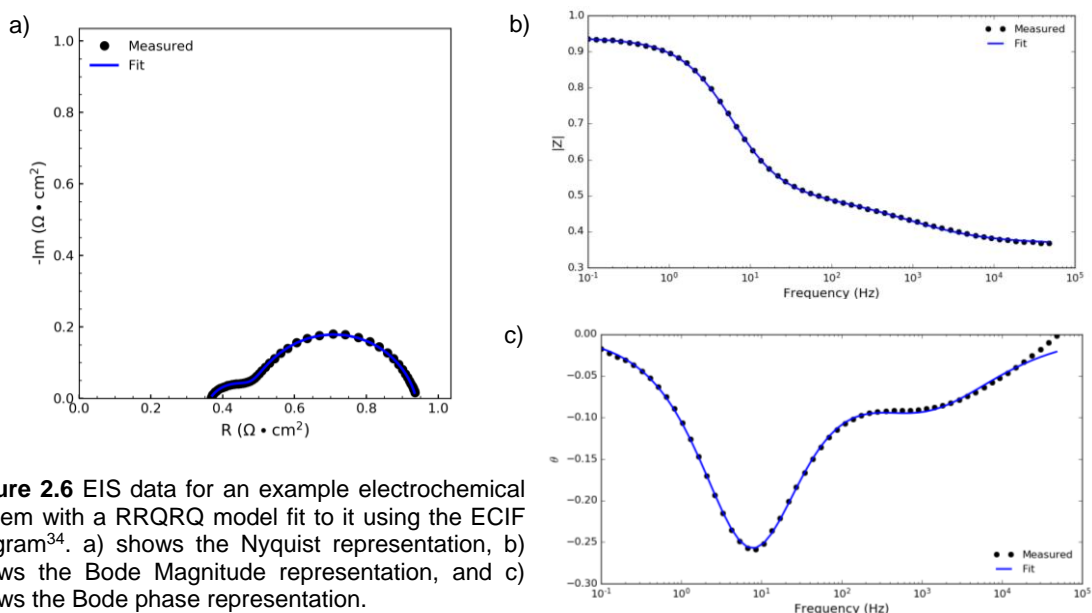


Figure 2.6 EIS data for an example electrochemical system with a RRQRQ model fit to it using the ECIF program³⁴. a) shows the Nyquist representation, b) shows the Bode Magnitude representation, and c) shows the Bode phase representation.

From Figure 2.6, one can see that the RQ elements makes a depressed semicircle with the Nyquist presentation. An ideal RC circuit would instead show a non-depressed semicircle and the depression

corresponds to a lower α value in Equation 2.10. This also shows how the different resistances are easily discernable from the Nyquist plot. The ohmic resistance is where the data first crosses the x-axis at around $0.37 \Omega\text{cm}^2$ and the total real portion of the resistance is around $0.95 \Omega\text{cm}^2$ being where the final crossing of the x-axis. The reaction resistance can then be found as the difference between these two values. Additional deconvolution between those two resistances is easily carried out by the modeling which also provides values of the capacitances and α values.

To gain a bit of intuition about how the different parameters effect an interactive demo was built into the ECIF program³⁴ that allows for manipulation of variables to see how this affects the impedance in the Bode magnitude representation of an RRQ circuit and some examples are shown in Figure 2.7.

From the differences between Figure 2.7a and Figure 2.7b. the ohmic and reaction resistances change independently and are easily discernable from each other by where they show a plateau. From Figure 2.7c

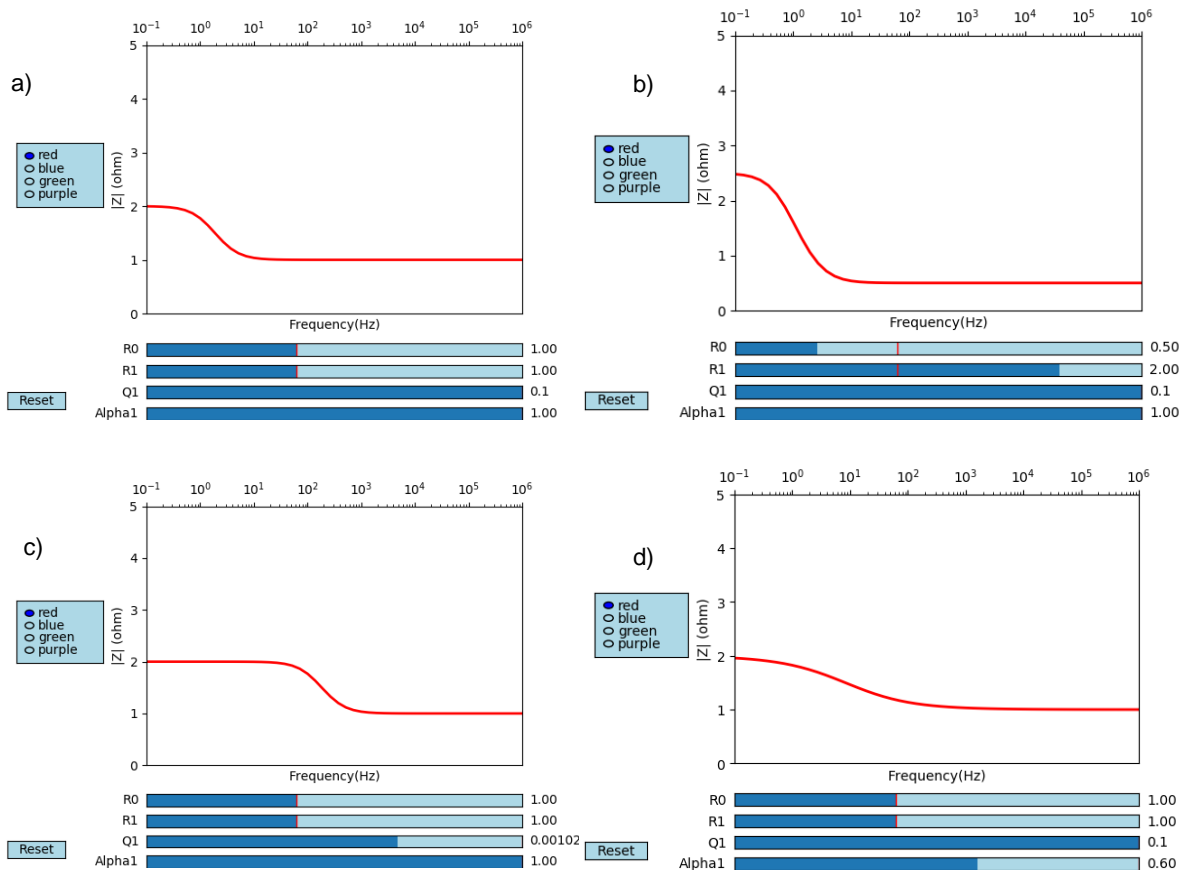


Figure 2.7 Demo of RRQ circuit with a) initial parameters, b) ohmic resistance halved while reaction resistance is doubled, c) capacitance lowered by two orders of magnitude d) α dropped from 1 to 0.6.

shows that by lowering the capacitance by two orders of magnitude, the point at which the impedance transitions from being impacted by both resistances to just the ohmic resistance shifts to two orders of higher magnitude frequency. This shows that the transition point frequency is negatively correlated with the capacity. Figure 2.7d shows that lower values of α make the transition between the two resistances more diffuse. Here, it should be noted that for almost all electrochemical reactions that lower frequencies correspond with higher real components of impedance.

Mass transport is typically modeled by so-called Warburg elements. These circuit elements are based on and derived from diffusion processes. If we consider an infinite length of diffusion, we get an infinite Warburg element with an impedance given by:

$$Z = \frac{\sigma_i}{\sqrt{\omega}}(1 - j) \quad (2.12)$$

where σ_i here is the Warburg Coefficient for a species i and is defined as:

$$\sigma_i = \frac{RT}{(n_i F)^2 A \sqrt{2}} \left(\frac{1}{c_i^0 \sqrt{D_i}} \right) \quad (2.13)$$

where A is the area of the electrode, c_i^0 is the bulk concentration of species i , and D_i is the diffusion coefficient of species i . This means that the Warburg coefficient shows the effectiveness of species i to or from reaction interface. By looking at Equation 2.13, we can see that if species i is abundant and diffusion is fast, then the Warburg coefficient will be small and the impedance from transport will be small. Additionally, at high frequencies, the Warburg impedance is small since diffusing reactants do not have to move far. Therefore, Warburg impedance is usually only prevalent at low frequencies, where reactants have to diffuse further. The Nyquist presentation of an infinite Warburg element appears as a diagonal line with a slope of one as shown in Figure 2.8a.

Of course, in regular fuel cells, the diffusion length typically has a finite length. Typically, the diffusion layer corresponds to the thickness of the electrode³. In cases with a finite diffusion length, it is better to use a Finite (porous bounded) Warburg model. This model has the form of:

$$Z = \frac{\sigma_i}{\sqrt{\omega}} (1 - j) \tanh\left(\delta \sqrt{\frac{j\omega}{D_i}}\right) \quad (2.14)$$

where δ is the diffusion layer thickness. At high frequencies or with large diffusion layer lengths, this model converges to the Infinite Warburg model. Conversely, at low frequencies and small diffusion layer lengths, this model's impedance moves back towards the real axis. The Nyquist representation of this model is shown in Figure 2.8b.

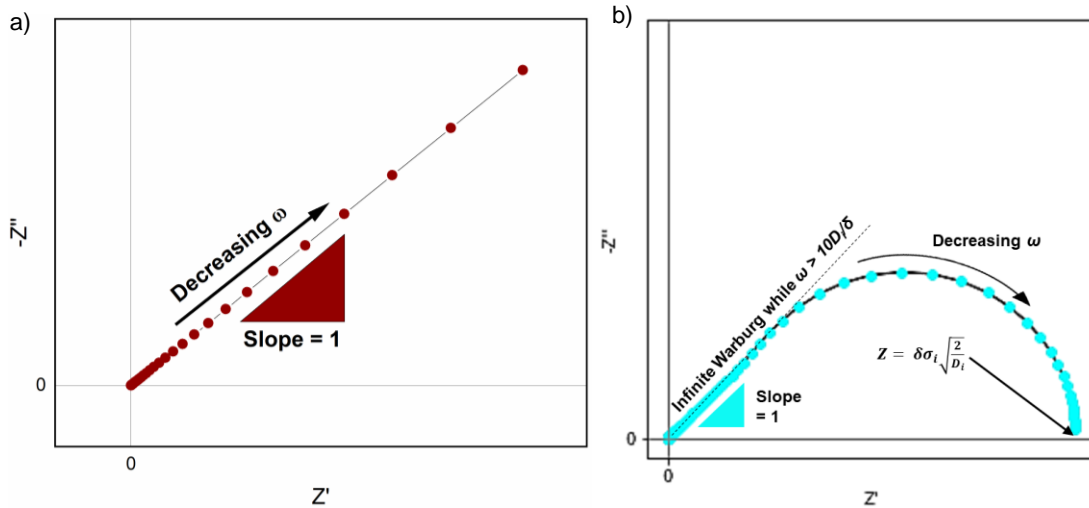


Figure 2.8 Nyquist plots of diffusion-based Warburg elements. a) shows the infinite Warburg case while b) shows the Finite (porous bounded) Warburg case.

2.3 X-ray Techniques

X-rays (electromagnetic waves with wavelengths on the order of 0.5-2.5 Å) are very powerful for two reasons: (1) they have wavelengths on the order of atomic spacings and (2) they have energies on the order of atomic electronic transitions. These make them a powerful asset in determining the chemical and structural identity of the materials we study. Here, the main materials characterization x-ray techniques that are implemented in this work will be described³⁵.

2.3.1 XRD

X-ray diffraction is a technique predominantly used to probe the structure of a given material utilizing the diffraction property of waves when their wavelength is on approximately the same order of length of a periodic spacing. Incident X-rays will interact with a material and scattered X-ray will interfere constructively and destructively. Scattered X-rays from adjacent planes of atoms that have a spacing of d

between them will constructively interact when the angle θ between the plane and the X-ray results in a path length difference that is an integer multiple n of the X-ray wavelength λ . This condition makes up what is known as Bragg's Law:

$$n\lambda = 2d\sin\theta \quad (2.15)$$

By knowing the angle of incidence and measuring the intensities at each angle, we gain knowledge about the structure of the material. One thing that is helpful to note when considering Equation 2.15 is the relationship between the lattice spacing and the angle. If it is noticed that scattered intensity is appearing at a lower angle, then d-spacing is expanding (while θ is $< 90^\circ$ which is the case for most XRD experiments) like in the case of thermal expansion³⁵.

In this work, exclusively powder X-ray diffraction is performed (as opposed to the Laue Method or Rotating-Crystal method). Further, most often the Bragg-Brentano geometry is most often employed where X-rays impact a flat sample and reflected X-rays are detected. Only in a few cases is the Debye-Scherrer geometry employed where incident is instead transmitted through the sample and detected. The Debye-Scherrer geometry is only employed for cases where there is little sample available and is noted where used.

XRD is also used routinely herein to predict particle size by calculating the crystallite size using Scherrer's Formula:

$$t = \frac{K\lambda}{B \cos\theta} \quad (2.16)$$

Where t is the thickness of the crystallite, K is a shape factor close to unity (typically close to 0.9), λ is the wavelength of the incident X-ray, B is the angular breadth of the peak be examined (i.e., the full-width of the peak at half of its maximum intensity), and θ is the angle at which the peak has its highest intensity. To isolate this effect out, other peak broadening effects need to be accounted for. The first is the instrument broadening, which can be considered by measuring a standardized sample that provides extremely minimal broadening to the pattern itself (typically LaB₆), and the broadening of that pattern as the instrumental broadening. A second broadening takes place in the presence of non-uniform strain in the sample:

$$B = \frac{-2\Delta d}{d} \tan \theta \quad (2.17)$$

where $\frac{\Delta d}{d}$ is the variation in strain. To isolate this effect, several peaks must be measured so that it is easy to separate the $\cos \theta$ breadth dependence from the $\tan \theta$ dependence³⁵.

2.3.2 XRF

X-ray fluorescence (XRF) is the emission of characteristic secondary (i.e., fluorescent) X-rays from a material that has been excited by X-rays. This happens because X-rays have sufficient energy to knock electrons out of the inner orbitals of atoms. This configuration is highly unstable, so an electron from a higher orbital will drop to the lower orbital to fill this. Upon doing this, an electromagnetic wave is released that corresponds to the energy difference between the two orbital levels. Since each element has orbitals with different characteristic energies, XRF can identify materials by their “orbital fingerprint”.

The detection of the spectrum of photons emitted is done by an energy dispersive spectrometer, so this technique is widely called energy dispersive X-ray spectroscopy (EDS or EDX). The probing radiation being X-rays means that the sampling volume penetrates well into the sample. This will change depending on several factors such as Z number and density, but tends to be on the order of μms ³⁶, while the areal resolution can be much more precise with a resolution on the order of the electron microscope’s resolving ability when using EDS through it. EDS is useful for getting an idea of a sample composition, but should not be the sole analyzing tool when a precise chemical composition needs to be achieved as measurements can have around 5% error³⁶.

2.3.3 XPS

XPS, much like EDS, relies on bombarding a sample with X-rays, but in this case, ejected photoelectrons are measured. The kinetic energy of the photoelectrons is detected and then the binding energy required to liberate the electron from the sample chemical potential is measured. This, like EDS, provides a characteristic chemical signature. The main reason why one uses XPS over EDS is that it is much more surface sensitive. Depending on the sample one is examining, the sampling depth arises from 1-10 nm of the sample. Additionally, the binding energy is sensitive to the oxidation state of materials, so there is also a higher degree of chemical specificity. The areal sampling resolution for XPS tends to be

large and typically requires greater than 10 μm . Additionally, while it is often cited that XPS composition analysis can be down to 0.1% error, depending on the sample the error can range to 10% error³⁷.

2.4 Chemical Vapor Deposition

Chemical Vapor Deposition (CVD) is a vacuum-based thin film deposition method that relies on a gas-phase precursor to react or decompose onto the surface of a sample. Often this needs to be coupled with a gas removal step since there are often volatile by-products after the precursor has reacted or decomposed. While there are many possible methods of employing CVD, we will look more in-depth at two methods employed in this work.

2.4.1 MOCVD

Metalorganic Chemical Vapor Deposition (MOCVD) is essentially a CVD process carried out by the reaction of a volatile metalorganic precursor. This is useful for clean metallic depositions since the organic part remains volatile after the reaction so that the sample is not as contaminated and leaves behind a metal of interest.

Many MOCVD methods use a flowing stream of the volatile precursor, which is often mixed with an inert carrier gas. This reactant stream is then flowed over a substrate of interest. This substrate is usually heated to induce the breakdown of the precursor when it collides with surface. For MOCVD, there is typically one continuously applied reactant gas and the amount of deposition is controlled by the amount of precursor supplied and the time allowed to react. This method can be challenging to apply to powders in the deposition of uniform films though since they can have high surface areas and many areas might have limited accessibility to the convective gas flow.

In the case for depositing on CDP, a unique MOCVD technique was developed. For this procedure, a solid metalorganic precursor is mixed directly with a fine CDP powder. This is then supplied to a reactor vacuum furnace in a container alongside a container of water that will volatilize to maintain humidity in the chamber. This is then brought to vacuum and purged with nitrogen several times, then finally allowed to remain in vacuum. This chamber is then heated to a point where the metalorganic precursor volatilizes and

deposits a uniform film on top of the CDP powder. The deposition amount here is controlled by how much of the precursor is mixed with the CDP³⁸.

2.4.2 ALD

Atomic Layer Deposition (ALD), much like CVD, relies on a volatile precursor gas to deposit thin films of a material of interest. The main distinguishing factor about this process is that it occurs on the order of a single atomic layer at a time. This is achieved by breaking the deposition process into at least two steps that are each self-limiting. The first step typically relies on a volatile precursor that will chemisorb to the surface of a substrate of interest. The secondary byproducts are then purged from the apparatus. Next, a second reactive gas is introduced into the chamber that also reacts with the surface in a self-limiting manner and is also followed by a purge (see Figure 2.9 for diagram). Together this makes one cycle, and the material can be built up layer by layer in this manner.

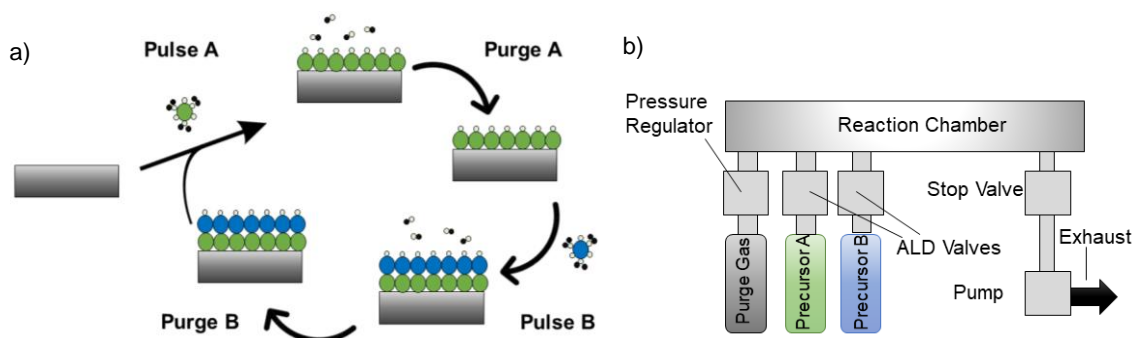


Figure 2.9 a) Diagram of general binary ALD sequence. Precursor A is pulsed into ALD reaction chamber and allowed to chemisorb to the surface of the substrate while secondary molecules remain volatile. The remaining volatile gas is then purged from the chamber. Then, precursor B is pulsed into the reaction chamber, and subsequently the secondary volatile materials are purged. This cycle is repeated till desired thickness achieved. b) Schematic of a typical ALD reactor setup. Reaction chamber is held under vacuum and heated to desired chamber. Dosage for ALD precursors is controlled by fast acting valves that are pulsed open for short periods of time. Optionally, as opposed to working in a continuous flow manner, the stop valve can be engaged to seal reactants in the reactant chamber for a period.

There are many benefits to this method over MOCVD including subnanometer thickness control, high conformality, stoichiometric control, low surface roughness, repeatability, and adhesion. The main disadvantages are that the process is more time intensive, more expensive as more precursor is wasted, and the options for precursors are more limited since it more challenging to get element carriers with a good ALD deposition window.

For the ALD process, it is strongly desired to have an irreversible saturating chemisorption bond for strong single layer formation over weak physisorption bonds that allow for multilayer formation³⁹. Typically, a desired temperature window must be found where ALD proceeds well in. At too low of temperatures, uncontrolled growth can occur because either the precursor can condensate on the surface of the substrate or the thermal energy is too small and does not allow for surface reactions. Too high of temperatures will lead to thermal decomposition of the precursors on the substrate surface or the precursor will have too high of a volatility to stay on the substrate surface⁴⁰. Having a low melting point is associated with branching and asymmetry.

Good ALD precursors should be chemically reactive, thermally stable, be volatile, and have self-limiting behavior⁴¹. Additionally, bulky ligands can prevent access to active sites leading to sub-monolayer deposition. Typical precursors are either halides or organometallics. Halides are thermally stable and inexpensive, but they tend to leave halogen impurities and are corrosive to the reaction chamber. Organometallic precursors are highly reactive and non-corrosive but suffer from thermal stability and will leave carbon impurities at times. A final important consideration for deposition from ALD is nucleation. If nucleation is favorable mostly on the substrate and subsequently on alternate layers, then ALD will proceed in a layer-by-layer fashion. If there is sufficient motivation to also deposit on like layers, then ALD processes can deposit in a more random fashion. If the nucleation is highly more favorable towards depositing on like materials over that of alternating layers or the substrate, then the deposited material will tend to form islands of depositing on itself. This is particularly true for deposition of metals⁴².

2.5 Cell Testing

Due to the myriad of parameters that can affect the performance of electrochemical cells, rigorous protocols were established for the fabrication and testing of said cells to limit cell to cell variation. Any deviation from these protocols to carry out a particular experiment is noted in the text.

2.5.1 Cell Fabrication

Cells constructed here were prepared by serially pressing several layers together using a uniaxial press. Before using the die set, all components are washed in isopropyl alcohol and then in deionized water and allowed to dry. The edges of the die rod are lightly wiped with steric acid in IPA. Initially, a 1.8 cm

stainless steel mesh is lightly pressed to ensure it is flat and then sonicated in IPA for five minutes and dried under N_2 . This disc is then placed inside a 1.9 cm die. Then a so-called "MPL layer" is spread on top of this die consisting of 75 mg of a mixture of CsH_2PO_4 , carbon black acetylene (Alfa Aesar, 99.9%) and naphthalene (Alfa Aesar, 99.8%) in a 3:1:2 mass ratio, where the naphthalene serves as a fugitive pore former. Before the powder is spread, the powder is chopped with a razor to break up any agglomerate particles. Care is taken when forming this layer to ensure that the powder is spread using a razor to a level even with the level of the opening of the die. Subsequently, a piece of weigh paper is placed on top of the opening and pressed down along the edges while a razor is combed over the surface. This aids in assuring the surface is smooth. Then a 0.102 mm shim is inserted and an electrocatalyst layer is spread on top composed of a mixture of CsH_2PO_4 + Pt on carbon (20 mass% Pt on carbon black, HiSPEC® 3000, Alfa Aesar) in a 6:1 mass ratio. The same steps to ensure smoothness with the weigh paper and razor are used. This is then pressed at three tons for three seconds and afterwards the pressure is slowly released. A razor is used to remove powder stuck to the edge of the disc and N_2 is lightly blown over the surface to remove any loose powder. What is fabricated up to this point will serve as the counter electrode.

At this point, the entire die set is cleaned again, once in IPA and a second time in deionized water and allowed to dry. The edges of the die rod are lightly wiped with steric acid in IPA. Then the cell in progress is placed back again in the hole for the die. 50 mg of a fine CDP powder are placed upon the top of the cell and spread evenly. The same steps with the razor and weigh paper are applied. At this point, a cap made with Kapton tape covering it is placed on top of the hole and the assembly is pressed at four tons for one minute after which the assembly is slowly depressurized. The powder on the edges of the cell is removed with a razor and the loose powder on the top is removed with N_2 . The cell is then double wrapped around the edges with Teflon tape. This is then lightly pressed on top to make the Teflon layer as thin as possible. A picture of this cell is then taken from a bird's eye view with sufficient lighting and a ruler for reference to obtain the active area of the cell not covered by the edge Teflon tape. An area calculation is then done using ImageJ on this image.

Now the final electrode powder is prepared to be added. At this point, a quick procedure for how the electrode powders were often made is that the metal on carbon and CDP are added to a mortar. These powders are mixed by mortar and pestle until the powder appears uniform. A spatula is used to scrape and pressed powder until all is loose. Then, a small amount of isopropyl alcohol is added to the mortar. This powder is again mortared and pestled for at least one minute until the isopropyl alcohol is close to drying. At this point, the pressed powder in the mortar is dried lightly under N_2 . The pressed powder is removed by a spatula and the removed powder at this point is very fine and by appearance should be black. This powder is then placed on top of the previously fabricated half-cell. This powder is spread evenly over the entire cell (including areas covered by Teflon). The same procedure for ensuring a smooth layer with the weigh paper and razor is applied. The cap with Kapton tape is then placed on top of the hole and this assembly is pressed at two tons for one second. The edges of the die rod are lightly wiped with steric acid in IPA. Then a layer of carbon paper is added on top (TGP-H-120 Toray paper) followed by a 1.9 cm stainless steel mesh. The cell is then double wrapped around the edges with Teflon tape and the cell is ready for use. A schematic of the complete cell is shown in Figure 2.10.

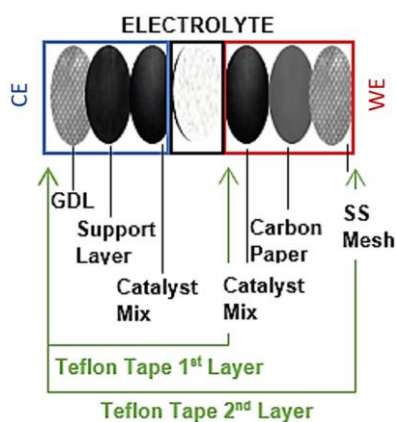


Figure 2.10 Schematic of a standard counter electrode supported electrochemical cell. Here, CE refers to the counter electrode, WE refers to the working electrode, GDL stands for gas diffusion layer (i.e. a 2-layer stainless steel mesh), SS refers to stainless steel. Employed electrolyte is always CDP for these cells. The counter electrode catalyst mix is typically a standard Pt/C composite. The WE catalyst mix is the varied electrode of interest.

As a note for materials handling, all materials were stored in a glovebox prior to use where the pO_2 and pH_2O are held to less than 0.5 ppm. The MPL powder could not be stored in the glovebox as the naphthalene would routinely volatilize upon transfer through the antechamber. This being the case, the MPL powder was stored in a desiccator when not in use. All powders were sieved with a 53 μm sieve before use, except for the working electrode powders. Additionally, all powders used were thoroughly mixed with

extensive mortar and pestling. The standard counter electrode powder was additionally ball-milled before mixing with mortar and pestle.

2.5.2 Testing Configuration

To test electrochemical cells, an in-house built electrochemical testing station was used (see Figure 2.11). For this station, four gas lines are setup to supply gases to the station that are flow-controlled with mass flow controllers (MFCs) calibrated by a Gilibrator. Two of these gas lines go through a furnace, inside which there are two glass bubblers. The lines run through these bubblers in order to humidify the gas to a degree which is determined by the temperature of the furnace and the associated water partial pressure. The exhaust of the bubblers then meets with the other two dry gas lines past the MFCs at T-joints. There is a check valve on the humidified gas line side of the T-joint to allow for solely dry gas to be supplied to the cell without causing backflow through the humidified line. These joint lines then lead into the oven where

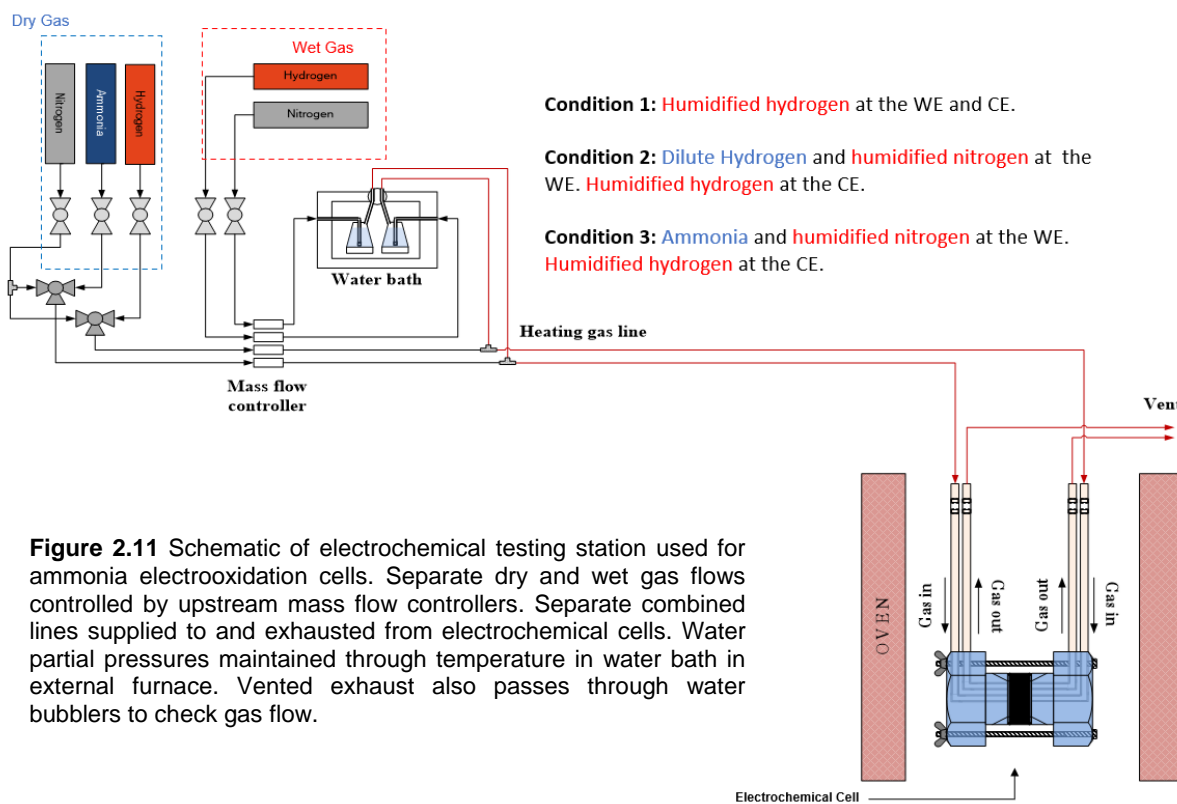


Figure 2.11 Schematic of electrochemical testing station used for ammonia electrooxidation cells. Separate dry and wet gas flows controlled by upstream mass flow controllers. Separate combined lines supplied to and exhausted from electrochemical cells. Water partial pressures maintained through temperature in water bath in external furnace. Vented exhaust also passes through water bubblers to check gas flow.

the cell holder is. One of the joint lines leads to the working electrode side while the other line leads to the counter electrode side. Similarly, each cell holder side exhausts separately to a vent.

Every portion of the gas lines that is potentially exposed to humidified gas is wrapped with heat rope and held at 150 °C with Omega temperature controllers to prevent condensation in the lines. Right before the cell, ceramic tubes are used to electrically isolate the cell. Otherwise, the remainder of the tubing is stainless steel. Before reaching the exhaust, venting lines are passed through another set of bubblers to check gas flow. This is used when loading the cell to ensure that proper sealing is achieved before ramping to operating conditions. Typical operation involves flowing no or dry gases up to 150 °C and then supplying humidified gas ($p_{\text{H}_2\text{O}} = 0.38$) when ramping from 150°C to 250 °C with ramp rates of 2 °C/min.

To do electrochemical measurements two silver wires are attached on each side of the cell holder in electrical contact with the cell electrodes in a pseudo four-point probe configuration. This allows for the ohmic contribution from the silver wire to be removed. There is still an unavoidable inductance signal that is found when doing AC impedance measurements that has to be corrected for. One way of achieving this is by inducing a short-circuit across the cell by contacting either side of the cell holder to the other. This data can then be subtracted from the non-short-circuited data. The inductance can also be accounted for with an equivalent circuit model as discussed in Section 2.2.2. The wires then lead to an instrument to carry out electrochemical measurements (Biologic, SP-300).

There were three gas conditions that were predominantly used as gas conditions to test electrochemical cells here, all at typically 50 standard cubic centimeters (sccm) of gas supplied to each electrode and a water partial pressure of 0.38 atm $p_{\text{H}_2\text{O}}$. The first is a condition where only humidified hydrogen is supplied to both electrodes. This leads to gas partial pressures of 0.62atm p_{H_2} for both sides. This was used as a reference condition and could be used to probe general hydrogen electrocatalysis measurements with high p_{H_2} such as hydrogen oxidation (HOR) and hydrogen evolution (HER).

The second condition involves maintaining the hydrogen partial pressure at the counter electrode at 0.62atm p_{H_2} while mixing dry and humidified hydrogen. The working electrode gas is then switched to a mixture of humidified nitrogen and 10% H_2 bal. Ar in a mixture that creates a p_{H_2} of 0.024-0.025 atm p_{H_2} (still $p_{\text{H}_2\text{O}} = 0.38$ atm, and bal. is N_2 and Ar). This condition served two purposes. One is that we could

check if hydrogen from the counter electrode is crossing over to the working electrode by measuring the OCV. The difference in the hydrogen chemical potential across the two electrodes causes a voltage of 71-73 mV (range from MFC error range) according to Equation 1.2. All cell results here passed this hydrogen crossover test and any results with OCVs less than 71 mV were disregarded. The second use of this condition was to test HOR/HER activity at the working electrode under dilute hydrogen conditions.

The third main condition employed maintained the counter electrode gas condition but switched the working electrode dry 10% H₂ bal. N₂ to dry NH₃. This made for a gas condition at the working electrode of 0.4 atm pNH₃, 0.38 atm pH₂O, and balance nitrogen. This was used to test ammonia oxidation at the working electrode. A variation of this was also made to investigate higher ammonia partial pressures. In this configuration the humidified nitrogen was no longer supplied to the working electrode. Instead, humidity was supplied directly to the gas line through the implementation of a syringe pump pumping water into the line directly above the cell at a T. A small amount of N₂ was supplied on this external line to help push the steam to the system. This alternate configuration maintained a gas condition at the working electrode of 0.6 atm pNH₃, 0.38 atm pH₂O, and balance nitrogen and at a flow rate of 50 sccm like in all the other conditions.

2.6 Adsorption Techniques

As heterogeneous catalysis and electrochemical catalysis occurs at the surface of materials and the associated catalytic activity is a function of the reaction surface area, it is important to be able to characterize the amount of available surface area to be able to make comparable results. This being the case, we will describe two techniques employed here used to characterize different types of surface areas.

2.6.1 BET Method

The Brunauer–Emmett–Teller (BET) theory is an explanation of the physical adsorption process for gas molecules on a solid surface and is often employed to evaluate the specific surface area of materials. The basis of this theory comes from Langmuir's theory which relates the fractional coverage θ from monolayer adsorption of gas molecules to the gas pressure P of a gas adjacent the solid surface at a given temperature:

$$\theta = \frac{KP}{1+KP} \quad (2.18)$$

where K is a constant independent of temperature. At a constant temperature K can be determined experimentally from this kinetic model. This model is built from several assumptions including that adsorbates form a monolayer, all surface sites have the same adsorption energies and are independent of one another, and each active site is matched with a single adsorbate particle⁴³. The BET theory covers for some of Langmuir's theories shortcomings by building a model for multilayer adsorption based on the assumptions that gas molecules physically adsorb on a solid in layers infinitely, gas molecules solely interact with adjacent molecules, Langmuir's theory can be applied to each layer, and that the enthalpy of adsorption for the first layer is a constant that is greater than the subsequent layers which have an enthalpy equivalent to the enthalpy of liquification⁴⁴.

The implementation of the BET method for surface area analysis today is performed with an inert gas (typically N_2) physisorption onto a surface. The measurement procedure involves cooling an inert gas to its boiling point where significant adsorption can occur. Known amounts of the gas are then released into a sample cell with known volume. Pressure changes due to the adsorption process are then being measured. The data is then collected in the form of an isotherm which shows adsorption as a function of relative pressure (see Figure 2.12).

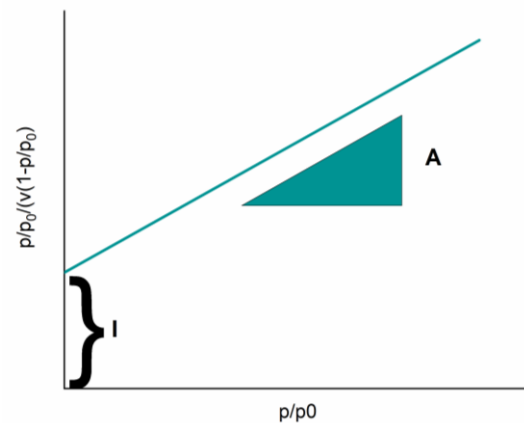


Figure 2.12 BET plot with fitting constants.

To obtain the surface area, the following equation is used for the monolayer adsorbed gas quantity,

V_{mono} :

$$V_{mono} = \frac{1}{A + I} \quad (2.19)$$

from which the surface area from BET S_{BET} can be determined from:

$$S_{\text{BET}} = \frac{v_{\text{mono}} N s}{V m} \quad (2.20)$$

where N is Avogadro's number, s is the absorption cross-section of the gas molecule, V is the volume of the gas molecule, and m is the mass of the sample.

2.6.2 Selective Chemisorption

For our catalytic systems, while the general surface area obtained from the BET method is helpful, it does not capture the entire picture of what we are after. We are interested in the reaction surface area which is particularly correlated with the metal surface area (excluding the available support surface area). This means we need techniques to isolate this surface area to compare catalysts on a one-to-one basis.

One way of testing this is by using a molecule that wants to selectively bind to the catalyst of interest and not the support. One good example of this is carbon monoxide which tends to selectively bind to transition metals. We must first know how the carbon monoxide binds to the metal to use this information. The nice thing is that the chemisorption reaction will form monolayers on the surface which makes the modeling easier. What changes from material to material is the sites to which CO bonds. This can be determined externally by in-situ infrared techniques such as Diffuse Reflectance Infrared Fourier Transform Spectroscopy (DRIFTS).

An example method of employing this involves a series of steps. First, the surface to be measured should be sufficiently cleaned (and degassed). Second, the sample of interest is placed in a measuring chamber from which the exhaust is being measured somehow (a thermal conductivity detector can accomplish this). Third, pulses of CO balance the inert gas are introduced to the sample and the thermal conductivity of the resultant gas is measured. CO uptake will manifest as differences in the thermal conductivity. Pulses are continued until subsequent pulses no longer exhibit a change indicating no more uptake. Now the pulses can be converted to an amount of CO adsorbed and using the relationship between the sites and the CO, the number of sites and thus the surface area can be obtained.

Chapter 3 Hydrogen Electrooxidation

Young people must break machines to learn how to use them; get another made!

– Henry Cavendish

3.1 Introduction

3.1.1 A General Prospective

Hydrogen is possibly the simplest atom to examine for electrocatalysis as it contains just one electron and one proton. It naturally exists as a diatomic gas and thus will produce two electrons and two protons when oxidized. Modern electrocatalysis was practically initiated by the work of Bowden and Rideal who first made measurements of the hydrogen reduction overpotential as a function of current density for several metals⁴⁵. Yet even as electrocatalysis of hydrogen could be one of the simplest cases and is among the longest studied electrocatalytic systems, substantial work is still being done today to understand and improve this system.

The fact that the hydrogen oxidation and reduction steps are fully reversible suggests similar binding energy dependences which is found in computational⁴⁶ and experimental work⁴⁷. However, there can be notable asymmetries in the ability of a catalyst to carry out these reactions (i.e., the oxidizing condition alters the chemical state of the catalyst whereas the reducing condition does not). This can lead to different microkinetic steps as rate limiting for the forward and reverse cases⁴⁸. Most of the work in this chapter is focused on the hydrogen oxidation reaction (HOR) due to its importance in ammonia oxidation as discussed in Chapter 4 and for its use in H₂/O₂ fuel cells, but since our testing conditions under symmetric hydrogen are similar for both reactions, the hydrogen evolution reaction (HER) was also occasionally explored and results will be noted when appropriate.

The net HOR for hydrogen gas involves the hydrogen molecule splitting into protons and electrons:



This reaction can be broken into distinct parts to describe a particular reaction pathway, as discussed in the following steps with H_{ads} as adsorbed hydrogen. In literature, the step for hydrogen chemisorbing to a surface is known as the Tafel step expressed as:



Hydrogen can also attach to a surface via an electrochemical transfer method. If the hydrogen adsorption must be coupled with a charge transfer reaction, this is known as a Heyrovsky step. When carried out with a proton conductor, this proceeds as:



If adsorbed hydrogen is oxidized to a proton and liberates an electron, this is known as a Volmer step. In the proton conducting electrolyte case, this proceeds as:



These Tafel, Heyrovsky, and Volmer steps can proceed in the reverse cases as well and are termed as such. Typically, during HOR, either a Tafel or Heyrovsky step must occur first, which is then followed by a Volmer step. Note that the Tafel step is not explicitly charge dependent so one might not expect its activation to be dependent on the voltage. It still has some voltage dependence though as the surface coverage of the catalyst will change with potential. This means there will be steric effects in addition to other possible coadsorbate effects previously discussed in Section 1.4.3.

It is noted here that the majority of HOR studies in literature have been performed in solution-based environments or studied in cells with hydronium conducting electrolytes (PEMFC) or hydroxide conducting electrolytes (AFC). These conditions will differ in many ways from SAECs including the distribution of reactant species, identity of the reactant species, kinetics, the activation required to form bubbles in the solution-based case, the mobility of species, and the temperature at which the reaction occurs. Thus, direct translation, direct translation of most work on HOR to the SAEC case, particularly for models. One such example is the Butler-Volmer equation when employed for rate-determining step analysis. Even in common ideal situations the Butler Volmer equation should only be applied in special circumstances. In general, systems should be considered with more generic microkinetic models that take into account surface coverage⁴⁸.

These realities notwithstanding, both the solution based and SAEC cases rely on hydrogen binding, so the wide body of HOR work is still a useful starting point for examining HOR in the SAEC case. To be

most accurate, though, we will compare to catalysts employed in SAEC environments. Specifically, we will look to the HOR research performed by Sasaki⁴⁹, Louie^{8,50}, and Paik^{51,52} for points of comparison.

3.1.2 In Solid Acid Cells

Sasaki studied HOR for SAFCs using three different types of electrodes he described as “wire”, “inverse”, and “powder”. For the “wire” electrodes, cylinders of catalyst materials are implanted into CDP and 12 wires are tested at a time without pressure on the electrical contacts. “Inverse” electrode geometries involve starting with a half-cell of CDP on a Pt and CDP mixture 3:7 (Pt:CDP) by weight. The top electrode is the material of interest and can be either a foil or sputtered material. In this case, the electrical contacts could be pressed. “Powder” electrodes refer to starting with similar half cells as the wire electrode case, but a PTFE mask is placed on top of the half cell with a small aperture in the center. Powder is subsequently placed on top of that aperture before pressing. All cells were tested in a single chamber environment with humidified H₂ gas (0.38 p_{H₂O}) at 236°C. Among candidate materials, Sasaki looked at Ni, Pd, Pt, Co, Au, and Ag with a focus on the former three⁴⁹.

Using wire electrodes, Sasaki found the HOR activity at 0.2 V was improved by catalysts in the following order: Pd>Pt>Ni>Co>Au. Pd had an order of magnitude greater activity than Pt, which had an order of magnitude greater activity than Ni which had an order of magnitude greater activity than the rest. For Ni, Sasaki’s inverse electrode tests suggested slightly higher resistance than the Pt case, but there was unusually high resistances for the Ni powder electrode study. For Pd it was found that the powder electrode geometry had two orders of magnitude lower resistance than Pt in the equivalent geometry.

Sasaki also found a strong p_{H₂} dependence for the resistance of Pd with higher p_{H₂} leading to lower resistances. From the SEM image provided for the Pd powder electrode, it is evident that there is a significant degree of densification for these electrodes. This could lead to Pd’s significantly higher hydrogen permeability (which is why Pd is often employed as a hydrogen membrane⁵³)⁴⁹. This hypothesis is also supported by the fact that for other cells Sasaki was routinely finding mass transportation limitation resistances, but none for the Pd case. When H₂ can travel so easily through Pd, it allows for easier accessibility of the hydrogen, particularly for these area-restricted geometries. Pd was also found to be less resistive under bias in contrast to the Pt and Ni cases which were found to be more resistive under bias.

After a period of 20 hours, Sasaki found a resistance increase of 0.3% per hour for the Pd wire study, but undetectable increase for the powder electrode study. Likely this level of degradation would not have been discernable in the powder electrode case as there was significant noise for that measurement (~30% error per measurement)⁴⁹.

Louie extended this research into hydrogen electrooxidation looking closer at the implementation of Pt and Pd as catalysts, with a particular examination of the thin film geometry. These cells were fabricated by DC magnetron sputtering directly onto smooth CDP discs. To test their activity, the cells were sandwiched with carbon paper and stainless-steel discs, and their impedance was measured under uniform H₂-H₂O-Ar environments⁵⁰. The real strengths of this testing lie in the geometry control as well as the ability to suggest possible reaction pathways.

From these tests it was clearly seen that in thicker films, hydrogen was diffusion limited displaying the classic 'distributed' finite-length Warburg diffusion element evidenced by its characteristic half tear drop shape on the Nyquist plot. For the thinnest films, it was clear that this element faded in prominence and instead was replaced with RQ elements. By looking at a series of thicknesses and the impact on resistance it was possible to obtain a diffusion coefficient. It was also possible to see that at less than 6 nm the diffusion resistance should totally disappear, and the reaction would only be limited by a surface reaction resistance. Furthermore, even though there were cracks in these films, by blocking the top surface with Au Louie was able to show that the top surface was the main reaction pathway for hydrogen oxidation as the Au overlayer greatly increased the resistance⁵⁰. This suggestion of two-phase reaction pathways opened up new possibilities for geometries. Thin films directly deposited (e.g., via MOCVD or ALD) on proton conductors have been demonstrated as good avenues for improving catalysis^{32,54}.

Pd films proved to be more of a challenge as they immediately suffered from a lack of electrical connectivity as the films had a tendency to form islands after electrochemical tests. It was also apparent from XRD that there was a reaction between Pd and CDP. As may be expected from the high diffusivity⁵⁵ and solubility⁵⁶ of hydrogen in Pd, the films showed no thickness dependence on the resistance. Furthermore, though there were additional RQ elements in the Pd film impedance, the total resistance was on the same order of resistance as Pt's surface reaction resistance⁸. This suggests that with clever design

Pd might be the superior catalyst, though not near the orders of magnitude difference that Sasaki suggested⁴⁹. Louie suggested Pt-Pd bilayer films might be a promising catalyst configuration since the activity, diffusivity, and solubility of Pd could be combined with the Pt structure. Louie also investigated Ni briefly, but samples reacted with CDP and she was unable to further test them⁸.

Paik extended on Louie's work by utilizing Louie's approach in thin films to learn more from cases incorporating Pd. First, Paik was able to determine that the reaction between CDP and Pd under hydrogen formed palladium phosphide as evidenced by XPS. This was tentatively assigned to Cs forming cesium hydroxide of oxide in tandem with water. As Louie had perhaps hoped, Paik found that when Pd was deposited on top of Pt, the overall reaction resistance was lowered. Interestingly this drop was more pronounced with thicker Pd films⁵². This drop in resistance was to the extent that the resistance was below what would be expected from bulk diffusion through the Pt, let alone the surface reactivity. EDS measurements revealed Pd-Pt interdiffusion despite limited miscibility⁵⁷ under the given operating conditions. Given these two findings, it was proposed that Pd diffused into the grain boundaries of Pt and provided a highway for hydrogen⁵².

This configuration allowed for improving Pt's surface and diffusion resistances simultaneously. This configuration was found to be superior to the method of cosputtering Pt and Pd, further suggesting the superior surface reactivity of Pd. Paik also found almost an order of magnitude lower surface reaction resistance than Louie for Pt⁵².

Paik then further investigated the reaction of Pd and CDP on the premise that the stabilized phosphide that interacted with CDP was still highly active. To test this, she mixed Pd/C (deposited by the NaBH₄ method) with CDP, annealed this sample under hydrogen, and then washed the sample with deionized water. Paik found that the predominant phases formed were Pd₆P and Pd₃P_{0.8} which coexisted with Pd. After testing in composite electrode structures, Paik found that higher activities than Pt were found in similar configurations despite having larger particle sizes (~2x). This suggested that even in the composite electrode structure, Pd can be more active than equivalent Pt cases for hydrogen oxidation.

3.2 Monometallic Systems

Herein, the studies have largely been conducted on composite electrolytes composed of CDP and a metal catalyst deposited on a carbon support. They were largely conducted with a so-called “standard anode” counter electrode composed of commercial 20 wt% Pt/C ball-milled and mortared and pestled with CDP in a 1:6 Pt/C:CDP ratio by weight with a loading of 25 mg. This counter electrode was placed on the initial part of the fabricated cell (i.e., the MPL layer is first placed on top of the stainless steel GDL disc, and this electrode is placed on top of the stack, pressed, and then subsequently CDP is placed and pressed). The working electrode powder is then placed on top of the half cell and pressed at two tons for one second and finally topped off with a piece of Toray carbon paper and a stainless-steel mesh disc. This fabrication is provided in more detail in Section 2.5.1.

3.2.1 Platinum

For Pt, two compositions were analyzed for this system. For the simplest analysis, a symmetric cell was fabricated. In this cell, the working electrode had the same composition and amount as the “standard anode” at the counter electrode. This composition gave a non-ohmic ASR of $0.1 \Omega \cdot \text{cm}^2$ under a symmetric humidified hydrogen environment ($0.38 \text{ pH}_2\text{O}$) with a gas flow rate of 50 sccm (see Figure 3.1a). Another attempt at making a symmetric cell was made by wrapping two standard anode half cells together, but this led to a higher ohmic resistance (expected $0.4\text{-}0.48 \Omega \cdot \text{cm}^2$) and a slightly higher non-ohmic resistance (see

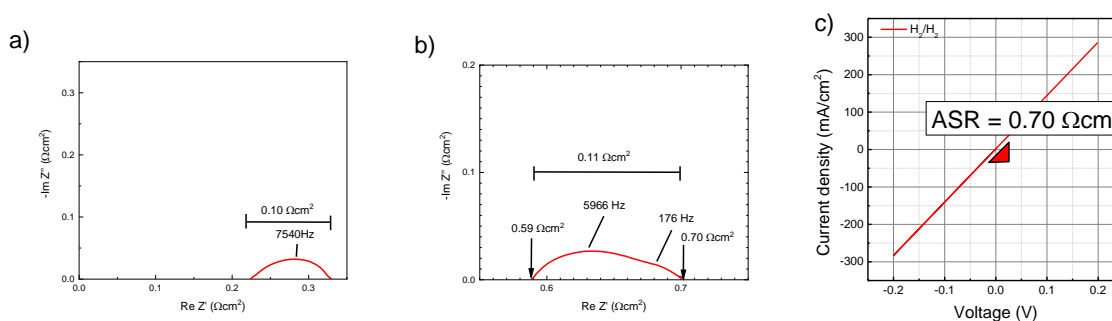


Figure 3.1 Electrochemical Analysis for symmetric Pt cells under humidified hydrogen to analyze HOR/HER. a) OCV impedance spectra of symmetric cell serially pressed (20 mV amplitude, 1 MHz to 0.1 Hz). b) OCV impedance spectra of symmetric cell composed of two “anode” half cells. c) LSV of symmetric cell composed of two “anode” half cells from reducing to oxidizing potential on the working electrode (negative to positive as displayed here). ASR reported is obtained from the inverse slope.

Figure 3.1b). For all cells attempted, a linear sweep of reducing to oxidizing potentials on the working

electrode produced highly symmetric currents with respect to OCV. This suggests that the fabrication process is reasonable at creating a uniform environment. If there was a discrepancy between HOR and HER, this discrepancy could be exacerbated by differences in the electrodes. Here it should be noted that the commercial Pt/C has a very small particle size (3.5 nm by XRD), is uniformly dispersed, and has a high electrochemically active surface area (90 m²/g metal surface area). When applying some fabrication procedures on the electrode that are proprietary to SAFCcell, this reaction resistance was lowered to 0.07 Ω·cm², but these procedures were not routinely implemented and were performed for proof of concept.

Tests were additionally performed with in house synthesized Pt on various carbon substrates such as multiwalled carbon nanotubes (MWCNTs) and Vulcan XC-72 (V). These tests were made as a point of comparison to Ru on carbon which will be explored in Section 3.2.4. For the Ru, it was found that catalysis stopped improving after a loading of ~60 wt% on high surface area carbon supports (see Appendix C.1 for evidence of this), so this loading was used as a standard for a maximum coverage and optimal for compact electrode layers. For a best apple to apples comparison between catalysts, it is ideal to have the same amount of reaction sites between the catalysts. It can be shown that when maximally loading a support, the surface area per amount of a support with its own given surface area will hold a constant area (see Appendix B.1). To try to best normalize the reaction area by maintaining volume or the closely following molar amount of catalyst material per amount of support. This is preferential to mass normalizing which can lead to poor comparisons between materials of different densities. To this end, 74 wt% Pt/C was used for the comparison to 60 wt% Ru/C. The Pt was deposited on the support by the NaBH₄ reduction method. Briefly, the support is sonicated in deionized water for five minutes. Subsequently an appropriate amount of Pt precursor is added and allowed to stir for five minutes. NaBH₄ dissolved in ice cold water is then added slowly dropwise to the main solution. The amount of NaBH₄ added is equivalent to double the number of moles of electrons required to fully reduce the precursor. Often with these reductions, the reaction completion was clearly noted as the solution transitioned from a vibrant color to clear. This main solution is allowed to react for at least 15 minutes. The product is then separated from the solution through vacuum filtration. Originally, Pt(NH₃)₄(NO₃)₂ was attempted as a Pt precursor, but it was found through TGA experiments that this procedure did not fully deposit the Pt from the precursor (~53 wt% loading for the nitrate precursor vs ~74 wt% for the chloride precursor). H₂PtCl₆·6H₂O was found to be a superior precursor

with full deposition from the precursor and a quick reduction (less than one minute by visual inspection) and was used for all tests herein. Both procedures produced single phase FCC Pt with no impurities, but the crystallite size using the nitrate precursor was 5 nm as compared to 7 nm for the chloride precursor (see Figure 3.2).

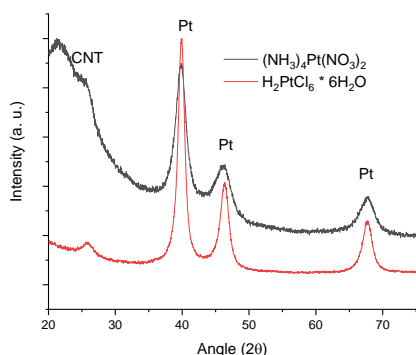


Figure 3.2 Powder XRD data for nominally 74 wt% Pt on MWCNTs by the NaBH_4 reduction method. Collected on an Rigaku Ultima diffractometer.

Additionally, attempts were made to synthesize the Pt on MWCNTs by first precipitating the chloroplatinic acid hexahydrate onto the nanotubes and then annealing them for an hour at 200°C under 5% H_2 bal. Ar. There were several drawbacks to this approach, including the crystallite size being slightly bigger (8 nm). Further inspection with SEM revealed this arose from a range of particle sizes (3-17 nm, see Figure 3.3) which is in line with what Thoi et al. found⁵⁸ following the same procedure. More troubling, when

EDS was conducted, it was found that there were high levels of chlorine detected in the sample which could act as a catalyst poison. It is suspected that higher temperatures and longer reduction times would be required to fully reduce the catalyst at which point sintering would likely greatly increase the particle size. Based on this, the NaBH_4 was implemented as the preferred synthesis route.

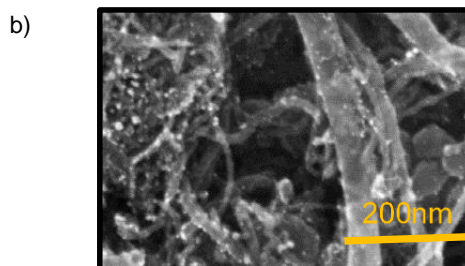
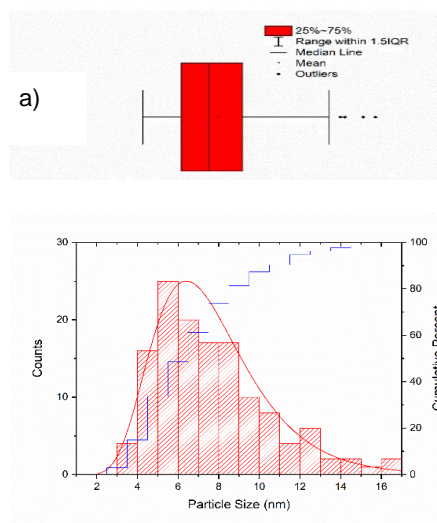


Figure 3.3 a) Distribution of particle sizes obtained from SEM imaging with a few statistical parameters. b) Selected SEM image of nom. 30 wt% Pt/MWCNT by precipitation then reduction method. Image taken at 25 kV at 200k magnification on Hitachi SU 8030.

Since regular MWCNTs were difficult to disperse in water, thus making the NaBH_4 reduction process challenging, functionalized MWCNTs (fCNT) were instead employed (COOH Nanolab). Through optimization in the Ru case, it was found that the optimal C:CDP ratio was 1:3. In this case the working electrode was composed of 100 mg of 74 wt% Pt/fCNT plus CDP with a C:CDP ratio of 1:3 by weight. These cells were tested under humidified hydrogen and humidified diluted hydrogen ($0.024 \text{ pH}_2\text{O}$) with a steam partial pressure of $0.38 \text{ pH}_2\text{O}$. Results are shown below in Figure 3.4.

From this measurement it was evident the Pt catalyst was less effective in this configuration. The H_2/H_2 non-ohmic resistance is 50% higher in this case as compared to the standard anode case while having a much higher Pt content in the electrode. Likely, one of the reasons for the decreased performance is the increase in the particle size (7 nm vs. 3.5 nm for the standard anode case). Other potential problems could be the dispersion (i.e., there could be a cluster of Pt particles from this deposition) or the compositing with CDP. It was much more challenging to mix CNT materials with CDP than to mix carbon black by visual evidence (i.e., mixed composites were less uniform and lighter in color than in the CNT case). For instance, fCNT samples would not readily form black powders when mixed with CDP until reaching a 1:3 C:CDP ratio, while carbon black mixtures are completely back at a 1:9 ratio.

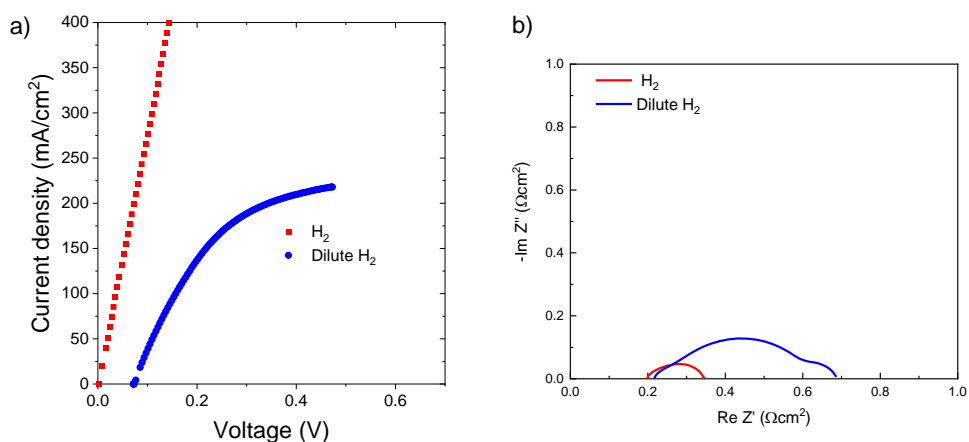


Figure 3.4 Electrochemical analysis of 74 wt% Pt/fCNT working electrode cell. a) Polarization curve taken at a sweep rate of 10 mV/s. b) EIS measurement taken at OCV with a frequency range from 1 MHz to 0.1 Hz with a 20 mV amplitude.

Additional composite Pt/C based electrodes fabricated with 74 wt% Pt/V were also synthesized by the $NaBH_4$ reduction method (which achieved the same crystallite size as those loaded on fCNT ~7 nm by XRD). The main difference in these cells was that a 1:9 ratio of C:CDP was applied in addition to using less than 50 mg ($4\frac{1}{3}$ mg C, 39 mg CDP) of total material for the electrode as opposed to 100 mg of electrode powder. Results for one such example cell is shown in Figure 3.5.

These results suggest similar results to the 74 wt% Pt/fCNT, but with a much lower Pt loading on the cell. The improved mixability is one possible reason for this, as is evidenced by color upon mixing the electrodes. This concept will be explored further in Section 3.2.4 where electron microscopy was performed

on cell cross-sections of the two types of supports. Relatedly, this could be due to less catalytic reaction sites from a difference in support contact area. Evoen reported in her thesis that the fCNTs that were used for this experiment had a surface area as determined from the BET method of $\sim 150 \text{ m}^2/\text{g}$ ⁵⁹, whereas we find a support area for the Vulcan XC-72 of $\sim 220 \text{ m}^2/\text{g}$ (see Appendix C.2 for BET analysis). Differences in the pore structure and the tortuosity in the electrode can also affect the capacity of the reactants to reach the electrode (see Appendix B.2 for calculation of the effect of porosity and tortuosity). This is particularly of interest since the main discrepancies lie the lower frequency region where mass-transport effects would manifest. Regardless of these differences, both the fCNT and Vulcan cells perform worse than the commercial 20 wt% Pt/C case which supports the hypothesis that the increased number of active sites due to better dispersion and smaller crystallite sizes is the most important. To test this hypothesis, a selective chemisorption experiment was carried out on 74 wt% Pt/V.

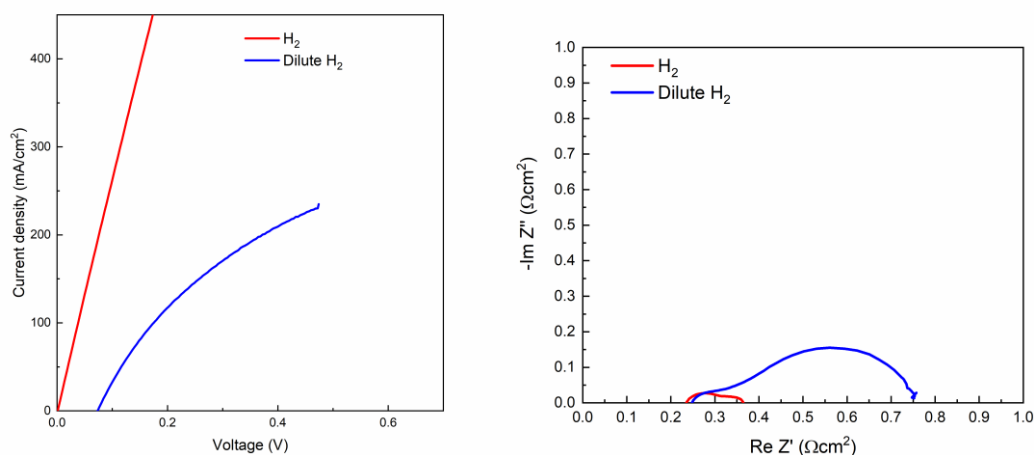


Figure 3.5 Electrochemical analysis of 74 wt% Pt/V working electrode cell. a) Polarization curve taken at a sweep rate of 10 mV/s. b) EIS measurement taken at OCV with a frequency range from 1 MHz to 0.1 Hz with a 20 mV amplitude.

First, the sample was pre-reduced under 10% H₂ at 350°C for one hour. After cooling, pulses of 5% CO bal. He (which selectively chemisorbs with Pt and not C) were introduced to the sample while the exhaust was monitored with for thermal conductivity (TCD). This TCD signal allows us to infer how much CO is taken up by the sample. The sample is subsequently purged with He, and then heated up to 400°C for the CO to desorb in a so-called temperature programmed desorption experiment (TPD) where again the exhaust is examined by TCD. Finally, the sample is cooled under He. These results were able to show that the sample had a catalyst surface area of 1 m²/g or about 4 m²/g of carbon (see Appendix C.3 for more

experimental details and results). This is significantly lower than the reported metal surface of the commercial carbon, which claims a metal surface area of $90 \text{ m}^2/\text{g}$ or $\sim 113 \text{ m}^2/\text{g}$ of carbon. This alone could readily account for the decrease in performance for the in-house fabricated Pt/V. It should be noted that the high reduction temperatures employed here likely lead to sintering but are not expected to lead to this magnitude of a difference as will be evident from descriptions of similar experiments in Section 3.2.4.

3.2.2 Palladium

The first comparison made for the Pd case was between commercial Pd and commercial Pt. Commercial 20 wt% Pd/V was purchased (The Fuel Cell Store) with a reported metal surface area of $100 \text{ m}^2/\text{g}$ and a particle size of 3-5 nm. This has a slightly higher surface area per amount of carbon in comparison to the Pt case but was close enough for relative analysis. A cell was fabricated with the normal standard Pt anode half-cell and a layer placed on top composed of commercial 20 wt% Pd/C ball-milled and mortared and pestled with CDP in a 1:6 Pd/C:CDP ratio by weight with a loading of 25 mg. This layer was pressed on the cell at 2 tons for 1 second. Subsequently, a piece of carbon paper was added, and the entire cell was wrapped with Teflon tape. Electrochemical test results are shown in Figure 3.6.

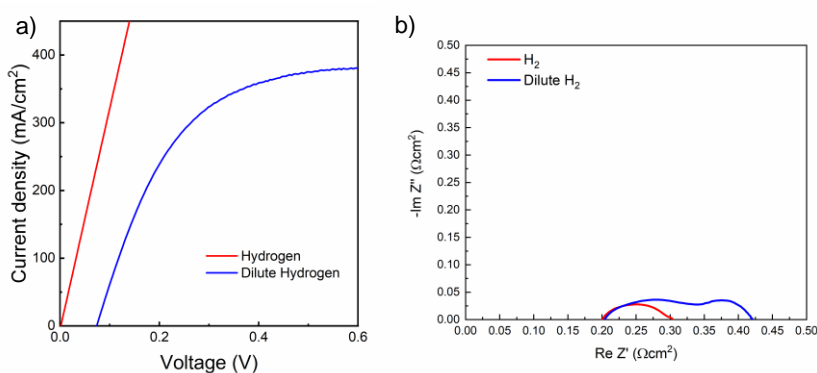


Figure 3.6 Electrochemical analysis of 20 wt% Pd/V working electrode cell. a) Polarization curve taken at a sweep rate of 10 mV/s. b) EIS measurement taken at OCV with a frequency range from 1 MHz to 0.1 Hz with a 20 mV amplitude.

This cell with Pd had a H_2/H_2 non-ohmic resistance that matched the performance of the Pt standard anode symmetric cell, suggesting that dispersed Pd/C has about the same activity as dispersed Pt/C. It has been established that Pd will react with Pt even under reducing conditions, but Paik's results suggested that the reacted Pd will still be active for HOR⁵², so some effort was put into looking at the stability of this cell when operating under reducing conditions. To do this, a constant oxidizing voltage of 0.15 V was applied in the dilute hydrogen condition while the current was monitored (see Figure 3.7a). Additionally, the cell was held under the dilute hydrogen condition overnight and electrochemical tests were run the next day for an onstream time of about 20 hours (Figure 3.7b and Figure 3.7c). Both results suggest stable performance under reducing conditions.

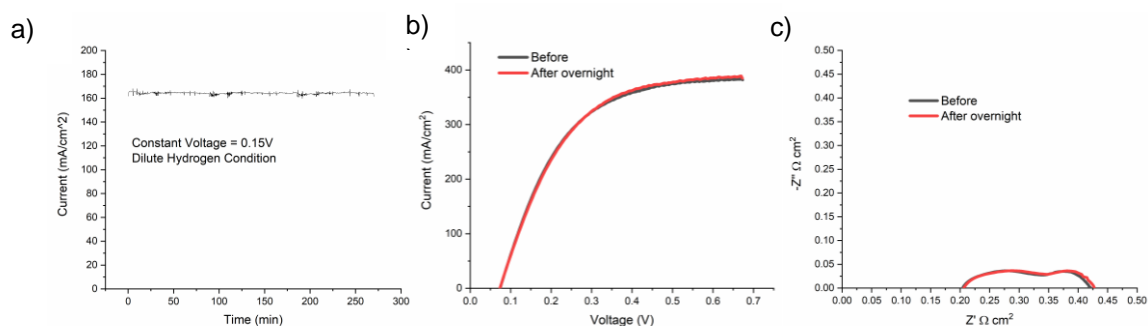


Figure 3.7 Stability tests for 20 wt% Pd/C cell. a) shows a constant voltage measurement taken under the dilute hydrogen condition taken over a period of four and a half hours. b) shows polarization curves drawn under the dilute hydrogen condition at sweep rates of 10 mV/s. c) shows impedance spectra taken at OCV under frequencies from 1 MHz to 0.1 Hz with a 20 mV amplitude.

A more completely symmetric cell was also attempted in which the composition of the working and counter electrodes was the same (both containing 20 wt% Pd/V pressed at three tons for three seconds). It was found that there was a large increase in resistance when using this configuration. Figure 3.8a shows an approximately three times increase in non-ohmic resistance for this cell. The main difference arises from a second arc appearing at low frequencies, possibly due to mass transport limitations. Upon investigating cell-cross sections for the previously fabricated cell, it was evident that the increased pressure on the Pd-based anode caused a large degree of fusion in the electrode (see Figure 3.8b and Figure 3.8c), decreasing the porosity in the electrode and thereby decreasing the reactant availability.

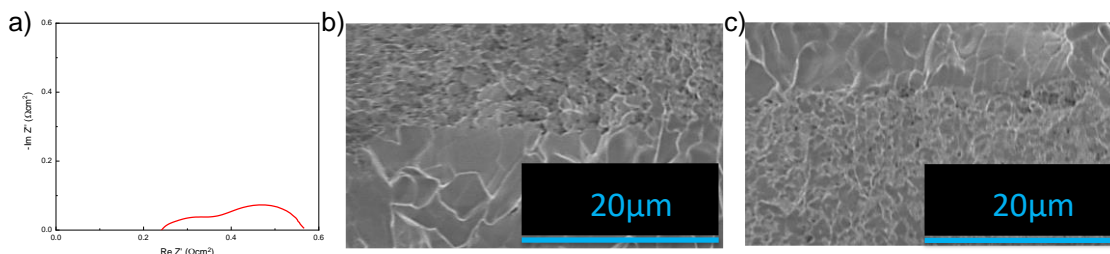


Figure 3.8 a) OCV impedance of 20 wt% Pd/V symmetric cell under the hydrogen condition. b) Working electrode of 20 wt% Pd/V symmetric cell pressed at two tons for one second. c) counter electrode of 20 wt% Pd/V symmetric cell pressed at three tons for three seconds. SEM images taken on Hitachi SU 8030 at 2 kV 2k magnification for both images.

Further clarification was sought for the results of Sasaki⁴⁹, particularly for the electrode composition of Pd black and CDP. A cell with a standard anode half-cell and an electrode matching Sasaki's composition of 30 mg Pd:CDP 3:7 was made using Sasaki's method and then pressed on the half cell at three tons for three seconds. This gave obvious increases in the mass transport-based resistance as is evidenced in Figure 3.9a and a closed structure was confirmed in Figure 3.9c. This being the case, a second attempt was made, but a pressure of two tons was applied for one minute which resulted in the elimination of the mass-transport resistance (see Figure 3.9) and an obviously more porous structure as evidenced by SEM (see Figure 3.9d). This second-attempt cell had a significantly lower resistance than what was seen for Pt, but not to the level that was noted in Sasaki's measurements. Further investigation was carried out using a different impedance analyzer (a Solartron instead of a Biologic, the Biologic of which was used for all the measurements herein) that incorporated a multiplexer to analyze samples in tandem. This impedance measurement setup was now identical to Sasaki's. Under this setup there was an obvious increase in the noise of the measurement which appeared like the measurement Sasaki read. Thus, Sasaki's measurement setup might be ill-suited to measure this low magnitude of impedance (Pt in this geometry had much higher resistance) and so the extremely low reaction resistance could have been experimental error. This still suggests though that Pd is effective even in a relatively dense configuration.

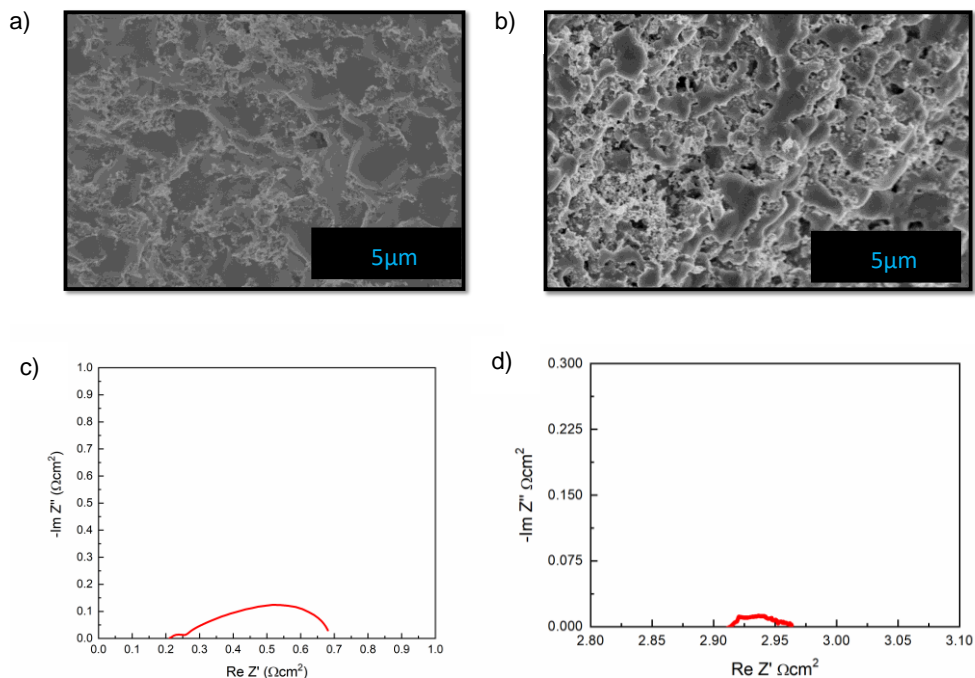
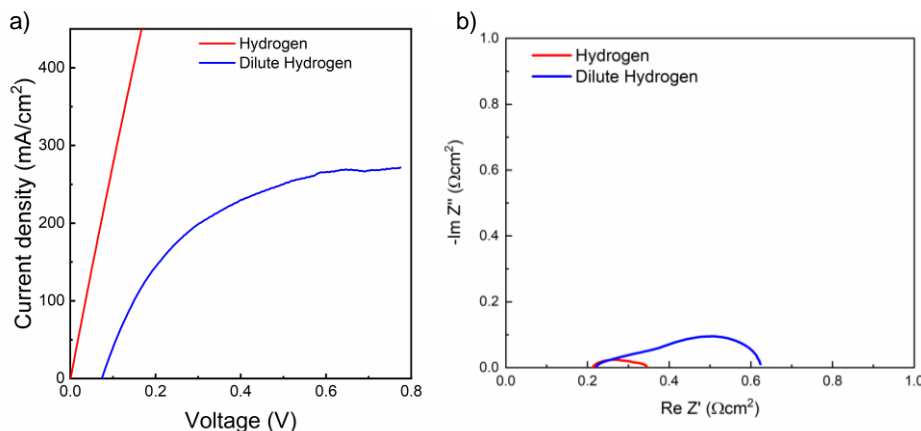


Figure 3.9 SEM images of cell-sections for the a) Pd:CDP 3:7 electrode pressed at three tons 3 seconds and b) identical electrode pressed at two tons for one minute. Both images taken with a Hitachi SU 8030 at 5 kV with 10k magnification. OCV impedance spectra under hydrogen of c) Pd:CDP 3:7 electrode pressed at three tons 3 seconds and b) identical electrode pressed at two tons for one minute. Both spectra collected with a frequency range of 1 MHz to 0.1 Hz and a 20 mV amplitude. d) tested in the single chamber impedance station.

The final configuration using Pd that was examined for was in a more “fully-loaded” case where Pd was deposited in an amount equimolar to 74 wt% Pt/V (61 wt% Pd/V). This was completed using a NaBH_4 reduction with PdCl_2 as the Pd precursor. XRD results for this sample suggested no impurity phase to the FCC Pd and a larger crystallite size of 14 nm. The working electrode for this measurement was also fabricated in a similar manner as the 74 wt% Pt/V in that 61 wt% Pd/V was mixed with CDP in a 1:9 C:CDP ratio and amounts of carbon and CDP were held constant ($4\frac{1}{3}$ mg C, 39 mg CDP). Results from electrochemical tests for this cell are shown in Figure 3.10.

**Figure 3.10**

Electrochemical analysis of the 61 wt% Pd/V working electrode “fully loaded” cell. a) Polarization curves taken at a sweep rate of 10 mV/s and the b) EIS measurements taken at OCV with a frequency range from 1 MHz to 0.1 Hz with a 20 mV amplitude.

Results from the electrochemical tests suggest that the 61 wt% Pd/V has a slightly lower HOR resistance under hydrogen compared to the 74 wt% Pt/V case but was less resistive under the dilute hydrogen case to a greater extent. Overall Pd appears to be at least as effective as Pt for HOR in a dispersed composite electrode on carbon supports and appears more effective than Pt in dense configurations. One caveat (aside from preventing the reactivity in environments with oxygen) lies in that Pd-based electrodes appear more sensitive to the pressure of fabrication, so care (i.e., lighter pressures) should be used when fabricating Pd cells.

3.2.3 Ruthenium

For the Ru case, it is evident that as fabricated cells degraded over time in ambient conditions (evidence of this provided in Appendix C.4), presumably for the reaction of RuO₂ with CDP. This being the case, all measurements performed herein were on cells fabricated and tested within the same day. All Ru samples were synthesized in-house by the NaBH₄ method. While XRD shows single phase Ru (~4 nm crystallite size), the reactivity in non-reducing conditions suggests that a small amount of amorphous RuO_x forms on the surface of the particles that can react with CDP and the oxygen is removed at elevated temperatures under reducing conditions. This is explored to a great extent in Appendix C.5 in which it is finally concluded that this indeed the case, at least sparsely on the surface. Nevertheless, consistent procedure allowed for only minimal degradation before samples would be tested made for consistent results that are explored in this section.

Initial tests were performed on Ru loaded onto functionalized carbon nanotubes (62 wt% Ru/fCNT – COOH) with a synthesis procedure completely analogous to the “fully loaded” Pt case on fCNT. Technically, to match the molar amount on Pt/fCNT, the loading should be 60 wt% Ru, but these samples were considered close enough to be comparable. Loading was confirmed by oxidizing the fCNTs away at high temperature under air and then reducing the sample under 3% H₂ (See Appendix C.6).

First, a few C:CDP ratios were explored to find optimal composite mixtures for 62 wt% Ru/fCNT – COOH. It was found that higher carbon ratio composites were more active (see Figure 3.11a and Figure 3.11b). This appeared to be due to the microstructures that formed in the composites. Post-operation cell cross-sections were analyzed by SEM and their areal porosity was determined using ImageJ. Higher carbon ratios were correlated with higher porosities (See Figure 3.11c), suggesting that greater reactant access resulted in lower reaction resistances.

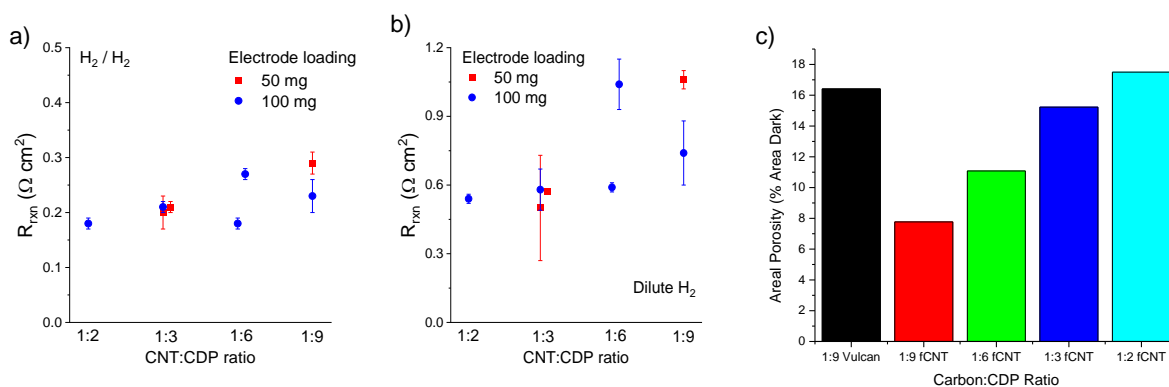


Figure 3.11 a) Non-ohmic resistance of Ru-fCNT-COOH cells with listed compositions with humidified hydrogen supplied to the working electrode. b) Non-ohmic resistance of Ru-fCNT-COOH cells with listed compositions dilute hydrogen supplied to the working electrode. Error bars for a and b show fitting error. c) areal porosity determined by ImageJ analysis of post-operation cell cross-sections. Determination done by thresholding images to an extent to where all pores selected in an image and calculating the % this threshold area takes up.

Additionally, the effect of annealing (tangentially of particle size) was explored by pre-annealing Ru/fCNT. A sample to be used for an electrode was annealed under 3%H₂ bal. Ar for one hour at 400°C. XRD showed an increase in crystallite size to 13 nm (from 4 nm). Performance decreased with the sample that was annealed at a higher temperature suggesting the effect of decreasing active area (Figure 3.12a). fCNT-COOH performance appeared unstable as well with a decrease in polarization current density when testing for ammonia oxidation after 10 hours (Figure 3.12b).

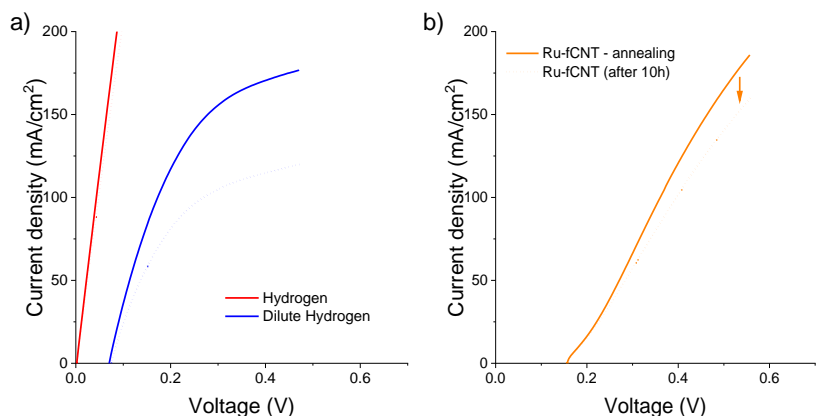


Figure 3.12 62 wt% Ru/fCNT, fCNT:CDP=1:3 cells with as synthesized (solid line) and annealed (dotted line) at 400 °C for 1 h tested in a) hydrogen and dilute hydrogen. b) Decrease in ammonia oxidation performance after cell left on stream for 10h (0.4 pNH₃, 0.38 p_{H2O}, bal. N₂). Sweep rates were 10 mV/s.

To test if another type of functionalized carbon nanotube might be more effective, amine functionalized carbon nanotubes were also tested (fCNT-NH₂). Results with amine functionalized CNT showed improved performance in higher CDP composition electrodes (also meaning less catalyst loaded) cells. 1:9 fCNT-NH₂ cells closely approached the performance of 1:3 fCNT-COOH cells (see Figure 3.13). Nevertheless, performance decreased after an extended period under ammonia suggesting these functionalized carbon nanotubes are also unstable.

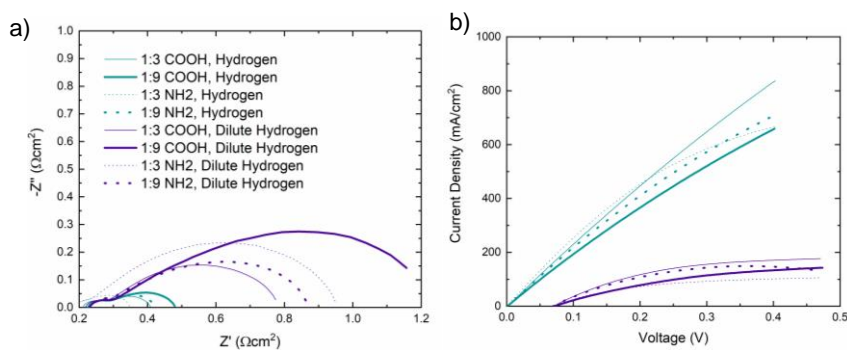


Figure 3.13 a) Impedance spectroscopy of 62 wt% Ru/fCNT 100 mg working electrode cells under hydrogen and dilute hydrogen. Frequency range from 1 MHz to 0.1Hz. b) Polarization curves of same cells and conditions with a 10 mV/s sweep rate.

A peculiar trend of a negative slope with higher oxidizing potentials in the dilute hydrogen condition was noted for Ru-based cells with larger ratios of CDP, for example, the 1:9 62 wt% Ru/fCNT-NH₂ case. One reason for this was the possibility of nitrogen adsorbing to the surface and blocking active sites at higher oxidizing potentials, since Ru has a more favorable nitrogen binding energy than Pt. This was explored by changing the balancing inert gas from N₂ to Ar which showed no difference in the polarization (see Figure 3.14a). A second possibility that was explored was the impact of water partial pressure. As gas conditions were held constant for the dilute hydrogen condition, the water partial pressure was increased

to 0.5 p_{H₂O}, then decreased to 0.3 p_{H₂O}, before returning to 0.38 p_{H₂O}. This test revealed that while the initial behavior was the same in all cases, the drop-off at higher oxidizing potentials was more pronounced when the water partial pressure was increased and less pronounced when it was decreased. In addition, the behavior was reversible. This behavior is in stark contrast to what happens in the Pt case where there are only small differences with water partial pressure and if anything, the polarization curve has a positive relationship with water partial pressure (See Figure 3.14b). Of course, there were a few differentiating factors between these cells such as the C:CDP ratio and the functionalization of the support. Additionally, this Ru cell was cycled through several conditions over an extended period and was degraded over the course of operation. This finding is later shown to be more robust after being confirmed on a more apples-to-apples basis when investigating the Vulcan support case.

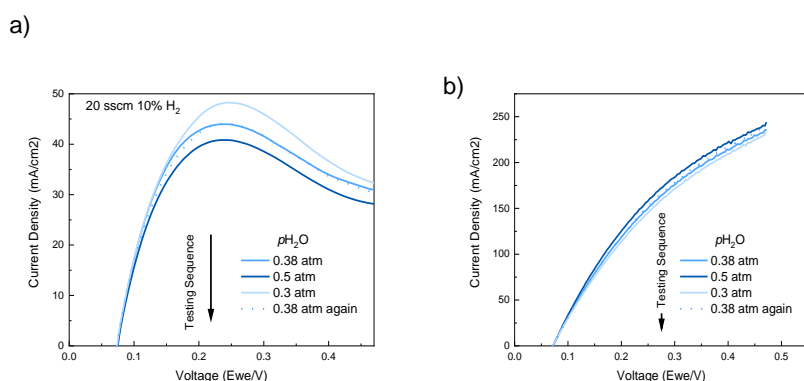


Figure 3.14 a) 62 wt% Ru/fCNT-NH₂ working electrode with a C:CDP ratio of 1:9 and 100 mg total mass. b) 74 wt% Pt/fCNT-COOH working electrode with a C:CDP ratio of 1:3 and 100 mg total mass. Tested under the dilute hydrogen condition with a scan rate of 10 mV/s.

Vulcan XC-72 was looked to as a potential support for the Ru system. A series of cells were tested to determine the optimal C:CDP ratio for cells with Vulcan while employing the Ru rich system (9:1 Ru:Pt/V) (see Appendix C.7), and it was found that an optimal C:CDP ratio sits around 1:9. Additionally, the loading was held at 60 wt% Ru/V to be equimolar with 74 wt% Pt/V. Cells were also prepared using 50 mg of total electrode powder. The result of the analysis of this cell are shown below in Figure 3.15.

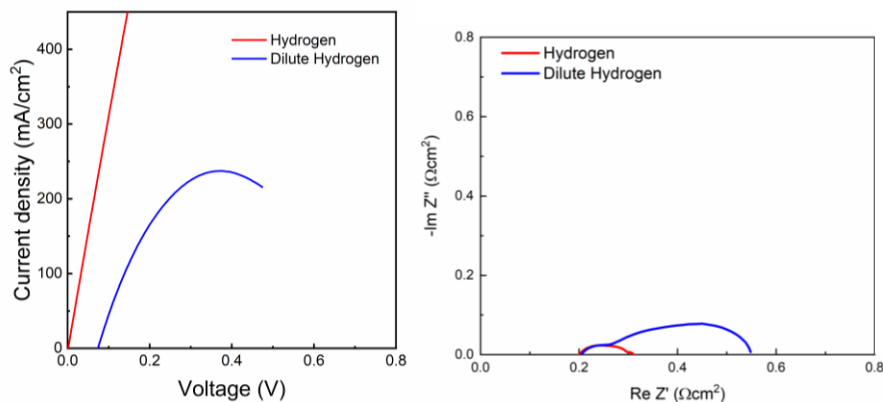


Figure 3.15 Electrochemical analysis of the 60 wt% Ru/V working electrode “fully loaded” cell. Electrode made with C:CDP ratio of 1:9 and used 50 mg in total.

It is clear that Ru performs hydrogen oxidation at lower oxidizing potentials better than in-house synthesized Pt/V in the hydrogen and dilute hydrogen conditions and even approaches values close to that of the standard anode commercial Pt. A challenge remains in that there is a turnover in the current at higher oxidizing potentials that appeared previously to be correlated with the steam partial pressure. This test with varying water partial pressures was performed again on this cell and then compared with the close analog for the Pt case (C:CDP 1:9, 50 mg electrode, Vulcan support) in Figure 3.16. This result affirmed the previous conclusion that higher p_{H_2O} levels negatively affect the hydrogen oxidation performance of Ru at higher oxidizing potentials.

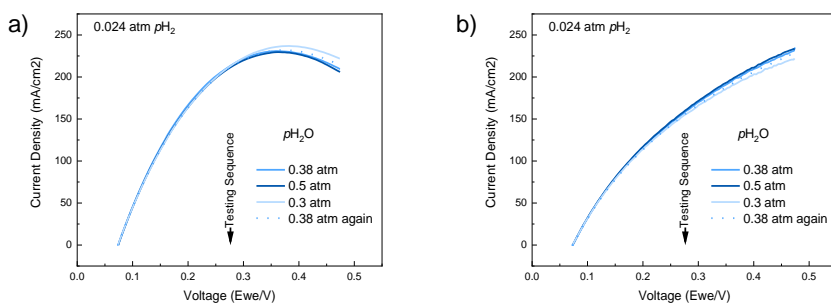


Figure 3.16 a) 60 wt% Ru/V working electrode with a C:CDP ratio of 1:9 and 50 mg total mass. b) 74 wt% Pt/V working electrode with a C:CDP ratio of 1:9 and 50 mg total mass. Tested under the dilute hydrogen condition with a scan rate of 10 mV/s.

This correlation noted with steam partial pressure led to the idea that perhaps ruthenium hydroxide was being formed. This turnover phenomenon necessitating the presence of H_2O and being coerced by oxidizing potentials can be explained from the following reaction:



Evidence of this can be found in the literature, particularly in the studies of PtRu catalysts for methanol oxidation. For these systems, it is found that Ru aids in these reactions by forming the hydroxide and this reacted hydroxide can then oxidize chemisorbed CO on neighboring Pt sites under oxidizing potentials. This has been shown through electrochemical analysis in tandem with techniques such as surface enhanced infrared absorption spectroscopy and x-ray absorption. Most experiments show that the formation of ruthenium hydroxide under oxidizing potentials is important for this mechanism⁶⁰⁻⁶³. Additionally, these note studies that excess Ru in the catalyst can lead to blocking active sites from the chemisorbed OH.

To investigate this further, cyclic voltammetry was performed at several different scan rates (see Figure 3.17). If enough is eventually known about the system, these cyclic voltammograms can help provide valuable information about the thermodynamics, kinetics, and active sites for this system and the possible ruthenium hydroxide formation and decomposition. Figure 3.17a shows that a hysteresis is formed when switching between oxidizing and reducing conditions and this is scan rate dependent, while the HER condition at the working electrode exhibits no hysteresis. Additionally, there is a wide gap between the peak in oxidation current and peak in the reduction current at faster scan rates, but this gap narrows at slower scan rates (see Figure 3.17b).

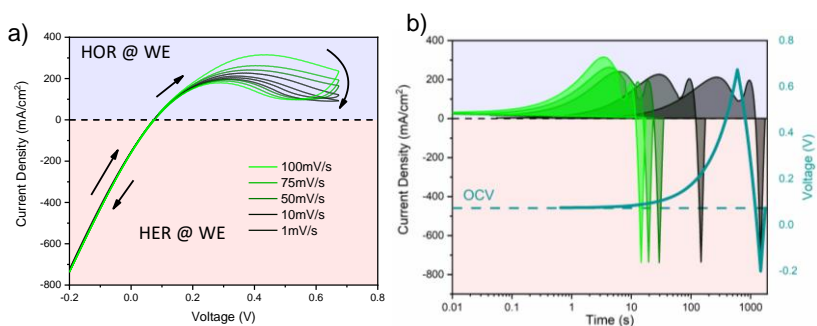


Figure 3.17 a) Cyclic Voltammetry scan under the dilute hydrogen condition for 60 wt% Ru/V from OCV to 0.6 V above OCV, to -0.2 V, and then back to OCV at various scan rates. b) Showing the same data as a function of current density versus time with an example voltage profile for the 1 mV/s case shown imposed on top of the data.

Further knowledge can be inferred though more detailed system information would be required to draw accurate conclusions (such as actual adsorbates, reaction area, reactions, etc.). For example, if a charge transfer reaction is occurring to oxidize the Ru and then again in the reduction of RuOH, then the oxidizing current would increase above the faradaic level when oxidizing and vice versa when reducing.

This suggests that the area of the hysteresis should be proportional to the amount of Ru reacting. Since we know the scan rate ν we can convert the x-axis of Figure 3.17a to time t by using:

$$t = \nu V \quad (3.6)$$

The area of that plot gives the charge density since the current density multiplied by time would give $((Q/At)*t)$ where Q is charge and A is the active surface area. An example of this integration is shown in Figure 3.18. This also shows that the hysteresis area increases linearly with time and that the increase in charge density still happens up to the slowest reaction. One might expect this trend to level off after all of the Ru is oxidized and all of the RuOH is reduced in the reverse direction, so the capacity for charge to be directed towards this non-faradaic purpose would have a ceiling.

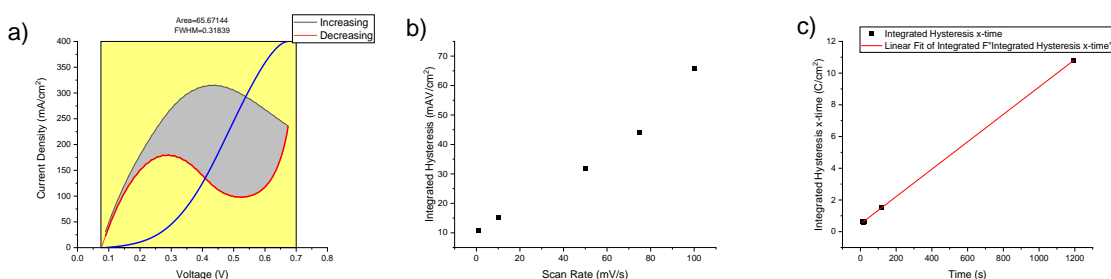


Figure 3.18 a) Showing integration of 100 mV/S measurement as example. Gray is the integrated area, and the blue line shows the cumulative integrated area across the profile. b) Integrated area for each of the measurements as a function of scan rate. c) Integrated area for each of the measurements as a function of the time to carry out the measurements.

One challenge in these measurements is that if the measurement is not carried out slow enough (which is difficult to tell within the contents of a single measurement) the effects of potential and time are challenging to deconvolute. To analyze the system in a more discrete fashion and have better time and voltage resolution for several selected points, a chronoamperometric approach was performed on a new cell of the same composition. For this series of measurements, first a given oxidizing potential was applied to the working electrode for ten minutes, followed by a reducing potential 0.1 V below OCV for five minutes, and followed a period of five minutes in which the system is allowed to rest before proceeding with the next measurement. Figure 3.19 shows a visual representation of this approach as well as the overall results.

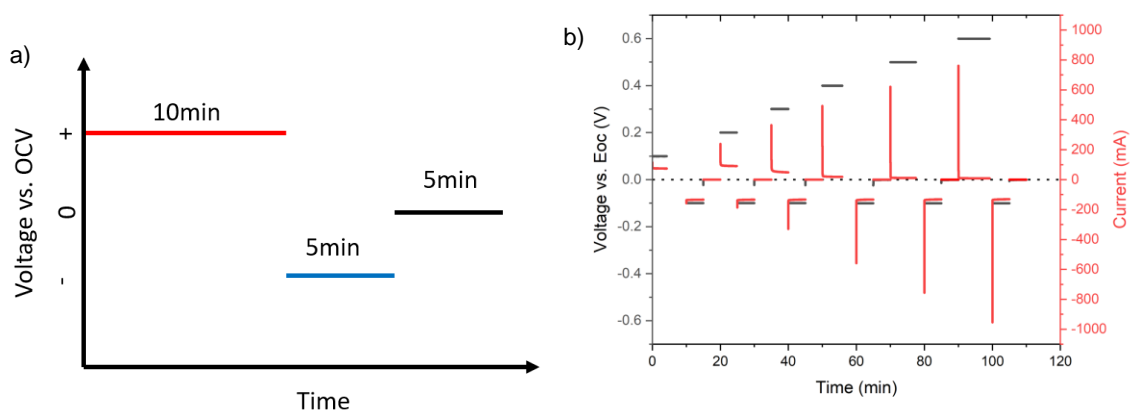


Figure 3.19 a) Schematic of dilute hydrogen 60 wt% Ru/V chronoamperometric voltage profile. b) results of tests ranging from 0.1 V to 0.6 V of oxidizing potential applied above OCV.

The results are more easily examined when considering them from a time normalized standpoint, looking at a period when the data is most dynamic, so this is presented in Figure 3.20. From these chronoamperometric results, it is clear somewhere between 0.2 V and 0.3 V above OCV that there is a poisoning effect limiting the current density. This is in line with what might be expected from the work of Strmcnik et al.⁶⁴, who found a similar poisoning effect above 0.2 V for HOR on Ru(0001). It is also apparent from the rate of drop-off that after 0.2 V there is a charge effect happening more diffusely than before 0.2 V. Perhaps this is because the original current drop-off is an artifact of the measurement if there is a capacitive charging current. Then the more diffuse effect corresponds to the oxidation of Ru. Additionally, there is not a difference in the steady-state current moving from 0.5 V to 0.6 V implying that perhaps at an oxidizing potential between 0.4 V and 0.5 V the poisoning effect is maximized.

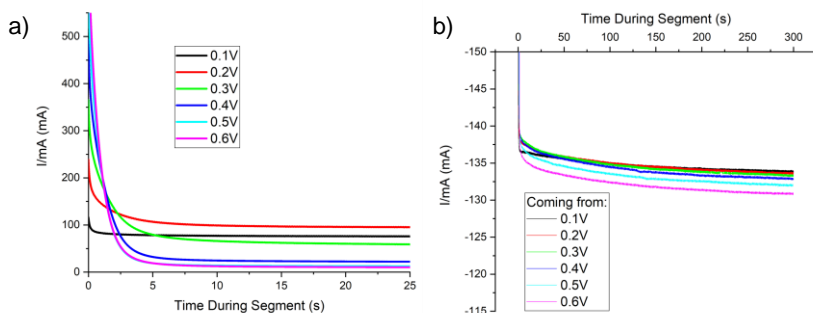


Figure 3.20 Constant voltage measurements for 60 wt% Ru/V under the dilute hydrogen conditions under a) various oxidizing conditions at the working electrode and b) under a reducing voltage of -0.1V vs. OCV. Indicated voltage in plots are versus OCV.

From the smaller crystallite size, it appears suggestive that Ru catalyst particles could be showing a higher effective surface area than for the Pt case. To explore the 60 wt% Ru/V active area, a similar selective chemisorption experiment was performed for Ru/V (detailed in Appendix C.8). Unlike the Pt case, the Ru bonding case can vary, so a CO Diffuse Reflectance Infrared Fourier Transform Spectroscopy (DRIFTS) experiment was performed to determine this. Indeed, it was found that Ru has a higher active surface area of 7.5 m²/g based on total weight and of 19 m²/g based on carbon weight. This higher area likely causes Ru to perform better than the in-house fabricated 74 wt% Pt/V. Still, the results of Ru/V perform close to the level of commercial Pt/C used for the standard anode configuration owing to the higher active area of commercial Pt/C. In the electrodes tested the 60 wt% Ru/V case has 812-1496 cm² of active surface area in the working electrode whereas the 20 wt% Pt/C case has 3,214 cm². Careful synthesis with the Ru case could possibly make it more active than the commercial Pt case for low oxidizing potentials. This is particularly appealing since the historical prices for Ru are significantly lower than those for Pt⁶⁵. Overall, both Pd and Ru appear to be promising hydrogen oxidation catalyst alternatives to Pt with the condition that they are kept in non-oxidizing conditions save the possibility that a diffusion barrier is developed for implementation in electrodes that prevents the interaction of Pd or Ru oxides with CDP.

3.3 Multimetallic Systems

Alloy metal catalysts hold the promise of aiding rational catalyst design to improve activity and selectivity⁶⁶. Maps have been laid out for how this might be achieved (see discussion in Section 1.4.3), and much research has since been pursued. For the solid acid systems, multimetallic systems have not been explored save for the investigations into the Pd-Pt system^{9,52} so some effort was performed here to see if alloying materials can aid in the HOR for SAECs. Promising alloys created using the previously discussed monometallic systems are discussed.

3.3.1 Platinum-Ruthenium

According to the Pt-Ru phase diagram⁶⁷, near ambient conditions HCP Ru is reasonably soluble in FCC Pt (up to 40 at% Ru), and Pt is hardly soluble in Ru leaving a wide two-phase region. Upon heating toward our operating temperature (523 K), it is expected that this region would increase Ru solubility in Pt

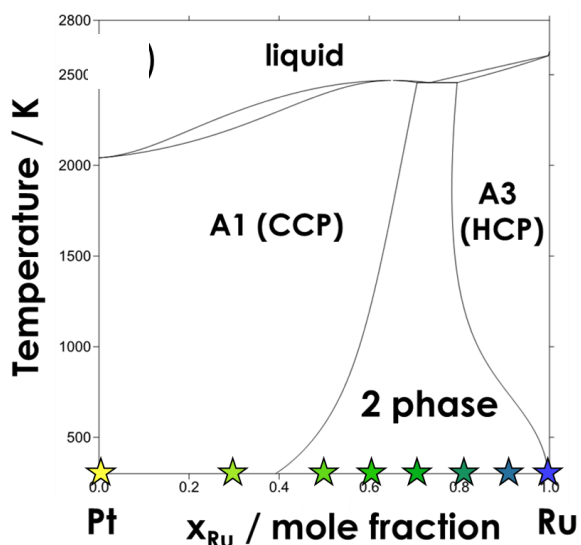


Figure 3.21 Calculated Pt-Ru phase diagram. CCP indicates close-packed cubic and HCP indicates hexagonal close-packed. Stars shown at bottom indicate compositions tested here. Modified from Cornish et al⁶⁷.

(up to 50 at% Ru) and Pt solubility in Ru (up to 5 at% Pt). The phase diagram is included here for reference in Figure 3.21. Based on surface energy calculations¹¹ and experimental results⁶⁸ it is largely expected that if a core-shell particle forms from this alloy composition that the Pt phase would sequester to the outside of the particle leaving a Ru-rich core. It was found that at a lower synthesis temperature (~200°C) Ru shell and Pt core particles were created, but these inverted upon

heating to 400°C⁶⁹.

To synthesize bimetallic Pt-Ru particles on Vulcan XC-72, Pt and Ru was co-deposited using the NaBH₄ method. The method is completely analogous to the previous NaBH₄ depositions save that the metal precursor was a combination of ruthenium chloride hydrate and chloroplatinic acid. The molar amount of metal was held constant at 60 mol% Ru/V. For phase determination, the samples were analyzed with XRD (see Figure 3.22). It was found that upon adding 10 mol% Pt, a second phase is not apparent, but additional Pt makes a second FCC phase apparent until 50 mol% Pt at which the HCP phase disappears. This is close to what might be expected from the phase diagram shown in Figure 3.21.

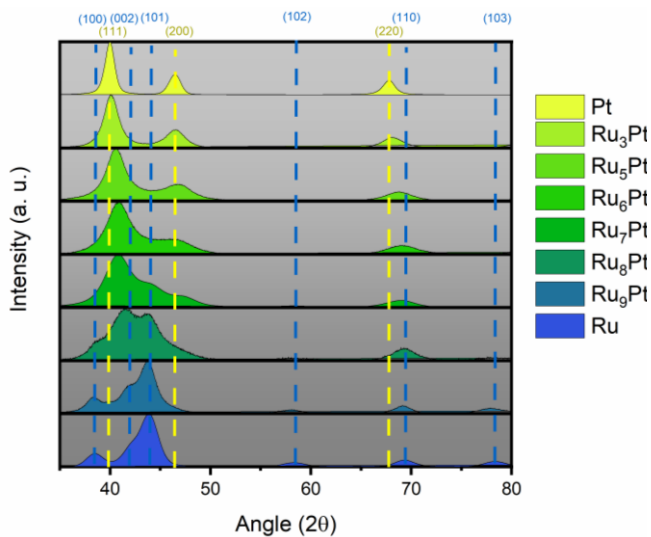


Figure 3.22 Powder XRD of co-deposited RuPt/V by the NaBH_4 taken by a Rigaku Ultima.

From TEM analysis, it was revealed that this synthesis resulted in the formation of core-shell particles (see Figure 3.23). From EDS analysis, it was apparent that Ru was present on the shells of these particles and the core was Pt-rich. It is not known at this point if upon operation at 250°C for an extended period of time this core-shell composition would invert as Nashner et al. found⁶⁹.

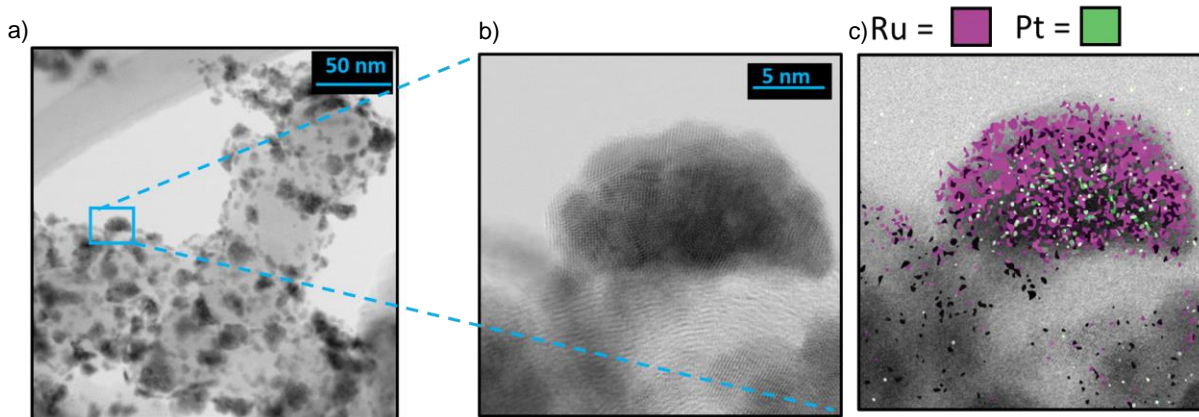


Figure 3.23 a) TEM image of 64 wt% $\text{Ru}_8\text{Pt}_2/\text{V}$. b) Increased magnification on a single particle. c) EDS measurement showing outside is Ru rich and inside is Pt rich with model particle on top left (JEOL ARM200CF).

Cells were then fabricated with these bimetallic catalysts. Working electrodes were composed of a constant carbon and CDP amount ($4\frac{1}{3}$ mg C, 39 mg CDP). These cells were predominantly tested in the dilute hydrogen condition, and results are shown in Figure 3.24. Bimetallic RuPt appears to be more effective at HOR than either Ru or Pt alone. OCV EIS shows the bimetallic system having the lowest overall reaction resistance. The polarization curves also show that even for the minimal 10 mol% Pt the current turnover at higher overpotentials is eliminated.

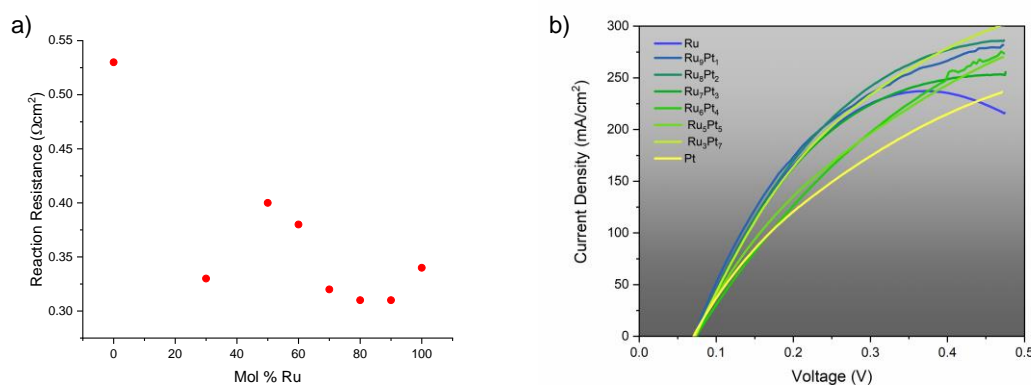


Figure 3.24 a) Reaction resistance obtained by OCV impedance for the RuPt/V cells under the dilute hydrogen conditions. Perturbation voltage was 20 mV with a frequency range from 1 MHz to 0.1 Hz. b) Polarization curves for the same cells under the same conditions. Oxidizing potential applied to 0.4V above OCV at the working electrode with a scan rate of 10 mV/s.

Doping Ru catalysts with Pt appears to allow for a high reaction resistance while simultaneously alleviating possible poisoning from formation of hydroxide. Indeed, in literature, several authors have found that RuPt combinations show more optimal hydrogen binding energies and some also find the effect of hydroxide formation from Ru synergistic to subsequent hydrogen desorption^{64,70-74}. These findings are in lower temperature settings often in solution and, as such, are likely to have different fundamental mechanisms compared to our case, though they can share an underlying phenomenon. One might consider that this could have some confounding effect on the available active surface area as we had seen previously that the in-house synthesized Pt had a much lower active surface area than the in-house synthesized Ru. A first-approximation look is given by the crystallite size from XRD (see Figure 3.25), while a more holistic view can be seen from the TEM image in Figure 3.24.

From Figure 3.25 it is apparent that the crystallite size of this alloy is slightly smaller than the Ru case, however, Figure 3.23 makes it evident that this is because the crystallites are combined and likely trend towards the Pt case. Apparent particle sizes in Figure 3.24 were much larger than for the Ru case. This suggests that there is likely an enhancement in activity. Furthermore, a test was performed where the reducing gas was switched to N_2 on stream and held for an hour (see Figure 3.26). Testing before and after this switch showed that performance was maintained, suggesting that the RuPt catalyst does not have to be held under reducing conditions to remain stable.

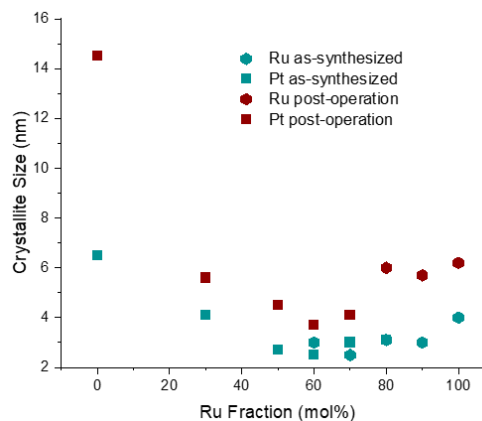


Figure 3.25 Catalyst crystallite size before and after operation for RuPt/V determined by XRD (Rigaku Ultima).

In addition to the Vulcan support tests, some tests were initially performed on fCNT-COOH where the catalysts were synthesized in the same manner, just substituting fCNT for the previous Vulcan XC-72. For these cells, 100 mg electrodes were used with a C:CDP ratio of 1:3 and equivalent molar masses of 60 wt% Ru were loaded on the carbon nanotubes. Electrochemical test results are shown in Figure 3.27. Again, for the fCNT supported bimetallic system, their hydrogen oxidation activity was much higher than either of the constituent monometallic systems with equivalent molar loading. Both sets of results suggest that the Pt-Ru system is effective for HOR and could even be used as a cheaper alternative to Pt alone.

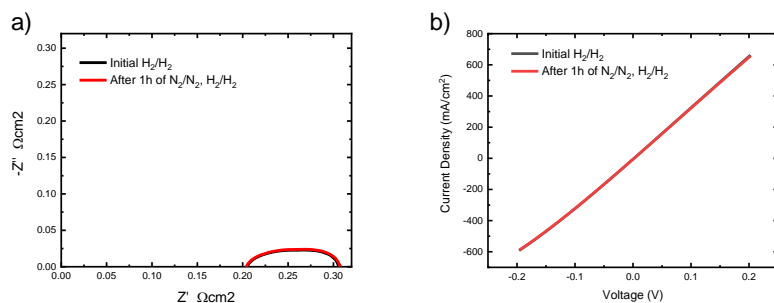


Figure 3.26 Electrochemical analysis of the Ru_8Pt_2/V working electrode cell. Measurements taken before and after a symmetric nitrogen gas applied to the cell at 50 sccm for 1 hour. a) EIS measurements taken at OCV with a frequency range from 1 MHz to 0.1 Hz with a 20 mV amplitude and b) polarization curves taken at a sweep rate of 10 mV/s.

Within this system, the Ru-rich side would likely be the most effective as it has shown the lowest reaction resistance and would be the cheapest to implement.

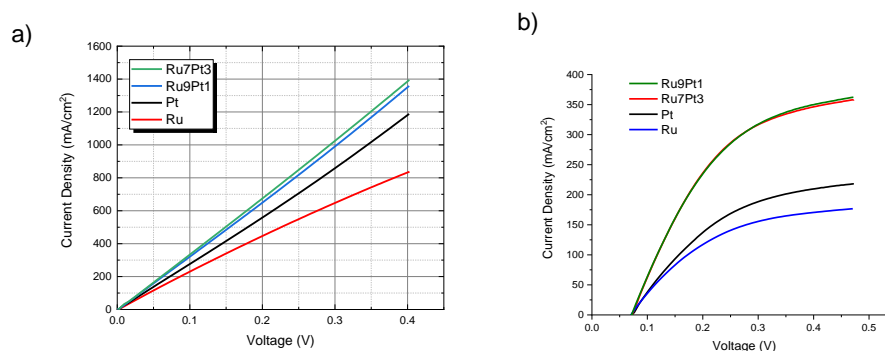


Figure 3.27 Polarization curves under the a) hydrogen condition and b) the dilute hydrogen condition for PtRu/fCNT-COOH 100 mg working electrodes with compositions of C:CDP of 1:3.

There are three main things pertaining to this system that would be interesting to examine with controlled studies. One is the activity differences of the RuPt system relative to the monometallic systems. In the above studies, there is always the convolution of number of active sites and activity since the available surface area between the systems is different. This would ideally be approached by starting with systems with the same electrochemically active surface area available. Then, the RuPt catalyst should also be tested as a HOR catalyst in a SAFC to demonstrate the potential replacement of all Pt anode catalysts with this relatively cheaper system. The second area to explore would be the mechanism by which Pt enhances the activity of Ru in Ru-rich alloy systems. TEM of the particles after operation would be highly suggestive of this (e.g., if Pt is sequestered to the surface, then it is reasonable to suggest that enhanced activity would arise from the Pt surface and the lack of hydroxide poisoning). On this note, the test examining HOR in the dilute hydrogen condition under various water partial pressures should be repeated for the RuPt system. The last main interesting area to explore would be the impact on stability. As was noted in Appendix C.4, Ru electrodes in ambient conditions will degrade. If Pt is sequestering to the top, it is possible that this could prevent the reaction of CDP with the catalyst. A good test to indicate stability would be to replicate the Ru ambient condition degradation cases for both Pt and RuPt. These stability tests should also be done with various pH₂O conditions for good measure. In total, this would encompass a compelling case for RuPt as a cheaper replacement HOR catalyst in SAECs.

3.3.2 Ruthenium-Palladium

Considering the Ruthenium-Palladium phase diagram from Tripathi et al.⁷⁵, both Pd and Ru are hardly miscible with each other. This system is not nearly as explored as the Pt-Ru system, but we can make a few inferences about the system from theory. From the surface energy, we would expect the system to strongly segregate with Pd rising to the shell like in the Pt case¹¹. From the work of Ruban et al.²⁵, we would expect a Pd overlayer on top of Ru to lower the center of the d-band, slightly less so than in the case of a Pt overlayer. Overall, we would likely expect Pd in a Ru-rich system to behave similarly to Pt. In the Pd-rich case, we might expect the behavior to differ due to the higher degree of segregation.

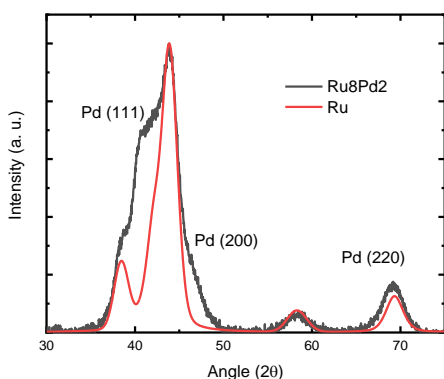


Figure 3.28 XRD of $\text{Ru}_8\text{Pd}_2/\text{V}$ compared to equivalent molar loaded 60 wt% Ru/V (Rigaku Ultima). Ru phase appears unchanged while separate Pd phase appears.

One composition of 80 at% Ru and 20 at% Pd on Vulcan XC-72 was attempted for this study. This composition was synthesized by co-deposition from ruthenium chloride hydrate and palladium chloride by the NaBH_4 method. The total molar loading is equivalent to the 60 wt% Ru/V case and the synthesis procedure is completely analogous. XRD analysis of this sample (see Figure 3.28) revealed that the Pd and Ru formed separate phases without any shift in the Ru peaks, as might be expected from the bulk phase diagram.

A cell was then fabricated with this bimetallic catalyst. The working electrode for this cell was

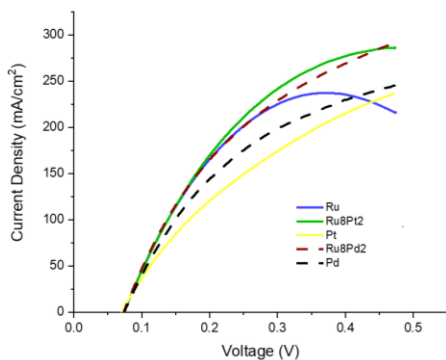


Figure 3.29 Polarization curves from equivalent molar metal on Vulcan working electrodes under the dilute hydrogen condition compared to the $\text{Ru}_8\text{Pd}_2/\text{V}$ at a 10 mV/s.

composed of a constant carbon and CDP amount ($4\frac{1}{3}$ mg C, 39 mg CDP). This cell was tested in the dilute hydrogen condition and the result is shown in Figure 3.29 where it is compared to the monometallic cases as well as the Ru_8Pt_2 case. This figure shows that bimetallic RuPd appears to be more effective at HOR than either Ru or Pd alone and is on par with the Ru_8Pt_2 case. The polarization curve also shows that Pd also eliminates the current turnover at higher oxidizing potentials. So, from this prospective, Pt and Pd appear equivalent in the terms of doping into the Ru-rich system.

3.3.3 Platinum-Palladium-Ruthenium

If little is known about the Pd-Ru system, even less is known regarding the Pt-Pd-Ru ternary system. A low temperature phase diagram for this system could not be found for reference. In addition, little is known about what stable configurations might be such as which systems might be sequestered to the surface in the catalyst systems. Much more work is needed to be able to target a particular catalytic outcome. For an exploratory study, $\text{Ru}_8\text{Pd}_1\text{Pt}_1/\text{V}$ was synthesized by co-

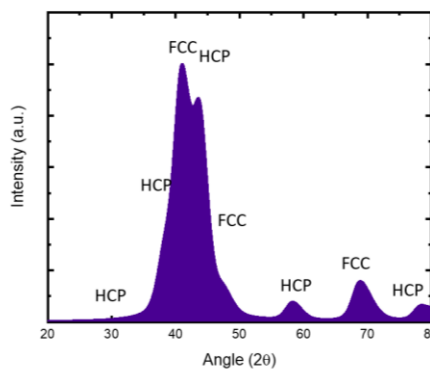


Figure 3.30 XRD of $\text{Ru}_8\text{Pd}_1\text{Pt}_1/\text{V}$ compared to equivalent molar loaded 60 wt% Ru/V (Rigaku Ultima).

deposition of the chloride precursors and reduced by NaBH_4 by the same methods previously described.

XRD of this sample showed a two-phase formation between a HCP and a FCC phase (see Figure 3.30).

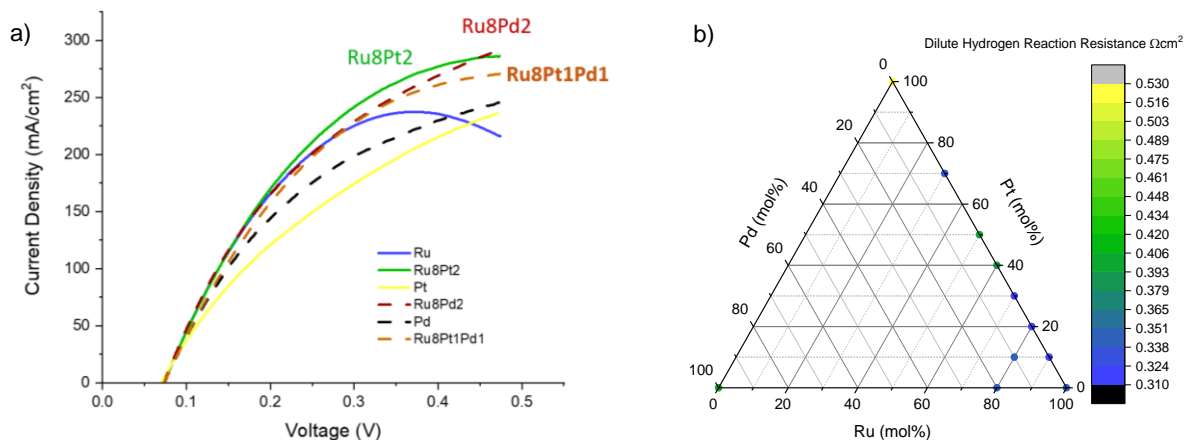


Figure 3.31 a) Polarization curves from equivalent molar metal on Vulcan working electrodes under the dilute hydrogen condition compared to the Ru₈Pd₁Pt₁/V at a 10 mV/s. b) Reaction resistance under dilute hydrogen conditions for all Pd-Pt-Ru/V samples tested here with equimolar loadings.

A cell was then fabricated with this ternary catalyst. The working electrode for this cell was composed of a constant carbon and CDP amount ($4\frac{1}{3}$ mg C, 39 mg CDP). This cell was tested in the dilute hydrogen condition and the result is shown in Figure 3.31a. where it is compared to the monometallic cases as well as the bimetallic cases. This figure shows that the ternary case is closest to the activity of the bimetallic cases and does not exhibit the current turnover effect seen in the pure Ru case. Figure 3.31b shows a wider view of the activity of the Pt-Pd-Ru catalysts explored in this work. We note that this is far from complete in exploring the composition space but shows how possible improvements in these catalytic systems can be achieved.

3.3.4 Platinum-Nickel

The work of Strmcnik et al.⁶⁴ suggested that Ni(OH)₂ as islands on Pt surfaces would improve the HOR on Pt by providing sites for the reactive hydroxide adsorbed species. Due to this being explained by a surface phenomenon, an attempt to recreate this was done using a sequential NaBH₄ process. First, $\frac{3}{4}$ of the equivalent molar loading of 74 wt% Pt was deposited by NaBH₄ reduction in the standard method from chloroplatinic acid. Subsequently, $\frac{1}{4}$ of the of the equivalent molar loading of 74 wt% Pt/V was deposited in the form of Ni(OH)₂ by NaBH₄ reduction. From preliminary tests, it was evident that the standard reduction was not sufficient for depositing from NiCl₂ 6H₂O. The procedure was changed by

doubling the amount of NaBH_4 (keeping concentration constant) and by allowing the system to react over two hours.

XRD analysis showed that the subsequent deposition of $\text{Ni}(\text{OH})_2$ did not appear to alter the diffraction pattern significantly, suggesting the $\text{Ni}(\text{OH})_2$ deposited on the surface was amorphous (see Figure 3.32a). XPS analysis confirmed that the Ni was indeed $\text{Ni}(\text{OH})_2$ (See Figure 3.32b) and that the Pt in the system remained unaltered (see Figure 3.32c).

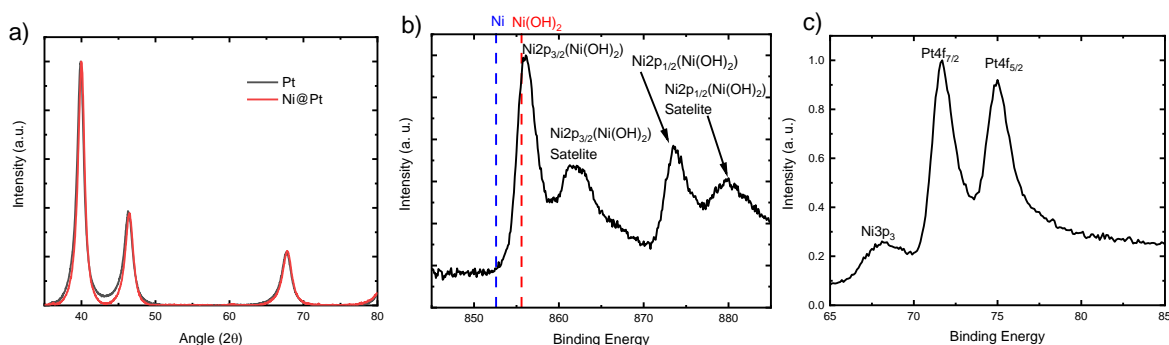


Figure 3.32 a) XRD of first deposited Pt/V and then of Ni compound deposited on top of Pt/V (Rigaku Ultima). b) XPS of Ni@Pt/V showing the Ni peaks that correspond to $\text{Ni}(\text{OH})_2$ and showing reference lines to where the far left peak would be expected to be if the compound was Ni. c) XPS of Ni@Pt/V showing the metallic Pt 4f peaks (Thermo Scientific ESCALAB 250 Xi).

A cell was then fabricated with the Ni@Pt/V catalyst. The working electrode for this cell was composed of a constant carbon and CDP amount ($4\frac{1}{3}$ mg C, 39 mg CDP). This cell was tested in the hydrogen and dilute hydrogen conditions and the results are shown in Figure 3.33. From Figure 3.33a, it is evident that the catalyst is more effective at HER than HOR. Furthermore, looking at the impedance spectroscopy results (see Figure 3.33b), it is evident that this catalyst is very poor when operating in the dilute hydrogen condition in that the activity is lower than all of the previously examined systems. An enhancement in the HOR activity such as what was reported from Strmcnk et al.⁶⁴ was not found and this catalyst seems like it would be most effective if employed in HER applications.

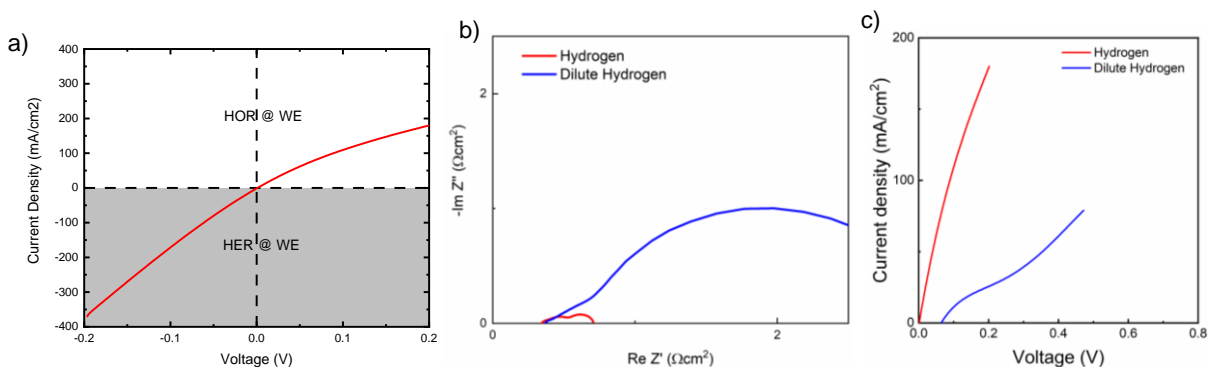


Figure 3.33 a) Polarization curve of Ni@Pt/V under the hydrogen condition with reducing and oxidizing potentials on the working electrode taken at 10 mV/s. b) OCV EIS measurements of the same cell under the hydrogen and dilute hydrogen conditions taken from 1 MHz to 0.1 Hz with a 20 mV amplitude. c) Polarization curves under oxidizing potentials at the working electrode under the hydrogen and dilute hydrogen.

3.4 Metal Phosphides

Paik demonstrated that Pd in contact with CDP formed palladium phosphide and this compound was still highly active for HOR⁵¹. Indeed, many researchers have begun investigating metallic phosphide catalysts for various reactions⁷⁶. The activity of phosphides points toward the exciting possibilities of potentially stable metal catalysts in CDP-based electrochemical cells. Here, we look at implementing nickel phosphide and nickel rhodium phosphide as HOR and HER catalysts.

3.4.1 Nickel Phosphide

Ni₂P nanoparticles were provided from Professor Brock's group at Wayne State University which were synthesized by an arrested precipitation technique. Briefly, nickel (II) acetylacetonate (Ni(acac)₂) and n-octyl ether was heated to 110°C under vacuum. This solution was then injected into a degassed solution at 110°C containing n-octyl ether, oleylamine and tri-octylphosphine. This combined solution was held at 350°C for one hour. Black Ni₂P nanoparticles were then washed and isolated using chloroform and ethanol, respectively. These particles have non-polar oleate capping ligands on the surface.

These particles as received were deposited on Vulcan in an amount equimolar to 60 wt% Ru/V in the following steps. Ni₂P was sonicated with Vulcan in hexanes for 330 minutes to promote dispersion. This solution was then mixed with ethanol to precipitate out Ni₂P on Vulcan. This sample was separated by centrifuging and allowed to dry overnight under vacuum. Finally, the sample was then heated in a tube

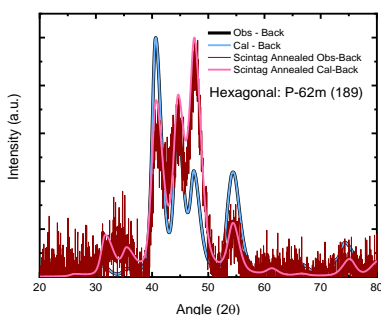


Figure 3.34 XRD before and after anneal for the $\text{Ni}_2\text{P}/\text{V}$ sample with observed minus background and calculated minus background patterns. Preannealed sample data was collected on a Rigaku Ultima while the annealed sample was collected on a Scintag XDS2000.

furnace to 400°C for one hour under 3% H_2 bal. Ar with a $5^\circ\text{C}/\text{min}$ ramp rate to remove the capping ligand. XRD analysis (see Figure 3.34) revealed the sample to be solely Ni_2P with a crystallite size of ~ 5 nm. TEM analysis from the Brock group confirmed that the Ni_2P average particle size is between 5-6 nm. The only difference noticed before and after annealing was that the relative peak intensities shifted. The preannealed sample's most prominent peak was the (111) peak while the annealed sample's was the (210) peak.

A cell was then fabricated with the $\text{Ni}_2\text{P}/\text{V}$ catalyst. The working electrode for this cell was composed of a constant carbon and CDP amount ($4\frac{1}{3}$ mg C, 39 mg CDP). This cell was tested in the hydrogen and dilute hydrogen conditions and the results are shown in Figure 3.35. This cell performed significant worse than $\text{Ni}@\text{Pt}/\text{V}$ for both HOR and HER and showed the same trend of worse performance under oxidizing conditions. The oxidizing condition effect was drastically more impactful for this case, particularly in the dilute case as is evident from the impedance data (Figure 3.35b) and from the polarization curves (Figure 3.35c). Nickel-based catalysts are ineffective under oxidizing conditions but perform

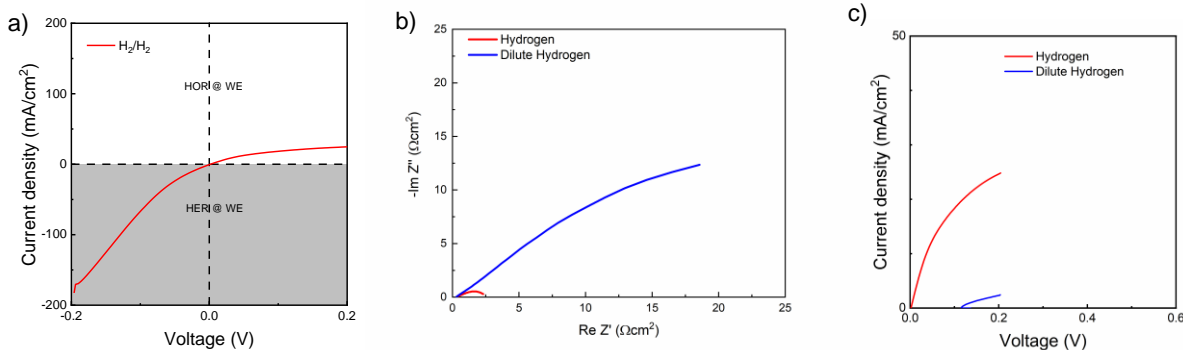


Figure 3.35 a) Polarization curve of $\text{Ni}_2\text{P}/\text{V}$ under the hydrogen condition with reducing and oxidizing potentials on the working electrode taken at 10 mV/s. b) OCV EIS measurements of the same cell under the hydrogen and dilute hydrogen conditions taken from 1 MHz to 0.1 Hz with a 20 mV amplitude. c) Polarization curves under oxidizing potentials at the working electrode under the hydrogen and dilute hydrogen.

reasonably for HER (though not as effectively as Pt). This is in-line with what Papandrew et al. found when testing nickel catalysts for solid acid cells⁷⁷.

3.4.2 Nickel Rhodium Phosphide

Rh can directly substitute onto Ni sites in the Ni₂P structure. Rh also has a more favorable binding energy for hydrogen and thus, can likely improve hydrogen catalysis with doping into the Ni₂P structure. For this reason, we also obtained Ni_{1.6}Rh_{0.4}P from Professor Brock's group at Wayne State University. These catalysts were synthesized in a similar way to the Ni₂P, save that a rhodium chloride hydrate precursor is added with the nickel precursor in the synthesis procedure. The Ni_{1.6}Rh_{0.4}

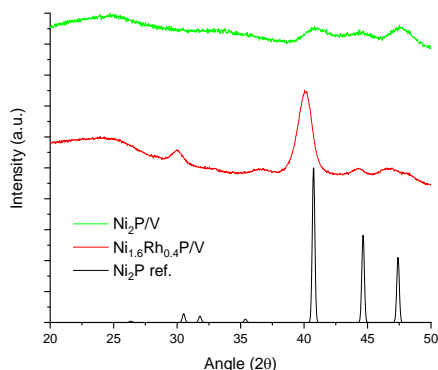


Figure 3.36 XRD of Ni_{1.6}Rh_{0.4} /V sample compared with previous Ni₂P sample and a Ni₂P reference. Sample data was collected on a Rigaku Ultima.

were deposited onto Vulcan XC-72 and annealed under 3%H₂/Ar in the same manner as discussed previously. XRD analysis is shown in Figure 3.36. The crystallite size here increases to ~7 nm and it is evident that the crystal structure remains, though the lattice parameter has shifted, suggesting successful substitution of Rh into the Ni sublattice.

A cell was then fabricated with the Ni_{1.6}Rh_{0.4}P/V catalyst. The working electrode for this cell was composed of a constant carbon and CDP amount (4 $\frac{1}{3}$ mg C, 39 mg CDP). This cell was tested in the hydrogen and dilute hydrogen conditions and the results are shown in Figure 3.37. From these tests it was evident that the substitution of 20% of the Ni sites with Rh greatly improved both the HOR and HER activity. Additionally, the asymmetry between the HOR and HER reaction was greatly reduced. These results

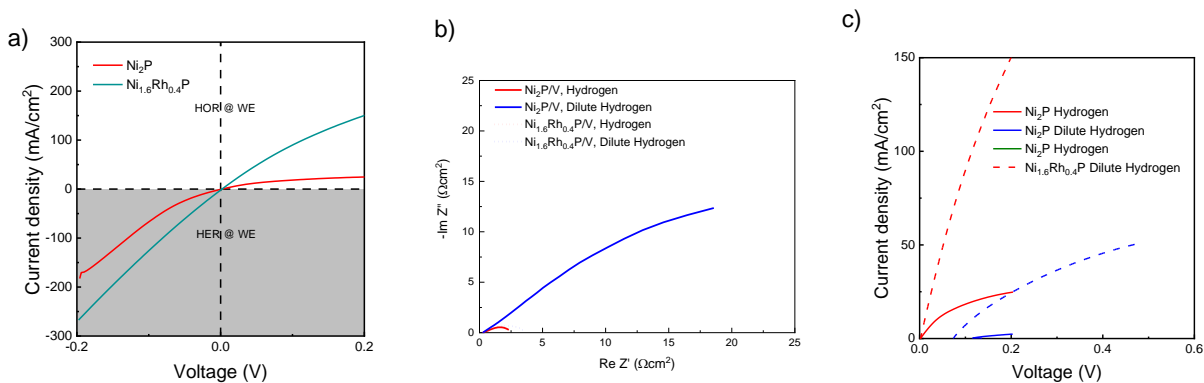


Figure 3.37 a) Polarization curve of $\text{Ni}_{1.6}\text{Rh}_{0.4}/\text{V}$ under the hydrogen condition with reducing and oxidizing potentials on the working electrode taken at 10 mV/s compared with the same measurement for the $\text{Ni}_2\text{P}/\text{V}$ working electrode. b) OCV EIS measurements of the same cells under the hydrogen and dilute hydrogen conditions taken from 1 MHz to 0.1 Hz with a 20 mV amplitude. c) Polarization curves under oxidizing potentials at the working electrode under the hydrogen and dilute hydrogen for the same cells.

suggest that minor doping of non-precious metals with precious metal catalysts has the possibility of having outsized impacts and can be an effective route to effective and cheaper catalysts in the future.

3.5 Summary

Here, work to systematically examine the HOR reaction for composite electrodes in comparison to past work for CDP-based electrochemical cells has been performed. Pd in composite electrodes appears to be at least as active as Pt for HOR if the cell is kept in reducing conditions. Furthermore, in certain geometries, Pd appears to be a more effective catalyst than Pt. Ru also appears to be an equally effective HOR catalyst at lower oxidizing potentials if the cell is maintained under reducing conditions. Ru suffers under higher oxidizing potentials from apparent hydroxide poisoning. Alloying Ru with Pd, Pt, or both Pd and Pt appears to make an alloy that is more active than the constituent metals alone and no hydroxide poisoning at higher oxidizing potentials is noted. The Ni@Pt test shows that the improvement in activity cannot simply be from an oxyphilic effect as suggested by Strmcnk et al⁶⁴. Ni is also apparently ineffective at executing the hydrogen oxidation reaction but performs adequately for hydrogen reduction. Additional work was also performed to expand on phosphide catalysts. While it was confirmed that Ni (this time in the form of Ni_2P) is ineffective at the HOR, substituting 20% of the Ni sites with Rh proved to dramatically improve the HOR and HER performance of Ni_2P . Phosphides continue to look like feasible catalysts that can be more stable with CDP. Partial substitution of non-precious metals with a small amount of supremely

active precious metals shows promise to be an effective strategy to have cheap, stable, and effective catalysts.

Chapter 4 Ammonia Oxidation

But still try for who knows what is possible. – Michael Faraday

4.1 Introduction

Hydrogen offers a promising direction for a sustainable energy future, but its implementation is not without challenges. Among its most prominent challenges are its low volumetric energy density, low flashpoint, and lack of wide infrastructure for storage and transport⁷⁸⁻⁸⁰. Widespread adoption of hydrogen technology will likely be dependent on how the challenges in logistics are overcome. Instead of transporting and storing pure hydrogen, another method of implementing hydrogen is by using a more portable molecule. Among candidate molecules, ammonia has been brought up as a promising hydrogen vector⁸¹⁻⁸³. The ammonia molecule is lightweight, much less flammable as compared to hydrogen, easily liquefiable, commercially produced at high volume, and can make use of an existing delivery infrastructure⁸⁴. Most importantly, when considering sustainable energy solutions, ammonia can be implemented without emitting green-house gases. While most ammonia production today utilizes hydrogen derived from natural gas and its production emits CO₂, the principal components of ammonia are nitrogen and hydrogen. Thus, hydrogen can be stored in and retrieved from ammonia without contributing to harmful CO₂ emissions.

Ammonia decomposition into nitrogen and hydrogen proceeds by the following reaction:



This reaction is mildly endothermic at standard conditions with $\Delta H = 45.9 \text{ kJ/mol}$ ⁸⁵; under standard pressure it proceeds spontaneously at temperatures greater than 183°C. Achieving a high yield for this reaction is challenging due to thermodynamic limitations and kinetic barriers, typically requiring reaction temperatures in excess of 400°C⁸⁶. This is particularly important for considering the implementation in PEMFCs as they are extremely sensitive to ammonia impurities; PEMFC catalysts can tolerate no more than ~0.1 ppm ammonia^{87,88}.

An alternative to high-temperature thermal decomposition that holds the possibility of lower operating temperatures, lower operating pressures, and higher purity hydrogen production lies in electrochemical decomposition. So far, electrocatalytic approaches which have mostly been attempted with

aqueous alkali electrolyte based electrochemical cells and require high operating potentials, implying poor energy efficiency. Additionally, these initial approaches have suffered from catalyst deactivation over time from adsorbate poisoning^{89,90}. Accordingly, innovations in ammonia-to-hydrogen conversion are required if ammonia is to provide hydrogen on demand and serve as a flexible energy delivery medium.

Here, we will provide a background that considers the current research regarding ammonia decomposition to rationalize considerations of our experimental conditions and to help elucidate the mechanisms of the observed phenomena. Several modern reviews have analyzed the current state of knowledge regarding ammonia decomposition from which further information about the topic can be gathered to a greater extent than what will be presented here⁹¹⁻⁹³.

4.1.1 Ammonia Decomposition

Current understanding of ammonia decomposition stands on the shoulders of the giants who have progressed the field of ammonia synthesis over the last century. It is easily understandable why this is the case when one considers the microscopic reversibility of the reaction. While it may be that the thermodynamics varies in opposite directions (lower pressures and higher temperatures favor ammonia decomposition and vice versa for ammonia synthesis), the kinetic limitations of the reactions remain similar as the rate governing binding energies on metal surfaces is key.

It is understandable why kinetics limitations are so dominant in the ammonia system when one considers that the formation or breakage of the nitrogen triple bond requires a whopping 9.76 eV! In the presence of a Ru catalyst, this energy drops down to approximately 1 eV⁹⁴. When one considers how ammonia must decompose, it is helpful to consider a possible series of microkinetic steps that has to occur such as the ones proposed by Bradford et al⁹⁵:





where * denotes a surface site, \rightarrow denotes a slow, irreversible step, and \rightleftharpoons equals a quasiequilibrated step. Stated simply, the ammonia molecule adsorbs to the surface (Equation 4.2), the ammonia dehydrogenates (Equations 4.3-4.5), then adsorbed hydrogen (Equation 4.6) and nitrogen (Equation 4.7) recombine and desorb. Clearly, to execute on these steps, the nitrogen needs to be able to sufficiently adsorb and desorb from the surface, leading to the following of the Sabatier principle. Additionally, the formation of the nitrogen triple bond takes a large amount of energy, making the recombinative desorption of nitrogen (Equation 4.7) the rate determining step⁹¹.

Due to nitrogen adsorption defining the rate limiting step, the nitrogen binding energy is the key descriptor governing this reaction. Indeed, one can make volcano plots of the activity with the x-axis in historical relations being the enthalpy for dissociative nitrogen adsorption⁹⁶ or more directly from the nitrogen binding energy⁹⁷. It might be expected that the same catalyst would be used for ammonia synthesis and decomposition since they are both governed by the same nitrogen binding energy. Contrary to this, while Fe acts as the near optimal catalyst for the ammonia synthesis reaction, Fe tends to significantly underperform other catalysts for the ammonia decomposition reaction⁹². This is due to the different concentrations of ammonia used for each condition. In ammonia synthesis, the environment tends to be ammonia dilute while in the ammonia decomposition case, the environment is ammonia concentrated. This leads to a difference in the nitrogen surface coverage arising from the different nitrogen chemical potential in each case. Since there is a higher nitrogen adsorption level in the ammonia decomposition case, the volcano curve is shifted towards weaker binding energies as there is already more available adsorbed nitrogen⁹⁸. Fe, in this case, binds strongly on an already covered surface. So, while the activities of both reactions are closely governed by the nitrogen binding energy, they are slightly shifted in their dependence. This being the case, the general activity trend for monometallic materials on activated alumina is: Ru > Ni > Rh > Co > Ir > Fe >> Pt > Cr > Pd > Cu >> Te, Se, Pb⁹⁹.

Additionally, all catalyst systems typically employ a support. The support primarily serves to enhance the dispersion of the catalyst and provide a high active surface area. Interestingly, for the ammonia decomposition reaction, the support has also been shown to influence the catalytic activity of the reaction. For example, Aika et al demonstrated that activity is positively correlated with the basicity of the support¹⁰⁰. Zhong and Aika found that activity was also improved by the removal of electronegative impurities such as S, N, O, and Cl¹⁰¹. Overall, it appears as though the most effective supports are those that facilitate electron donation. Thus, the most desirable supports are those that are basic, conductive, are stable, lack electron withdrawing groups, and have a high surface area⁹¹.

4.1.2 Alkali Promotion of Ammonia Decomposition

Alkali promotion has been critical in the development of ammonia catalysts. In fact, the breakthrough of incorporating alkali promoters with iron catalysts was what enabled the first commercially viable iteration of the Haber-Bosch process¹⁰². While alkali, alkaline earth, and rare earth metal ions have been shown to be effective promoters, alkali promoters have been the most successful⁹¹.

The promotion effect is typically thought to occur through two avenues. First, the structure of the heterogeneous catalyst could be impacted by several mechanisms including decreased catalyst sintering⁹¹ and prevention of support methanation¹⁰³. There is also an apparent electronic effect as the effectiveness of promoters is negatively correlated with their electronegativity. Additionally, electronically withdrawing anions (e.g., halide, SO_4^{2-} , PO_4^{3-}) inhibit the reaction¹⁰³. This relationship is explained through electrostatic interactions between the promoter, metal, and transition-state adsorbates. When an electron donating promoter (i.e., an electropositive material) gives an electron to the metal catalyst, an electric dipole is formed between them. This dipole is attractive to the induced dipole from the N_2 transition state and repulsive to NH_x transition states^{28,104}. Electron withdrawing co-adsorbates act conversely and thus inhibit the net reaction. The electrostatic nature of the promotional effect makes the promoter beneficial to catalysts with nitrogen binding energies that are higher or lower than optimal according to the Sabatier relationship. This electrostatic effect manages to lower the transition state energy without changing the nitrogen binding energy as discussed in Section 1.4.3.

4.1.3 Ammonia Electrooxidation

Another route to producing hydrogen from ammonia that has been sought is through electrooxidation. This has most commonly been accomplished through the use of electrochemical cells operating at near ambient temperatures with alkaline solution with precious metal catalysts. In alkaline solution, first the ammonia reacts with hydroxide anions to form nitrogen gas, water, and electrons:



Subsequently, the generated electrons will react with water to form hydrogen and hydroxide ions:



For this reaction, Pt-Ir catalysts have been found to be the most effective. Significant challenges remain to be overcome in the implementation of this technique. For one, high overpotentials must be applied to have decent rates of hydrogen production which leads to a lower energy efficiency and thus more expensive operation. A second challenge is that catalysts in these systems tend to be poisoned over the course of operation¹⁰⁵.

4.2 Ammonia Decomposition in Solid Acid Cells

Both previously described methods have inherent problems that limit their feasibility to enable ammonia to be an effective hydrogen vector. For the thermal decomposition case, achieving high conversion requires prohibitively high temperatures (~400°C) to overcome thermodynamic limitations and kinetic barriers⁸⁶ and is inherently limited in its capacity to deliver high purity hydrogen. Ambient temperature electrooxidation in alkaline solution suffers from high overpotentials and catalyst poisoning over times.

The implementation of a SAEC cell to facilitate ammonia decomposition can obviate all the challenges described for the previously described methods. When examining the free energy of

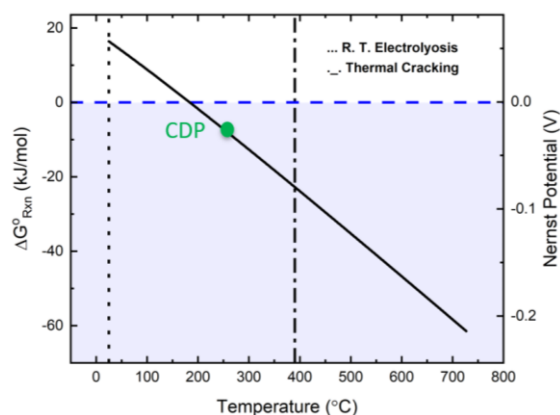


Figure 4.1 Free energy of ammonia decomposition and associated Nernst potential with temperature at which CDP cell operates noted.

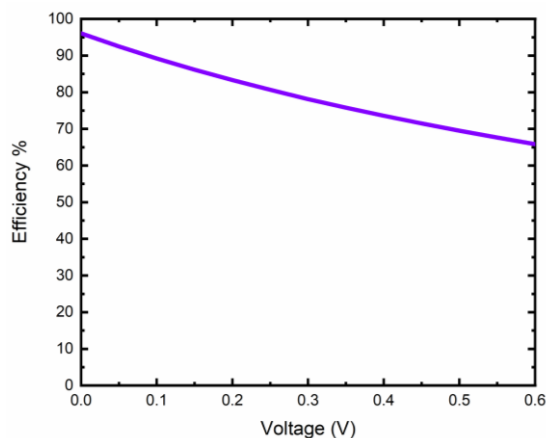


Figure 4.2 Efficiency of ammonia decomposition considered as the lower heating value of hydrogen obtained divided by the lower heating value of ammonia used, heat of the reaction (slightly endothermic), heat to bring ammonia up to temperature, and electrical work to drive the reaction.

ammonia decomposition⁸⁵ (see Figure 4.1) it is apparent that operating at a higher temperature makes the reaction more favorable lowering the potential required to carry out the reaction (as compared to the near ambient temperature case). In fact, when carrying out the reaction in the 0.4 pNH₃ operating conditions described in Section 2.5.2, the theoretical voltage across the cell is 19 mV (see Appendix B.3 for calculation details). When applying modest voltages to encourage the oxidation of the ammonia, high energy efficiencies can be achieved considering the electrical and heat

work (see Figure 4.2 and Appendix B.4 for calculation details). SAEC cells are also vastly more resistant to poisoning from the reactant stream⁶. Over the thermal decomposition methods, SAECs offer lower operating temperatures allowing for lower thermal budgets, faster cycling, and more portable systems. Furthermore, since the SAEC already incorporates a proton-only permeable membrane, SAECs also

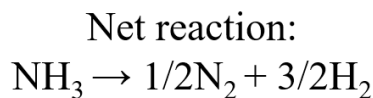
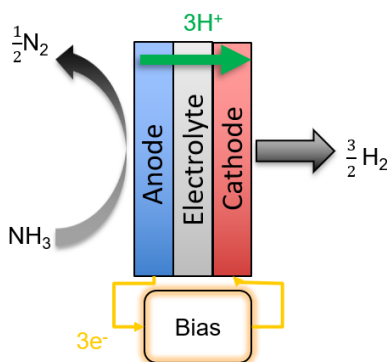


Figure 4.3 Schematic of ammonia decomposition SAEC. Ammonia is fed to the cell anode. Upon applying a potential, nitrogen, protons, and electrons are split. Protons and electrons recombine at the cathode to generate hydrogen.

naturally produce high-purity hydrogen. A schematic of the concept of a solid-acid-based ammonia electrooxidation cell is depicted in Figure 4.3.

4.2.1 Anode Development

SAEC cells for ammonia decomposition were constructed in manners described in Section 5.2.1 and more in detail in the “fully loaded” descriptions in Chapter 3. From the literature, promoted Ru on carbon nanotube supports were found to be the most successful ammonia decomposition catalysts, so this system was primarily used for investigation¹⁰⁶. The ammonia condition here refers to either the 0.4 or 0.6 pNH₃ ammonia conditions described in Section 2.5.2.

First, it was helpful to compare how well the cell can oxidize ammonia as opposed to hydrogen. In the case of an anode composed of a 62 wt% Ru/fCNT with a C:CDP ratio of 1:3 for a total electrode mass of 100 mg, we see that clearly the ammonia oxidation resistance is much higher than the dilute hydrogen oxidation resistance (see Figure 4.4).

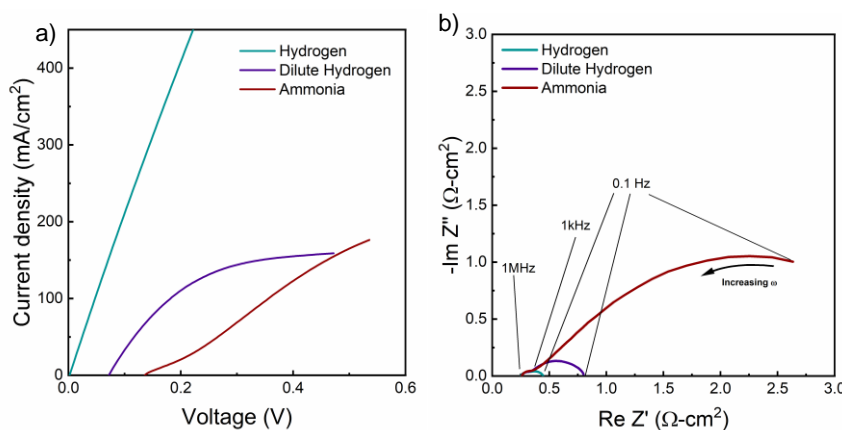


Figure 4.4 Electrochemical polarization curves (a) and impedance spectra at OCV (b) of a cell with an anode composed of a 62 wt% Ru/fCNT with a C:CDP ratio of 1:3 for a total electrode mass of 100 mg. Ammonia condition here is the 0.4 pNH₃ described condition. Polarization curves taken with a scan rate of 10 mV/S. Voltage amplitude for impedance scans was 20 mV.

This high of a resistance would make it challenging to operate this cell with high efficiency at a reasonable rate. ARPA-E targets for this system include currents upward of 100 mA/cm² at an operating potential of 0.15 V¹⁰⁷. From the SAEC composite electrode configuration, likely the optimal catalyst is close to the optimal catalyst for the thermal decomposition heterogeneous catalyst Ru as the reaction will be dominant at gas-metal interfaces. To probe this hypothesis, a few other transition metal catalysts were tested to see if similar trends were followed. Figure 4.5a shows the ammonia decomposition performance

of the above tested Ru/fCNT cell with an equivalent Pt/fCNT cell. The higher OCV for the Pt case certainly suggests that the system without electrical bias is more activated in the Ru-case, as would be expected from the thermal decomposition case⁹⁹. Interestingly, the resistance is lower for Pt at higher oxidizing potentials and eventually overtakes the Ru ammonia decomposition. This was also tested for the Vulcan support case where 50 mg electrodes (39 mg CDP, C:CDP 1:9, metal loading equimolar to 60 wt% Ru/V) of Ru/V, and Pd/V was compared (see Figure 4.5b). Pd showed the highest OCV and highest resistance at higher oxidizing potentials. This suggests that Pd has the worst ammonia oxidation capabilities, again as

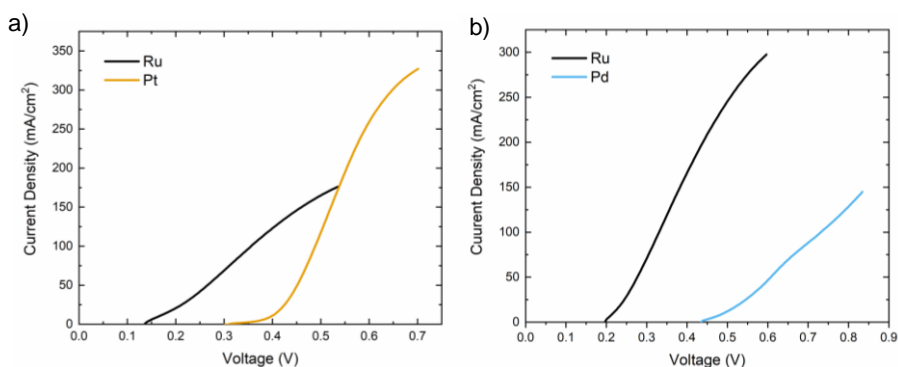


Figure 4.5 Polarization curves of a) Ru vs. Pt on fCNT and b) Ru vs. Pd on Vulcan with metal loadings equimolar to 60 wt% Ru/V under the ammonia condition ($p_{\text{NH}_3} = 0.4 \text{ atm}$). Scan rate was 10 mV/S for all measurements.

would be expected from the thermal catalytic case⁹⁹.

It was hypothesized that the reason for the lower resistance for Pt at higher oxidizing potentials was that while the Pt had a less optimal N-binding energy, it could likely dehydrogenate the ammonia better than Ru. This inspired the synthesis of Ru-Pt catalyst that might be able to take advantage of both the optimal N-binding energy for the Ru metal and the superior H-binding for the Pt metal. Results of a series of Ru-Pt catalysts tested under ammonia (whose synthesis is previously described in Section 3.3.1) reveal that there exists a tradeoff in these catalysts (see Figure 4.6). While the resistance at higher oxidizing potentials improves, the OCV increases as Pt is doped. It appears that the co-depositing method for Ru-Pt is incapable of moving past this catalytic tradeoff. This might be expected as we know from previous work that this method leads to the formation

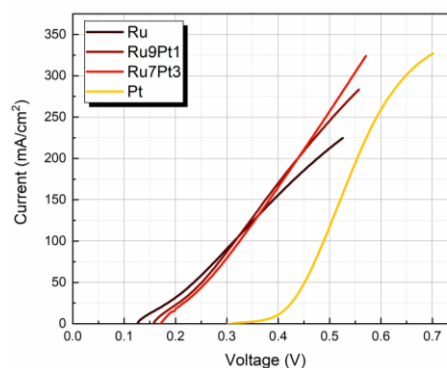


Figure 4.6 Polarization curves under 0.4pNH₃ ammonia condition for PtRu/fCNT-COOH 100 mg working electrodes with compositions of C:CDP of 1:3. Scan rates of 10 mV/s were used.

of core-shell particles (see Figure 3.24). Likely, doping with Pt is increasing the N-binding energy, but allowing for more favorable hydrogen catalysis.

Ni has been one of the most successful transition metal catalysts for ammonia decomposition not in the platinum group metal (PGM)^{93,99}. Additionally, when Hangsen et al. explored bimetallic catalysts, it was found that Pt with Ni overlayers have a particularly favorable N-binding energy. This being the case, the Ni-based catalysts synthesized in Sections 3.3 and 3.4 were tested under the ammonia condition.

The results of these tests are shown in Figure 4.7.

For one, it is apparent that Ni appears to help thermochemical catalysis based on the changes in OCV. For instance, Ni@Pt shows a lower OCV than Pt alone but a higher OCV than Ru as evidenced from Figure 4.5. Further, the higher concentration of Ni sample, Ni₂P, has a lower OCV than the Ni deposited on Pt sample. Additionally, the Ni₂P doped with Rh has a higher OCV. Figure 4.7 also reveals that Ni catalysts struggle under oxidizing potentials and have high resistances to ammonia oxidation. It appears

necessary for Ni to be coupled with a catalyst with an effective hydrogen binding catalyst to carry out ammonia oxidation at a meaningful rate.

Based on the foregoing results, it was concluded that Ru was close to the optimal catalyst for this reaction and auxiliary strategies to optimize the performance were pursued. One of the first things to be optimized was the cell microstructure. For one, it is important for the membrane to be dense to facilitate the electrochemical reaction properly and ensure the purity of the hydrogen generated at the cathode. The microstructure was investigated by looking at post-operation cell cross-section images (see Appendix C.7). These images could also be used to determine the porosity of the electrodes as described in Section 3.2.3. It is evident that the ammonia oxidation resistance was correlated with the porosity in the same manner as the hydrogen oxidation resistance (see Figure 4.8a). fCNT-supported electrodes were found to be more effective with higher carbon proportions (~1:3) while Vulcan XC-72 supported electrodes were optimal with

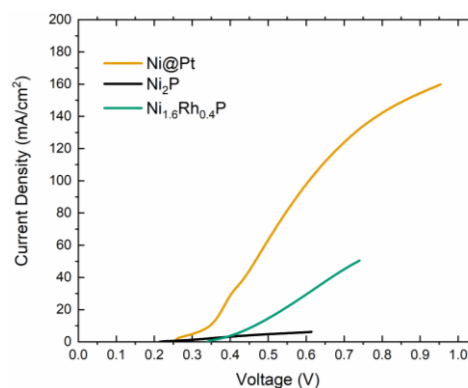


Figure 4.7 Polarization curves under the 0.4pNH₃ ammonia condition for Ni-based catalysts on Vulcan loaded equimolar to 60 wt% Ru/V with C:CDP ratios of 1:9. Scan rates of 10 mV/S were used.

lower carbon proportions (~1:9, see Appendix C.7). Thus, in this proportion, Vulcan was a much more effective support than fCNT-COOH (see Figure 4.8b).

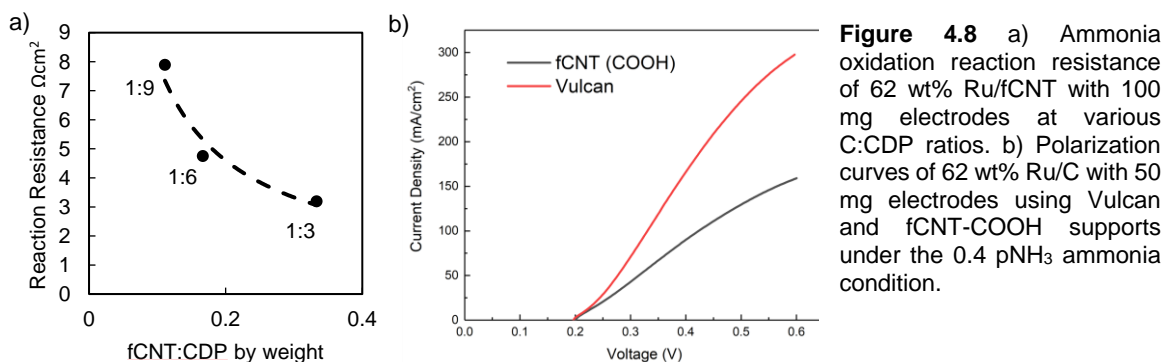


Figure 4.8 a) Ammonia oxidation reaction resistance of 62 wt% Ru/fCNT with 100 mg electrodes at various C:CDP ratios. b) Polarization curves of 62 wt% Ru/C with 50 mg electrodes using Vulcan and fCNT-COOH supports under the 0.4 pNH₃ ammonia condition.

Amine functionalized MWCNTs (fCNT-NH₂) were also tested in addition to the COOH functionalized MWCNTs. The amine functionalization similarly increases the hydrophilicity of the MWCNTs but might be more stable under the ammonia condition, and it was anticipated that fCNT-NH₂ may possess structural differences and be more stable under the ammonia condition. Furthermore, the difference in anion functionalization likely impacts the activity from possible poisoning effects¹⁰³. Tests under the ammonia condition showed that fCNT-NH₂ supported samples had higher OCVs, suggesting less thermochemical activity (see Figure 4.9). Despite this, there was not a significant difference between the activity of the 1:3 C:fCNT-NH₂ and 1:9 C:fCNT-NH₂ showing that amine functionalized carbon nanotubes might be more optimal for CDP-rich electrodes.

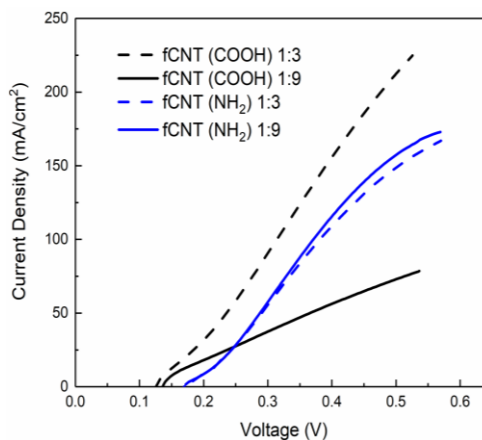


Figure 4.9 Polarization curves of 62 wt% Ru/fCNT with 100 mg electrodes under the 0.4 pNH₃ ammonia condition at different C:CDP ratios. Scan rates for these measurements were 10 mV/s.

While effective progress using this configuration was made to both understand and make more effective ammonia oxidation cells, our method was falling short of the goal of high H₂ production rates at

and double wrapping the cell with Teflon paper. A schematic of the two-layer cell is depicted in Figure 4.10¹⁰⁸.

The catalyst for the TCL was prepared following the polyol method¹⁰⁹ in which ethylene glycol (Fisher Chemical, > 95% purity) served to reduce a metal chloride precursor ($\text{RuCl}_3 \cdot 4.5\text{H}_2\text{O}$, Alfa Aesar, 99.9% metals basis). Here, this approach was used over the NaBH_4 method as it was desired to use unfunctionalized MWCNTs which achieved better dispersion in ethylene glycol as compared to dispersion in water. The Ru loading on the ~30 nm diameter multi-walled CNTs (NanoLab, greater than 95% purity) was 60 wt%. Ru deposited in this manner resulted in 7 nm particles as determined by XRD and TEM analysis. Cesium promotion was achieved by dispersing the 60 wt% Ru/CNT into a 50 mM aqueous solution of CsNO_3 (Alfa Aesar, 99.9%) with 1:1 molar ratio of Ru:Cs. The water was evaporated with mild heating to induce precipitation of the CsNO_3 . To aid uniformity, the powder was dispersed in ethanol and the solvent evaporation repeated at least two more times.

Three cells were constructed in this above-described manner to ensure reproducibility of the performance. First, OCV testing in the dilute hydrogen condition showed that there was negligible crossover across the three cells. Polarization curves and impedance spectra obtained under both ammonia conditions (0.4 atm $p\text{NH}_3$ and 0.6 atm $p\text{NH}_3$) revealed excellent activity for ammonia decomposition and cell-to-cell reproducibility (see Figure 4.11). The ohmic resistance is constant under all three conditions. The

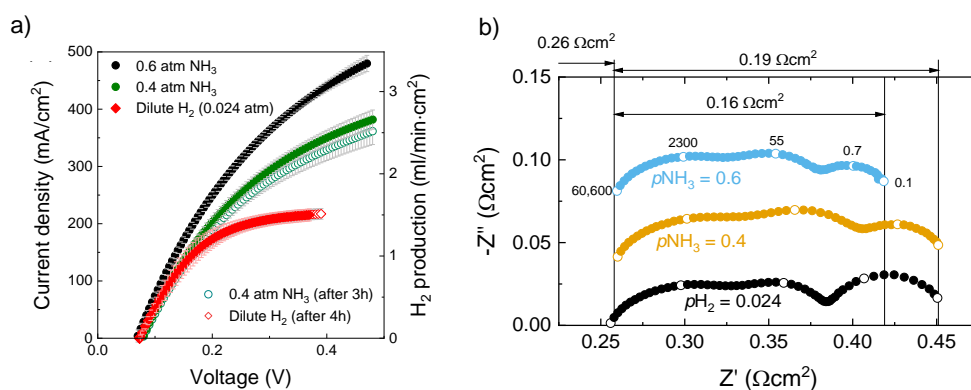


Figure 4.11 a) Polarization curves obtained upon supply of the gases indicated, along with computed H_2 production for 100% faradic efficiency. Scan rates of 10 mV/s were used. Error bars are from the variation in the averages of the three distinct cells. b) Electrochemical impedance spectra at OCV for a representative electrochemical cell measured at 250 °C with indicated gas supplies. Selected data points correspond to the frequency values (Hz) indicated. Voltage amplitude of 20 mV applied for these measurements. Reprinted from Lim et al¹⁰⁷.

electrochemical reaction resistance under the 0.4 pNH₃ is similar to the resistance for the dilute hydrogen condition and is significantly lower in the 0.6 pNH₃ case. The coincidence of the curves for the low NH₃ condition, measured before and after exposure to high NH₃, indicated reasonable stability¹⁰⁸. The decrease of 5-6% in the current density noticed here will be further discussed in Section 4.3.2.

Significantly, as expected for a solid-state electrolyte displaying pure protonic conduction, the faradic efficiency for hydrogen production was 100% (i.e., all of the electrons moving across the cell recombined with protons to form hydrogen gas) as determined by mass spectrometry, Figure 4.12a, and the generated hydrogen was free of impurities, (see Appendix C.10 for more details on the mass spectrometry analysis). Estimates from measurements on the cathode exhaust stream suggest <3 ppb ammonia in the produced hydrogen (see Appendix B.5 for calculation details). Since we have the observation that the current is fully faradaic, we were able to calculate the produced hydrogen (see Figure 4.12b) from the ammonia using Faraday's Law of Electrolysis:

$$n = \frac{It}{Fv} \quad (4.10)$$

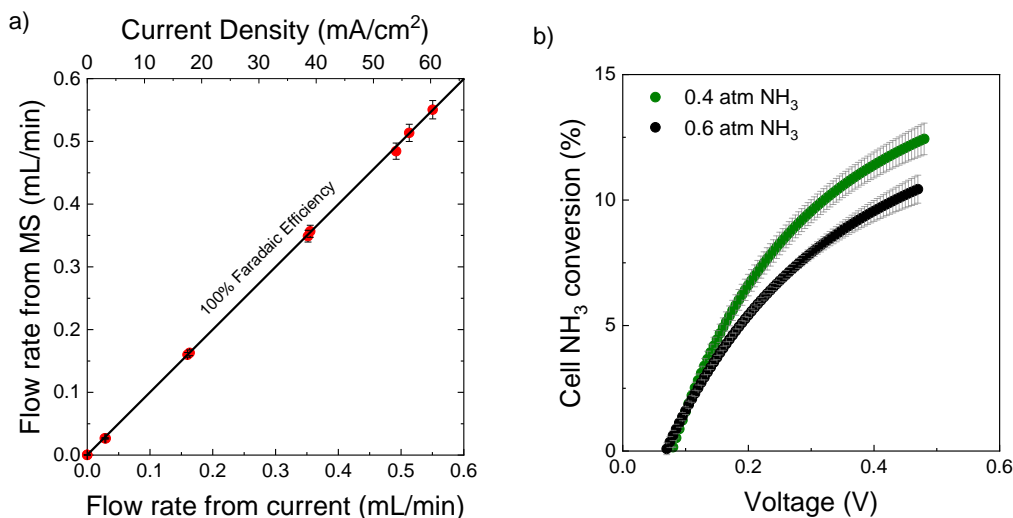


Figure 4.12 a) Measurement of H₂ evolved from cathode by mass spectrometry (MS) and from the current by Faraday's Law of Electrolysis demonstrating 100% faradic efficiency. Error bars are from the error from the mass spectrometer, from the H₂ calibration, and from the mass flow controllers. b) Implied NH₃ to H₂ conversion in Fig. 4.11a upon supply of the gases indicated. Error bars are from the variation in the averages of the three distinct cells. Reprinted from Lim et al¹⁰⁷.

where n is the amount of the substance in moles, I is the current, t is the time, F is Faraday's constant, and v is the valence of the ion. The possibility of NO_x formation on the anode side was eliminated by chemical analysis of the anode side exhaust (see Appendix C.10)¹⁰⁸.

The cells had OCVs of 78 ± 1 and 68 ± 4 mV for the respective ammonia partial pressures of 0.4 and 0.6 atm. These voltages can suggest the partial pressure of hydrogen formed at the working electrode by inverting the Nernst Equation and imply hydrogen partial pressures at the working electrode of 0.019 and 0.033 atm, respectively. From these partial pressures, we calculate chemical ammonia-to-hydrogen conversion rates of $3.4\% \pm 0.1\%$ and $3.5\% \pm 0.7\%$ at the two ammonia concentrations, respectively. These conversion rates are on par with the results reported by Hill et al. (2–10% conversion) for similar catalyst materials, with the values differing depending on Cs and Ru loadings¹¹⁰. Even for identical loadings, differences are expected due to variations in precursor types, deposition methods, CNT source, and gas flow conditions. The general agreement between the results suggests that poisoning of Ru by H_2O , present in high concentration in this experiment and absent in Hill's work¹¹⁰, does not significantly interfere with ammonia decomposition at 250°C , even at higher oxidizing potentials.

Upon applying oxidizing potential at the working electrode, the current rises under both ammonia and dilute hydrogen with relatively low overall cell resistances that are similar to each other. Because the hydrogen partial pressures are similar between the three conditions ($p_{\text{H}_2} = 0.024, 0.019,$ and 0.033 atm in dilute hydrogen and at OCV in the lower and higher ammonia concentrations respectively), the similarities in polarization characteristics suggest that poisoning of the Pt electrocatalyst by unreacted NH_3 is negligible. This is also evident in the impedance results shown in Figure 4.11b¹⁰⁸.

With increasing voltage, the polarization curves deviate both from linearity and from one another. The concave nature of the curves suggests mass transport limitations rather than catalytic activation limitations. In the dilute hydrogen case, the polarization curve plateaus relatively sharply at a current density corresponding to $\sim 90\%$ of the limiting value which is consistent with the depletion of hydrogen being responsible for the declining rate of increase in cell current density. Under ammonia, the polarization curves followed a significantly more gradual change in slope. Furthermore, the maximum current densities (382 and 480 mA/cm^2 at low and high p_{NH_3} , respectively) with their implied amount of hydrogen produced were

only 12% and 10% of the respective limiting capacity from the ammonia supplied. The overall conversion process appears limited by the characteristics of the TCL in the ammonia decomposition process since there is an absence of EL catalyst poisoning. It is important to note that at these maximum conditions the hydrogen partial pressure at the cathode is estimated to increase from 0.62 to 0.65 atm, which will in turn slightly increase the measured voltage¹⁰⁸.

Another important feature of Figure 4.11a is the substantially higher current achieved with the 0.6 atm pNH₃ condition as compared to the 0.4 atm pNH₃ condition. This behavior is consistent with the source of current being the electrochemical oxidation of ammonia. Moreover, the reactant depletion in the TCL can be compensated, at least partially, by increasing the reactant concentration or possibly the rate of ammonia supplied. The resulting increase in the hydrogen production rate was accompanied by a decrease in conversion efficiency as shown in Figure 4.12b. This indicates that the increase in ammonia concentration did not result in a proportional increase in the availability of hydrogen (proportional to the amount of ammonia supplied). This observation points toward possible improvements by tailoring the catalyst architecture to facilitate the removal of product N₂, or by increasing the thickness of the TCL to increase the residence time of NH₃ in the reaction zone which has to be balanced against possible increases in mass transport resistance. Dramatic improvements may also be possible by leveraging recent advances in TCL catalyst development¹¹¹. Even without implementing these improving steps, the performance here is far superior to those reported for alkali electrolysis cells in which large overpotentials (~0.4 V above OCV) must be overcome to produce hydrogen at a significant rate¹⁰⁸.

It is clear that this hybrid cell is far superior to the previous single layer electrochemical cells (see Figure 4.13). Without the incorporation of the TCL, the standard anode gave a relatively high OCV of ~ 365 mV under $p\text{NH}_3$ of 0.4 atm, implying that there is negligible thermal ammonia decomposition ($< 1 \times 10^{-5}$ % conversion). Upon applying oxidizing potentials, currents were $\sim 1\%$ of the values obtained from the hybrid cells. For all intents and purposes the Pt serves only to oxidize the hydrogen until a bias of 0.36 V and the Ru-based catalyst accounts for almost the entirety of the NH_3 decomposition. The hybrid cell is also superior to the cell with only the Ru/CNT + CDP single layer cell as can be seen in Figure 4.13. Under the 0.4 $p\text{NH}_3$ condition, the OCV was 170 mV ($\sim 0.05\%$ conversion) for the single layer Ru/CNT electrode, in contrast to 78 mV recorded from the bilayer-electrode system. Ru has previously been shown to be an efficient HOR catalyst, so the difference is likely due to the absence of an effective promoter. CDP is ineffective as a promotor, likely due to the presence of the phosphate anion which could poison the reaction¹⁰⁸.

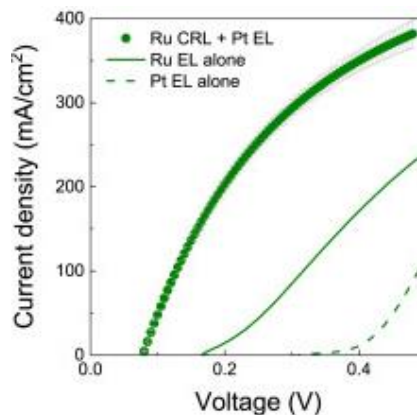


Figure 4.13 Comparison of polarization curves of bilayer electrode and single component electrodes under the 0.4 atm $p\text{NH}_3$ condition. Reprinted from Lim et al¹⁰⁷.

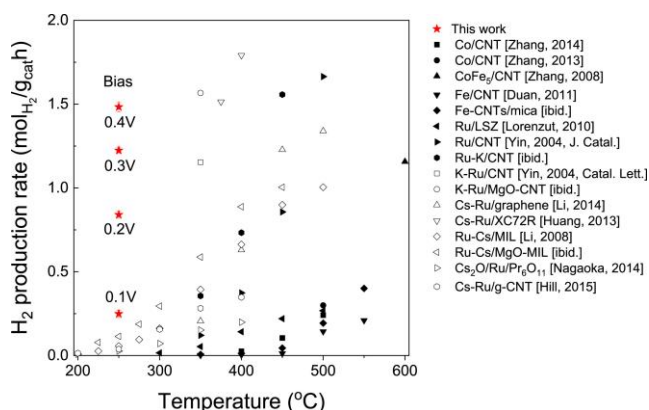


Figure 4.14 Comparison of the hydrogen generation rate obtained from the hybrid thermal-electrochemical approach of this work ($p\text{NH}_3 = 0.6$ atm) with prior work by thermal decomposition¹⁰⁷.

By integrating electrochemical product removal with thermal decomposition of ammonia, this hybrid cell generates hydrogen at a substantially higher rate than by thermal decomposition alone at lower temperatures. To add context to these results, the hydrogen production rates achieved here were compared to those from conventional thermal-cracking experiments reported in the literature on a mass-

normalized basis (see Figure 4.14)^{106,110,112-121}. The catalyst in the TCL, EL, and counter electrode were

included in the normalization results shown in Figure 4.14. This figure makes evident that the application of moderate bias (0.4 V) results in a catalyst-mass normalized hydrogen production rate that is on par with results obtained from thermal decomposition at much higher temperatures between 350-500°C. Furthermore, the evolved hydrogen is generated with a high-purity and is free of residual ammonia. This configuration is also amenable to the electrochemical compression of hydrogen, or to the operation of a direct ammonia fuel cell without the risk of generating NO_x. While a detailed efficiency analysis, which would require design of a system to minimize thermal inputs, a simple consideration of the minimum energy inputs relative to the energy content of the output hydrogen suggests high efficiencies are possible (see Appendix B.4). In summary, the hybrid thermal-electrochemical approach demonstrated here shows great promise for ammonia-to-hydrogen or even ammonia-to-electricity conversion on demand¹⁰⁸.

4.3.2 Investigating Phenomena in the Hybrid Cell Anode Compartment

XRD was used for a first-pass analysis of the state of the cell components undergoing the operating conditions. It was important to establish that CDP was stable under the ammonia condition, so a sample of pure CDP was subjected to 50 sccm of 0.4 pNH₃, 0.38 pH₂O, and balance N₂ at 250°C for 24 hours. These results revealed that CDP was stable under this condition (see Figure 4.15a). Additionally, the states of the

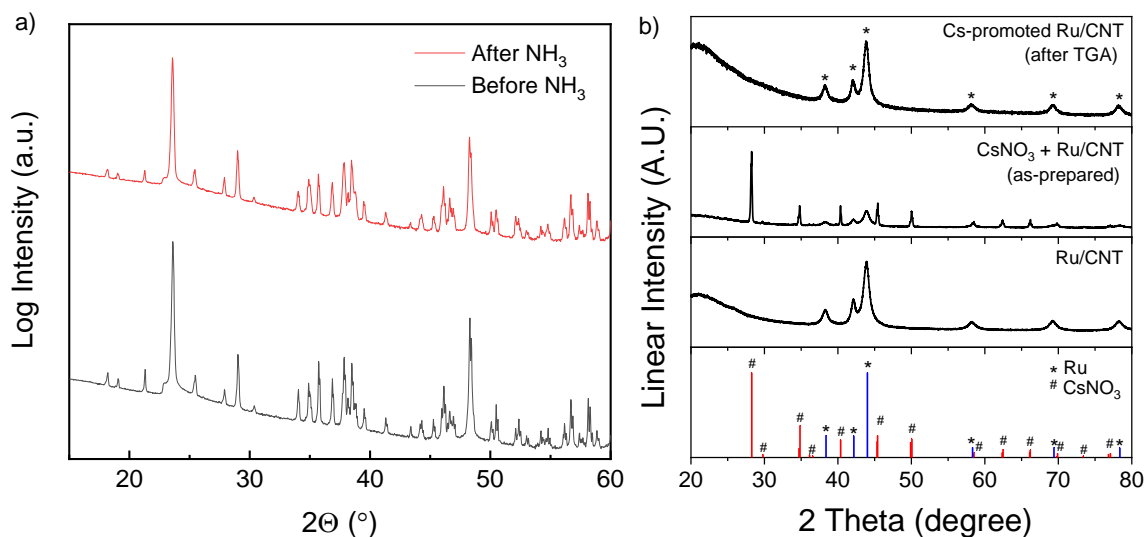


Figure 4.15 a) X-ray powder diffraction patterns (Rigaku SmartLab) of CsH₂PO₄ before (as-received) and after exposure to flowing humidified NH₃ for 24 h at 250 °C (pNH₃ = 0.4 atm, pH₂O = 0.22 atm, balance N₂; total gas flow rate = 50 sccm). The electrolyte is stable against reaction with ammonia at the cell operating conditions. b) . X-ray diffraction patterns (Rigaku Ultima IV) collected from catalyst materials as indicated: (bottom) 60 wt% Ru/CNT as prepared; (middle) 60 wt% Ru/CNT with CsNO₃ promotor, as prepared; and (top) Cs-promoted 60 wt% Ru/CNT after humidified dilute hydrogen. Reprinted from Lim et al¹⁰⁷.

TCL components were analyzed before and after heating to 250°C under humidified dilute hydrogen ($p_{\text{H}_2} = 0.03 \text{ atm}$, $p_{\text{H}_2\text{O}} = 0.03 \text{ atm}$). Upon initial promoter deposition, there are clear CsNO_3 peaks that were sharp and easily detectable in the XRD pattern. Post-operating conditions however, the pattern hid any presence of CsNO_3 suggesting that a new amorphous phase of the promoter had formed (see Figure 4.15b)¹⁰⁸.

Further analysis of the catalyst condition was pursued with thermogravimetric analysis (TGA). By measuring the weight change of constituent catalyst components when brought to operating conditions, the chemical state of these constituents can be inferred. TGA experiments shown here were performed on a Netzsch STA 443 with 10 mg of sample. Heating procedures were carried out with a 5°C ramp rate. Wet gas was achieved by flowing the gas through a room temperature bubbler prior to the gas entering the TGA instrument. The mass profile for CsNO_3 under dry and wet (0.03 atm $p_{\text{H}_2\text{O}}$) 3% H_2 bal. Ar (shown in Figure 4.16a) suggests that CsNO_3 is stable at 250°C under reducing conditions without the presence of a catalyst. The Ru@CNT synthesized by the polyol method subjected to the same experiment incurs a mass loss of ~ 2.3% at 85°C and continues to lose mass until levelling off at 220°C, where the total mass loss reaches ~3.3 wt% as shown in Figure 4.16b. Possible reasons for this mass loss include the desorption of water from the humidified condition in addition to the possible removal of residual ethylene glycol on the surface. To examine the change in behavior of CsNO_3 when in proximity to Ru, the Ru profile is subtracted from the TGA profile of the combination of CsNO_3 with Ru@CNT and is shown in Figure 4.16c. A mass loss of 11.0% is observed in the promoted catalyst during the initial heating step under the lightly humidified condition. This reaction could be accelerated due to higher humidity and reducing conditions experienced in the operating conditions of the electrochemical cell. The introduction of dry hydrogen increases the mass loss to 12.2%. From this, it can be inferred that CsOH formed, as complete conversion of the CsNO_3 to CsOH would be accompanied by a mass loss of 12.3%. Returning to humidified H_2 induces a slight mass gain in the sample, and the final cooling step induces significant mass gain due to the absorption of H_2O as the hydroxide is relatively more hygroscopic.

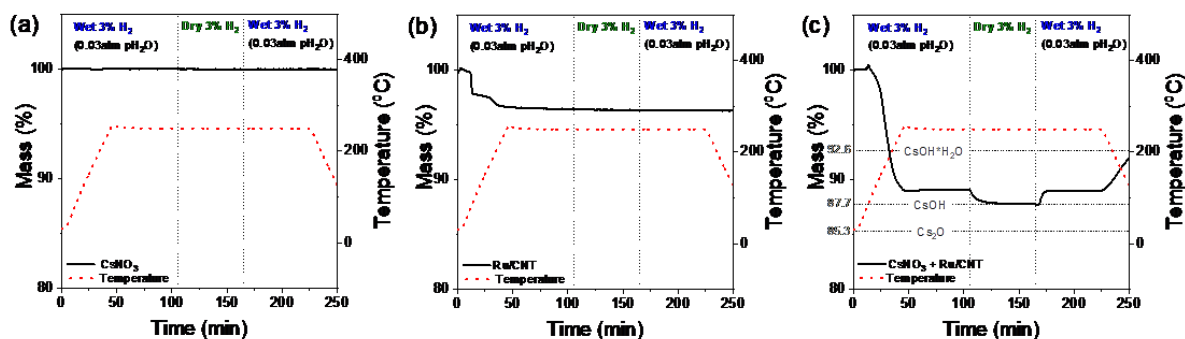


Figure 4.16 TGA (Netzsch STA 443) of (a) as-received commercial CsNO_3 ; (b) in-house prepared 60 wt% Ru/CNT; and (c) 60 wt% Ru/CNT treated with CsNO_3 . Gas atmosphere of measurements as indicated. Gray reference lines in (c) indicate expected weight lost with listed material formation. Reprinted from Lim et al¹⁰⁷.

A thermodynamic calculation using HSC was performed to assess the validity of the hydroxide formation hypothesis. The parameters for this calculation included setting a system pressure of 1 atm, a gas composition of $p_{\text{H}_2\text{O}} = 0.38$ atm, $p_{\text{H}_2} = 0-0.025$ atm, p_{N_2} as the balance gas, and an initial excess of gas amount totaling 100 kmol as opposed to the CsNO_3 starting amount of 1 kmol. This calculation shows that CsOH is more favorable in these conditions as the atmosphere gets more reducing (see Figure 4.17). This suggests that the hydroxide formation hypothesis is thermodynamically feasible.

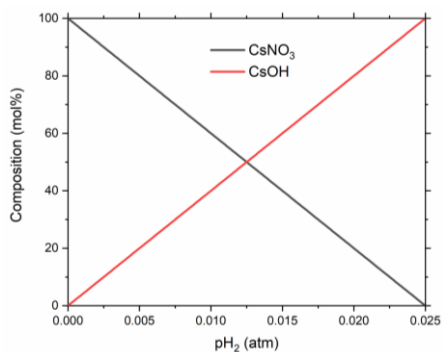


Figure 4.17 HSC calculation for CsNO_3 stability in a range of reducing conditions.

Here, it is important to note a peculiarity that became apparent when testing with samples using an alternate carbon support known as nano-graphite (nGr). Samples using nano-graphite supports exhibited some presence of the CsNO_3 after operation, though to a much lower extent. It is noted in Appendix C.11 that the nano-graphite has some residual nitrogen that can be picked up by CsOH . It seems

challenging to believe this would be the sole reason for the CsNO_3 presence though since the peaks are minorly present even in the case of 1100 hours of operation. Noted also in Appendix C.11 is cesium hydroxide's (or cesium acetate's) remarkable ability to pull other trace anions from seemingly anywhere including chlorine from catalysts prepared at SAFCell and sulfur from the Vulcan XC-72. This coupled with

CsOH's water solubility allow it to be an effective agent to remove potential poisons from catalyst system, and such a method is discussed in Appendix C.11.

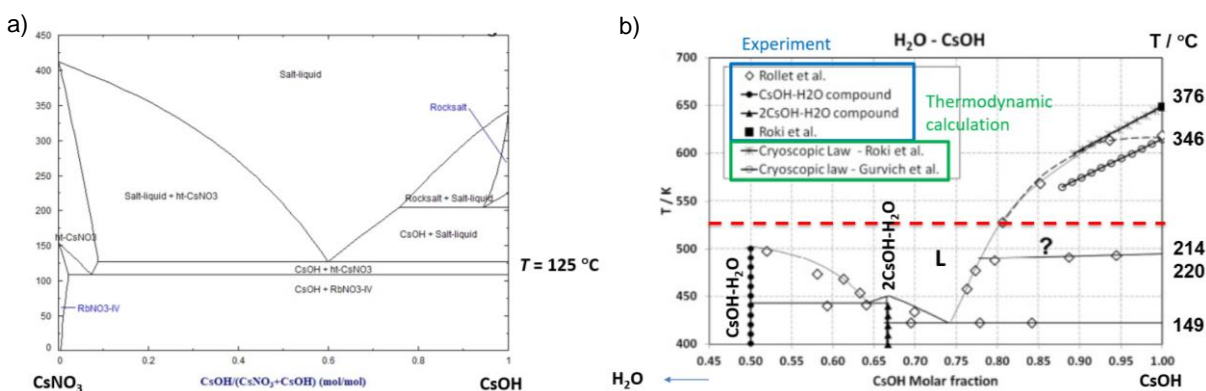


Figure 4.18 a) Thermodynamic CsNO₃-CsOH phase diagram modified from the FactSage database¹²². Constructed phase diagram modified from the work of Roki et al¹²³.

If one considers the phase equilibria of constituent promoter components, it is likely the promoter is in a liquid state during the operating conditions. For instance, if there is a mixture of CsOH and CsNO₃ coexisting during the operating conditions, the melting point is drastically lowered to where it would be in a liquid phase during operation (see Figure 4.18a)¹²². Similarly, CsOH in the presence of H₂O will dramatically lower its melting point to where it is a liquid under operating conditions (see Figure 4.18b)¹²³. These points suggest that, unless a confinement method is in place, the promoter is likely to have free movement throughout the catalyst system.

XPS analysis of the CRL material before and after operation under the ammonia conditions reveals the apparent loss of the nitrate bond accompanied by a peculiar peak arising at a binding energy of 398 eV (see Figure 4.19). As this energy tends to align with the presence of metallic nitride peaks, we suspect this corresponds to the formation

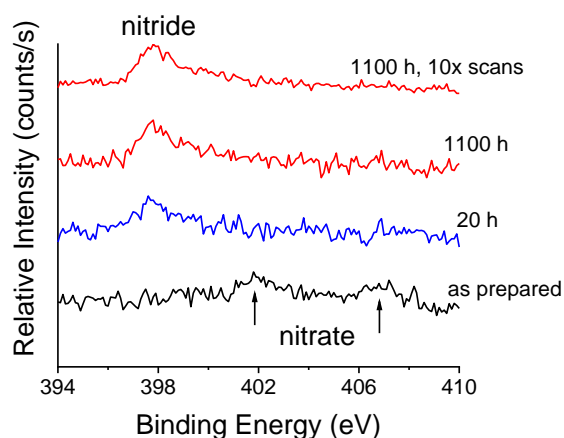


Figure 4.19 XPS of 40 wt% Ru-nanoGr (NaBH₄) CsNO₃ promoted Ru:Cs = 0.5:1 mol ratio CRL powder before and after operation under the ammonia condition (Thermo Scientific ESCALAB 250 Xi).

of a ruthenium nitride. The shape and position of the peak match what was found by Cattaruzza et al. in their sputter deposited RuN film¹²⁴.

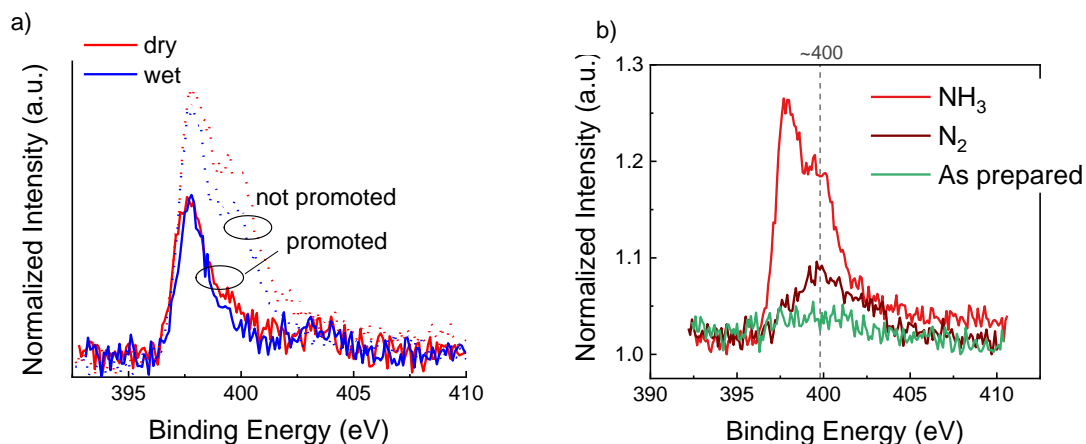


Figure 4.20 XPS of tube furnace annealed 40 wt% Ru/nGr + CsNO₃ (Cs:Ru 0.5:1) (Thermo Scientific ESCALAB 250 Xi). a) Shows samples that were annealed with and without the addition of humidified Ar and with and without the CsNO₃ promoter. b) shows a comparison of an as prepared unannealed sample with a sample annealed under N₂ and a sample annealed under NH₃.

To analyze the environmental dependencies of this formation in the 40 wt% Ru/nGr + CsNO₃ (Cs:Ru 0.5:1), ammonia annealing processes were carried out in a controlled tube furnace. The baseline test utilized humidified ammonia (the “wet” case), in which 100 sccm of ammonia was supplied to the reactor while simultaneously humidified argon was flowed through a room temperature bubbler. The system was ramped to 250°C at 5°C/min and held at this temperature for 20 hours and subsequently cooled to room temperature at 5°C/min. One way in which this baseline test was varied was by performing the “dry” case in which the humidified Ar supply was closed. In addition, a sample was tested where the 40 wt% Ru/nGr was left unpromoted before undergoing the annealing “wet” and “dry” processes. XPS results of these tests are shown in Figure 4.20a. Finally, an unpromoted sample was annealed in the dry case, but with N₂ gas replacing the ammonia gas. XPS results of the comparative N₂ gas case are shown in Figure 4.20b.

This comparative analysis illuminated several critical points. First, it does not appear that humidification in either the promoted or unpromoted case made any significant impact on bonded nitrogen, at least for the low humidity we achieved with this experiment. Second, the presence of the promoter did have a significant impact in this case as the absence of the promoter resulted in a large shoulder peak at 400 eV. When testing with the unpromoted sample under nitrogen, we are able to achieve an isolation of the 400 eV peak (no metallic nitride peak formed). This suggests that the 400 eV peak is associated with adsorbed nitrogen. These analyses reveal two phenomena that are important for the consideration of ammonia catalysis in this system: 1) annealed Ru in the presence of ammonia forms a metallic nitride and 2) the presence of a promoter facilitates the removal of adsorbed nitrogen (likely one of the mechanisms benefitting ammonia catalysis via making reaction sites available). The second point is particularly intriguing as Ru is thought to be slightly under-binding for nitrogen by Sabatier analysis. To determine if this formation of a Ru nitride was associated with the degradation noted earlier in the study, one of the CRLs that was “pre-nitrided” under wet ammonia for 20 hours was tested as a comparative CRL material (see Figure 4.21). This cell performed identically to a cell without a pre-nitrided cell suggesting that this formation of the RuN

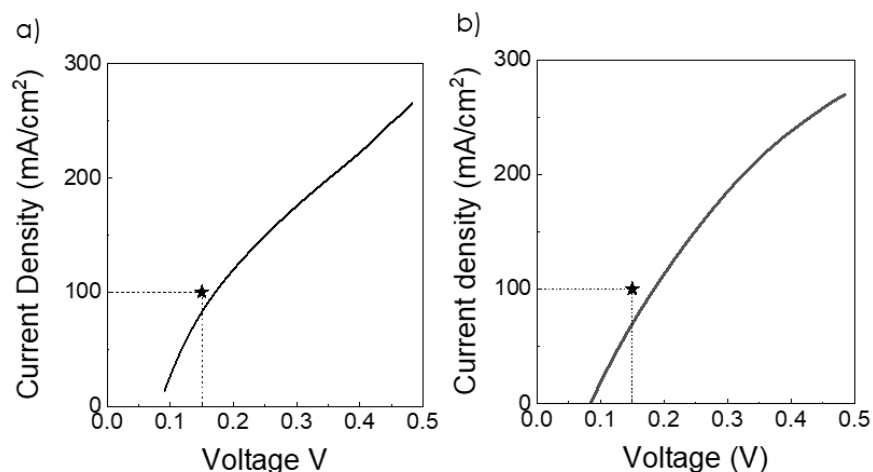


Figure 4.21 Polarization curves under the 0.4pNH₃ ammonia condition of cells with CRLs composed of CsOH promoted 40 wt% Ru/nGr (Cs:Ru 0.5:1) that were incorporated a) as prepared or b) pre-nitrided for 20 hours under humidified ammonia at 250 °C. The scan rate used here was 10 mV/s.

is not the source of degradation. To establish a baseline of degradation hybrid-type ammonia decomposition cells, a longer-term study was carried out over a period of 48 hours. CsOH was used as the promoter in this case as it was noted that degradation (manifested in increasing cell potentials) tends to occur most rapidly in these cells. A hybrid cell using 65 mg of CsOH promoted 40 wt% Ru/nGr was used in tandem with the “standard anode” working and counter electrodes. The results of this degradation test are shown in Figure 4.22. The decrease in voltage appears constant over the measured 48 hours, increasing at a rate of approximately 0.2 mV/h when held under a constant current of $\sim 75 \text{ mA/cm}^2$ (equivalent to an initial 150 mV overpotential) (see Figure 4.22a). The difference in the initial and final polarization curves arises in a current density gap that increases up to an oxidizing potential at the working electrode of $\sim 0.25 \text{ V}$ after which the gap remains constant (see Figure 4.22b). The increases in resistance appear to come from both ohmic and non-ohmic sources which both increase $\sim 15\%$ at OCV (see Figure 4.22c). All supports tested experienced similar degradation (Vulcan XC-72, nanographite, MWCNT).

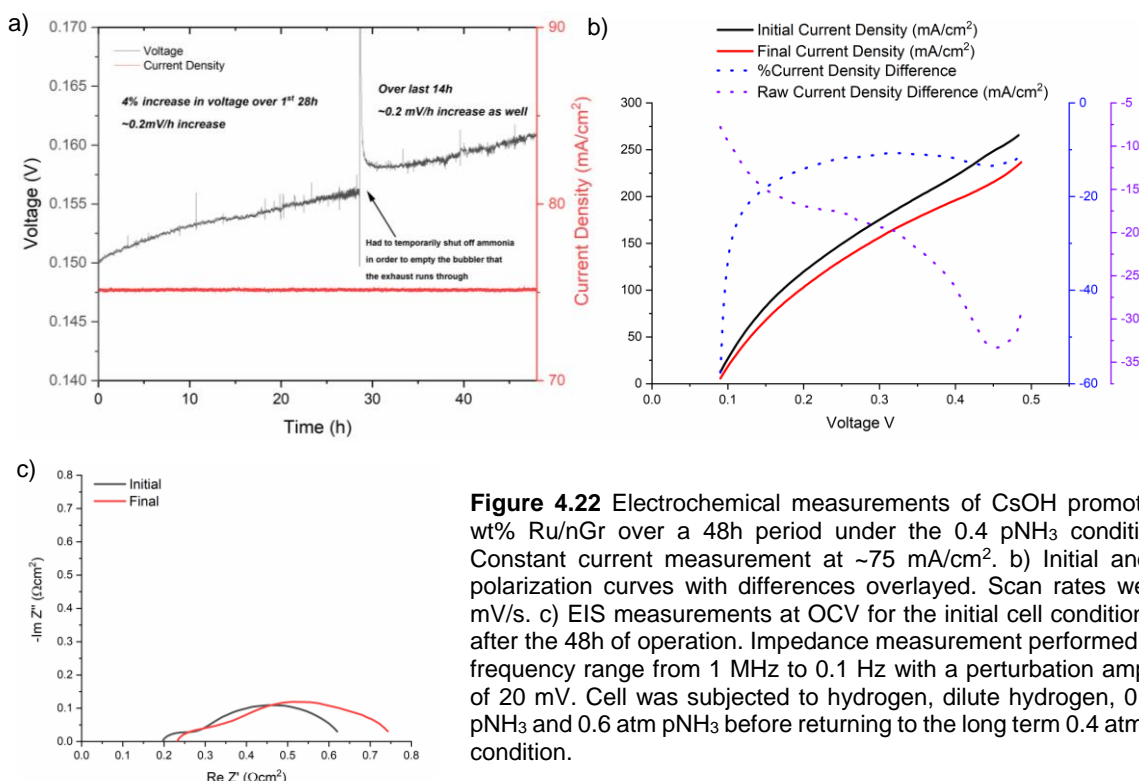


Figure 4.22 Electrochemical measurements of CsOH promoted 40 wt% Ru/nGr over a 48h period under the 0.4 pNH₃ condition. a) Constant current measurement at $\sim 75 \text{ mA/cm}^2$. b) Initial and final polarization curves with differences overlaid. Scan rates were 10 mV/s. c) EIS measurements at OCV for the initial cell conditions and after the 48h of operation. Impedance measurement performed with a frequency range from 1 MHz to 0.1 Hz with a perturbation amplitude of 20 mV. Cell was subjected to hydrogen, dilute hydrogen, 0.4 atm pNH₃ and 0.6 atm pNH₃ before returning to the long term 0.4 atm pNH₃ condition.

To further probe possible sources of degradation XRD analysis of the CRL powder (CsNO_3 promoted 40 wt% Ru/nGr Cs:Ru 0.5:1) was performed after short and long-term operation (see Figure 4.23a). While there is a substantial crystallite size increase within the first 20 hours of operation (3.3(3) to 8.8(8) nm), there was no further crystallite broadening after 1100 hours of operation (8.4(8) nm). The possibility of Cs intercalation into the carbon support was also considered, but it was found that the lattice parameters for the graphite remained constant. XRD analysis was unable to suggest any mode of degradation. Findings suggested from the XRD analysis were confirmed with TEM analysis (see Figure 4.23b). Indeed, there was significant particle coarsening after operation, but this was not further exasperated with extended operation. Neither did the dispersion appear to change from 20 to 1100 hours of operation. While the presence of Cs was able to be detected with EDS generally throughout the sample, its location and form were unable to be determined as an isolated portion of Cs material was not able to be found despite multiple extensive searches.

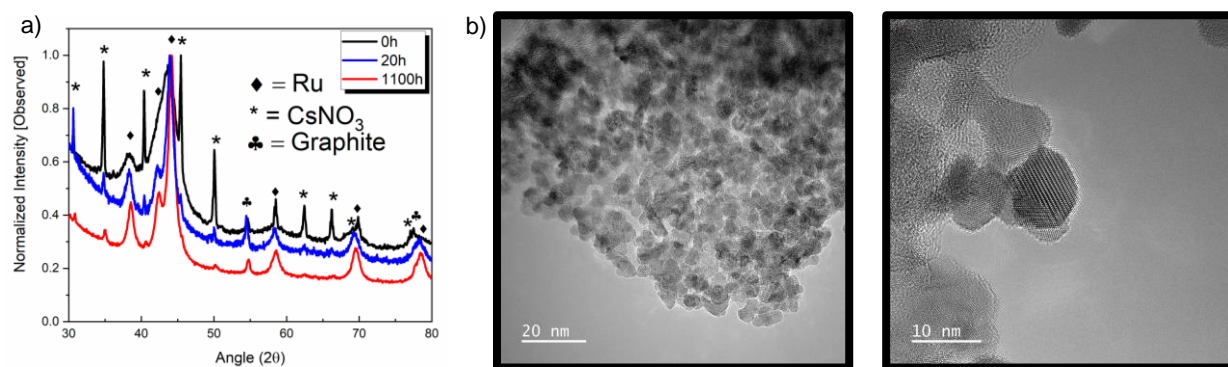


Figure 4.23 a) XRD analysis of the CRL powder (CsNO_3 promoted 40 wt% Ru/nGr Cs:Ru 0.5:1) performed after short and long-term operation (Rigaku Ultima IV). b) TEM analysis of the same CRL powder after zero hours of operation (left) and 1100 hours of operation (right) (JEOL ARM200CF).

Further XRD analysis was able to be performed in the presence of ammonia using the in-situ capabilities in the J. B. Cohen facility. We were able to perform XRD on our CsNO_3 promoted 40 wt% Ru/nGr Cs:Ru 0.5:1 sample as it was ramped to 250°C under ammonia (see Figure 4.24). Ramping to and from 250°C over a period of 80 minutes, the sample was held at 250°C for 80 minutes, and measurements were taken every 20 minutes. Full gas condition replication was not able to be achieved at this time, but it is expected that the capability should be available in the future. From these results, it is apparent that post-

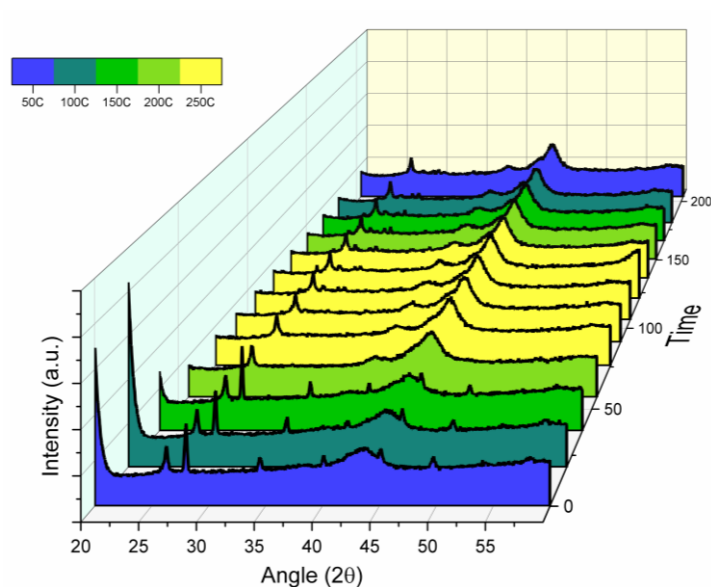


Figure 4.24 In-situ XRD performed in the J. B. Cohen Facility at Northwestern University performed under ammonia flow for the CsNO_3 promoted 40 wt% Ru/nGr Cs:Ru 0.5:1 sample.

operation effects manifest relatively quickly. Cesium nitrate peaks disappear by 200°C suggesting the phase is either completely converted to CsOH by this point or is in a liquid phase. Additionally, peak broadening appears to stop soon after reaching 250°C suggesting the sintering process happens rapidly. After being held at 250°C for 40 minutes, the cesium bicarbonate phase forms with lower intensity. Upon cooling again, the cesium bicarbonate peaks begin to phase from prominence again. It is important here to note several distinctions of this measurement from actual operating conditions including lack of humidity, higher ammonia partial pressure, different level of gas access, and lack of current flowing through the conductive support. The first two conditions can likely be addressed with minimal alterations to the experimental setup while the second two challenges would be rather challenging to mitigate.

operation effects manifest relatively quickly. Cesium nitrate peaks disappear by 200°C suggesting the phase is either completely converted to CsOH by this point or is in a liquid phase. Additionally, peak broadening appears to stop soon after reaching 250°C suggesting the sintering process happens rapidly. After being held at 250°C for 40 minutes, the cesium bicarbonate phase forms with lower intensity. Upon cooling again, the cesium bicarbonate peaks begin

As noted in Appendix C.5, the as-prepared Ru catalyst likely has some degree of oxidation. To analyze if the initial oxidation effect of Ru has any impact on the performance of the ammonia decomposition cell, one such cell was constructed with the fully oxidized amorphous ruthenium catalyst described in Appendix C.5. The cell was constructed equivalently to the baseline CsNO₃ promoted 40 wt% Ru/V Cs:Ru 1:1 sample. Polarization results of this cell reveal that the performance starts poorly but improves over time

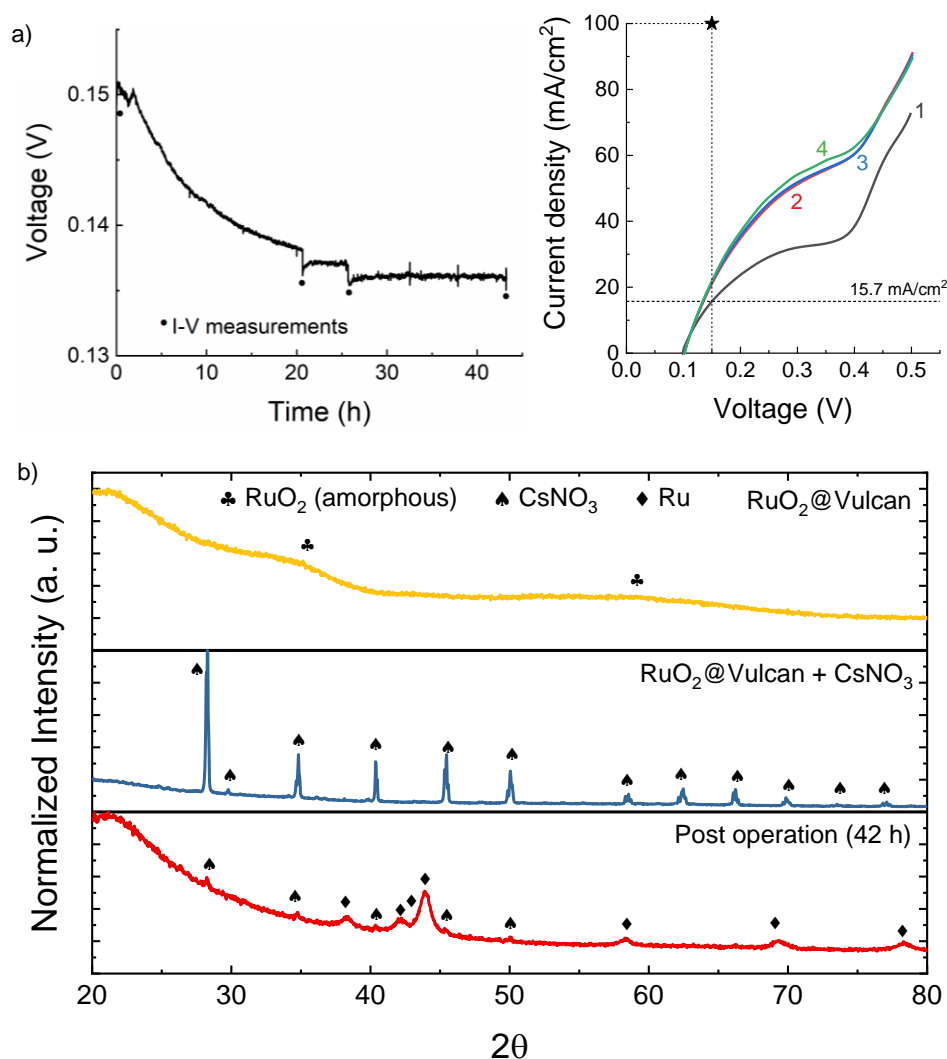


Figure 4.25 a) (left) Constant current measurement in a cell prepared with a bilayer working electrode measured under the 0.4 pNH₃ ammonia condition of 15.7 mA/cm². The CRL is 58 mg of CsNO₃ promoted 66wt% RuO₂@Vulcan with a Cs:Ru mole ratio of 1:1. (right) Polarization curves of measurements taken at points in time order indicated in the constant current measurement taken at a scan rate of 10 mV/s. b) Diffraction pattern collected from as-synthesized 66 wt% RuO₂@Vulcan, after promotion by CsNO₃, using a Ru:Cs molar ratio of 1:1; and post operation of the promoted material in ammonia electrochemical conversion. Exposure to humidified ammonia for 42 hours under constant current and at 250°C converts the amorphous RuO_x to crystalline Ru with a crystallite size of ~ 8 nm (Rigaku Ultima IV).

and levels off after a period of 25 hours (see Figure 4.25a). XRD of the post-operation CRL reveals that the oxidized ruthenium was effectively reduced over the course of the operation (see Figure 4.25b).

As was mentioned in Section 4.3.1, there was consideration if the reaction residence time could be improved in our configuration. To investigate this, two thicknesses of CRL were tested (one with the original 25 mg and the second with 70 mg) using the CsNO_3 promoted 40 wt% Ru/nGr catalyst system. The results, shown in Figure 4.26, reveal that a thicker CRL layer does in-fact improve the rate of reaction at given

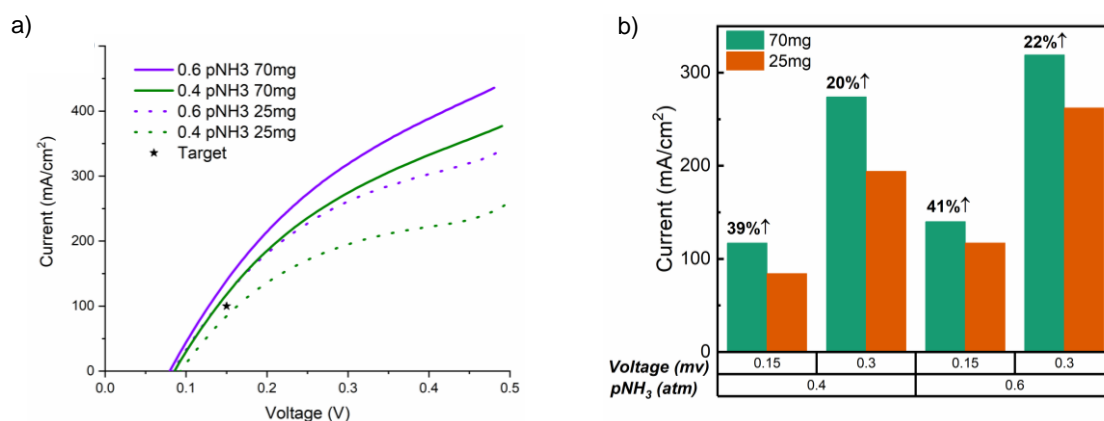


Figure 4.26 a) Polarization curves of CsNO_3 promoted 40 wt% Ru/nGr Cs:Ru 0.5:1 cells with two CRL thicknesses under the 0.4 pNH₃ and 0.6 pNH₃ conditions. b) Comparison between the cells at two overpotentials at the two gas conditions.

overpotentials. While the increase is not proportional to the increase in catalyst material, the increase in activity in the 0.4 and 0.6 atm pNH₃ conditions is proportional. This suggests that improvement was made by increasing the amount of time ammonia is in the reaction zone, and electrode design improving residence time could substantially improve activity.

4.4 Summary

Overall, great promise has been shown for using SAECs in a hybrid construction to generate high-purity hydrogen from ammonia at modest temperatures and overpotentials. These alleviate the challenges that previous methods utilizing ammonia as a hydrogen vector faced and offer new opportunities for developing a hydrogen infrastructure. Investigations into the catalyst series in the single anode layer cells reveal that intuitions from previous work in heterogeneous catalysis and theoretical surface science provide helpful insight into future catalyst design. Additionally, much was learned about the state of the catalyst

system under SAEC operating conditions such as the condition of the metal catalyst, the promoter, and the effects of supports. While many avenues of possible degradation were explored and eliminated as possibilities, the source of degradation in these cells remain an open mystery (though tests at SAFCell have demonstrated that degradation can be prevented if the TCL is external to the cell). Finally, cesium has been shown in a myriad of ways to be a useful element, from serving as the bedrock cation in our SAEC electrolytes, to an agent to bolster ammonia catalysis, to a means of removing catalyst poisons.

Chapter 5 The Economic Case for Solid-Acid Ammonia Synthesis

Maddest of all is to see life is instead of how it should be. – Miguel De Cervantes

While we have demonstrated a technology that efficiently and effectively extracts hydrogen from ammonia, the other side of the coin remains to be addressed (i.e., efficiently and effectively putting hydrogen into an ammonia molecule). While in principle ammonia can be implemented as a sustainable solution for a hydrogen vector, the means to do so do not exist widely today. Over 96% of ammonia used today is produced through the Haber-Bosch process with fossil fuels (e.g., natural gas, oil, and coal) used as the hydrogen source¹²⁵. In the best-case scenario, this process releases 1.9 tons of CO₂ for every ton of ammonia produced. This being the case, ammonia in current use cases are responsible for ~1.2% of anthropogenic CO₂ emissions and this number would only grow if ammonia was to be implemented as a hydrogen vector using currently implemented production methods¹²⁶.

To utilize ammonia in a sustainable manner, solutions that obviate these emissions challenges are needed. Macfarlane et al. suggested a possible roadmap that could be utilized to effectively implement an ammonia-mediated energy economy in a sustainable way⁸⁴. The first generation of technology Macfarlane et al. suggested was to simply pair carbon sequestration with existing production methods. While this is the simplest technologically, this strictly adds to the ammonia production cost and external mechanisms would need to be implemented to incentivize this production route. The second proposed generation mechanism would involve sourcing the hydrogen from water electrolysis and pairing this hydrogen with the standard Haber-Bosch process to produce ammonia⁸⁴. There are mechanisms where this can be advantageous over current ammonia production methods¹²⁶, but there are technological challenges that remain for this process to be competitive with existing ammonia production. The third generation of technology proposed involves directly reducing nitrogen in an electrochemical cell which bypasses the need for the high pressure and temperature Haber-Bosch process. This method in theory can be done the most efficiently and with the best utilization of intermittent energy sources but requires the most technological advancement to be realized⁸⁴.

Here, we perform a technoeconomic analysis that demonstrates the feasibility of utilizing an SAEC for a third-generation ammonia synthesis technology. Based on the microkinetic reversibility of nitrogen

adsorption, progress made on the ammonia decomposition (though the optimal binding energy slightly different as noted in Chapter 4) should aid realization of this technology. The main unique challenge to overcome is the selectivity challenge (nitrogen reduction must be favored over hydrogen evolution). Several benefits of a SAEC system (e.g., the advantageous operating temperature and membrane able to withstand high pressures) make such a system attractive as a direct ammonia electrochemical synthesizer. The groundwork for an economic case allowing such an SAEC to acquire market adoption will help motivate the proof-of-concept of such a technology and provide an avenue for this technology to be adopted.

A wide breadth of sources was consulted to facilitate this feasibility analysis including market research reports and informational interviews. Findings from market research reports, which were mostly used to gauge addressable energy and ammonia markets, have been kept intentionally vague and anonymous based on the propriety of said reports. Interviews were conducted with individuals from a range of industries relevant to this technology including energy producers (e.g., solar, wind, and nuclear), energy utilities, ammonia producers, ammonia distributors, ammonia users (including farmers and farmer co-ops), relevant regulators, analysts, and policy specialists. The names of these sources are kept anonymous for privacy reasons.

5.1 Market

Ammonia is a widely produced and used chemical with a global annual production of 175 million tons addressing a 70 billion USD market⁸⁴. It is apparent that the highest consumption of ammonia comes from the fertilizer industry which is commonly cited to take up 80-90% of the market whereas the remainder is consumed by textiles, pharmaceuticals, refrigeration, explosives, and other industries. As the fertilizer market is by and large the most significant and easily accessible consumer of ammonia, this will be addressed as a target market. For a technology launched in the US, the North American market has a significant amount of demand. Commonly, ammonia is

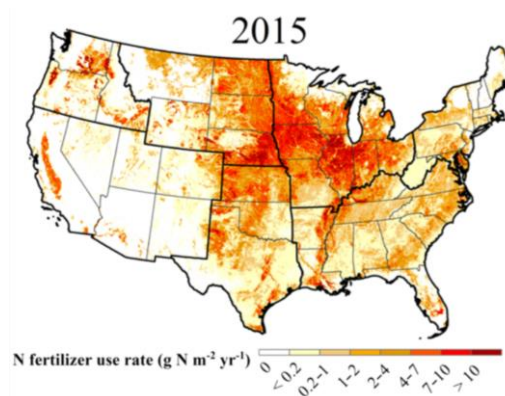


Figure 5.1 Spatial distribution of nitrogenous fertilizer use in the contiguous US.¹²⁷

reacted with other compounds to form final products such as NH_3 reacted with CO_2 to form urea. Adding processes to form value-added products could be costly to launch new technologies, but fortunately in the US there is a large market for direct ammonia applied as fertilizer. Here it is noted that market research was performed using valid market research reports that were acquired for academic use by Northwestern University during the course of performing this technoeconomic analysis. These reports explicitly outline that the contents are not available for public distribution and therefore market claims here are made intentionally vague and do not point to a particular source. As can be seen from the work of Cao et al., the largest consumers of nitrogenous fertilizers lie in the central and midwestern regions of the US (see Figure 5.1)¹²⁷. They point out that the Midwest consumes a large fraction of nitrogenous fertilizer directly (~45%). This suggests the widest and most easily addressable ammonia market for such a technology would be in the central and midwestern US.

The demand side concern of an electrochemical ammonia production technology lies with energy producers for two reasons. On one hand, to generate ammonia generated by electrochemical sustainably, the energy input into the process must be produced in a GHG-free manner. On the other, the price of input electricity must be low as this will be the main driver of unit cost (as opposed to the cost of natural gas for ammonia produced by the Haber Bosh process in the US). As will be discussed in Section 5.4, it is challenging for the ammonia to be produced profitably unless a renewable energy producer is utilizing on-site produced electricity (mitigating transmission costs of utilities). Thus, our target market for this technology will be clean energy producers located close to ammonia off takers, and it is important to discuss why clean energy producers would be interested in this technology.

It is apparent that with increasing penetration of energy from renewable sources, the energy intermittency, owed to the variable nature of generation, increasingly becomes a challenge. Even with the lower penetration of renewables today there are significant portions of time when load generated on national grids are too high and power generation from renewable sources has to be cut-off in a practice known as

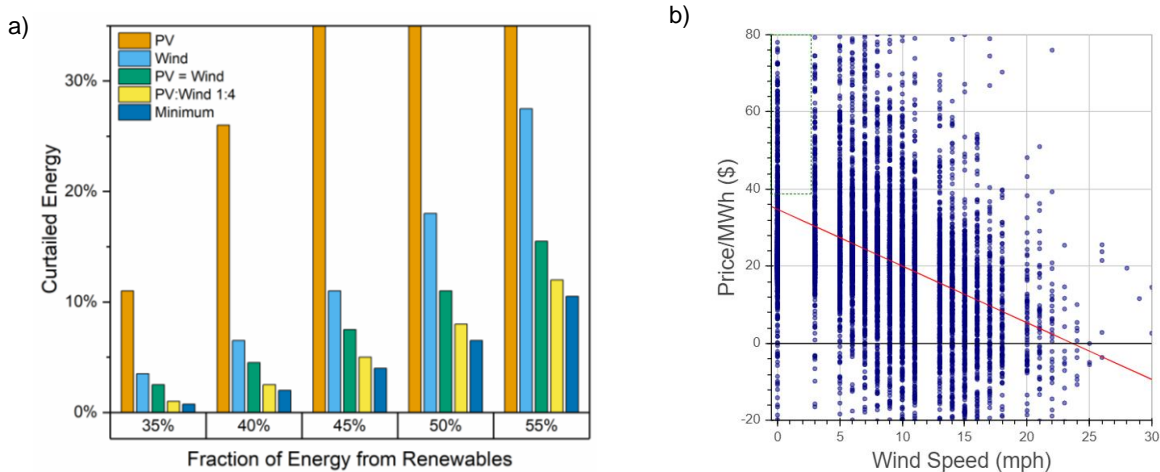


Figure 5.2 a) Models predicted percentages of energy generated from renewables that would need to be curtailed given different percentages of renewable energy generation under different generation mix scenarios for the Electric Reliability Council of Texas (ERCOT) grid using data from Denholm et al¹²⁹. b) Electricity prices as a function of wind speed from a given grid node in the Midcontinent Independent System Operator (MISO) zone generated using the EPAT tool¹³⁰.

'curtailment'¹²⁸. With increasing levels of renewable energy penetration in the grid, levels of energy curtailment will increase even with idealized levels of available transmission that are not yet realized (see Figure 5.2a)¹²⁹. Aside from strict curtailment, merchant energy producers must also face a vast ranges of possible electricity prices in each time that can even go to negative levels (see Figure 5.2b)¹³⁰. Utilities who sign power purchase agreements (PPAs) with renewable producers increasingly need to reckon with the hourly, daily, and seasonal mismatches between electricity demand and supply. This has led renewable energy producers to seek uses for low demand electricity and have sought energy storage as a possible solution.

One thought to mitigate this pricing challenge is to store the electricity while demand is low and provide this electricity when the demand is high. By far, pumped hydro is the most common form of energy storage in the US (~95%) from its many benefits including cost, power rating, discharge time, efficiency, and lifetime¹³¹. As one might expect, this leads a large majority of the prevailing energy storage solutions to lie along large bodies of water (see Figure 5.3a). This tends to not align with geographical area where renewable energy is being generated, like wind energy (see Figure 5.3b)¹³². Other forms of energy storage (aside from similarly geographically limited compressed air storage) are more costly, though prices have been coming down and alternative energy storage solutions are seeing more use cases that are profitable¹²⁹. In certain cases, batteries make sense to implement for shorter day-long energy storage while reversible hydrogen fuel cells have been shown to be more effective for longer term and duration energy storage. Still, with ever depressing energy prices in an increasingly competitive landscape these might not be as cost effective in many scenarios. What we instead propose is that producers use cheap, excess electricity to turn air and water into the value-added product of ammonia for the purposes of fertilizer distribution. This would be of particular interest to wind developers that are located coincident with ammonia off takers that pay a premium for it as fertilizer.

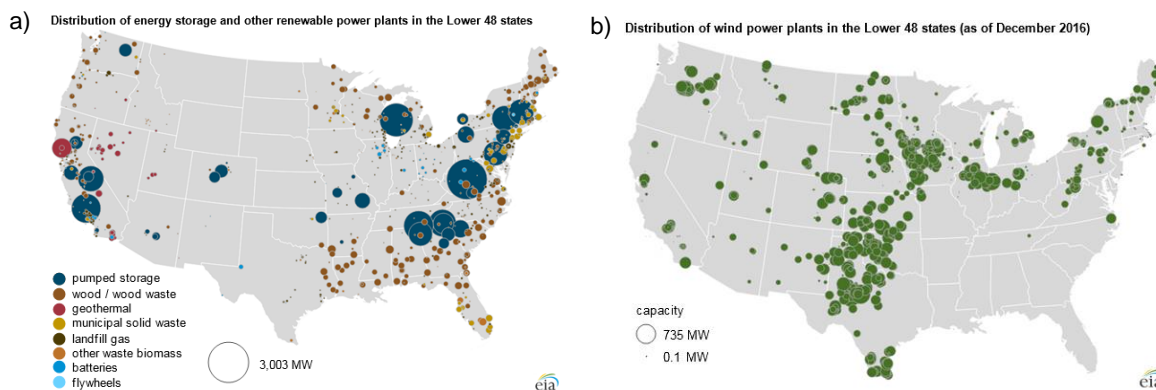


Figure 5.3 a) Map showing the distribution and scale of energy storage in the US. b) Map showing the distribution of wind power sources by capacity. Both sets of data provided by US Energy Information Administration in their Electric Generator Report¹³².

5.2 Logistics

If a SAEC device was able to generate ammonia cheaply and effectively, there still lies the challenges in storing and distributing the ammonia to the end consumers. Storage is particularly important because the procurement of ammonia as fertilizer is largely seasonal. Fortunately, ammonia is a relatively

cheap chemical to store and move. We will investigate currently applied methods of storing and transporting ammonia so that these aspects can be factored into our techno-economic analysis.

Ammonia is typically stored in pressurized vessels for smaller use cases and in refrigerated vessels for the largest storage solutions. Ammonia is a liquid at ambient temperature and has a pressure of about 9 bar; in this state, ammonia has a high volumetric energy density (13.8 MJ/L). This being the case, ammonia pressure vessels commonly employ a working pressure of 17 bar to account for fluctuations in temperature and ensure ammonia is kept in the liquid state. This modest pressure allows for simple carbon steel to be employed as the tank construction material of choice. Using this method vessels comprised of one tonne of steel per about three tonnes of ammonia can be stored in such pressure vessels up to 270 tonnes^{133,134}.

Large scale ammonia storage is typically carried out at atmospheric pressure through cooling of ammonia to the point at which it is liquid (-33°C). This system only requires an insulated tank combined with a refrigeration system and has a much lower strength requirement than the pressurized tank system. Since the only strength requirement is to withstand the static pressure of the fluid, the steel requirements of the cooled system are much less. There is also the added benefit of the ammonia having a higher energy density in this cooled setting (~15.4 MJ/L). Overall, this system needs about 15x less steel than the pressurized system. The minimal vaporized ammonia can be recirculated into the system with recondensation and the overall storage process can be carried out with a reasonable energy efficiency even including the ammonia synthesis component (~94%). Using this method, up to 60,000 ton storage containers are made^{133,134}. Currently, a majority of ammonia storage points across the US exist in the Midwest and a map of this can be found in the policy briefing "*Ammonia: Zero-Carbon Fertiliser, Fuel and Energy Store*" provided by the Royal Society¹³⁵.

Ammonia is shipped primarily in four ways: by truck, railcar, barge, and pipeline. The greatest amount of ammonia is shipped by pipeline at some point in distribution, followed by moderately less shipping with truck and railcar shipping, and even less shipping with marine vessels (including river barges). When normalizing by the distance traveled for each transportation mode, it is apparent that a large share of the ammonia carrying is performed by rail transportation and truck distance is relatively short, emphasizing that truck shipping is predominantly used for localized shipping (see Figure 5.4a). The bulk shipping methods tend to be implemented equally year-round, while truck transportation is largely carried out right before fertilizer is applied in the Spring and Fall (see Figure 5.4b)¹³⁶.

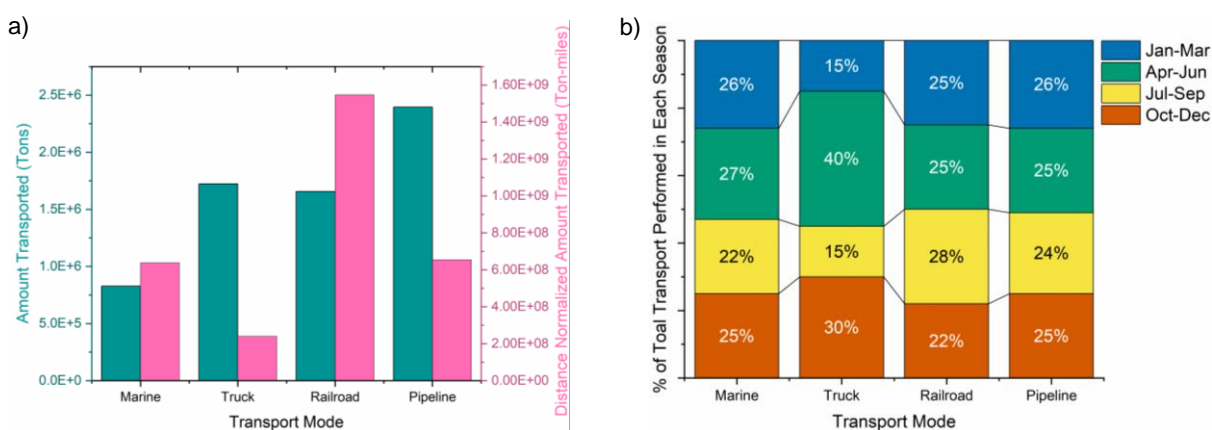


Figure 5.4 a) Ammonia transported on a mass basis and mass-distance normalized basis by transport mode. b) Fraction of ammonia transported by each transportation mode that is conducted in each season¹³⁶.

Each transportation mode is used for different scales of transportation. Ammonia is transported by truck and rail as a pressurized liquid with about 27 ton and 78 ton tanks respectively. Barges are typically moving ammonia either in pressurized or refrigerated modes at a larger scale around 2,500 tons with oceangoing capable of moving up to 50,000 tons of low temperature stored ammonia. Of course, high volumes can be transported by pipeline economically as no movable tank is required^{133,134}. The cost of ammonia shipping scales similarly with marine shipping being the cheapest followed by pipeline (aside from distances <250 km where pipeline shipping would be cheaper), then rail, and then truck^{135,137}.

5.3 Comparison to Hydrogen

Hydrogen has a considerably lower volumetric energy density than ammonia. At ambient temperatures, hydrogen is required to be pressurized at 300 bar to achieve an energy density of 3 MJ/L

which is less than a fourth of the energy density of ammonia under mild conditions coupled with the requirement of a much stronger tank. Alternatively, hydrogen can be cooled to a liquid state at -253°C at ambient pressure using a two-step cycle where first the hydrogen is cooled with liquid nitrogen and subsequently the hydrogen is allowed to expand¹³⁸. Not only are the materials requirements significantly more challenging, but the efficiency is much less than for the ammonia case ($\sim 77\%$ vs. 94% for ammonia) and the energy density in the liquid form is less than two-thirds that of ammonia¹³³. This leads ammonia to have lower spatial footprint requirements in addition to less operational expenses. The material requirements leads to ammonia being $\sim 6\text{x}$ cheaper for smaller scale storage applications in terms of capital expenses¹³⁹. For large scale storage, it has been found that storing hydrogen in salt caverns can be done at costs comparable to that of ammonia storage though this method still falls short on different storage metrics relative to ammonia such as flexibility considering scale, location, and transportation from site¹³⁵.

Hydrogen transportation by pipeline, ship, rail, and truck faces disadvantages comparatively to ammonia due to analogous limitations discussed for storage solutions. For the same energy density reasons hydrogen is more expensive to transport by ship, rail, and truck for both the pressurized hydrogen and liquid hydrogen cases. Hydrogen pipelines require judicious selections of steel as they are prone to embrittlement and face additional issues with corrosion and fatigue. The existing hydrogen pipeline infrastructure in the US is much more limited than what is available for ammonia, and is primarily located on the Gulf Coast¹⁴⁰. Additionally, transporting hydrogen by pipeline takes three times the amount of energy to transport an equivalent amount of hydrogen in ammonia over a distance of 1,600 km while also being delivered with less energy efficiency (87% vs 93% (including NH_3 synthesis)¹³³. Relative shipping rates for hydrogen are much more expensive than for ammonia; shipping by truck is estimated to be about three times as expensive and shipping by rail is estimated to be about nine times more expensive on a $\$/\text{ton-mile}$ basis. Hydrogen is also more expensive to transport on a large scale; taking a 1400 km travel distance as an example, pipeline shipping is 1.5x more expensive in the hydrogen case and about eight times more expensive when comparing ship transport¹³⁵.

Overall, considering market entry for a hydrogen generation technology relative to an ammonia generation technology, one should consider three things: the available market, available infrastructure, and

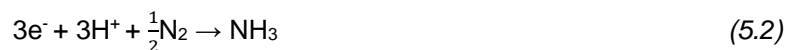
logistics. The hydrogen market has a comparable size to the ammonia market though more buyers are industrial and there is a higher degree of consolidation among existing providers. Existing hydrogen infrastructure is mostly located on the Gulf Coast directed to targeted consumers and there is also a lack of a distributed storage network. The transport and storage cost of hydrogen is both more capital intensive and more expensive than transporting ammonia from a unit cost perspective. Thus, in areas where more local and ready use of hydrogen is desired, direct hydrogen generation will be a more favorable technology. In cases of long-term storage and long distance, ammonia as a medium will likely be more economical. Furthermore, there could be a unique short term market opportunity for green ammonia generation whereas market entry is more challenging for hydrogen generation.

5.4 Technoeconomic Analysis

A proposed SAEC system to synthesize ammonia from air and water would involve supplying steam as the hydrogen source to the anode and nitrogen to the cathode. The water oxidation on the anode would split water into oxygen (this gas would be vented) and protons to be shuttled to the cathode (Equation 5.1).



The cathode would be involved in fulfilling the nitrogen reduction reaction (NRR) to react nitrogen with the shuttled protons to make ammonia (Equation 5.2).



This results in the net reaction shown in Equation 5.3.



The net proposed SAEC system is depicted in Figure 5.5.

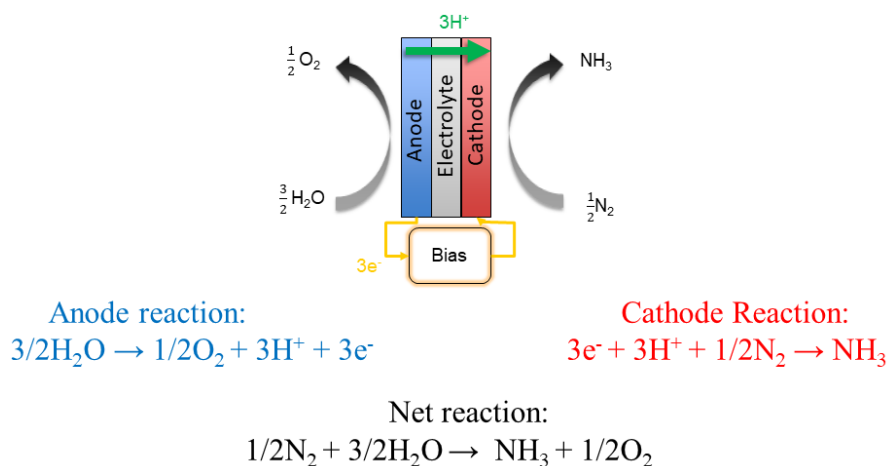


Figure 5.5 Schematic of ammonia synthesis SAEC. Water is fed to the cell anode. Upon applying a potential, oxygen, protons, and electrons are split. Protons and electrons recombine with nitrogen at the cathode to form ammonia.

The overall system would require several auxiliary components that would need to be separately considered. First, the supplied reactants would need to be purified. Water prices can vary by location and a moderate value of \$5/kgal was assumed for this analysis. Here, we choose to implement a reverse osmosis water purification system. While most water purification plants consume electricity on the order of 3.5-4.5 kWh/m³, we will assume a conservative value of 10 kWh/m³ for this process¹⁴¹. Air will be used as the nitrogen source, but oxygen must be removed from the air to avoid shuttling protons combining with the oxygen to form water. To do this, we implement an Air Separation Unit (ASU) which requires 0.21 kWh/kg of nitrogen¹⁴². This system would also require significant heating to maintain the system at 250°C, where most of the heat requirement would arise from raising water to this temperature. Additionally, a compressor would be required to provide pressurized gases to the cell. A flash tank would be required at the anode exhaust to separate the ammonia from the auxiliary gases. Finally, a storage system to collect ammonia from the flash tank should be implemented. The final electricity component to be considered on a unit cost basis would be for the electrical work by the SAEC which depends on its operational power consumption as well as its faradaic efficiency. We will set a target of 75% faradaic efficiency which is more conservative than the ARPA-e stated goal conversion of 90%¹⁴³ and an operational voltage of 1.5 V. This voltage was chosen as it is in line with some literature values of reasonable operating voltage and much high voltages

tend to lead to a domination of HER¹⁴⁴. For the SAEC electrical work, it is estimated that 5.7 MWh of electricity will be consumed per ton of ammonia generated, leading to an overall energy consumption of 8.3 MWh per ton of ammonia produced. A workflow schematic of this process is depicted in Figure 5.6a and an energy consumption breakdown is shown in Figure 5.6b. An important note from this process high-purity oxygen from both the ASU and the SAEC will be produced as a byproduct, and this could be also possibly sold for local applications. One such possibility is for aeration of water in aquaculture as lack of oxygen availability limits productivity¹⁴⁵.

The main capital costs for this operation lie in the SAEC system and the storage system. Typically, the capital costs of electrolysis systems scale with the nameplate power of the system with typical PEM electrolyzers costing around \$300/kW¹⁴⁶⁻¹⁴⁸. Stack and associated power electronics dominate the capital costs making them not as sensitive to auxiliary components such as the reactant and product handling components (excluding storage)¹⁴⁸⁻¹⁵¹. For our case, to account for having a newer system, possible shortfalls in power density, and potentially higher auxiliary capital costs we assume a capital cost of \$1,000/kW. For smaller scale storage systems we assumed the use of 30,000 gallon underground pressurized tanks at a cost of \$100,000¹³⁹, whereas for the largest scale system we assumed as refrigerated ammonia storage facility capable of storing 60,000 tons of ammonia at a cost of \$25,000,000^{137,152}. Local anhydrous ammonia selling is mostly conducted during a small window in the spring (~2/3 of total sales) and a small window in the fall (~1/3 of total sales). For this reason, we estimate our storage capacity needs to be 60%, 65%, and 70% of total production for the 2.5, 25, and 100 MW systems, respectively.

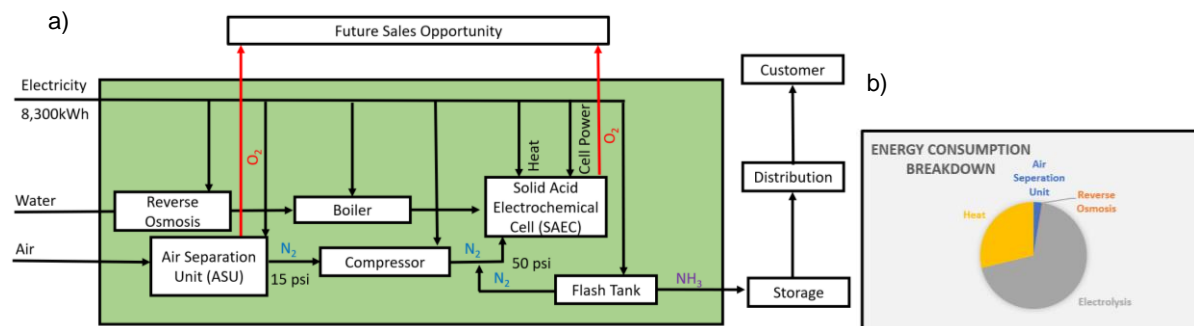


Figure 5.6 a) SAEC for ammonia synthesis workflow diagram for producing a ton of ammonia. b) energy consumption breakdown of ammonia synthesis SAEC.

For our systems, we expect the operations and maintenance (O&M) costs to scale along with the capital costs. In our model, we assume O&M costs to be 3%, 2% and 1% of capital costs for 2.5 MW, 25 MW, and 100 MW systems, respectively. Since we expect that our capital costs will tend to be relatively high compared to our operational expenses, we implement a licensing fee of 5% instead of a system cost markup for our pricing structure. The sum of all these costs can be added to determine unit costs and find the prices of electricity needed to make our system profitable (see Figure 5.7). Roughly speaking, we found that retailers in the Midwest would buy ammonia for around \$400/ton of ammonia and local farmers would buy at around \$500/ton of ammonia which implied that the SAEC system could operate profitably at electricity prices less than 3 ¢/kWh.

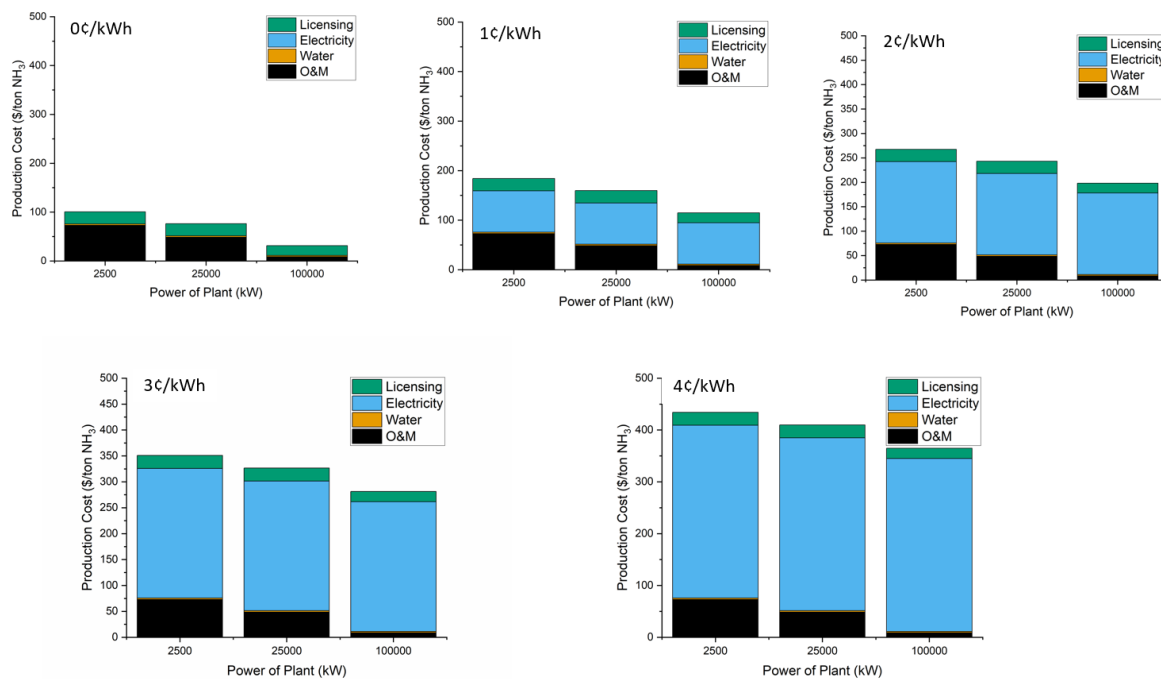


Figure 5.7 Unit economic price for SAEC ammonia production at different electricity prices.

Because of these unit costs, we set a price threshold at 3 ¢/kWh. Given that our system would take on the order of an hour to ramp up, we considered targeting continuous demand windows in the time of day for this operation. Analyzing the locational marginal prices (LMPs) at various PJM and MISO (these are two relevant regional transmission organizations) nodes we determined that at a favorable node is a LMP less than 3 ¢/kWh for 85% of the time with a weighted electricity price of 1.6 ¢/kWh that could be obtained

through continuous operation. An example of time-of-day variance in electricity pricing is included in Figure 5.8 to help envision how one might operate an SAEC in such a manner throughout the day¹⁵³. It is noted here that to operate in this manner, the energy supplier must either be supplying electricity in a merchant manner where they choose to sell electricity at their own discretion, or they must have formulated a power purchasing agreement (PPA) in which they agree to only devote 15% of their capacity to delivering grid electricity with the remainder supplying for the SAEC system.

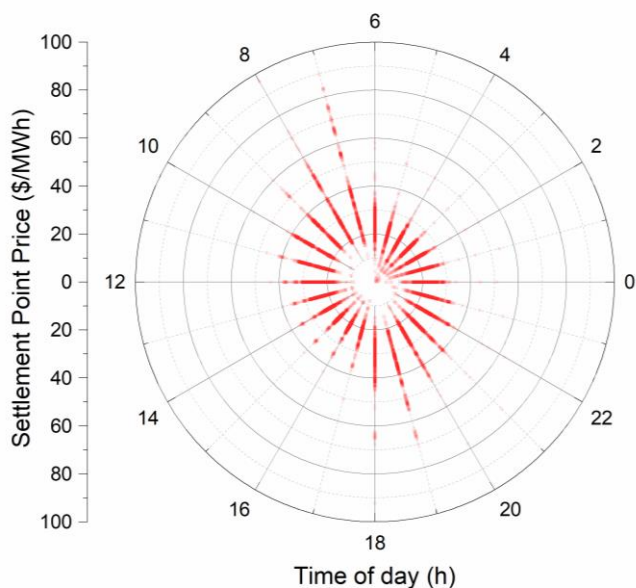


Figure 5.8 Settlement point prices for nodes across the ERCOT system by time of day in military time for January 2019¹⁵³.

Given that the system price scales with peak power, this tends to favor systems with more continuous operation with higher capacity factors and longer periods of the day in which they operate. Lower capacity factors and periods of day use in solar power systems (10-30% capacity factors, ~20% in the Midwest¹⁵⁴) make them more challenging to implement with the proposed SAEC system. Wind systems have the ability to operate for longer periods throughout the day and operate with much higher capacity factors (average in 40% with newer installing systems capable of surpassing 50%)¹²⁸. This made wind seem like a promising candidate, which is why our smallest system considered corresponds with the power of an average wind turbine built today (~2.5 MW)¹²⁸. For our analysis purposes we considered the 2.5 MW and 25 MW systems to be supplied by wind systems with capacity factors of 47%. Nuclear power generation

facilities have extremely high capacity factors with several facilities operating at around 95%, and close to around 100% when load factors do not have to be followed¹⁵⁵. We consider the 100 MW system here to be powered by a nuclear site with a capacity factor of 99%. Another factor that would aid in the nuclear case is the possibility of heat recycling reducing the heat consumption needs, but this was not considered in our analysis. We assume that 3% of the operating time required will be lost due to maintenance on the SAEC giving lower net capacity factors.

One can estimate how much ammonia is consumed in a local area by determining the fraction of an area that is farmland of given crops and discovering the rate of ammonia applied per crop. Corn and wheat tend to be high consumers of nitrogen, demanding around 220 pounds applied per acre. This also can aid in determining how ammonia can be sold to a local market. In Figure 5.9, we show the cost of average local distribution to given farm

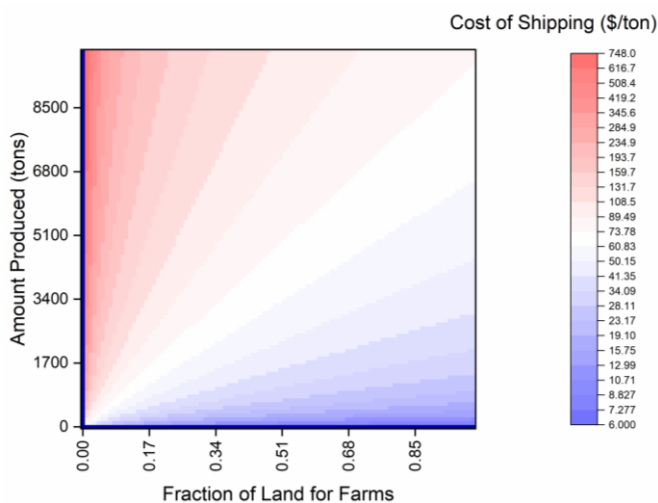


Figure 5.9 Cost of shipping by truck for a given fractional area of land for corn/wheat farms based on an annual ammonia production rate.

area fractions at given production rates (see details in Appendix B.6). We determined that the two wind cases would be able to distribute locally, while the nuclear supplied case would require distribution through agricultural retailers.

By estimating for a 20-year system lifetime (5% depreciation) and a 25% corporate income tax rate, we project the annualized metrics summarized in Table 5.1.

Table 5.1 Annualized Metrics for SAEC Cases Considered

Annualized Metrics	2.5 MW	25 MW	100 MW
Plant Size (ton)	1018	10184	85809
Capital Cost	\$ 1,800,092.25	\$ 18,000,922.46	\$ 72,003,689.85
Storage (% of Annual Prod)	60%	65%	70%
Storage Capital Cost	\$ 814,753.29	\$ 8,826,493.96	\$ 25,000,000.00
Total Capital Cost	\$ 2,614,845.53	\$ 26,827,416.42	\$ 97,003,689.85
O&M (% Capital Cost)	3%	2%	1%
O&M Cost	\$ 78,445.37	\$ 536,548.33	\$ 750,036.90
Water Price (\$/kg)	\$ 0.0013	\$ 0.0013	\$ 0.0013
Water Use (kg)	2,036,883	20,368,832	171,618,246
Water Cost	\$ 2,647.95	\$ 26,479.48	\$ 223,103.72
Electricity Use (kWh)	8,492,391	84,923,912	715,529,133
Netplate Power (kW)	2,500	25,000	100,000
Capacity	39%	39%	82%
Equivalent Constant Electricity Use (kW)	969	9,695	81,681
Electricity Price (\$/kWh)	\$ 0.016	\$ 0.016	\$ 0.016
Electricity Cost (\$)	\$ 135,878.26	\$ 1,358,782.60	\$ 11,448,466.13
Ammonia Cost (\$/ton)	\$ 213.04	\$ 188.70	\$ 144.76
Carbon Price (\$/ton CO ₂)	\$ -	\$ -	\$ -
Carbon Cost (\$/ton NH ₃)	\$ -	\$ -	\$ -
Ammonia Price (w/ carbon) (\$/ton)	\$ 500.00	\$ 500.00	\$ 400.00
Annual Revenue (\$)	\$ 509,220.81	\$ 5,092,208.05	\$ 34,323,649.16
Licensing Fee (% Revenue)	5%	5%	5%
Licensing Cost (\$)	\$ 25,461.04	\$ 254,610.40	\$ 1,716,182.46
Total Cost	\$ 242,432.61	\$ 2,176,420.81	\$ 14,137,789.20
Annual Gross Margin (\$)	\$ 266,788.19	\$ 2,915,787.24	\$ 20,185,859.96
Depreciation (\$)	\$ 90,004.61	\$ 900,046.12	\$ 3,600,184.49
Pre-Tax Profit (\$)	\$ 176,783.58	\$ 2,015,741.12	\$ 16,585,675.47
Taxes (\$)	\$ 44,195.89	\$ 503,935.28	\$ 4,146,418.87
Earnings (\$)	\$ 132,587.68	\$ 1,511,805.84	\$ 12,439,256.60
Cash Flow (\$)	\$ 222,592.30	\$ 2,411,851.96	\$ 16,039,441.09

These metrics show that increased scale will effectively drop the cost of ammonia. The wind powered systems would expect a return on investment between 11 and 12 years while the nuclear-powered system would expect a 6-year return on investment owing largely to decreased unit storage costs and a higher net capacity factor, despite requiring selling to whole sellers at a lower margin. Furthermore, a carbon tax would likely raise the price of ammonia due to the heavy correlation of ammonia prices with hydrocarbon prices. If fully translated, every \$/ton of a CO₂ tax would equate to a \$1.80/ton cost increase for ammonia. This would greatly increase the efficacy of employed SAEC systems.

5.5 Competitive Advantage

Compared to the conventional Haber-Bosch process, the SAEC process can be carried out with a lower unit cost (\$325/ton at \$5/MMBtu for Haber-Bosch ammonia). Haber-Bosch ammonia demands scale with costs almost tripling when lowered to a production rate of 3,400 tons per year¹⁴³. If the proposed SAEC system can reach the proposed operating targets and operate over a reasonable lifetime, this system promises to be more efficient in addition to being more sustainable.

The most important difference between the two systems lies in the fact that the hydrogen source is from water rather than in a hydrocarbon. This has the added benefit of lower volatility and susceptibility to influence from foreign actors (given global markets). A second key benefit would lie in the fact that this could be accomplished with gentler environmental conditions with a lower operating temperature (250°C vs 400-500°C) and pressure (1-40 bar as vs 150-250 bar)¹⁴³. In addition to lowering material requirements, the SAEC system also helps for faster on/off cycling (making this an advantage over water electrolysis and Haber-Bosch as well). This can be done with lower energy consumption as well with a projected 8.3 MWh/ton compared to the 9-11 MWh/ton required for Haber-Bosch ammonia synthesis¹⁵⁶. This energy consumption is also lower than the projected 9.5 MWh/ton for water electrolysis followed by Haber-Bosch¹⁴³. Lower achievable system sizes allow for smaller systems to be constructed to serve local markets which allow for both high profit margins and reduction of shipping needs. Directly producing ammonia removes the need for the temporary housing of hydrogen which is both expensive and hazardous in a unique way that other system components are not. SAECs are likely uniquely able to facilitate this reaction this efficiently as lower temperature systems will be much more sensitive to catalyst poisoning by ammonia in addition to suffering from sluggish kinetics. Higher temperature solid oxide-based systems would not be able to capitalize on the time of day shifts as easily due to slower on/off cycling. Additionally, higher temperature cells would be required to operate at higher pressures due to the shift in the ammonia chemical equilibrium. Finally, the higher temperature cells would require more expensive cell components to match the environmental conditions.

5.6 Summary

Here we have presented an economic case for a SAEC-based ammonia synthesis system that has the promise to be implemented more sustainably, more distributed, and more efficiently than existing methods. Using air and water, SAEC-based ammonia synthesis can enable green fertilizer production in the near future and green hydrogen capacity in the long term. A zero GHG emissions ammonia production method would represent a huge step in decarbonizing an otherwise challenging sector to make sustainable. This method would also complete the round-trip “ammonia as a hydrogen vector” cycle sustainably (as we have already demonstrated efficacy of generating hydrogen from ammonia). This SAEC-based system can produce ammonia in a more distributed and local manner in a stark contrast to the over billion-dollar plants producing ammonia today. Not only will this reduce transportation needs, but it will enable production projects in otherwise underserved areas and enable greater access to fertilizer. One can even envision farmer owned co-ops producing their own nitrogen fertilizer, much like the many that have bought their own ethanol, biodiesel, and wind energy projects¹⁵⁷. Finally, this analysis shows that such a method could be implemented without making sacrifices in efficiency, without burdening agriculture and making food more expensive, and without radical technology changes to be implemented aside from the SAEC itself. This analysis will hopefully inspire the development of a proof-of-concept for such a technology and then perhaps propel us towards a sustainable future.

Appendix A Derivations

A.1 Relation Between the Free Energy of a Reaction and the Nernst Potential

A change in the free energy of a system is a combination in the change in internal energy dU and a function of temperature and pressure:

$$dG = dU - TdS - SdT + pdV + Vdp \quad (\text{A.1-1})$$

where T is the temperature, S is the entropy, p is the pressure, and V is the volume. The two ways energy can be transferred between a closed system is by heat Q and work W so that a change of internal energy is defined as:

$$dU = dQ + dW \quad (\text{A.1-2})$$

A system's is usually inferred based on how heat transfer will cause the entropy of the system to change. At a constant pressure, the entropy will change as:

$$dS = \frac{dQ}{T} \quad (\text{A.1-3})$$

We will for now consider work coming from mechanical and electrical sources. With this consideration and rearranging Equation A.1-3, Equation A.1-2 becomes:

$$dU = TdS - (pdV + dW_{elec}) \quad (\text{A.1-4})$$

which makes a change in free energy of:

$$dG = -SdT + VdP - dW_{elec} \quad (\text{A.1-5})$$

At a constant temperature and pressure this expression reduces to:

$$dG = -dW_{elec} \quad (\text{A.1-6})$$

This means that the maximum electrical work that can be performed from a reaction carried out at a constant temperature and pressure is given by the negative of its free energy:

$$-\Delta g_{rxn} = W_{elec} \quad (\text{A.1-7})$$

The potential of a system to do electrical work is measured by voltage. Electrical work is performed by moving an electrical charge Q through an electrical potential difference E :

$$W_{elec} = EQ \quad (\text{A.1-8})$$

In the case where this charge is being carried by electrons then the charge is equal to the moles of electrons n times the charge per mole of electron (i. e. Faraday's constant F):

$$Q = nF \quad (\text{A.1-9})$$

By combining Equations (A.1-7), (A.1-8) and (A.1-9), it can be seen that:

$$\Delta\hat{g} = -nFE \quad (\text{A.1-10})$$

Which is equivalent to Equation 1.1. Thus, the reversible voltage for a given electrochemical reaction is determined by the Gibbs free energy of said reaction.

A.2 Generalized Thermodynamic Electrochemical Potential

First, we want to know how the voltage derived in A.1-1 will change when the concentration of reaction components changes from the standard state. To do this, we must introduce the concept of a chemical potential which measures how the Gibbs free energy of system changes as the amount of a species in a system. Each species in a system is assigned a unique chemical potential:

$$\mu_i^\alpha = \left(\frac{\delta G}{\delta n_i}\right)_{T,p,n_{j \neq i}} \quad (\text{A.2-1})$$

where μ_i^α is the chemical potential of species i in the α phase and $\left(\frac{\delta G}{\delta n_i}\right)_{T,p,n_{j \neq i}}$ is the Gibbs free energy change for change in the quantity of species i with the temperature, pressure, and quantity of other species held constant. Then the chemical potential can be related to the concentration of the species through the activity a by:

$$\mu_i = \mu_i^0 + RT \ln a_i \quad (\text{A.2-2})$$

where μ_i^0 is the reference chemical potential of species i at standard-state conditions. The activity of a species determined by its chemical nature and we will discuss a few that are most prevalent here. For an ideal gas $a_i = p_i / p^0$ where p_i is the partial pressure of the gas and p^0 is the standard-state pressure. In the case of a nonideal gas, a factor γ is multiplied to the partial pressure term where γ is a coefficient describing departure from ideality. For pure components such as a pure metal, water, or electrons in metal, $a_i = 1$.

So now with A.2-1 and A.2-2 we can calculate changes in the Gibbs free energy for changes in concentration of chemical species i by:

$$dG = \sum_i (\mu_i^0 + RT \ln a_i) dn_i \quad (\text{A.2-3})$$

To consider how this would influence a given reaction, consider the following arbitrary reaction:



Where the dotted lowercase coefficients show the number of moles of each species. This allows for to calculate the $\Delta\hat{g}$ on a molar basis from the various chemical species interacting:

$$\Delta\hat{g} = (\dot{c}\mu_C^0 + \dot{d}\mu_D^0) - (\dot{a}\mu_A^0 + \dot{b}\mu_B^0) + RT \ln \frac{a_C^{\dot{c}} a_D^{\dot{d}}}{a_A^{\dot{a}} a_B^{\dot{b}}} \quad (\text{A.2-5})$$

The first two terms here are equivalent to the standard-state molar free energy change of the reaction $\Delta\hat{g}^0$ so A.2-5 can be reduced to:

$$\Delta\hat{g} = \Delta\hat{g}^0 + RT \ln \frac{a_C^{\dot{c}} a_D^{\dot{d}}}{a_A^{\dot{a}} a_B^{\dot{b}}} \quad (\text{A.2-6})$$

Then using A.1-10 this can be put in terms of a reversible voltage:

$$E = E^0 + RT \ln \frac{a_C^{\dot{c}} a_D^{\dot{d}}}{a_A^{\dot{a}} a_B^{\dot{b}}} \quad (\text{A.2-7})$$

Which can be generalized for any arbitrary reaction to the form known as the Nernst Equation:

$$E = E^0 - \frac{RT}{nF} \ln \frac{\prod a_{products}^{v_i}}{\prod a_{reactants}^{v_i}} \quad (\text{A.2-8})$$

This form accounts for pressure effects but does not fully account for how the reversible voltage changes with temperature. A.2-8 is modified when moving to a temperature $T \neq T_0$ as:

$$E = E_T - \frac{RT}{nF} \ln \frac{\prod a_{products}^{v_i}}{\prod a_{reactants}^{v_i}} \quad (\text{A.2-9})$$

Where E_T is how the voltage changes with temperature. To understand how this changes briefly consider the differential expression for the Gibbs free energy:

$$dG = -SdT + Vdt \quad (\text{A.2-10})$$

from which we can see that:

$$\left(\frac{d(\Delta g)}{dT}\right)_P = -\Delta \hat{s} \quad (\text{A.2-11})$$

Then combining A.2-11 with A.1-10 we have:

$$\left(\frac{dE}{dT}\right)_P = \frac{\Delta \hat{s}}{nF} \quad (\text{A.2-12})$$

So at a given temperature T under constant temperature, we have a new reversible voltage:

$$E_T = E^0 + \frac{\Delta \hat{s}}{nF}(T - T_0) \quad (\text{A.2-13})$$

Thus, by combining A.2-9 and A.2-13, we have the full expression that can describes how the reversible cell voltage varies with pressure, activity, and temperature as:

$$E = E^0 + \Delta \frac{\hat{s}_{rxn}^0}{nF}(T - T_0) - \frac{RT}{nF} \ln \frac{\prod a_{products}^{v_i}}{\prod a_{reactants}^{v_i}} \quad (\text{A.2-14})$$

A.3 Overall Rate of Adsorption Reaction

Consider the adsorption reaction:



Given the relation with the Michaelis-Menten model¹⁰ we have the overall rate of the reaction as the product of the rate of conversion plus desorption times the number of molecules in state AS:

$$\frac{r}{A_s} = k_2 \theta = \frac{k_2 k_1 p}{1 + k_1 p} \quad (\text{A.3-2})$$

We show the Arrhenius dependence of k_2 with the activation energy for the conversion of A to B and with the desorption of B using a constant c_1 :

$$k_2 = c_1 e^{\frac{-E_a}{kT}} \quad (\text{A.3-3})$$

If the Brønsted relation applies, then the activation energy becomes:

$$E_a = a\Delta G_2 + b \quad (\text{A.3-4})$$

where a and b are positive constants. Since the total free energy difference for the conversion from A to B is independent of the catalyst the sum of the free energies of the steps to and from the catalyst equal the free energy of the net reaction. This makes A.3-4 expressed in terms of the binding free energy as:

$$E_a = a(\Delta G - \Delta G_1) + b = \text{constant} - a\Delta G_1 \quad (\text{A.3-5})$$

Which in turn makes A.3-3 into:

$$k_2 = c_2 e^{\frac{a\Delta G_1}{kT}} = c_2 K^{-a} \quad (\text{A.3-6})$$

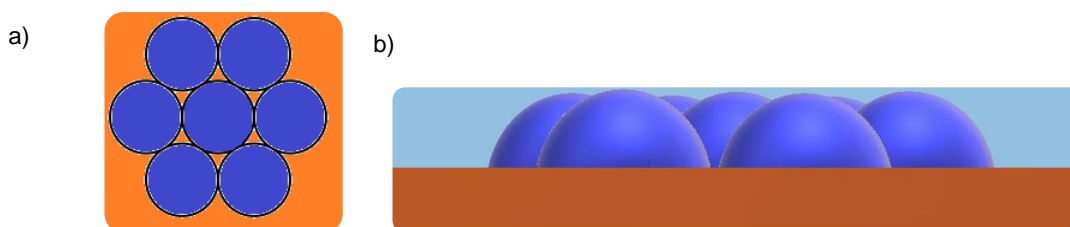
where $c_2 = c_1 e^{\frac{-a\Delta G-b}{kT}}$ is a constant that is independent of the binding rate constant. Combining A.30 with A.2-10 gives the overall rate of:

$$\frac{r}{A_s} = k_2 \theta = \frac{c_2 k_1^{1-a} p}{1+k_1 p} \quad (\text{A.3-7})$$

Appendix B Calculations

B.1 Theoretical Maximum Catalyst Surface Area for a Given Support

For a case example we will suppose hemispherical Ru particles are deposited onto an infinite support plane in a hexagonal close-packed manner. Appendix Figure B.1-1 depicts this model configuration for clarity.

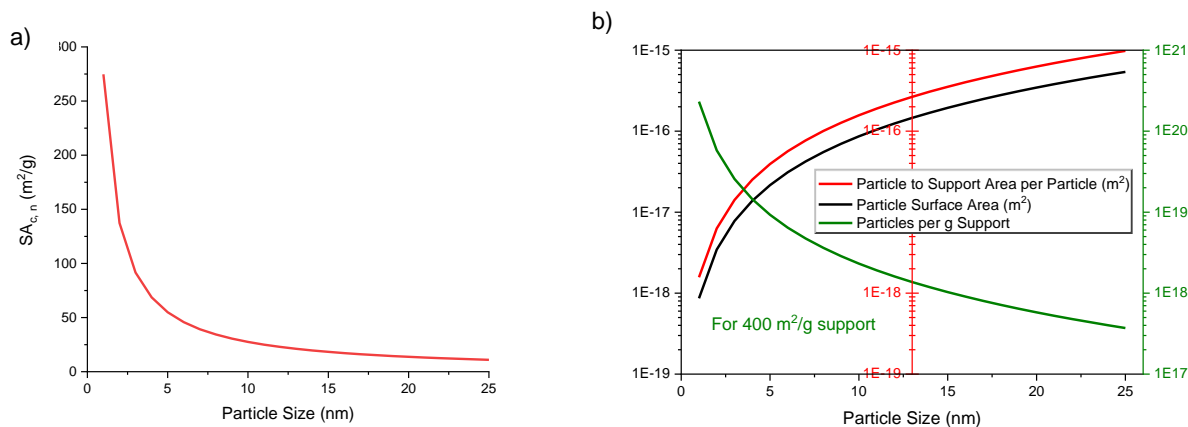


Appendix Figure B.1-1 a) Shows top-down view of hexagonal close-packed particles deposited onto infinite support plane. One hexagonal unit is depicted, but this unit is repeated across the whole support plane. b) Depicts the same situation as a), but from an in-plane view to highlight the hemispherical structure of model particles.

In this case, the particle-support contact area A_c is defined by the radius r of the particle and is the area of a circle. These hemispheres are assumed to be half spheres so the radius for the circle cross-section is the same as the radius for the particle. Since this is hexagonally close-packed, the 2-D packed fraction is ~ 0.91 . So this implies that the effective area taken by a particle A_{ec} is $\frac{1}{0.91} \pi r^2$. For half-sphere the surface area of a particle SA_p is $2\pi r^2$ and the volume V_p is $\frac{2}{3} \pi r^3$. This makes the mass per particle $M_p = V_p \rho$ where ρ is the catalyst bulk density. If the surface area of the support is SA_s then the max total particles that can be loaded on that surface $N_p = \frac{SA_s}{A_{ec}}$.

Typical support surface areas are normalized by weight of the support $SA_{s,n}$ (m^2/g). We can similarly normalize the max particle number $N_{p,n} = \frac{SA_{s,n}}{A_{ec}}$ and the max particle loading (weight of catalyst per weight of support) as $M_{p,n} = M_p N_{p,n}$. This allows us to obtain a few quantities of interest. Then we can for one obtain the normalized catalyst surface area, $SA_{c,n}$ (m^2/g_c) = SA_p/M_p . We can also get the normalized max catalyst surface area ($\frac{SA_c}{g_s}$): $MSA_{c,n} = SA_p N_{p,n}$. Then finally we can get the max weight fraction of a catalyst for a support: $\frac{Catalyst}{Support} = \frac{M_{p,n}}{M_{p,n+1}}$. Using this value we can obtain some quantities of interest.

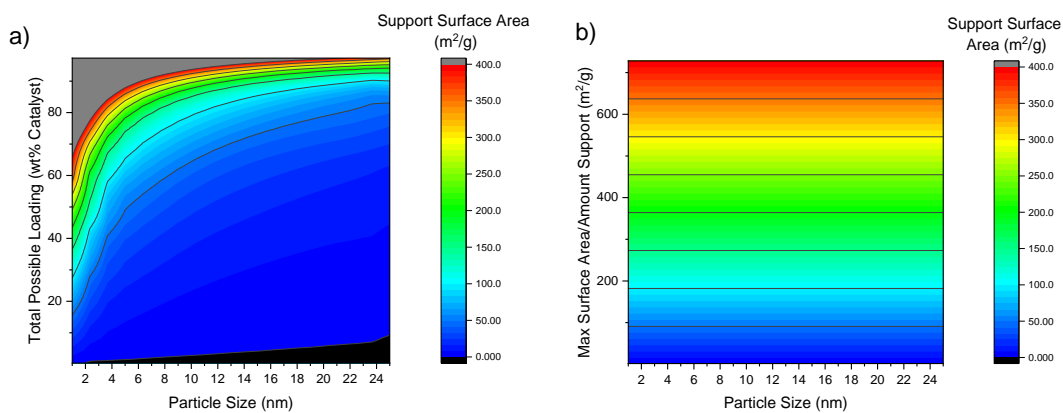
One quantity that should be pretty intuitive is that the surface area of the catalyst normalized is larger for smaller particles (due to the surface area to volume ratio). This can be readily seen in Appendix Figure B.1-2a that the $SA_{c,n}$ is proportional to $1/r$. Each individual particle increases its surface area exposed as the particle size is increased, but at a penalty to the support area consumed by a particle which leads to a decrease in the amount of particle per a given amount of support as can be seen in Appendix Figure B.1-2b.



Appendix Figure B.1-2 Particle size and surface area relations. a) shows the relationship between particle size and the amount of surface area per weight of catalyst. b) shows that area per particle increases with size, but at the cost of taking up more of the support and the max number of particle loading of the support decreases accordingly.

These combined together allow us to take a holistic view of catalyst loading by particle size. This view is depicted in Appendix Figure B.1-3a, which lets us draw a few conclusions. As might be expected higher surface area supports allow for higher weight fractions of catalysts to be loaded. Similarly, larger particle sizes allow for higher weight loadings onto supports. This leads to the interesting case shown in

Appendix Figure B.1-3b that if you fully load the catalyst onto a support, you will obtain the same exact surface area whatever the particles size is. This happens because larger particles area able to have higher equivalent weight loadings onto supports. So if fully loaded, then there isn't a difference what the particles size is for effective catalyst surface area, you can just obtain full loading with less catalyst for the smaller particles.



Appendix Figure B.1-3 a) Total possible weight fraction of catalyst loading for Ru on a support by catalyst particle size (in diameter) and by the support surface area. b) the max catalyst surface area per amount of a support achievable with different catalyst particle sizes and support surface areas.

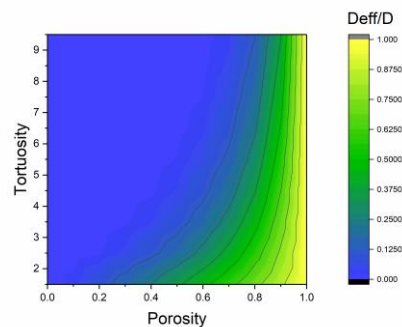
Of note here looking at Appendix Figure B.1-3a is that it is reasonable to assume that 60 wt% Ru/C is nearing maximum loading capacity given that the particle size is ~4 nm and that the estimated support area is around 200 m²/g. Larger particles would of course imply a higher required loading and similarly higher support surface areas would lead to higher required loadings.

B.2 Effect of Porosity and Tortuosity on Diffusivity

Increased porosity and decreased tortuous paths improve electrode reaction kinetics by increasing diffusivity of reactants by:

$$D^{eff} = D\varepsilon^\tau \quad (B.2-1)$$

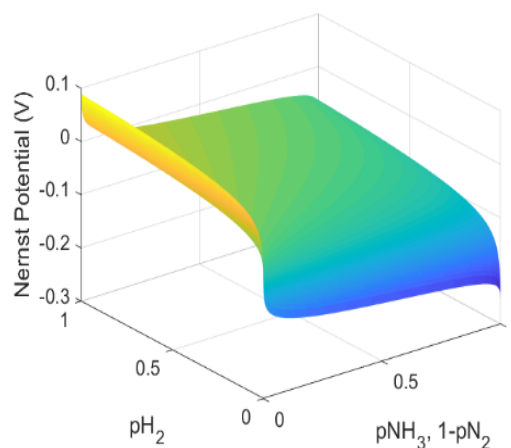
Where D is the diffusivity, D^{eff} is the effective diffusivity, ε is the porosity (i.e., the ratio of pore volume to total volume), and τ is the tortuosity (i.e., more mazelike means more tortuous) ranging from 1.5 to 10. This relationship can be seen in Appendix Figure B.2-1.



Appendix Figure B.2-1 Effect of porosity and tortuosity on effective diffusivity.

B.3 Thermodynamic Potential for Ammonia Decomposition System

In our system, hydrogen is supplied to the counter electrode and a mixture of ammonia and nitrogen are supplied to the working electrode. Based on Equation 1.2, we can see how in this scenario the Nernst potential would vary as a function of pH_2 and a balance between pNH_3 and pN_2 at 250°C (see Appendix Figure B.3-1). As one might expect, the potential becomes more favorable as the ammonia concentration increases and the hydrogen partial pressure decreases (negative Nernst potential here suggests a spontaneous reaction).



Appendix Figure B.3-1 Nernst potential as a function of gas partial pressures at 250 °C

For our situation we are considering the net reaction of ammonia decomposition to be:



where the oxidizing half-reaction at the anode is:



and the reducing half-reaction at the cathode is:



From NIST thermodynamic data⁸⁵, the free energy of the reaction at 523K is -7321 J/mol. By Equation 1.1 this gives a Nernst potential of:

$$E_{0,523K} = \frac{\Delta G_{rxn,523K}}{nF} = \frac{-7321 \text{ J/mol}}{3 \left(\frac{96485 \text{ C}}{\text{mol}} \right)} = -25.3 \text{ mV} \quad (B.3-4)$$

We can account for the reactant and product activities by incorporating our process conditions into Equation 1.2:

$$E_{523K} = E_{0,523K} + \frac{RT}{nF} \ln \left(\frac{p_{H_2}^{\frac{3}{2}}(\text{Cathode}) p_{N_2}^{\frac{1}{2}}(\text{Anode})}{p_{NH_3}(\text{Anode})} \right) = -25.3 \text{ mV} + \frac{8.31 \frac{\text{J}}{\text{mol K}} 523K}{3 \left(\frac{96485 \text{ C}}{\text{mol}} \right)} \ln \left(\frac{0.62^{\frac{3}{2}} 0.22^{\frac{1}{2}}}{0.4} \right) = -33.7 \text{ mV} \quad (B.3-5)$$

This, however, does not account for the impact on system pressure (since more moles of gas are generated than are input). From this reaction we can determine the equilibrium constant:

$$K = e^{\frac{-\Delta G_{rxn,523K}}{RT}} = e^{\frac{-7321 \frac{\text{J}}{\text{mol}}}{8.314 \frac{\text{J}}{\text{mol K}} (523K)}} = 5.386 \quad (B.3-6)$$

Using this equilibrium constant, we can see the impact on standard condition pressures:

$$K = \frac{p_{H_2}^{\frac{3}{2}} p_{N_2}^{\frac{1}{2}}}{p_{NH_3}} \Rightarrow p_{H_2}(\text{Anode}) = \left(\frac{K p_{NH_3}}{p_{N_2}^{\frac{1}{2}}} \right)^{\frac{2}{3}} = \left(\frac{5.386(0.4)}{0.216^{\frac{1}{2}}} \right)^{\frac{2}{3}} = 2.76 \text{ atm} \quad (B.3-7)$$

would already be on top of the water partial pressure not reacting applied to the counter electrode. Since we are operating in a free-flowing reactor, we do not expect a pressure to be able to build up and the reaction should be constrained to 1 atm of pressure.

From the stoichiometry of the reaction, if we have x moles of ammonia decomposing, then we have $1 - x$ moles of NH_3 , $\frac{3}{2}x$ moles of H_2 , and $\frac{1}{2}x$ moles of N_2 . This makes the total number of moles in the system to be:

$$n_T = 1 - x + \frac{3}{2}x + \frac{1}{2}x = 1 + x \quad (B.3-8)$$

The partial pressure p_i of any component i in the system is equal to its mol fraction times the total system pressure P :

$$p_i = \frac{n_i}{n_T} P \quad (\text{B.3-9})$$

This makes the partial pressures of each component of the reaction as:

$$pNH_3 = \frac{(1-x)P}{(1+x)} \quad (\text{B.3-10})$$

$$pH_2 = \frac{\frac{3}{2}xP}{(1+x)} \quad (\text{B.3-11})$$

$$pN_2 = \frac{\frac{3}{2}xP}{(1+x)} \quad (\text{B.3-12})$$

With these expressions, we can define K as:

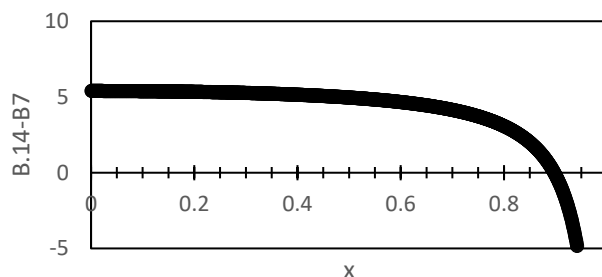
$$K = \frac{pH_2^{\frac{3}{2}} pN_2^{\frac{1}{2}}}{pNH_3} = \frac{\left(\frac{3}{2}xP\right)^{\frac{3}{2}} \left(\frac{3}{2}xP\right)^{\frac{1}{2}}}{\frac{(1-x)P}{(1+x)}} \quad (\text{B.3-13})$$

Since we already know K from B.3-6, we can solve for x numerically by finding what value of x makes the difference of K from B.3-13 and the K from B.3-6 zero. This is done in Appendix Figure B.3-2 which shows that $x=0.9$. This 90% conversion then gives a hydrogen partial pressure of:

$$pH_2(\text{Anode}) = pNH_3 * \%NH_3 \text{ converted} * \text{Hydrogen partial pressure converted} (P = 1 \text{ atm}) = 0.4 * 0.9 * 0.75 = 0.27 \text{ atm} \quad (\text{B.3-14})$$

This then gives an OCV based on the hydrogen concentration potential of:

$$E_{523K} = \frac{-RT}{nF} \ln\left(\frac{pH_2(\text{Anode})}{pH_2(\text{Cathode})}\right) = \frac{8.31 \frac{J}{\text{mol} \cdot K} 523K}{3 \left(\frac{96485 \text{ C}}{\text{mol}}\right)} \ln\left(\frac{0.27}{0.62}\right) = 18.7 \text{ mV} \quad (\text{B.3-15})$$



Appendix Figure B.3-2 K difference as a function of x

B.4 Efficiency calculation for ammonia decomposition for SAEC

The calculation is performed assuming the output to be the work available from the generated hydrogen, and the input to be the work available from the consumed (not supplied) ammonia as well as the heat required to raise the temperature of the consumed ammonia to the operating temperature and to drive the reaction. For the energy content of the fuels, the lower heating values are used. No recovery of heat from the generated H₂ and N₂ is presumed. Similarly, the energy cost of heating steam and excess (non-reacted) ammonia is not considered. Thus, for the reaction in Equation B.3-1, the efficiency is:

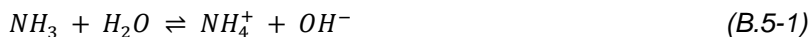
$$\varepsilon = \frac{3\Delta H_{H_2,LHV}}{2\left(\Delta H_{NH_3,LHV} + \int_{298}^{523} C_p(NH_3)dT + \Delta_{rxn}H\right) + 6FV} \quad (B.4-1)$$

where F is Faraday's constant. Because overpotential losses increase monotonically with increasing voltage (V) and no penalty is assigned for the need to recycle un-utilized NH₃, the efficiency monotonically decreases in this calculation with increasing voltage (or equivalently, current density).

B.5 Ammonia Detection in Cathode Exhaust

Since all gas exhaust was flown through a water trap after the cell, any gas passing through the cathode would be bubbled through the water trap at the cathode exhaust. Ammonia gas when bubbled through water easily forms ammonium hydroxide, so this water trap would be an effective way to tell if any ammonia gas was passing through the cathode gas stream (where the hydrogen is produced in the ammonia decomposition cell). This amount of ammonia in the water trap would only increase with time, so longer time scales allow for a greater detection capability. Greater concentrations of ammonia make the water in the trap raise in pH, so a pH strip could be used to detect the presence of ammonia. The pH strip makes a difference between 7 and 8 clearly visible, so a pH of 8 will be our detection threshold. The water at the exhaust was always measured before disposal to ensure ammonia was disposed of properly. The longest period that was measured with ammonia on stream was a period of 48 hours, so this was used for this measurement.

Ammonia in contact with water will take protons from water to yield ammonium and hydroxide ions:



The equilibrium constant K_b for this reaction is:

$$K_b = \frac{[NH_4^+][OH^-]}{[NH_3]} = 1.76E-5 \quad (B.5-2)$$

For the pH of a solution with ammonia to have a value of 8, this would imply that the concentration of ammonium and hydroxide ions would be $1E-6$. This means that the ammonia concentration equal to $5.68E-8$. In a 5 mL water trap, this would be $2.84E-7$ mL or $2.5E-7$ g of ammonia. This would translate to $2.5E-7$ g = $3.6E-4$ cc of ammonia at 25°C . Since this was performed over a period of 48 hours (or 2880 minutes), this means the flow rate would be $1.25E-7$ cc/min. Given that the exhaust flow rate is 50 sccm, this would translate to being able to detect $1.25E-7/50 = 2.5E-9$ or 2.5 ppb in the gas stream.

B.6 Cost of Ammonia Transport by Truck in a Given Area by Production Volume

To determine the cost of local ammonia distance by truck, one must know the rate for shipping (S_r) a given weight of ammonia (w in tons) a given distance (r in miles). Consulting industry experts, we determined this to be a rate of \$5 per mile on a truck carrying 21 tons of ammonia. This makes:

$$S_r = \$5r*w \quad (B.6-1)$$

One must also consider the amount of ammonia needed for a given area of land. We consider here wheat and corn crops which demand a relatively high amount of nitrogen fertilizer on the order of 220 lb per acre or 70.4 tons per square mile. Also, we must consider that a given area to serve has some fraction that is farmland which we will deem as f .

For this model we will consider shipping ammonia from a central point to every point within a radius of a circle R with evenly distributed farmland populated at a fraction f . The cost at a given distance is:

$$C(r) = \int_0^{2\pi} \int_0^r r dr d\theta S_r = \frac{10w\pi r^3}{63} \quad (B.6-2)$$

The radius per ton of ammonia is:

$$R = \sqrt{\frac{70.4w}{f\pi}} \quad (B.6-3)$$

Where A is the area of the circle with radius R , one can calculate the average cost per ton from shipping S_A by plugging B.6-3 into B.6-2:

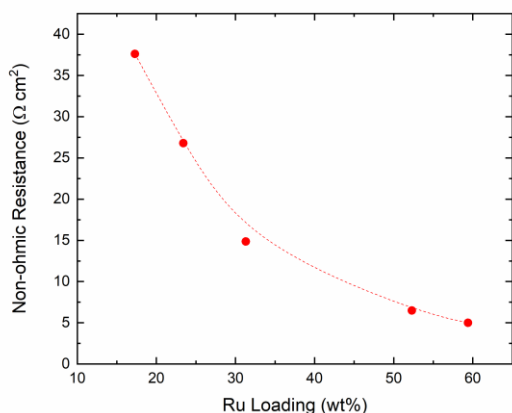
$$S_A = C(R)/A \quad (B.6-4)$$

Appendix C Auxiliary Experiments

C.1 Ceiling for Metal Loading on CNT

Ruthenium on multi-walled CNTs (NanoLab, >95% purity) with ~30 nm diameter was prepared using the ethylene glycol reduction method. The loading was determined in the TGA heating a sample of the catalyst material up to 800°C under air to combust the MWCNTs, switched to Ar to purge air from the TGA, and then reduced under 3% H₂. The remaining weight with the residual iron catalyst weight subtracted was used to determine the loadings displayed here.

Samples were electrochemically analyzed under a mixture of humidified nitrogen and dry ammonia at the working electrode (0.4 pNH₃, 0.3 pH₂O, bal. N₂) and humidified H₂ at the counter electrode (0.38 pH₂O) with a total gas flow rate of 50 sccm to each side. EIS was performed at OCV with a 20 mV amplitude from a range of 1 MHz to 0.1 Hz. Results shown in Appendix Figure C.1-1.



Appendix Figure C.1-1 Nonohmic resistance under ammonia for various Ru/MWCNT samples synthesized by the ethylene glycol method. Working electrode mixed with C:CDP ratio of 1:3 with a total mass of 50 mg in the electrode.

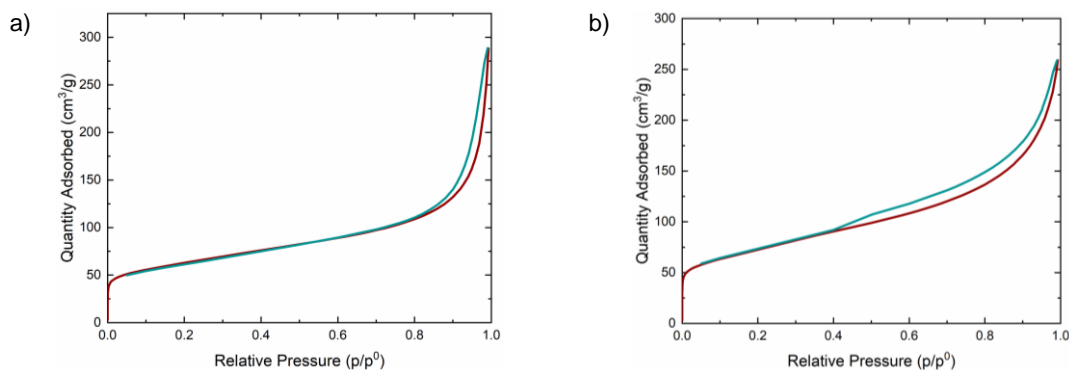
C.2 BET Method Analysis for Supports Implemented

The BET method was applied to get the surface area and structural characteristics of Vulcan XC-72 and Nanographite employed for the experiments herein. Measurements were carried out using a 3Flex instrument from Micrometrics with N₂ as the physisorption gas. A table of the results is shown in Appendix Table C.2-1 and relative pressure plots (Appendix Figure C.2-1) and incremental pore volume plots (Appendix Figure C.2-2) are shown subsequently. Briefly, both have high surface areas with nanographite having the highest surface area. Both have similar total pore volumes, but the Vulcan XC-72 has a peak in

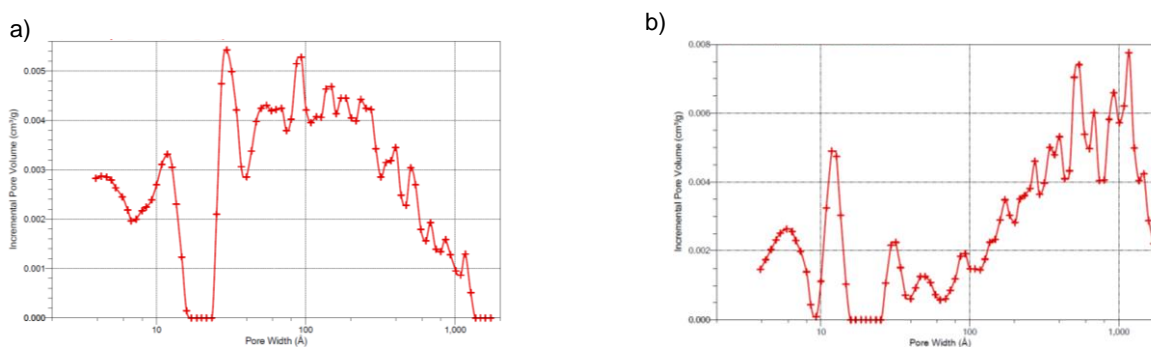
its pore distribution are the 10 nm length scale whereas the nanographite has a peak around the 100 nm length scale.

Appendix Table C.2-1 BET Analysis of Supports

Support	Surface Area (m ² /g)	Total Volume in Pores ≤ 1,720.79 Å (cm ³ /g)	Area in Pores > 1,720.79 Å (m ² /g)	Total Area in Pores ≥ 3.93 Å (m ² /g)
Vulcan XC-72	223.3 ± 0.3	0.22	63.7	186.6
Nanographite	256.8 ± 0.3	0.22	48.2	219.9



Appendix Figure C.2-1 BET method measurements for a) Vulcan XC-72 and b) nanographite. The maroon-colored line shows the absorption portion of the measurement while the teal-colored line shows the desorption portion.

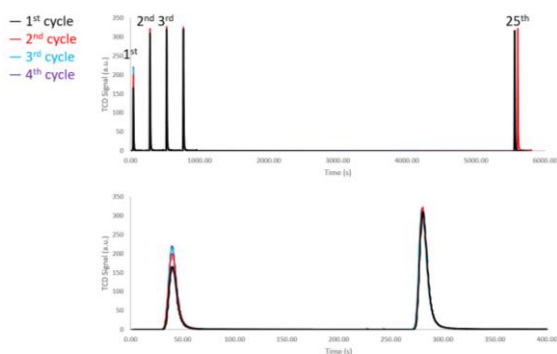


Appendix Figure C.2-2 Incremental pore volume plots for for a) Vulcan XC-72 and b) nanographite.

C.3 Pt/V Selective Chemisorption Experiment

Pt/Vulcan samples were tested in our AMI200 instrument equipped with a thermal conductivity detector (TCD). 30 mg of the sample was used for this experiment. In this experiment, the sample was heated to 350°C with a rate of 10°C/min and held isothermal for 1 hour in 10% H₂ in balance N₂ (certified analytical grade) flowing at 30 ml/min. Then, the sample was cooled to 40°C in pure He (UHP grade). Subsequently, 25 pulses of 5% CO in balance He (certified analytical grade) was dosed into the sample by using pure He (UHP grade) flowing at 30 ml/min (Pulse Chemisorption). Each pulse was monitored by using the TCD. The sample was purged with pure He at 40°C for an additional 30 minutes before the reactor bed temperature was ramped to 400°C with a rate of 10°C/min and held at 400°C for 30 minutes (TPD). This step was also monitored with the TCD. Finally, the sample was cooled to 40°C in flowing He. The chemisorption TPD, and cooldown was a cycle which was repeated four times. For the last cycle, in step 4), final temperature was set to 550°C instead. The pulsed chemisorption experiments are shown in

Appendix Figure C.3-1, the TPD experiments are inconclusive to low signal likely due to low sampling so are not shown here, and the results are tabulated in Appendix Table C.3-1 along with some calculation notes.



Appendix Figure C.3-1 Results of selective chemisorption experiment for 74 wt% Pt/V showing CO uptake by differential TCD signal.

Appendix Table C.3-1 Pt/V Chemisorption Calculation Details

Cycle	1 st	2 nd	3 rd	4 th
moles CO adsorbed	0.64E-6	0.44E-6	0.41E-6	0.40E-6
^A moles Pt surface	0.64E-6	0.44E-6	0.41E-6	0.40E-6
# of Pt atoms (Pulse)	3.87E+17	2.67E+17	2.46E+17	2.39E+17
Pt surface area (nm ²)	3.00E+16	2.07E+16	1.91E+16	1.85E+16
Pt surface area (m ² /g total)	1.00E+00	6.91E-01	6.36E-01	6.18E-01
# of Pt atoms (Loading)	1.85E+19	1.85E+19	1.85E+19	1.85E+19
Volume (nm ³)	2.63E+17	2.63E+17	2.63E+17	2.63E+17
^B Particle size (nm)	26.3	38.1	41.4	42.6
^C Adjusted size (nm)	13.1	19.0	20.7	21.3

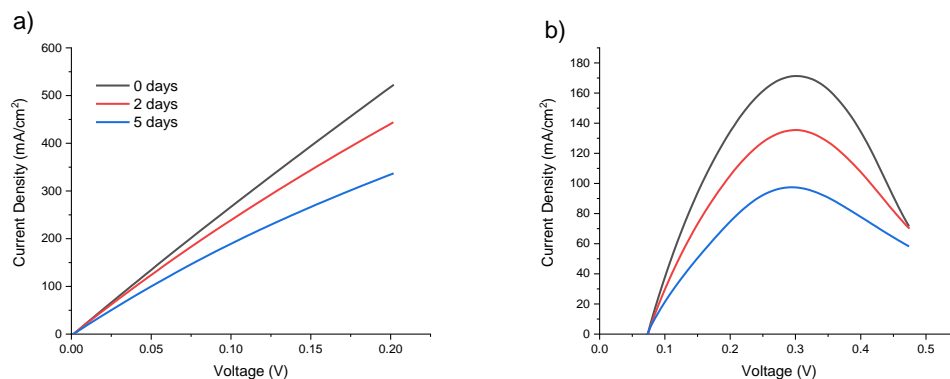
^A assuming a CO to Pt ratio of 1 (Pt typically doesn't deviate from this).

^B a spherical model with planar and bulk packing densities of 12.9 per nm² and 70.3 per nm³ are used based on a FCC unit cell along (111), (100) and (110) planes averaged and Pt atomic radius of 0.136 nm. Individual surface packing densities are 15.6, 13.5 and 9.6 per nm² along the (111), (100) and (110) planes, respectively.

^C further assuming particles are half-embedded in the (Vulcan) substrate.

C.4 Ru Ambient Condition Degradation

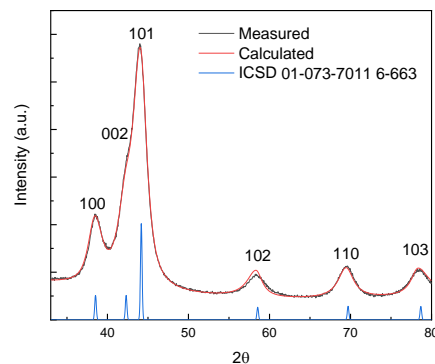
60 wt% Ru/V was synthesized using the NaBH₄ reduction method and three cells were fabricated with standard anode half-cells. On-top of these cells were placed electrodes containing 50 mg of 60 wt% Ru/V mixed with CDP in a C:CDP ratio of 1:9. These cells were left in an ambient condition desiccator for 0, 2, and 5 days after fabrication. Longer wait times correlated with increased resistance for HOR for both the hydrogen and dilute hydrogen conditions. Data for this is shown in Appendix Figure C.4-1.



Appendix Figure C.4-1 Polarization curves of HOR for 60 wt% Ru/V after cell waiting for a variable amount of days under ambient condition under a) the hydrogen condition and b) the dilute hydrogen condition. Scan rates for polarization measurements here were 10 mV/s.

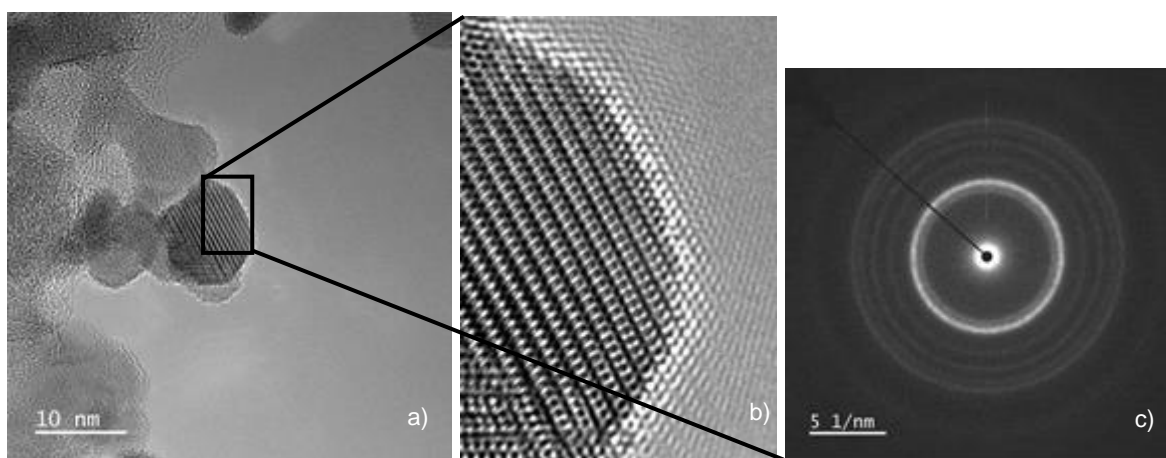
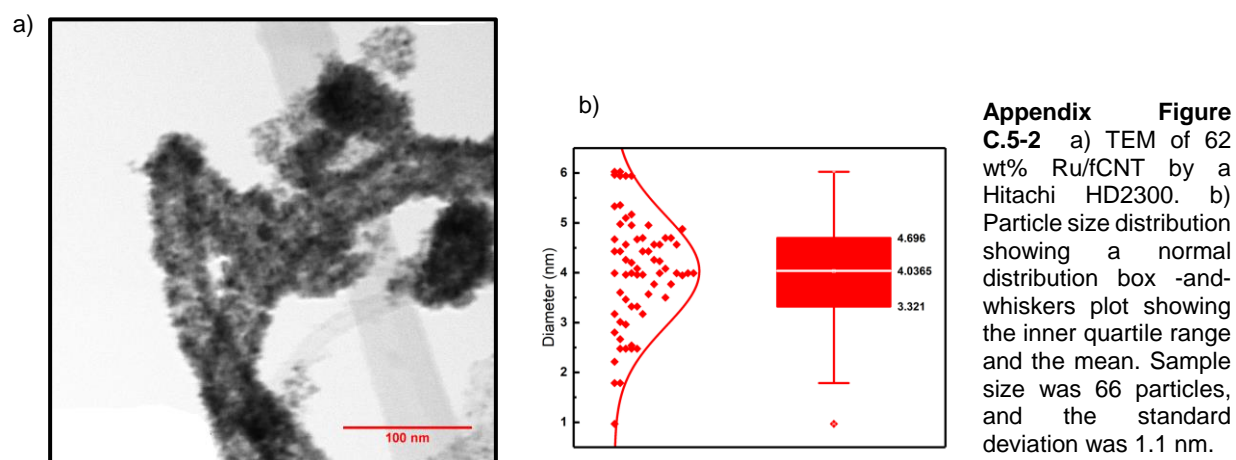
C.5 Probing the Oxidation State of In-house synthesized Ru

60-62 wt% Ru/C routinely investigated by XRD would reveal ~4 nm Ru (HCP) without any suggestion of another present crystalline phase (For example, see Appendix Figure C.5-1). Investigation by TEM was able to confirm that the crystallite size implied by XRD analysis also corresponds to the nanoparticle diameter (see Appendix Figure C.5-2). Using an aberration-corrected TEM and analyzing the surface of Ru/nGr particles showed perfectly crystalline surfaces and similarly TEM



Appendix Figure C.5-1 XRD of 62 wt% Ru/fCNT (COOH) showing single phase HCP Ru with a 4 nm crystallite size.

diffraction revealed the single present Ru (FCC) phase without a presence of a so-called “amorphous halo” (see Appendix Figure C.5-3).



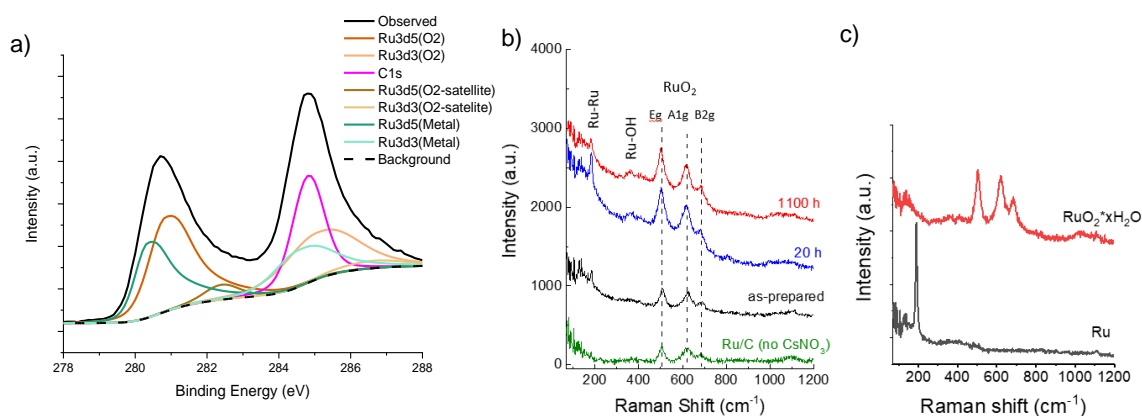
Appendix Figure C.5-3 a) TEM image of 40%Ru/nGr + CsNO₃ (Cs:Ru 0.5:1) after 1100h of operation provided by SAFCCell. b) Shows a zoomed in image of a) highlighting a particle edge. c) TEM diffraction pattern showing the clear single phase crystallinity for HCP Ru. Instrument used was a JEOL ARM200CF.

Additionally, bare Ru was synthesized without a carbon support. This was analyzed via TGA analysis (Netzsch STA 443). The idea for this experiment would be to get a very accurate initial weight and then purposefully oxidize the Ru by heating in air. This should go up to a certain level depending on the phase formed (presumably RuO₂). Subsequently, the Ru could then be reduced under H₂ again. If the sample had no oxide on the surface, then presumably this would return exactly to the original measured mass. This effect would be expected to be pronounced as the particle size is still very small (~4 nm in the unsupported case). Results for this experiment are shown in Appendix Figure C.5-4. The mass not

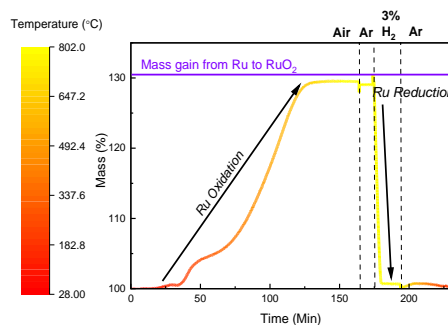
increasing to the theoretical weight gain from Ru to RuO₂ leaves a possibility of some of the Ru being previously oxidized, though we would expect in the reduction step in that case for the weight of the Ru to drop below the initial. This suggests that the background noise is too high to examine this phenomenon (unless there is something preventing full oxidation/reduction) and that if there is an amount of ruthenium oxide on the surface, it is a very small amount.

Surface analysis techniques were then applied that were highly suggestive of the presence of an oxide. First, XPS analysis of the 3d_{5/2} and 3d_{3/2} binding energies were suggestive of a combination of metallic Ru and RuO₂ to be able to obtain the results achieved (Appendix Figure C.5-5a). Additionally, Raman spectroscopy of the Ru/C compared with metallic and oxidized Ru standards suggests the presence of both the metallic and oxidized Ru (Appendix Figure C.5-5b and Appendix Figure C.5-5c).

This suggests that perhaps the TEM itself was reducing the sample before the images were taken,



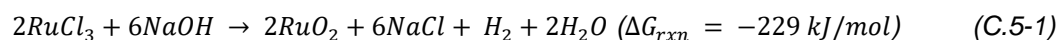
Appendix Figure C.5-5 a) XPS of 40 wt% Ru/nGr and CsNO₃ (Cs:Ru 0.5:1) with Ru and RuO₂ peaks fit (Thermo Scientific ESCALAB 250 Xi). b) Raman spectra of 40 wt% Ru/nGr and 40 wt% Ru/nGr with CsNO₃ (Cs:Ru 0.5:1) under various operation times. c) Raman spectra of standard metallic and oxidized Ru samples. Raman spectra collected on SPID Horiba LabRam Confocal Raman.



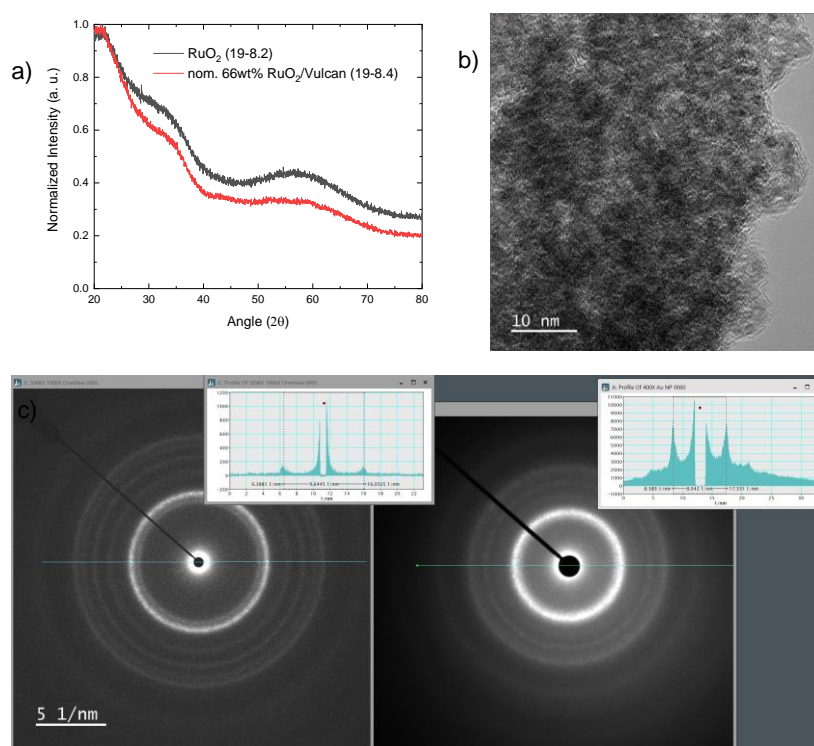
Appendix Figure C.5-4 10 mg of Ru nanoparticles heated analyzed by TGA being oxidized under air and then reduced in 3% H₂ bal Ar. Pure Ar was used between steps to avoid mixing oxidizing and reducing gases. Purple reference line suggests the mass gain if original sample was pure Ru being fully oxidized to RuO₂.

hiding the original oxidized state of the Ru surface. To try to probe this hypothesis, an amorphous RuOH/V

was synthesized. By thermodynamic calculations performed using HSC it was determined that RuCl_3 could be converted to RuO_2 by the addition of NaOH or KOH. For example, for the NaOH case we have:



For this synthesis, $\text{RuCl}_3 \cdot X\text{H}_2\text{O}$ ($X \sim 5$) and Vulcan XC-72 are added to a beaker with deionized water and the solution is sonicated for five minutes. Then KOH was added to the solution until the pH reached ~ 9 by pH strip determination. This was then allowed to stir for 24 hours. After this, the solution became clear. This solution was then centrifuged and rinsed with deionized water three times. XRD analysis afterwards revealed an amorphous structure (See Appendix Figure C.5-6a). TEM analysis of this sample showed a partially crystalline structure that had an amorphous halo with diffraction, that was getting increasingly crystalline as the probing of the sample continued. The crystalline structure was for HCP Ru (Appendix Figure C.5-6b and Appendix Figure C.5-6c). This confirmed that the TEM analysis itself can

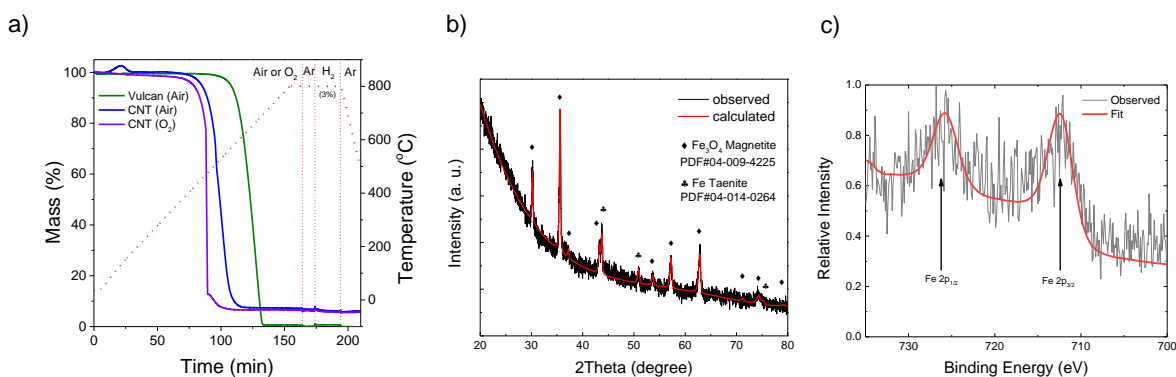


Appendix Figure C.5-6 a) XRD analysis of bare synthesized RuO_2 and RuO_2 on Vulcan XC-72 (Rigaku Ultima). b) TEM image of RuO_2 on Vulcan. c) TEM Diffraction pattern of 40 wt% Ru/nGr (left) compared to 66 wt% RuO_2 /V (right). Insets show intensity along line drawn. TEM on JEOL ARM200CF.

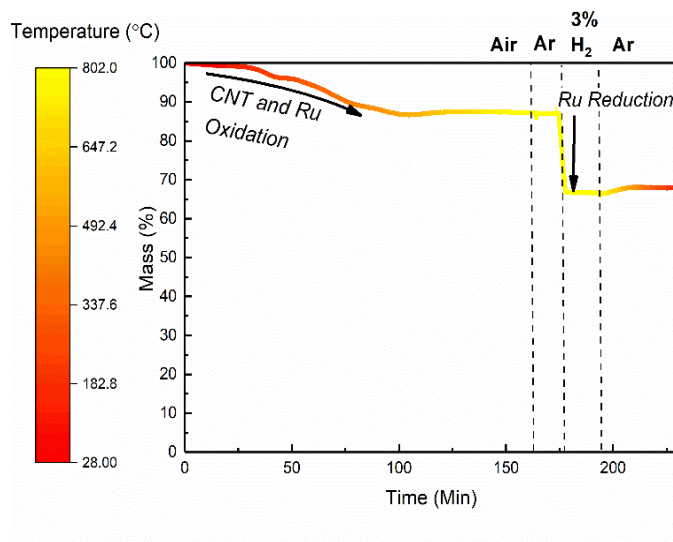
reduce amorphous oxidized Ru and thus TEM analysis alone cannot determine if an oxide layer on the surface of the Ru nanoparticles can exist.

C.6 Ru Loading Determination by TGA

Ru loading was determined by oxidizing the carbon support away at high temperature under air and then reducing the sample under 3% H₂. Separate TGA measurements confirmed the removal of carbon upon heating up under oxidizing conditions (see Appendix Figure C.6-1a). For CNT samples, it is apparent that there was residual iron that was in the samples, supposedly as catalysts for the CNT production. Identity was confirmed by XRD and XPS (see Appendix Figure C.6-1b and Appendix Figure C.6-1c). After this determination it was possible to carry out the oxidation to reduction experiment to determine the loading of Ru/C (Appendix Figure C.6-2).



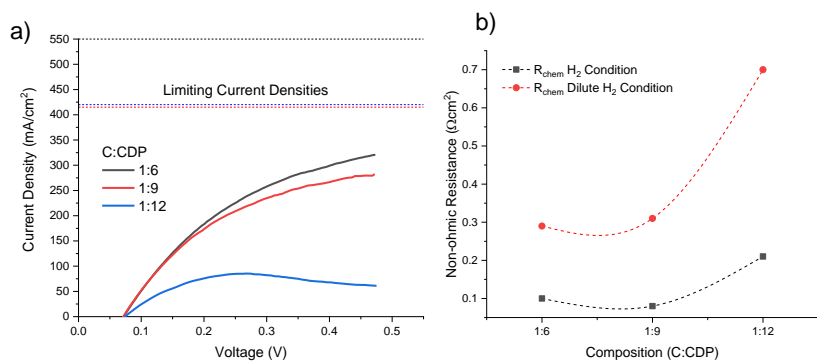
Appendix Figure C.6-1. a) TGA analysis of carbon supports determining at what temperature they are completely oxidized (Netzsch STA 443). b) XRD (STADI P) and XPS (Thermo Scientific ESCALAB 250 Xi) of residual powder after TGA experiment showing largely residual Fe₃O₄.



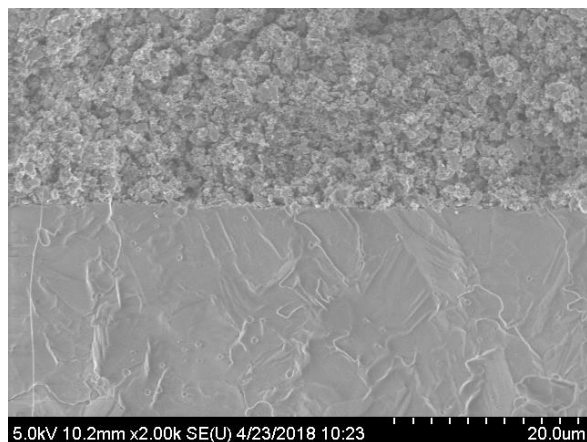
Appendix Figure C.6-2 10 mg of Ru/fCNT-COOH heated analyzed by TGA being oxidized under air and then reduced in 3%H₂ bal Ar. Pure Ar was used between steps to avoid mixing oxidizing and reducing gases.

C.7 Optimizing C:CDP ratio on Vulcan XC-72

To optimize the C:CDP ratio on Vulcan XC-72, catalyst powder of 51 wt% Ru 11 wt% Pt/V co-deposited by NaBH₄ reduction was employed. Cells were constructed in the typical manner with standard anode half-cell counter electrodes and 50 mg of this working electrode of interest. Results are shown in Appendix Figure C.7-1 below.



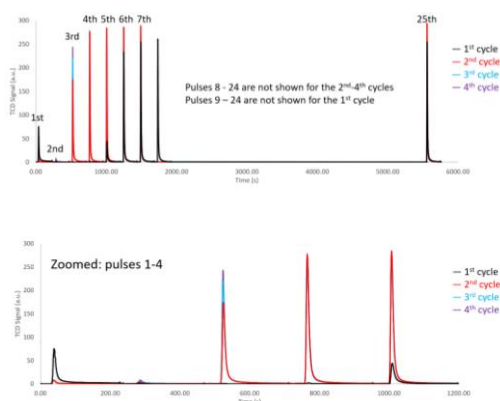
Appendix Figure C.7-1 Ru₉Pt₁/V cells with various C:CDP ratios. a) polarization curves under the dilute hydrogen condition. Limiting current densities reference lines refer to the maximum amount of current possible from the hydrogen supplied to the working electrode. b) Non-ohmic resistances of cells under hydrogen and dilute hydrogen conditions obtained by EIS at OCV.



Appendix Figure C.7-2 Post-operation cell cross-section for 50 mg 60 wt% Ru/V cell with 1:9 C:CDP with SEM (Hitachi SU 8030). Top is anode, bottom is electrolyte.

Cell cross-sections of Vulcan supported electrodes after their operation were shown to be quite uniform and had high-porosity electrodes. Such a cross-section is shown in Appendix Figure C.7-2.

C.8 Ru/V Selective Chemisorption Experiment



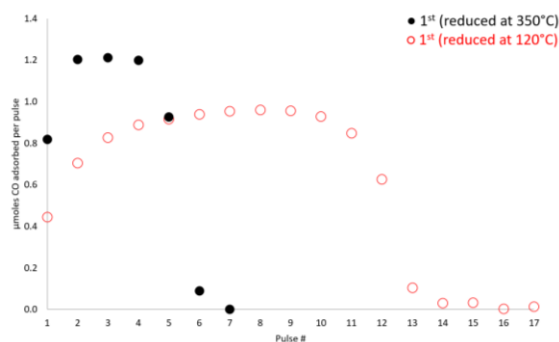
Appendix Figure C.8-1 Results of selective chemisorption experiment for 60 wt% Ru/V showing CO uptake by differential TCD signal for the 350 °C prereluction case.

Ru/Vulcan samples were tested in our AMI200 instrument equipped with a thermal conductivity detector (TCD). 45 mg of the sample was used for this experiment. In this experiment, the sample was heated to 350°C (120°C in a second experiment) with a rate of 10°C/min and held isothermal for one hour in 10% H₂ in balance N₂ (certified analytical grade) flowing at 30 ml/min. Then, the sample was cooled to 40°C in pure He (UHP grade).

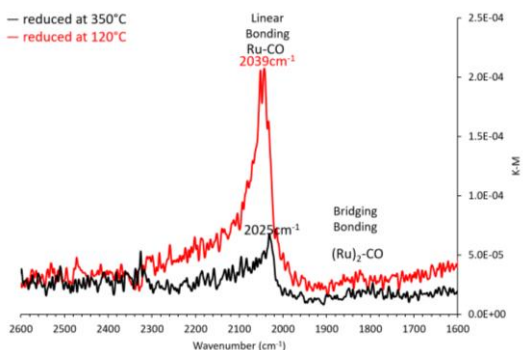
Subsequently, 25 pulses of 5% CO in balance He (certified analytical grade) was dosed into the sample by using pure He (UHP grade) flowing at 30 ml/min (Pulse Chemisorption). Each pulse was monitored by using the TCD. The sample was purged with pure He at 40°C for an additional 30 minutes before the reactor bed temperature was ramped to 400°C with a rate of 10°C/min and held at 400°C for 30 minutes (TPD). This step was also monitored with the TCD. Finally, the sample was cooled to 40°C in flowing He. The chemisorption TPD, and cooldown was a cycle which was repeated four times. For the last cycle, in step 4), final temperature was set to 550°C instead (see Appendix Figure C.8-1).

These CO pulse uptakes can then be calculated to determine an amount of CO adsorbed over those pulses, which is shown in Appendix Figure C.8-2 in which it can be seen that lower pre-experiment reduction temperatures leads to higher overall amounts of CO adsorbed. To convert the amount of CO adsorbed to surface area, how the CO is bonding to the Ru must be determined. This was done by a DRIFTS

experiment with CO which revealed that the Ru bonding in this case was linear like in the Pt case so that the CO:Ru ratio is 1:1 (See Appendix Figure C.8-3). With this information, the results are calculated in Appendix Table C.8-1 along with some notes on the calculations.



Appendix Figure C.8-2 Amount of CO adsorbed per pulse for both prereluction conditions.



Appendix Figure C.8-3 CO-DRIFTS experiment for 60 wt% Ru/V. For both the spectra, the peaks are assigned to atop CO on metallic Ru sites. The peak maximum for the sample reduced at 120 °C is 2039 cm⁻¹. For the sample reduced at 350 °C, the peak maximum is red shifted to 2025 cm⁻¹, indicating stronger CO binding. Oxidized Ru-CO bond would be greater than 2100 cm⁻¹.

Appendix Table C.8-1 Ru/V Chemisorption Calculation Details

Cycle	1 st	2 nd	3 rd	4 th	1 st	2 nd
	(350 °C)	(350 °C)	(350 °C)	(350 °C)	(120 °C)	(400 °C)
moles CO adsorbed	5.44E-6	2.90E-6	2.67E-6	2.61E-6	10.16E-6	2.26E-6
^A moles Ru surface	5.44E-6	2.90E-6	2.67E-6	2.61E-6	10.16E-6	2.26E-6
# of Ru atoms (Pulse)	3.28E+18	1.74E+18	1.61E+18	1.57E+18	6.12E+18	1.36E+18
Ru surface area (nm ²)	3.39E+17	1.80E+17	1.66E+17	1.63E+17	6.33E+17	1.41E+17
Ru surface area (m ² /g total)	7.53E+00	4.00E+00	3.69E+00	3.62E+00	1.41E+01	3.13E+00

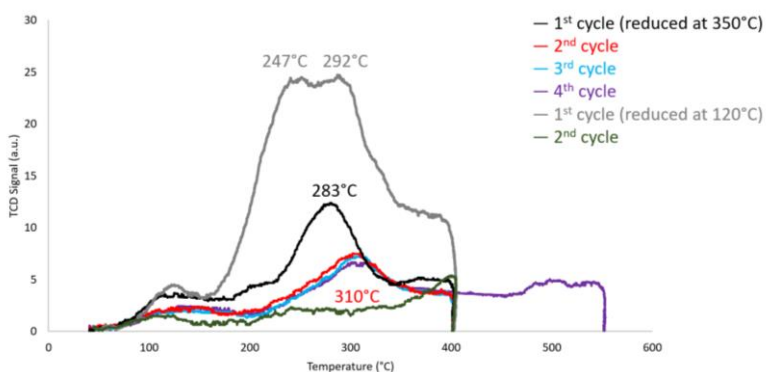
# of Ru atoms (Loading)	5.36E+19	5.36E+19	5.36E+19	5.36E+19	5.36E+19	5.36E+19
Volume (nm ³)	9.44E+17	9.44E+17	9.44E+17	9.44E+17	9.44E+17	9.44E+17
^B Particle size (nm)	8.356	15.712	17.048	17.400	4.476	20.111
^C Adjusted size (nm)	4.178	7.856	8.532	8.700	2.238	10.056

^A assuming a CO to Ru ratio of 1 per CO/DRIFT experiment results.

^B a spherical model with planar and bulk packing densities of 9.7 per nm² and 56.8 per nm³ are used based on an HCP unit cell along (0001), (10-10) and (11-20) planes averaged and Ru atomic radius of 0.146 nm. Individual surface packing densities are 13.5, 7.2 and 8.3 per nm² along the (0001), (10-10) and (11-20) planes, respectively.

^C further assuming particles are half-embedded in the (Vulcan) substrate.

Additionally, a temperature programmed desorption experiment of CO was performed and is shown in Appendix Figure C.8-4. The peak maximum for the 1st cycle (sample reduced at 350°C) is about 280°C. For the subsequent cycles, the peak maximum is shifted to about 310°C. For the 1st cycle (sample reduced



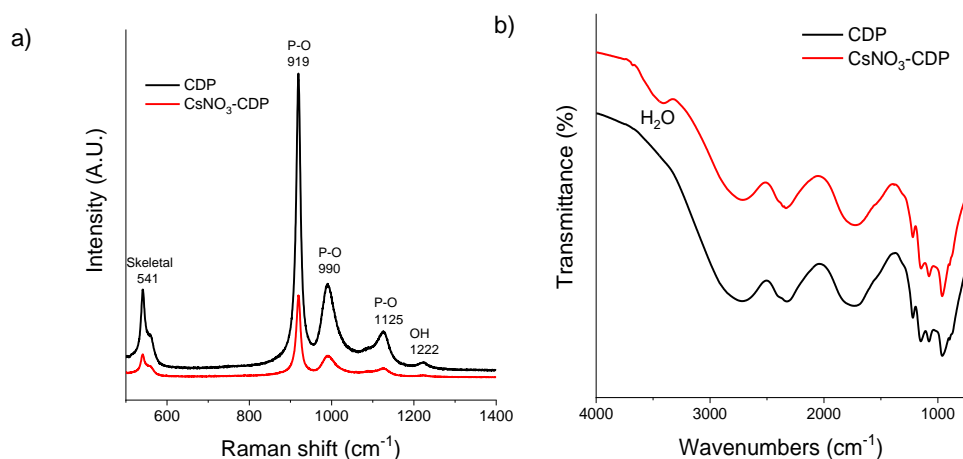
Appendix Figure C.8-4 TPD experiment of CO for all cycles considered for the 60 wt% Ru/V selective chemisorption experiment.

at 120°C), a doublet is observed. The peak to the higher temperature is likely due to the decomposition/degassing of the substrate, the oxidation of CO, or any combination thereof. The peak to the lower temperature is likely due to the desorption of CO on metallic Ru sites, in agreement with the CO probed DRIFT studies (*vide supra*).

C.9 Incorporating CsNO₃ into CDP

As mentioned in Chapter 4, there were attempts to directly incorporate CsNO₃ into CDP in the hopes of directly promoting ammonia oxidation in the electrochemical portion of the cell. SAFCell supplied Northwestern with 10 mol% CsNO₃-CDP to characterize through X-ray diffraction and spectroscopic methods.

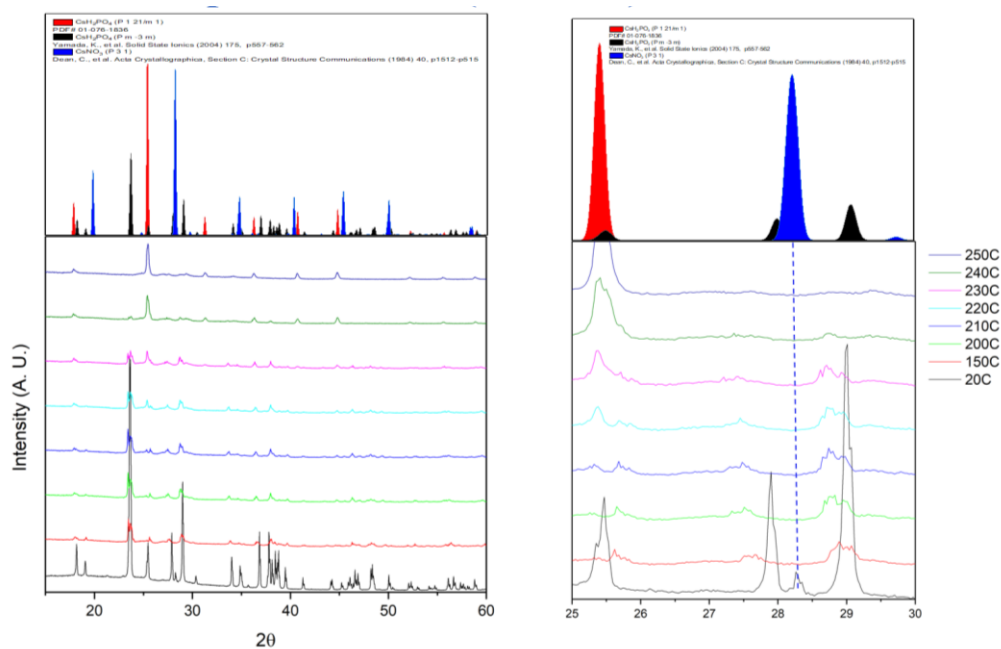
Raman spectroscopic analysis of the nitrate-doped CDP revealed little difference relative to



Appendix Figure C.9-1 a) Raman analysis of the CsNO₃-doped and undoped CDP. Three scans were performed with a 532 nm laser at 50mW and a 10% filter applied (HORIBA LabRAM HR Evolution Confocal RAMAN). b) FT-IR analysis of the CsNO₃-doped and undoped CDP. 64 scans were performed in the diffuse reflection mode (Thermo Nicolet, iS50).

undoped CDP aside from a decrease in observed peak intensity relative to the background (see Appendix Figure C.9-1a). Peaks were matched with reference peaks for CDP^{158,159}. Similarly, DRIFTS analysis of the nitrate-doped CDP showed little difference aside from the presence of a peak that was attributed to the presence of surface water (see Appendix Figure C.9-1b).

The sample was also analyzed using in-situ XRD on a Rigaku Ultima with a modified setup to allow for diffraction under a humidified condition (see Appendix Figure C.9-2). The single point of evidence pointing towards the presence of CsNO₃ is revealed in the room temperature pattern where an apparent CsNO₃ peak exists at 28.3° 2θ. Upon heating, this peak quickly vanishes and there is no further evidence of the CsNO₃. The peaks for the CsH₂PO₄ phases also do not shift, suggesting that the CsNO₃ is not incorporating into the CDP lattice. This suggests CsNO₃ is existing in some amorphous form.

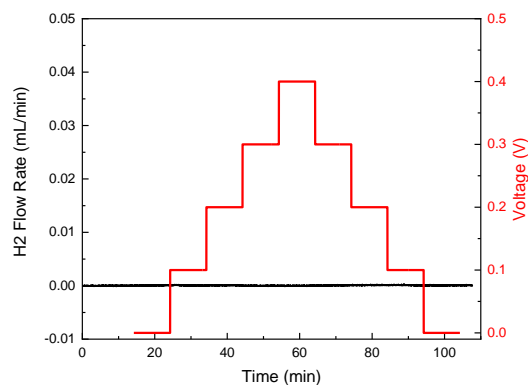


Appendix Figure C.9-2 In-situ XRD under a humidified condition of CsNO_3 -doped CDP. Reference spectra with sources shown on the top.

C.10 In-Operando Mass Spectrometry Tests for Ammonia Decomposition Cell

To measure the gas compositions from both exhaust streams of the ammonia decomposition, a mass spectrometer (MS) was used (Thermostar Pfeiffer GSD 301 T2) directly connected to the exhaust of the in-operation cell. Calibrations for H₂ concentration were performed from a system connected in parallel with the MS that could sample a range of hydrogen concentrations by mixing Ar and H₂. Gas flow rates at each exhaust line were doubled to 100 sccm for the purposes of these measurements.

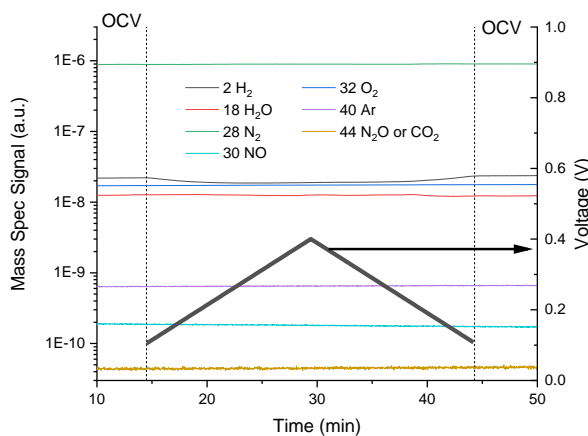
The first measurement to be considered was the possibility of non-faradaic efficiency arising from the hydrogen being sourced from water split on the anode side. To test this, humidified N₂ (0.38 p_{H₂O}) was supplied to both sides of the cell and increasing oxidizing bias was applied at the working electrode while the exhaust from the cathode was being directed to the mass spectrometer. The results of this test (shown in Appendix Figure C.10-1) reveal that no appreciable level of H₂ was generated under oxidizing potentials up to 0.4V across the cell from the H₂O alone.



Appendix Figure C.10-1 Hydrogen flow rate as determined by the MS from the cathode exhaust of the ammonia decomposition cell under a symmetric nitrogen environment and oxidizing potentials applied across the cell.

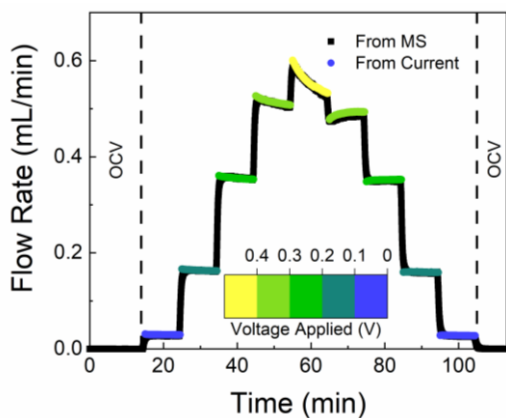
A second possibility that was explored was the possibility that ammonia was being oxidized to a form of NO_x whenever being subjected to an oxidizing bias in the presence of H₂O. To test this, the exhaust of the anode under the 0.4 pNH₃ condition was measured while steps of oxidizing potential were applied (see Appendix Figure C.10-2). These measurements clearly showed that no detectable level of NO or N₂O was formed. It is also clear from this measurement that at OCV, there is hydrogen that is formed and is shuttled away (to the cathode) upon applying oxidizing potentials.

Finally, the amount of H₂ in the cathode exhaust was measured while the cell was under the 0.4 pNH₃ condition. Even small amounts of H₂ in the baseline gas stream could harm the calibration process



Appendix Figure C.10-2 Time evolution of mass spectrometry signals of relevant species in the gas evolved from the anode upon changing the cell voltage at a sweep rate of 0.33 mV/sec. Due to experimental limitations, detection of NO_2 (amu 46) was not undertaken. Test was performed under the 0.4 pNH₃.

for the MS measurement, so humidified nitrogen was supplied to the counter electrode instead of H₂ as was typical in the rest of the measurements. The results (shown in Appendix Figure C.10-3) show that the amount of hydrogen implied from 100% faradaic efficiency in the current corresponds exactly with the amount of hydrogen measured from the MS.

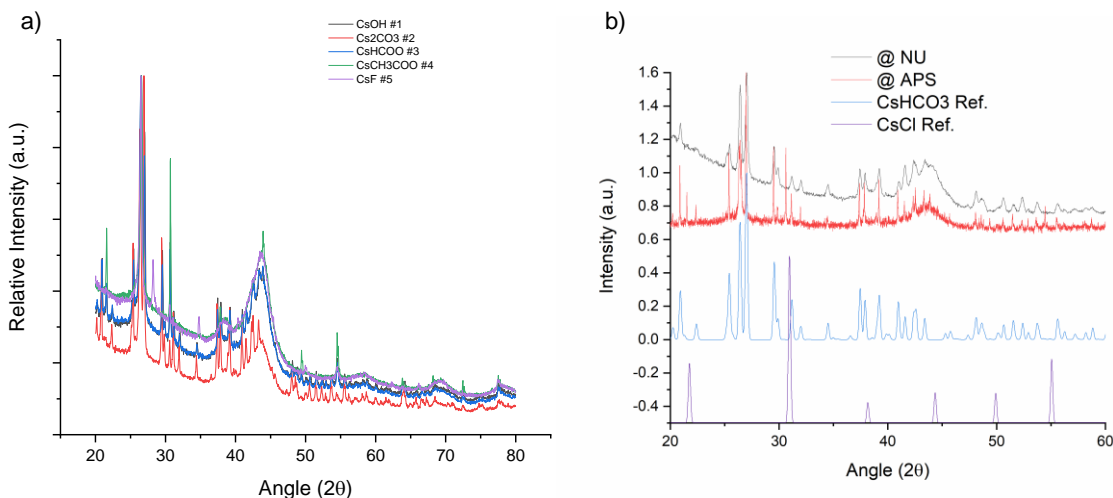


Appendix Figure C.10-3 Hydrogen flow rate as determined by the MS and as implied from the cathode exhaust of the ammonia decomposition cell with oxidizing potentials applied across the cell. This test was performed under the 0.4 pNH₃ condition.

C.11 Investigating Different Cs Promoters and Cs as an Anion Snatcher

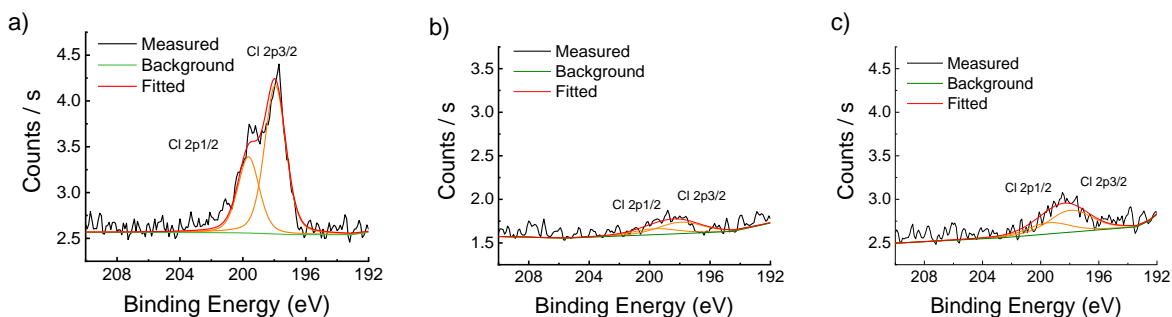
In primary exploration of the promotion phenomenon, several Cs containing compounds were explored in addition to the standard CsNO_3 including: CsOH , Cs_2CO_3 , CsHCOO , CsCH_3COO , and CsF . Results from SAFCell suggested that the above-mentioned promoters were successful at improving reaction rate while CsBr , CsI , CsCl , CsClO_4 were not. HSC calculations were performed to assess each promoter's stability in reducing conditions aside from CsHCOO whose thermodynamic data was not in the HSC database. These calculations suggested that most catalysts were stable aside from cesium acetate which is predicted to decompose into cesium carbonate with carbon and cesium perchlorate which is predicted to decompose into cesium chloride.

XRD analysis of the "successful promoters" was performed on promoted catalyst systems provided by SAFCell where all promoters were deposited by incipient wetness impregnation with a Cs:Ru ratio of 0.5:1 on 40 wt% Ru/nGr (see Appendix Figure C.11-a). The cesium fluoride sample was the only sample to show solely the deposited phase represented. The cesium acetate sample's diffraction pattern revealed a cesium chloride pattern. Presumably, there was remnant chloride leftover from the sodium borohydride reduction process with the ruthenium chloride precursor carried out at SAFCell. The remaining patterns were largely identical but were unable to be matched to any known phase of a Cs-containing compound with any combination of H, C, O, and/or N. To investigate further, high resolution diffraction was performed at the Advanced Photon Source (APS) at Argonne, using 20 keV X-rays. The studies reveal that the previously unidentified phase (obtained from CsOH -promoted and CsCO_3 -promoted 40 wt% Ru@nGr with Cs:RU = 0.5:1 molar ratio) is CsHCO_3 , cesium bicarbonate (in addition to the presence of CsCl) (see Appendix Figure C.11-b).



Appendix Figure C.11-1 a) XRD of “successful” promoters as prepared from SAFCell (Rigaku Ultima IV). b) High resolution diffraction (20 keV synchrotron) of CsOH promoted sample compared to CsOH pattern collected at NU and relevant reference patterns. The cesium carbonate sample was also tested and produced an identical pattern. Here, angle is translated to equivalent angle of Cu K α radiation for comparison purposes.

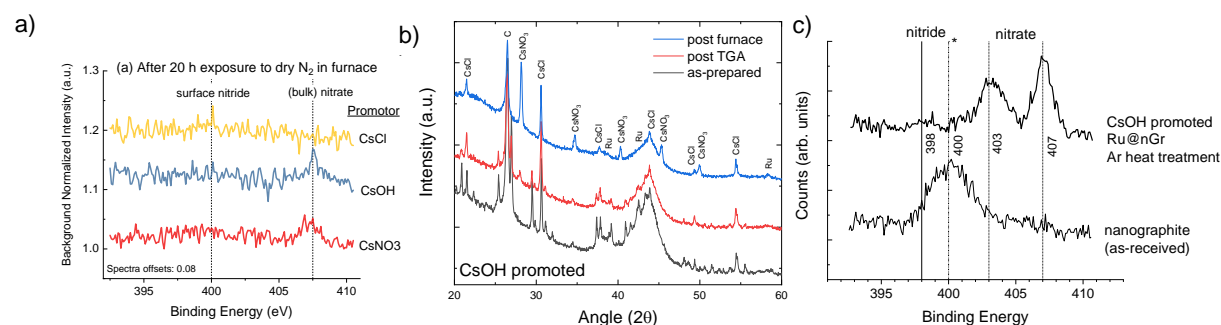
To validate that chlorine was present in the as-prepared catalysts from SAFCell, XPS and XRD were used. Both techniques showed the presence of chlorine in the catalyst material. Furthermore, XPS revealed that after extended operation, the Cl peaks remain albeit to a much less degree (see Appendix Figure C.11-). Presumably, the chlorine is being evolved as gaseous HCl. Similar analysis of the working electrode before and after operation revealed no chlorine, suggesting that even if the chlorine is evolving, it is not migrating to poison the working electrode.



Appendix Figure C.11-2 XPS of CRL powders prepared at SAFCell after a) 0h b) 20h, and c) 1100h of operation (Thermo Scientific ESCALAB 250 Xi).

Interestingly, it was found that 40 wt% Ru/nGr promoted with CsOH when annealed under nitrogen (for 20 hours at 250°C) would still form CsNO₃. This was evidenced in both the XRD and XPS analysis of the post-operation catalyst materials (Appendix Figure C.11-1a and Appendix Figure C.11-1b). It was later found that there was a source of single-bonded nitrogen in the support material (likely an amine functional

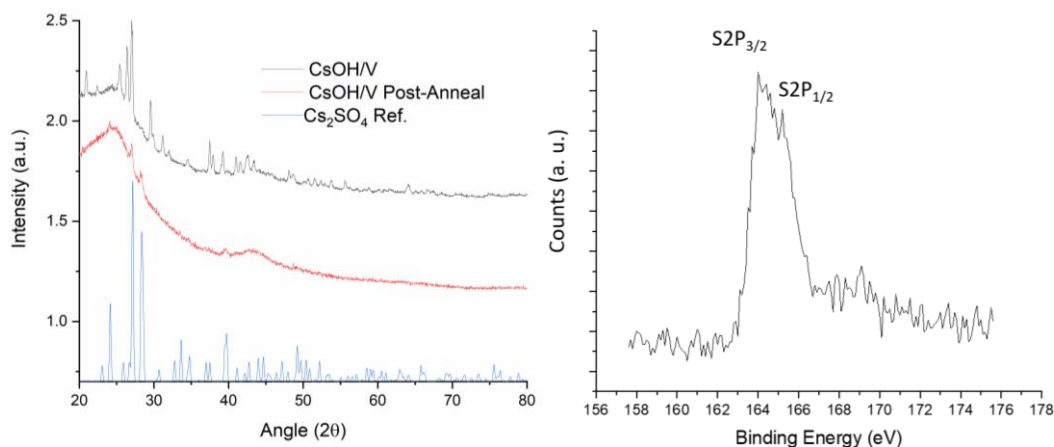
group from the binding energy). Further evidence that the source of the nitrogen was from the support material as opposed to the reaction nitrogen gas was found that if the flowing gas during the annealing procedure was switched to Ar, the CsNO_3 still formed (see Appendix Figure C.11-1c). This demonstrated that nitrogen could be pulled from the nanographite by using cesium hydroxide which would turn into the nitrate by doing so. The same technique was tried with KOH, but KOH was unable to form the nitrate under



Appendix Figure C.11-1 a) XPS analysis of promoted 40 wt% Ru/nGr samples (Cs:Ru 0.5:1) after annealing under dry nitrogen in a tube furnace for 20 hours at 250 °C. b) XRD analysis of the same CsOH promoted sample before and after annealing under dry nitrogen in either a tube furnace or in a TGA experiment. c) XPS analysis of as received nanographite and CsOH promoted sample annealed under Ar instead of N_2 . Peak at 400 eV attributed to an amine functional group on the carbon. XPS conducted on a Thermo Scientific ESCALAB 250 Xi and XRD performed on a Rigaku Ultima IV.

the same conditions.

Additionally, CsOH loaded on Vulcan alone was annealed under nitrogen for 20 hours at 250°C. It was discovered by XRD that this formed cesium sulfate (Appendix Figure C.11-2a). Analyzing the support under a) revealed that sulfur was present in the b) ng support material (Appendix Figure C.11-2b).



Appendix Figure C.11-2 a) XRD patterns of CsOH loaded onto Vulcan XC-72 as prepared and after annealing under nitrogen for 20 hours at 250 °C next to a cesium sulfate reference pattern (Rigaku Ultima IV). b) XPS analysis in sulfur binding region of Vulcan support (Thermo Scientific ESCALAB 250 Xi).

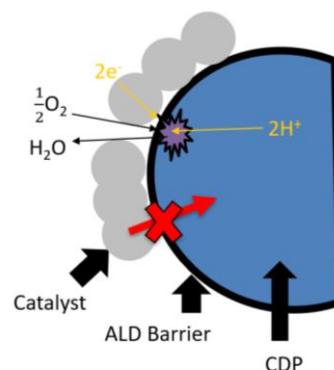
These results together showed that CsOH can pull a variety of anions from a material including chlorine, carbon, nitrogen, and sulfur. This can serve to detect impurities otherwise undetectable by XRD, but also can serve as a method to purify materials.

An application of Cs compounds as an anion purifier was used to remove chlorine from catalysts. As mentioned before, it was noted that chlorine was present in catalysts provided from SAFCcell and was detectable from EDS and XPS (in-house NaBH_4 reduction synthesized catalysts showed no signs of chlorine present). To accomplish this, 40 wt% Ru/nGr from SAFCcell was dispersed in a solution of cesium acetate in deionized water, sonicated for 15 minutes, and then stirred for 15 minutes. This solution was then vacuum filtered to remove the cesium acetate containing solution and rinsed thoroughly with deionized water. The catalyst was then allowed to dry overnight in a 60°C oven. EDS and XPS analysis of this purified sample showed no signs of Cl indicating that the purification technique was sound. This method could possibly be used in tandem with the precipitation and thermal reduction technique to remove residual chlorine that was found for those samples as well.

Appendix D Miscellaneous Experiments

D.1 ALD films for CsH_2PO_4 -based Electrochemical Cells

It is apparent that several catalyst materials, particularly when oxidized, will react with CsH_2PO_4 . This was particularly noticed for the Pd and Ru cases under air conditions (see discussions in Chapter 3). If one were able to either prevent the oxidation of these metal catalysts or prevent the diffusion of the catalyst to the electrolyte, one in theory could employ these catalysts in SAECs. For these reasons, we sought to develop such a thin film barrier. This barrier would need to fulfill many functions and thus have several tailored properties. First, it should be chemically stable with both the catalyst material of interest as well as with CDP. Secondly, this material should prevent diffusion of the catalyst material and/or the oxidation of



Appendix Figure D.1-1 Schematic of ALD barrier implemented in a SAFC cathode. In this instance, the barrier layer would prevent the diffusion of the catalyst to CDP. This barrier should also not inhibit electron or proton movement to the ORR reaction site. Alternatively, the catalyst could be coated to prevent oxidation in a similar manner.

the catalyst material. Thirdly, it would need to be sufficiently ionically and electronically conductive to not impede the electrochemical reaction of interest. Finally, it must be able to be deposited conformally onto CDP powders. A schematic of the proposed ALD diffusion barrier

is shown in Appendix Figure D.1-1.

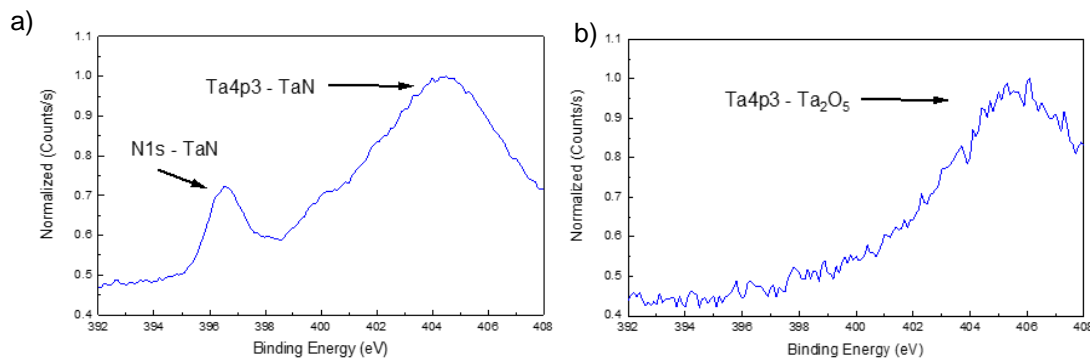
Earlier tests had suggested that tantalum might be a good candidate material that could be stable with CDP⁸, so this material was sought to be deposited for this barrier layer application. While the oxide is very resistive¹⁶⁰, extremely thin films have shown to have lower electronic resistances when tunneling can occur¹⁶¹. Alternatively, tantalum nitrides offer a higher bulk electronic conductivity and might not be held to as stringent material requirements of a tantalum oxide and could be similarly resistant to reacting with CDP. Several works have showed that the deposition of tantalum nitride is possible at lower temperatures (low enough to deposit on CDP without CDP dehydrating) with ammonia as a nitriding source¹⁶²⁻¹⁶⁴. All of these ALD procedures were carried out with the organometallic (tert-butylimido)tris(diethylamido) tantalum (TBTDET) as this precursor has a high volatility with an ALD window at low temperatures.

ALD depositions were performed on a Cambridge NanoTech Savannah S100 ALD system. Depositions were performed in a four-step cycle involving first a primary precursor pulse followed by a purge followed by a secondary precursor pulse followed by a purge. Deposition recipes were developed on silicon substrates whereas growth was screened using ellipsometer. Deposition parameters optimized included chamber temperature, tantalum precursor temperature, and pulse times. Optimization goal was to achieve highest consistent growth rate that was self-limiting (increasing pulse time no longer corresponded with increased growth). Final growth rate and film density was confirmed using XRR. Optimized deposition procedures for the tantalum oxide and tantalum nitride are shown in Appendix Table D.1-1.

Compound	Primary Precursor	Secondary Precursor	Timing Sequence(s)	Primary Precursor Temperature (°C)	Chamber Temperature (°C)	Growth rate (Å/cycle)
TaN	TBTDET	NH ₃	2-15-0.020-20	120	150	0.29
Ta ₂ O ₅	TBTDET	H ₂ O	2-15-0.020-20	120	150	0.95

Appendix Table D.1-1 Ta-based ALD films deposition parameters

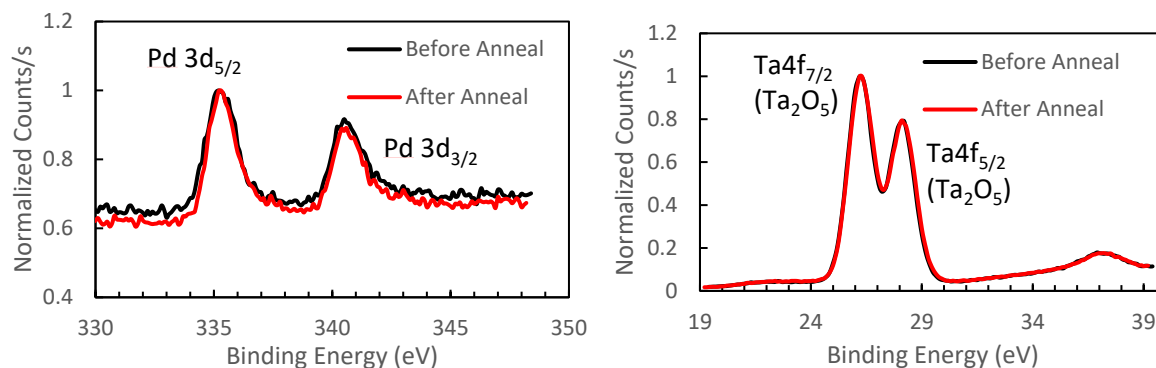
It was evident that the growth rate for the nitride was much slower than that for the oxide. XPS revealed that the nitride was successfully able to be formed (see Appendix Figure D.1-2a), but there was



Appendix Figure D.1-2 XPS over tantalum 4p3 range for a) tantalum nitride and b) tantalum oxide deposited on Si substrate by ALD.

also the presence of oxygen detected. This oxidation, particularly toward the surface, is in-line with what was reported by Burton et al¹⁶⁴. Assuming the oxide formed Ta_2O_5 , the remaining Ti:N ratio was found to be approximately 1:1, also in-line with what was found by Burton et al¹⁶⁴. XPS revealed that the tantalum oxide deposition was very successful reaching good agreement with the 2:5 Ta:O ratio expected with a high growth rate (see Appendix Figure D.1-2b). XPS analysis revealed no impurities (after etching), including carbon within the sample (contrary to what has been found in other tantalum oxide ALD procedures)¹⁶⁵. Given that the oxide deposition procedure was more successful, and it appeared that the nitride would always form some degree of oxide without the changing of nitriding precursor (e.g., hydrazine) or deposition method (e.g., plasma-enhanced atomic layer deposition), it was decided to proceed with the tantalum oxide as the candidate diffusion barrier material of choice.

Next, this candidate ALD tantalum oxide's capacity to act as a diffusion barrier was evaluated. To test this, 16 nm of palladium was deposited onto two MgO substrates via magnetron sputtering, and 6 nm of Ta_2O_5 was deposited on top of the palladium by the above described ALD procedures. Deposition here was confirmed by XRR. One of these samples was then annealed at 250°C under 0.47 atm p_{H_2O} of wet

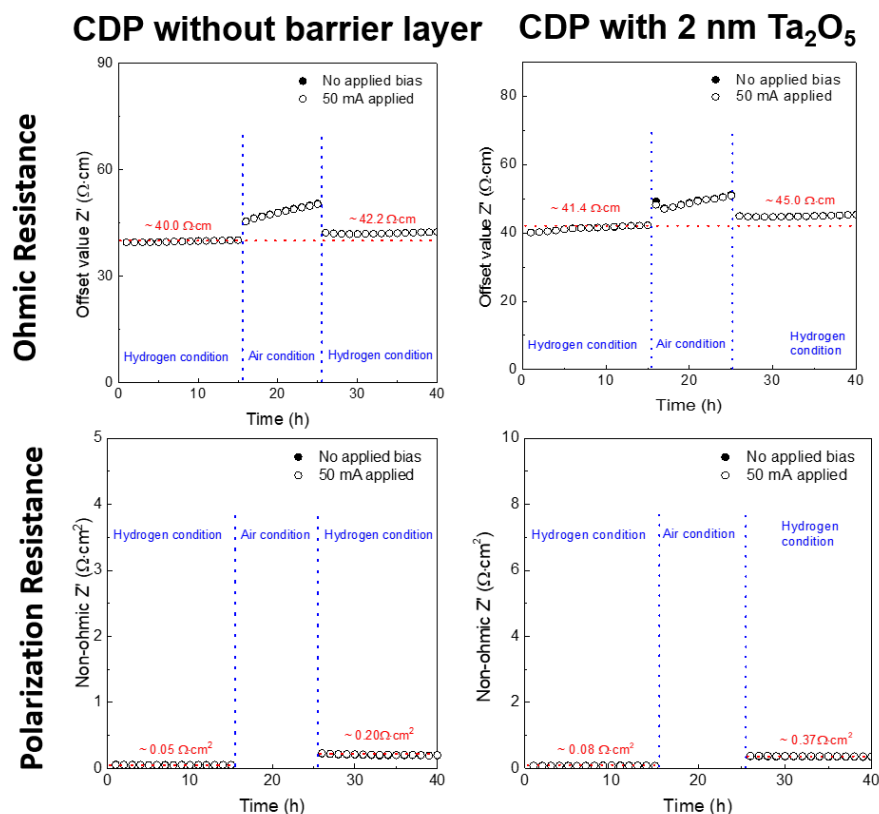


Appendix Figure D.1-3 XPS analysis of Ta₂O₅/Pd/MgO samples before and after wet air anneal covering the palladium and tantalum peaks. This analysis revealed that the annealing did not alter the electronic states of either palladium or tantalum. XPS conducted on a Thermo Scientific ESCALAB 250 Xi and XRD performed on a Rigaku Ultima IV.

air flowing over the sample at 50 sccm for 40 hours. Both the unannealed samples and annealed samples were analyzed by XPS. This XPS analysis showed that the tantalum oxide film was indeed able to prevent the oxidation of Pd, suggesting that Pd was unable to diffuse through the ALD film and the film prevented oxygen diffusion to the Pd (see Appendix Figure D.1-3).

Next, it was sought to evaluate the films impact on conductivity, particularly protonic conductivity. To do this, a sandwich cell was constructed that incorporated the tantalum oxide thin film. Briefly, two half cells were constructed composed of a GDL with a 'standard anode' pressed on, and finally a dense CDP pellet (~0.8 mm thick) finely polished on both sides (2000x alumina grit followed by a 3-micron alumina polish) was added on top and the entire half-cell was double wrapped with Teflon tape. To ensure quality for the CDP pellet, thickness uniformity to 0.01 mm was checked on all portions of the cell and the surface was ensured to be reflective and free of eye-visible scratches. Before the polish, the pellets were also annealed on a hot plate at 150°C for 30 minutes. Subsequently, a nominal amount of 1 nm Ta₂O₅ was deposited on top of the CDP pellets. To ensure pellet integrity, the heating ramp inside the ALD chamber was controlled to be 2°C/min. For the full sandwich cell, two these two half-cells were held together with CDP surface contacting CDP surface and they were again double wrapped with Teflon tape. As a reference, a second such sandwich cell was constructed in the same manner save for the Ta₂O₅ deposition.

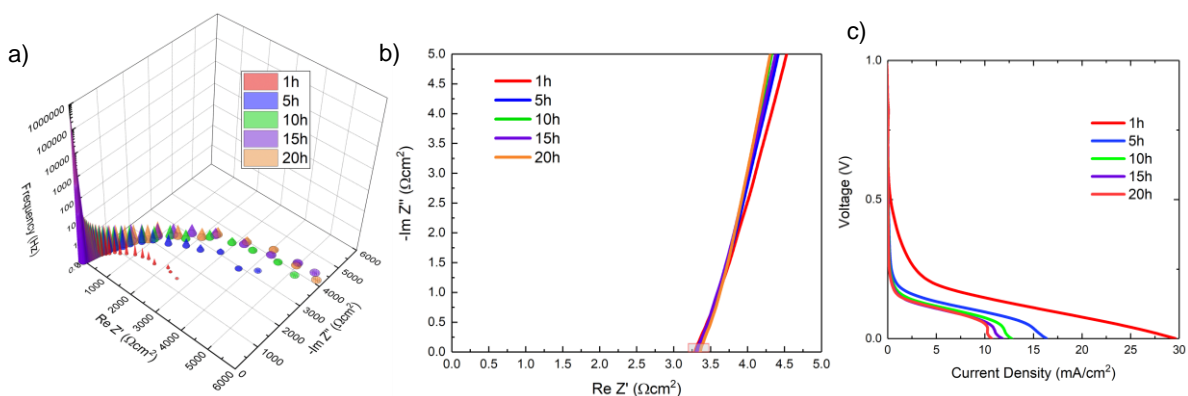
The sandwich cells were tested under a symmetric humidified hydrogen condition for 15 hours, a humidified air condition for 10 hours, and then a humidified hydrogen condition for 15 hours ($p_{\text{H}_2\text{O}} = 0.38$



Appendix Figure D.1-4 Sandwich cell tests with and without tantalum oxide barrier layers. Impedance spectroscopy tests ran from frequencies of 1 MHz to 0.1 Hz OCV and 50mA bias every hour for 40 hours. Cells tested under wet hydrogen and wet air (0.38 atm $p_{\text{H}_2\text{O}}$). Cell area here was 2.8 cm².

atm) at 250°C. Every hour, an impedance measurement at OCV and with a 50 mA bias across the cell was taken to obtain the ohmic and non-ohmic resistances of the cells (See Appendix Figure D.1-4). It is expected that there could be significant differences between the two cells, particularly as the cells were polished independently (could have different thicknesses and roughness). Instead, here we are looking in trends over time to see if there is degradation under either condition, or if there is a proton build-up at the ALD layer which would result in an increase in resistance in the bias condition compared to the OCV condition. Appendix Figure D.1-4 shows that there is no evidence of the ALD layer increasing the rate of degradation and the absence of a difference in the resistances of the biased and unbiased cases suggest negligible protonic resistances.

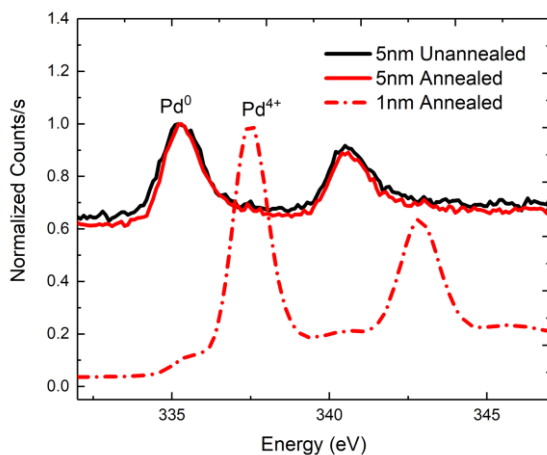
Then, flat fuel cells were constructed to test the fuel cell application of these barrier layers. Briefly, a half cell was constructed in the above-described manner. Then a 1 nm layer of Ta_2O_5 was applied on top of this half-cell. On top of this, nominally 30 nm of Pd was sputtered by magnetron sputtering. The cell was topped off with a sheet of carbon paper and a stainless-steel mesh. The full cell was double wrapped with Teflon tape. This cell was brought to operation under a fuel cell condition (humidified hydrogen at the Pt anode of 30 sccm and humidified air of 75 sccm at the Pd cathode, where $p_{\text{H}_2\text{O}} = 0.38 \text{ atm}$) and held for 20 hours where OCV impedance and polarization measurements were taken every hour (See Appendix Figure D.1-5). This test showed that both the initial performance was poor and that there was a significant amount of degradation arising from the increase in electrochemical reaction resistance. While additional tests were unable to be performed to determine there was some cell fabrication error, this test suggests that the ALD layer might hinder activity. Further, this test demonstrated that 1 nm of Ta_2O_5 was insufficient to prevent the Pd reaction with CDP.



Appendix Figure D.1-5 Flat cell test for 1 nm Ta_2O_5 barrier layer under fuel cell operating conditions. a) Shows OCV impedance measurements over time revealing increasing activation resistances. b) Shows the same data highlighting the ohmic region that remains relatively unchanged. c) Shows the polarization curves of the cell indicating decreasing performance overtime which appears to settle after about 20h.

Another annealing test was performed with 1 nm of Ta_2O_5 as opposed to the original 6 nm film test. XPS analysis of this sample revealed that indeed palladium was able to oxidize only 1 nm of the diffusion layer was applied (See Appendix Figure D.1-6). This is strongly suggestive that thicker layers need to be applied for this application to be successful. Due to the timeline for this research, methods had to be applied fast and not as many controls were able to be applied that would be ideal for optimizing this application. Further research might be able to make this application successful with either the optimization of existing

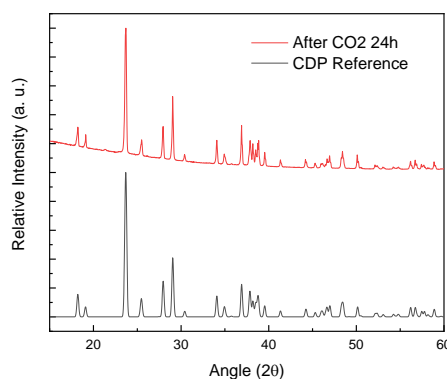
deposition (such as finding an optimal Ta₂O₅ thickness) or by exploring novel materials to apply in this system.



Appendix Figure D.1-6 XPS analysis of Ta₂O₅/Pd/MgO samples before and after wet air anneal covering the palladium and tantalum peaks. This analysis revealed that the annealing did not alter the electronic states of palladium when the diffusion barrier was 5 nm but did when the barrier was only 1 nm. XPS conducted on a Thermo Scientific ESCALAB 250 Xi and XRD performed on a Rigaku Ultima IV.

D.2 Electroreduction of CO₂

Previous strategies of reducing atmospheric CO₂ revolve around mitigating the need to emit CO₂ in energy applications. Another strategy of accomplishing this task is by capturing the CO₂ that is already in the atmosphere. As this is just an added cost to existing processes, in the absence of external incentives there is a lack of motivating factor for private enterprises to capture CO₂. This has motivated the development of ways to turn CO₂ into valuable chemical or fuel products to properly incentivize private enterprises to pursue this practice. CO₂ reduction is typically sluggish, but conversion into useful molecules is possible with judicious catalyst design in electrochemical systems. The challenge lies in the vast number of possible reaction pathways and possible end products, but the promise lies from the combination of H₂ and CO₂ to form products such as formic acid, methanol, ethanol, ethylene, methane, and carbon monoxide^{166,167}. One example is that it has been found methanol/methane formation has

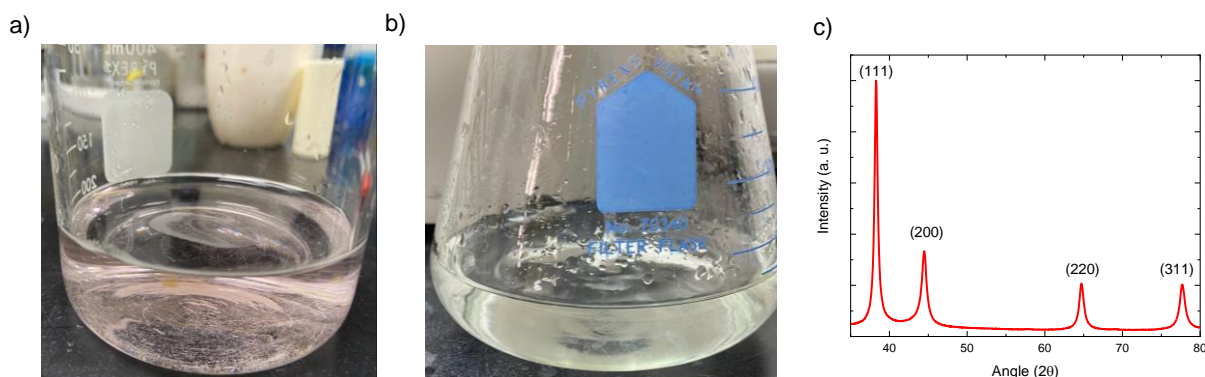


Appendix Figure D.2-1 XRD analysis of CDP after annealing run compared to reference pattern (Rigaku SmartLab).

been found to be correlated with the CO binding energy which tends to be optimized around Group 11 materials¹⁶⁸.

For a first pass at employing a SAEC for this application, a gold on carbon catalyst was developed since gold appears to have a favorable binding energy for CO₂ and gold is stable with CO₂¹⁶⁸. Prior to testing this system, it was important to consider if CDP would be stable under a pure humidified CO₂ atmosphere at operating temperature. To test this, a sample of CDP powder was annealed at 250°C for 24 hours under 100 sccm of humidified CO₂ (pH₂O = 0.38 atm). The sample was first ramped to 150°C under dry CO₂ at a ramp rate of 2°C/min and then to 250°C under humidified CO₂ at the same ramp rate. Ramping down rates were identical to ramping up rates. XRD analysis of after this annealing run indicate that CDP is stable under this condition (see Appendix Figure D.2-1).

After this a procedure to deposit gold nanoparticles on Vulcan XC-72 was developed. First, Vulcan placed in a beaker with deionized water and sonicated for five minutes. This was then placed onto a hotplate and was magnetically stirred. Then, an amount of HAuCl₄ 3H₂O was added to the beaker in an amount that would be equivalent to 20 wt% on Vulcan. Then an ice-cold NaBH₄ solution was added dropwise to the solution in an amount where the molar ratio of NaBH₄ to Au was 2:1. This was then allowed to stir for 10 minutes. This was then vacuum filtered and rinsed with deionized water. This filtrate was pink (see Appendix Figure D.2-2a), suggesting that Au nanoparticles had formed, but at least some had not deposited onto the Vulcan support. The powder was then dried on the filter paper at 250°C for one hour. The powder was removed from the filter paper and added to a beaker. The pink filtrate was then poured into the beaker. This

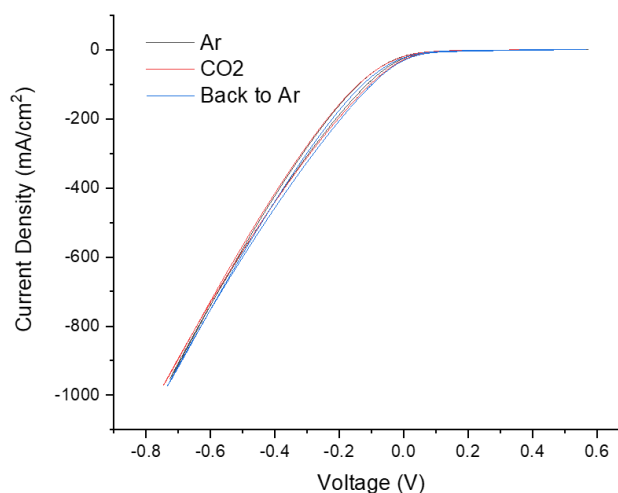


Appendix Figure D.2-2 a) Filtrate after first round of NaBH₄ reduction. b) Filtrate after second round of filtrate. c) XRD analysis of catalyst powder after full deposition procedure revealing single phase FCC gold with an 11 nm crystallite size (Rigaku SmartLab).

solution was sonicated for five minutes. The same amount of ice-cold NaBH_4 solution was then again added dropwise to the solution. The solution was allowed to stir for 90 minutes this time. Upon vacuum filtering and rinsing this time with deionized water, the filtrate was clear (see Appendix Figure D.2-2b) suggesting that the deposition was complete. The powder was dried on the filter paper at 80°C overnight. XRD analysis of this powder revealed single phase FCC gold was deposited with a crystallite size of approximately 11 nm (see Appendix Figure D.2-2c).

A cell was then constructed to test the CO_2 reduction capability of this catalyst in an SAEC cell. Briefly, a 'standard anode' half-cell composed of a GDL disc, a 75 mg MPL layer, and a layer comprised of 25 mg 20 wt% Pt/C and CDP (Pt/C:CDP, 1:6) pressed on at three tons for three seconds was used as the counter electrode. This was topped off with 50 mg of fine CDP pressed onto the electrode at four tons for one second. This half-cell was double wrapped with Teflon tape. For the working electrode, a 50 mg electrode of 20 wt% Au/V and CDP (Au/V :CDP, 1: 6) was pressed onto the half cell at two tons for one second. A sheet of carbon paper and a stainless-steel mesh were added and then the final cell was double wrapped with Teflon tape a final time.

This cell was predominantly tested in two configurations. The first configuration was a baseline where humidified hydrogen was supplied to the counter electrode and humidified Ar was supplied to the working electrode ($p_{\text{H}_2\text{O}} = 0.38 \text{ atm}$). For the working test, the Ar gas was switched to CO_2 . After testing in the working condition, CO_2 was switched back to Ar to test reversibility. The electrochemical tests run involve cyclic



Appendix Figure D.2-3 CO_2 reduction test for 20 wt% Au/V catalyst. CV scans were used here with 10 mV/s sweep rates.

strongly reducing potentials at the working electrode, and subsequently return to OCV. The results of this are shown in Appendix Figure D.2-3. The lack of a substantial difference between the Ar and CO_2 runs

suggest that the presence of CO₂ on the working electrode is not lowering the necessary driving force to shuttle protons and that likely in both cases, hydrogen evolution is predominantly occurring. It appears at these operating potentials that gold is quite capable of facilitating hydrogen evolution but also points to the fact that selectivity will be critical in designing this system. Future work in analyzing this system should incorporate methods of analyzing the exhaust gas for quantitative amounts of carbon-containing products.

Appendix E Software Developed

E.1 Electrochemical Impedance Fitting Program (ECIF)

This program fits impedance data with equivalent circuit models using Python. This program will provide fitted variables along with a fitted pattern corresponding with those variables. Additionally, an error of these fitted variables is provided via a bootstrapping error calculation method. The main code for this program is available at the following link: <https://github.com/hailegroup/ECIF>³⁴. Here, using the code and the main logic of the code will be discussed in addition to future improvements that can be made to the program.

To run this program, the following steps should be followed. First, a version of Python greater than 3.0 should be installed onto the device of interest. Next, the libraries that are used in the python files here should be installed using your favorite library installation method (e.g., pip, conda). Next, from the program homepage on Github all the files should be downloaded into a location on the local device. For running the program, data should be formatted into a csv file with frequency in the first column, the real component of impedance in the second column, and the imaginary component of impedance in the third column. This file should be placed in the folder /main/General_Circuit. In /main/General_Circuit/config.py, user-based inputs should be filled in including the circuit type to be fitted, initial parameters, parameter bounds, output filename, and the frequency range that is desired to be analyzed. Finally, run /main/General_Circuit/Test_Fitting.py to perform the analysis. This will produce Bode Plots, a Nyquist plot, a correlation matrix, the fitted data, and the fitted parameters alongside their fitting errors. If the meta data is filled out in the Experiment_Data.yml file, a meta data report will also be generated at this point.

The main structure of the program is operated through the Test_Fitting file which works modularly relying on the other files within the General_Circuit directory. Below, the Test_Fitting file code is provided

to aid in the description of the functionality where it helps to aid in following logic. Initially, this program obtains the parameters written into the config file:

```
params = config.Initial_Parameters
```

```
modelname = config.Circuit_Type
```

```
filename = config.Filename
```

```
FreqLB = config.Frequency_Domain[0]
```

```
FreqUB = config.Frequency_Domain[1]
```

The program will then open the data file and read the data into arrays within the specified bounds. This data is then input into a complex array:

```
FArr=numpy.array(F)
```

```
RArr=numpy.array(R)
```

```
ImArr=numpy.array(Im)*1j
```

```
TotArr=RArr+ImArr
```

The program then carries custom fitting function from the Fitting.py file:

```
fit_result, ParamNames = fit.custom_fitting(F, TotArr, params)
```

```
Fitted_variables = fit_result.x
```

This function takes the circuit defined in the Circuits.py file, takes the residual fitting function defined in fitting.py, and then performs a least-squares fitting of the data to the circuit model. After this first pass fitting is performed, the residuals between this fit and the original data is obtained:

```
residuals = fit.res_vec( Fitted_variables, FArr, TotArr)
```

These residuals are then modeled by a statistical distribution. It is key for this step to ensure that the residuals are being appropriately modeled. It is assumed that these residuals are normally distributed, but this might not always be the case. The bootstrap function then makes new sets of data replicating these

residuals randomly distributed (normally in this case) on the original data. The noise level here should be approximately what was seen with the original data and the residuals generated here should have the same distribution as the initial set of residuals. Each of these sets of data is then fit again by the same procedure. An error based on the residuals is then obtained by the variance between these multiple parameter fits. This also gives the correlation between the parameters which is also returned:

```
boot_params, corr = boot.strap(residuals, FArr, TotArr, Fitted_variables, ParamNames)
```

It is important to ensure that convergence is reached with this bootstrapping function. Enough simulated patterns should be run so that the parameters and their errors converge within a tolerance of interest.

After this, the remaining tasks remain in reporting the data. The data is output into csv files, plots are generated, and the data is sorted into fitting report and plotting folders. Additionally, a meta data report is generated to include in the fitting report:

```
mr.meta_report("Experiment_Data.yml")
```

The Batch folder is similar, except that it will try to read every csv file in the directory as an input file and will generate separate reports for each. There is also a script in this directory to aid in data extraction from EC_Lab generated .mpt files generated from the usual Biologic operating program. The Demo directory contains an interactive graphical plot that allows for the manipulation of circuit properties to see how this affects the impedance in the Bode magnitude representation of an RRQ circuit.

Several aspirational goals remain for this program to reach its true potential. For one thing, the library of equivalent circuit models should be expanded. Most of the work conducted here merely needed to implement RQ circuits, but several other equivalent circuit models are relevant to electrochemical systems. Adding them to the library what greatly increase the utility of the program. A second improvement that would aid usability would be to create a graphical user interface (GUI) that would be intuitive for newer users to operate. This could allow for easy plug and play modeling that would improve the efficiency of use. Combining the first two goals, a graphical equivalent circuit builder would be helpful. If one could drag and drop circuit elements into a single circuit and the equivalent circuit model is generated at that point, this would greatly expedite the expansion of use cases for the program and perhaps make some understanding

of the models more intuitive. A final aspirational goal would lie in using the documentation section to provide introductory material in helping the understanding and usage of electrochemical impedance spectroscopy along with documentation about the software itself. One day perhaps new users can download the program, learn about EIS, and then quickly and intuitively apply the program on their own data.

E.2 Pytentiostat

At JUAMI 2016 an international group of students conceived an idea to make a low-cost, research grade potentiostat that would make experimental electrochemistry accessible to resource-constrained communities. This group, led by Y. Christopher Li of Penn State, created a teaching kit that combines the fabrication of a low-cost microcontroller-based potentiostat and a LabVIEW-based interface. This effort, supported by the MRS Foundation, resulted in a publication describing the device and interface¹⁶⁹.

The materials cost of this microcontroller is relatively cheap (est. \$40) and has a simple assembly process where the parts and process are described in detail in the above-mentioned publication. The LabVIEW-based program acted as a graphical user interface (GUI) to the microcontroller, allowing the user to interact with the microcontroller on a more intuitive level while also allowing for real-time display of their data as an experiment is being conducted. This hardware/software combination allowed for the conduction of common electrochemical experiments (e. g. three-probe cyclic voltametry) with a respectable operating range (± 2.5 V, ~ 10 mA current range and ~ 10 μ A resolution). The main challenge left to the accessibility of this potentiostat to resource-constrained communities lied in its reliance on LabVIEW.

There are several problems that arise when using LabVIEW as the program to interface with the primary problem lying in that LabVIEW is proprietary and expensive for code developers (\$399 for base student version). Additional challenges lie in code portability, database communication, implementing a remote client, limited user community, web-based application development, mobile device application development, and code version portability. This inspired the development of an open-source interface that was based on Python and can have broader generalizability.

The new interface relies on a firmware code is to be uploaded to the Arduino Uno to allow it to interpret python as well as establishes some parameters on the board to enable high-performance measurements. This code is freely available and can be found online at

https://github.com/juami/potentiostat_firmata/. After the firmware code is installed, the microcontroller can easily be interfaced with using the newly developed Pytentiostat program freely available at <https://github.com/juami/pytentiostat/>.

There are several easy ways to install Pytentiostat program onto one's computer and are outlined inside the Pytentiostat page's documentation. All necessary programs and code to run this interface are freely available online. Additionally, there is a version of the code written that can be downloaded to a flash drive and then physically delivered to a user who can fully install the code and necessary packages to be able to run the code. This can allow for people to access the program even under the circumstance that they lack internet access.

There are two operating versions of the code oriented towards different types of users. The most intuitive one to operate is a GUI-based version that visually guides the user when making an experiment. This GUI-version comes with file directory navigation, steps to setup an experiment visually displayed in logical order, experiment builder windows that allow for previewing the voltage steps over time one is designing to apply, an automatic configuration file writer, the capacity to load several written experiments into a queue to be executed in order and is coupled with a real-time display of the data while in operation.

The second version of the code is a more robust and is oriented towards developers. This version must be operated through command line inputs. While less intuitive to use, this version has robust unit tests in place to ensure that functionality is maintained when changes are made to the base operating code. It is also easier in this version to make small changes to add new functionality.

The main structure of the program is operated through the main.py file which works modularly relying on the other files within the pytentiostat directory. Below, the main file code is provided to aid in the description of the functionality where it helps to aid in following logic. Initially, places instances from the microcontroller into a class including the COM port it is connected to, the serial communication, the two analog input pins, and the digital output pin:

```
class BoardCom:
```

```
    def __init__(self):
```

```
self.com, self.board, self.pin_a0, self.pin_a2, self.pin_d9 = startup_routine()
```

The program will then prompt and enter in configuration data defining experimental parameters:

```
parse = input("Press enter to load the config file.")
```

```
config_data = parse_config_file()
```

The program will then run the prescribed routines with the option to interrupt during the routine. After finishing the routines, the program will prompt if data would like to be saved and if another program would like to be ran. Finally, when no more experiments are desired, a closing routine will be implemented to stop communication with the potentiostat and to stop all current operations. The GUI-based version has a similar operating principle except that the operational interface is visually generated using Pyside2 and has a little more flexibility in operation. Basic operating instructions are provided in the program documents at: https://github.com/juami/pytentiostat/blob/master/docs/basic_operation.rst.

Inherently with this device, there is a tradeoff in how accurate of a voltage you can measure and how fast can you take a measurement. There are two ways the code allows the to be altered: (1) in the amount of times a measurement is taken at a given point and averaged or (2) the rest time allowed for each given point (both found in advanced parameters in advanced config):

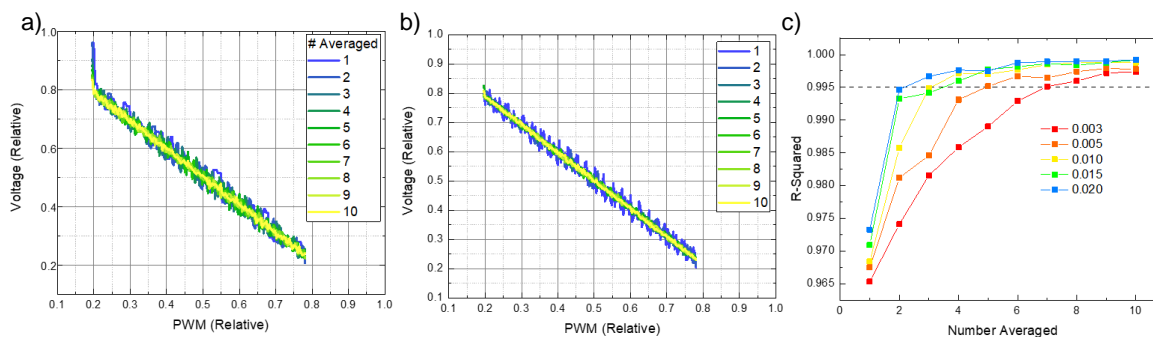
```
time_step: 0.003 #s
```

```
average_number: 9
```

More averaging and longer time steps lead to less noisy voltage readings but increase the amount of time to measure a point. Edge case testing found that below 3 ms rest times lead to inconsistent readings (occasionally not returning values) which would cause errors in serial readings, so this was established as a lower bound. Additionally, while the lower bound for time required for a step is the average number times the rest time, the interface naturally has a random degree of lag associated with it. When executing a scheduled routine, the program will execute the number of measurements per point at the rest time per point, and then continually check whenever it is time to run the next step. In order to account for this random lag factor, a lag tolerance factor of two is added so that the routine is never run behind schedule. So, the

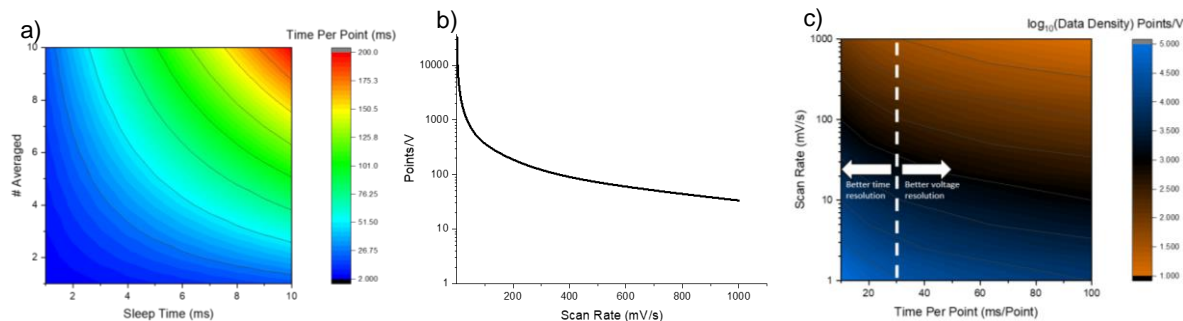
real time per point is the measurements per point times the rest time per point times the lag tolerance factor.

One might want to alter this tradeoff in time and voltage resolution, so an approach is shown here (see Appendix Figure E.2-1). One approach would be to threshold a measurement speed and then improve the voltage resolution as much as possible. In this approach, one simply should establish the time per measurement and increase the average number and rest time to high as allowable and can adjust them to have the least noisy data possible. An approach done here is to run a linear sweep across a resistor and take the deviation from linearity as the level of noise. A second approach is to have a voltage resolution threshold and then make the measurement as fast as possible if it passes this threshold. We will note here that it is found that a combination of the rest time and averaging number is optimal (i.e., a moderate increase in average number and rest time improves resolution greater than a massive increase in average number and minor increase in rest time and vice versa).



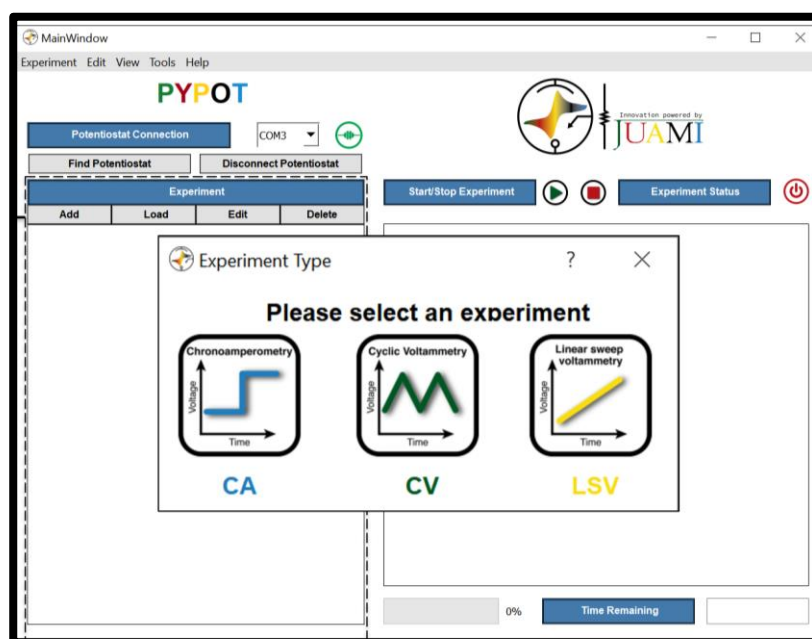
Appendix Figure E.2-1 Relative voltage analog read signal versus the input to the plane wave modulator (PWM) which is negatively correlated on this measurement across a resistor. The signal point is measured, and averaged a given number of times. a) Shows these measurements with a 3 ms rest time while b) shows these measurements with a 20 ms rest time. c) shows the R^2 values of these measurements with a range of rest times from a linear fit model and an arbitrary 0.995 cutoff. With this threshold, the optimal measurement is at 3 ms averaged seven times.

If one looks at the time per point measurement space across these two optimizing parameters (see Appendix Figure E.2-2a) one can gauge how they can navigate across this space to carry out a measurement. An easy way to conceptualize this is by considering how much points can be measured in a given scan range (see Appendix Figure E.2-2b). This can then lead to a related optimization where one can determine they need a given point density over a range and determine the usable optimization space given that parameter (see Appendix Figure E.2-2c).



Appendix Figure E.2-2 a) Time per point based on number of averaged points, sleep time, and a lag threshold of two. b) Points per volt measured as a function of scan rate with a 30 ms time per point. c) Data density measured as a function of scan rate and time per point. The white dashed reference line shows the 30 ms time point threshold used in b).

With the development of the Pytentiostat program we have made a great step towards the democratization of electrochemistry. One can now with relatively cheap components, an open-source design, and an open-source program begin conducting their own electrochemistry project. On the lines of this mission, we are also writing an electrochemistry resource accessible from the program to help users learn electrochemistry concepts. With an intuitive user interface (see Appendix Figure E.2-3) and streamlined operating mechanism, the Pytentiostat program has promise to help facilitate the next generation of electrochemists. With open-source program and associated level of documentation, hopefully this program will grow as a collaborative project with an open-source community able to organically improve the program for general use.



Appendix Figure E.2-3 Pytentiostat graphical user interface after potentiostat connected in the process of adding an experiment.

Many aspirational goals remain for this program and many are detailed in the issues section on the Github page. One not listed yet would be to broaden the scope of the graphical user interface beyond facilitating experiments. For instance, the menu tab options shown in Appendix Figure E.2-3 are not functional at the moment but serve as placeholders. Two helpful ways to broaden this interface would be to include an analysis tab that allows for real time analysis electrochemical data collected. A second one would be to link the help tab to a wiki that provides information on the potentiostat, the program, and electrochemistry in general. Currently the program is accessible via Windows and Linux operating systems but are not accessible to Macintosh and mobile ones. The Macintosh accessibility should be simple to implement with a few small changes, but the mobile accessibility might prove more challenging particularly considering the GUI implementation. A final aspirational goal would be to create a way to add modular add-ons to the program that increase functionality. One such example would be to incorporate a temperature controller with the pytentiostat program. This would allow simultaneous temperature and voltage scheduling and reading from the same device in a unified output. Overall, we would like to enhance primarily the accessibility and functionality of the potentiostat and the operating program.

References

1. Boysen, D. A.; Uda, T.; Chisholm, C. R. I.; Haile, S. M., High-performance solid acid fuel cells through humidity stabilization. *Science* **2004**, *303* (5654), 68-70.
2. Versatile Fuel Cells Stop Natural Gas Emissions at Oil Wells. https://spinoff.nasa.gov/Spinoff2020/ee_5.html.
3. Ryan O'Hayre, S.-w. C., Whitney Colella, Fritz B. Prinz, *Fuel Cell Fundamentals*. Third ed.; John Wiley & Sons, Inc.: Hoboken, New Jersey, 2106; p 580.
4. Department of Energy, O. o.; ENERGY, E. E. R. Comparison of Fuel Cell Technologies. https://www.energy.gov/sites/prod/files/2016/06/f32/fcto_fuel_cells_comparison_chart_apr2016.pdf.
5. Haile, S. M.; Chisholm, C. R. I.; Sasaki, K.; Boysen, D. A.; Uda, T., Solid acid proton conductors: from laboratory curiosities to fuel cell electrolytes. *Faraday Discuss* **2007**, *134*, 17-39.
6. Chisholm, C. R. I. B., D. A.; Papandrew, A. B.; Zecevic, S; Cha, S; Sasaki, K. A.; Varga, A; Giapis, K. P.; Haile, S. M., From Laboratory Breakthrough to Technology Realization: The Development Path for Solid Acid Fuel Cells. *The Electrochemical Society Interface* **2009**, *18*, 53-59.
7. Ikeda, A.; Haile, S. M., The thermodynamics and kinetics of the dehydration of CsH₂PO₄ studied in the presence of SiO₂. *Solid State Ionics* **2012**, *213*, 63-71.
8. Louie, M. W. *Electrocatalysis in Solid Acid Fuel Cells*. California Institute of Technology, Pasadena, California, 2011.
9. Papandrew, A. B.; Chisholm, C. R. I.; Zecevic, S. K.; Veith, G. M.; Zawodzinski, T. A., Activity and Evolution of Vapor Deposited Pt-Pd Oxygen Reduction Catalysts for Solid Acid Fuel Cells. *J Electrochem Soc* **2013**, *160* (2), F175-F182.
10. Michaelis, L.; Menten, M. L., The kinetics of the inversion effect. *Biochem Z* **1913**, *49*, 333-369.
11. Hammer, B.; Norskov, J. K., Theoretical surface science and catalysis - Calculations and concepts. *Adv Catal* **2000**, *45*, 71-129.
12. Pettifor, D. G., *Bonding and Structure of Molecules and Solids*. Varendon Press: Oxford, 1995; p 272.
13. Lundqvist, B. I.; Gunnarsson, O.; Hjelmberg, H.; Norskov, J. K., Theoretical Description of Molecule-Metal Interaction and Surface-Reactions. *Surf Sci* **1979**, *89* (1-3), 196-225.
14. Hammer, B.; Norskov, J. K., Why Gold Is the Noblest of All the Metals. *Nature* **1995**, *376* (6537), 238-240.
15. Hammer, B., Norskov, J. K., *Chemisorption and Reactivity on Supported Clusters and Thin Films* Kluwer Academic: Dordrecht, 1997.
16. Anderson, O. K., Jepsen, O., Glotzel, D., *Highlights of Condensed Matter Theory*. Corso Soc. Italiana di Fisica: Bologna, 1985; Vol. LXXXIX.
17. Norskov, J. K., Effective Medium Potentials for Molecule-Surface Interactions - H₂ on Cu and Ni Surfaces. *J Chem Phys* **1989**, *90* (12), 7461-7471.
18. Medford, A. J.; Vojvodic, A.; Hummelshoj, J. S.; Voss, J.; Abild-Pedersen, F.; Studt, F.; Bligaard, T.; Nilsson, A.; Norskov, J. K., From the Sabatier principle to a predictive theory of transition-metal heterogeneous catalysis. *J Catal* **2015**, *328*, 36-42.
19. Gsell, M.; Jakob, P.; Menzel, D., Effect of substrate strain on adsorption. *Science* **1998**, *280* (5364), 717-720.
20. Pallassana, V.; Neurock, M., Electronic factors governing ethylene hydrogenation and dehydrogenation activity of pseudomorphic Pd-ML/Re(0001), Pd-ML/Ru(0001), Pd(111), and Pd-ML/Au(111) surfaces. *J Catal* **2000**, *191* (2), 301-317.
21. Ramsier, R. D.; Gao, Q.; Waltenburg, H. N.; Yates, J. T., Thermal-Dissociation of NO on Pd Surfaces - the Influence of Step Sites. *J Chem Phys* **1994**, *100* (9), 6837-6845.
22. Kose, R.; Brown, W. A.; King, D. A., Energetics and kinetics of step-terrace adsorbate distribution: C₂H₂ on Pt{211}. *J Am Chem Soc* **1999**, *121* (20), 4845-4851.
23. Dietrich, H.; Jacobi, K.; Ertl, G., Coverage, lateral order, and vibrations of atomic nitrogen on Ru(0001). *J Chem Phys* **1996**, *105* (19), 8944-8950.
24. Dahl, S.; Logadottir, A.; Egeberg, R. C.; Larsen, J. H.; Chorkendorff, I.; Tornqvist, E.; Norskov, J. K., Role of steps in N₂ activation on Ru(0001). *Phys Rev Lett* **1999**, *83* (9), 1814-1817.

25. Ruban, A.; Hammer, B.; Stoltze, P.; Skriver, H. L.; Norskov, J. K., Surface electronic structure and reactivity of transition and noble metals. *J Mol Catal a-Chem* **1997**, *115* (3), 421-429.
26. Ertl, G., Surface Science and Catalysis - Studies on the Mechanism of Ammonia-Synthesis - the Emmett, P.H. Award Address. *Catal Rev* **1980**, *21* (2), 201-223.
27. Rostrup-Nielsen, J. R., Linking science and industrial catalysis. *Top Catal* **1994**, *1* (3-4), 377-382.
28. Mortensen, J. J.; Hammer, B.; Norskov, J. K., A theoretical study of adsorbate-adsorbate interactions on Ru(0001). *Surf Sci* **1998**, *414* (3), 315-329.
29. Norskov, J. K.; Rossmeisl, J.; Logadottir, A.; Lindqvist, L.; Kitchin, J. R.; Bligaard, T.; Jonsson, H., Origin of the overpotential for oxygen reduction at a fuel-cell cathode. *J Phys Chem B* **2004**, *108* (46), 17886-17892.
30. Norskov, J. K.; Studt, F.; Ablid-Pedersen, F.; Bligaard, T., *Fundamental Concepts in Heterogeneous Catalysis*. John Wiley & Sons: 2014.
31. Garcés-Pineda, F. A.; Blasco-Ahicart, M.; Nieto-Castro, D.; Lopez, N.; Galan-Mascaros, J. R., Direct magnetic enhancement of electrocatalytic water oxidation in alkaline media. *Nat Energy* **2019**, *4* (6), 519-525.
32. Lim, D. K.; Liu, J.; Pandey, S. A.; Paik, H.; Chisholm, C. R. I.; Hupp, J. T.; Haile, S. M., Atomic layer deposition of Pt@C₅H₂PO₄ for the cathodes of solid acid fuel cells. *Electrochim Acta* **2018**, *288*, 12-19.
33. Barsoukov, E., Macdonald, J. R., *Impedance Spectroscopy: Theory, Experiment, and Applications*. 2nd ed.; John Wiley & Sons, Inc.: Hoboken, 2005; p 595.
34. Plymill, A., Huang, R. *Electrochemical Impedance Fitting Program*, <https://github.com/hailegroup/ECIF>, 2019.
35. Cullity, B. D., Stock, S. R., *Elements of X-ray Diffraction*. Prentice-Hall, Inc.: Upper Saddle River, 2001; p 664.
36. Kanaya, K.; Okayama, S., Penetration and Energy-Loss Theory of Electrons in Solid Targets. *J Phys D Appl Phys* **1972**, *5* (1), 43-&.
37. Baer, D. R.; Artyushkova, K.; Brundle, C. R.; Castle, J. E.; Engelhard, M. H.; Gaskell, K. J.; Grant, J. T.; Haasch, R. T.; Linford, M. R.; Powell, C. J.; Shard, A. G.; Sherwood, P. M. A.; Smentkowski, V. S., Practical guides for x-ray photoelectron spectroscopy: First steps in planning, conducting, and reporting XPS measurements. *J Vac Sci Technol A* **2019**, *37* (3).
38. Chisholm, C. R. I., Papandrew, A. Efficient and Simple Method for Metalorganic Chemical Vapor Deposition. USOO9650711B2, 2017.
39. Puurunen, R. L., Surface chemistry of atomic layer deposition: A case study for the trimethylaluminum/water process. *J Appl Phys* **2005**, *97* (12).
40. Lu, J. L.; Elam, J. W.; Stair, P. C., Atomic layer deposition-Sequential self-limiting surface reactions for advanced catalyst "bottom-up" synthesis. *Surf Sci Rep* **2016**, *71* (2), 410-472.
41. Koponen, S. E.; Gordon, P. G.; Barry, S. T., Principles of precursor design for vapour deposition methods. *Polyhedron* **2016**, *108*, 59-66.
42. George, S. M., Atomic Layer Deposition: An Overview. *Chem Rev* **2010**, *110* (1), 111-131.
43. Langmuir, I., The constitution and fundamental properties of solids and liquids Part I Solids. *J Am Chem Soc* **1916**, *38*, 2221-2295.
44. Brunauer, S.; Emmett, P. H.; Teller, E., Adsorption of gases in multimolecular layers. *J Am Chem Soc* **1938**, *60*, 309-319.
45. Bowden, F. P.; Rideal, E. K., The electrolytic behaviour of thin films Part I - Hydrogen. *P R Soc Lond a-Conta* **1928**, *120* (784), 59-79.
46. Skulason, E.; Tripkovic, V.; Bjorketun, M. E.; Gudmundsdottir, S.; Karlberg, G.; Rossmeisl, J.; Bligaard, T.; Jonsson, H.; Norskov, J. K., Modeling the Electrochemical Hydrogen Oxidation and Evolution Reactions on the Basis of Density Functional Theory Calculations (vol 114, pg 18182, 2010). *J Phys Chem C* **2010**, *114* (50), 22374-22374.
47. Conway, B. E.; Tilak, B. V., Interfacial processes involving electrocatalytic evolution and oxidation of H₂, and the role of chemisorbed H. *Electrochim Acta* **2002**, *47* (22-23), 3571-3594.
48. Shinagawa, T.; Garcia-Esparza, A. T.; Takanabe, K., Insight on Tafel slopes from a microkinetic analysis of aqueous electrocatalysis for energy conversion. *Sci Rep-Uk* **2015**, *5*.
49. Sasaki, K. A. *Electrochemical Characterization of Solid Acid Fuel Cell Electrodes*. California Institute of Technology, 2010.

50. Louie, M. W.; Haile, S. M., Platinum thin film anodes for solid acid fuel cells. *Energ Environ Sci* **2011**, *4* (10), 4230-4238.
51. Paik, H. Development of Electrocatalysts in Solid Acid Fuel Cells. California Institute of Technology, 2019.
52. Paik, H.; Berenov, A. V.; Skinner, S. J.; Haile, S. M., Hydrogen oxidation kinetics on platinum-palladium bimetallic thin films for solid acid fuel cells. *Appl Mater* **2019**, *7* (1).
53. Kay, B. D.; Peden, C. H. F.; Goodman, D. W., Kinetics of Hydrogen Absorption by Pd(110). *Phys Rev B* **1986**, *34* (2), 817-821.
54. Papandrew, A. B.; Chisholm, C. R. I.; Elgammal, R. A.; Ozer, M. M.; Zecevic, S. K., Advanced Electrodes for Solid Acid Fuel Cells by Platinum Deposition on CsH₂PO₄. *Chem Mater* **2011**, *23* (7), 1659-1667.
55. Wipf, H., Topics in applied physics - Introduction. *Top Appl Phys* **1997**, *73*, 1-4.
56. Boudart, M.; Hwang, H. S., Solubility of Hydrogen in Small Particles of Palladium. *J Catal* **1975**, *39* (1), 44-52.
57. Okamoto, H., *Pd-Pt (palladium-platinum)*. 2nd ed.; ASM International: 1990.
58. Thoi, V. S.; Usiskin, R. E.; Haile, S. M., Platinum-decorated carbon nanotubes for hydrogen oxidation and proton reduction in solid acid electrochemical cells. *Chem Sci* **2015**, *6* (2), 1570-1577.
59. Evoen, V. Electrocatalysis in Solid Acid Fuel Cell Electrodes. California Institute of Technology, Pasadena, CA, 2016.
60. Holstein, W. L.; Rosenfeld, H. D., In-situ x-ray absorption spectroscopy study of Pt and Ru chemistry during methanol electrooxidation. *J Phys Chem B* **2005**, *109* (6), 2176-2186.
61. Scott, F. J.; Roth, C.; Ramaker, D. E., Kinetics of CO poisoning in simulated reformat and effect of Ru island morphology on PtRu fuel cell catalysts as determined by operando X-ray absorption near edge spectroscopy. *J Phys Chem C* **2007**, *111* (30), 11403-11413.
62. Pelliccione, C. J.; Timofeeva, E. V.; Katsoudas, J. P.; Segre, C. U., In Situ Ru K-Edge X-ray Absorption Spectroscopy Study of Methanol Oxidation Mechanisms on Model Submonolayer Ru on Pt Nanoparticle Electrocatalyst. *J Phys Chem C* **2013**, *117* (37), 18904-18912.
63. Chen, D. J.; Tong, Y. Y. J., Irrelevance of Carbon Monoxide Poisoning in the Methanol Oxidation Reaction on a PtRu Electrocatalyst. *Angew Chem Int Edit* **2015**, *54* (32), 9394-9398.
64. Strmcnik, D.; Uchimura, M.; Wang, C.; Subbaraman, R.; Danilovic, N.; van der Vliet, D.; Paulikas, A. P.; Stamenkovic, V. R.; Markovic, N. M., Improving the hydrogen oxidation reaction rate by promotion of hydroxyl adsorption. *Nat Chem* **2013**, *5* (4), 300-306.
65. Precious Metals Charts.
https://www.heraeus.com/en/hpm/pm_prices/charts/charts.html?currency=usd&charttype=line&dateFrom=01.01.2007&dateTo=02.11.2020&ru=1&pt=1&pd=1.
66. Greeley, J.; Mavrikakis, M., Alloy catalysts designed from first principles. *Nat Mater* **2004**, *3* (11), 810-815.
67. Cornish, L. A.; Suss, R.; Watson, A.; Preussner, J.; Prins, S. N.; Wenderoth, M.; Volkl, R.; Glatzel, U., Building a database for the prediction of phases in Pt-based superalloys. *J S Afr I Min Metall* **2007**, *107* (11), 713-724.
68. Gasteiger, H. A.; Ross, P. N.; Cairns, E. J., Leis and Aes on Sputtered and Annealed Polycrystalline Pt-Ru Bulk Alloys. *Surf Sci* **1993**, *293* (1-2), 67-80.
69. Nashner, M. S.; Frenkel, A. I.; Somerville, D.; Hills, C. W.; Shapley, J. R.; Nuzzo, R. G., Core shell inversion during nucleation and growth of bimetallic Pt/Ru nanoparticles. *J Am Chem Soc* **1998**, *120* (32), 8093-8101.
70. Durst, J.; Siebel, A.; Simon, C.; Hasche, F.; Herranz, J.; Gasteiger, H. A., New insights into the electrochemical hydrogen oxidation and evolution reaction mechanism. *Energ Environ Sci* **2014**, *7* (7), 2255-2260.
71. Wang, Y.; Wang, G. W.; Li, G. W.; Huang, B.; Pan, J.; Liu, Q.; Han, J. J.; Xiao, L.; Lu, J. T.; Zhuang, L., Pt-Ru catalyzed hydrogen oxidation in alkaline media: oxophilic effect or electronic effect? *Energ Environ Sci* **2015**, *8* (1), 177-181.
72. Elbert, K.; Hu, J.; Ma, Z.; Zhang, Y.; Chen, G. Y.; An, W.; Liu, P.; Isaacs, H. S.; Adzic, R. R.; Wang, J. X., Elucidating Hydrogen Oxidation/Evolution Kinetics in Base and Acid by Enhanced Activities at the Optimized Pt Shell Thickness on the Ru Core. *ACS Catal* **2015**, *5* (11), 6764-6772.

73. St John, S.; Atkinson, R. W.; Unocic, R. R.; Zawodzinski, T. A.; Papandrew, A. B., Ruthenium-Alloy Electrocatalysts with Tunable Hydrogen Oxidation Kinetics in Alkaline Electrolyte. *J Phys Chem C* **2015**, *119* (24), 13481-13487.
74. Wang, J. X.; Zhang, Y.; Capuano, C. B.; Ayers, K. E., Ultralow charge-transfer resistance with ultralow Pt loading for hydrogen evolution and oxidation using Ru@Pt core-shell nanocatalysts. *Sci Rep-Uk* **2015**, *5*.
75. Tripathi S., B. S., Dharwadkar S. , The Pd-Ru system (palladium-ruthenium). *Journal of Phase Equalibria* **1993**, *14*, 638–642.
76. Feng, L. G.; Xue, H. G., Advances in Transition-Metal Phosphide Applications in Electrochemical Energy Storage and Catalysis. *Chemelectrochem* **2017**, *4* (1), 20-34.
77. Papandrew, A. B.; Zawodzinski, T. A., Nickel catalysts for hydrogen evolution from CsH₂PO₄. *J Power Sources* **2014**, *245*, 171-174.
78. Markert, F.; Marangon, A.; Carcassi, M.; Duijm, N. J., Risk and sustainability analysis of complex hydrogen infrastructures. *Int J Hydrogen Energ* **2017**, *42* (11), 7698-7706.
79. Schlapbach, L.; Zuttel, A., Hydrogen-storage materials for mobile applications. *Nature* **2001**, *414* (6861), 353-358.
80. Rivard, E.; Trudeau, M.; Zaghbi, K., Hydrogen Storage for Mobility: A Review. *Materials* **2019**, *12* (12).
81. Klerke, A.; Christensen, C. H.; Norskov, J. K.; Vegge, T., Ammonia for hydrogen storage: challenges and opportunities. *J Mater Chem* **2008**, *18* (20), 2304-2310.
82. Rouwenhorst, K. H. R.; Van der Ham, A. G. J.; Mul, G.; Kersten, S. R. A., Islanded ammonia power systems: Technology review & conceptual process design. *Renew Sust Energ Rev* **2019**, *114*.
83. Lamb, K. E.; Dolan, M. D.; Kennedy, D. F., Ammonia for hydrogen storage; A review of catalytic ammonia decomposition and hydrogen separation and purification. *Int J Hydrogen Energ* **2019**, *44* (7), 3580-3593.
84. MacFarlane, D. R.; Cherepanov, P. V.; Choi, J.; Suryanto, B. H. R.; Hodgetts, R. Y.; Bakker, J. M.; Vallana, F. M. F.; Simonov, A. N., A Roadmap to the Ammonia Economy. *Joule* **2020**, *4* (6), 1186-1205.
85. Chase, M. W., NIST-JANAF Thermochemical Tables. American Chemical Society; American Institute of Physics for the National Institute of Standards and Technology: 1998.
86. Chiuta, S.; Everson, R. C.; Neomagus, H. W. J. P.; van der Gryp, P.; Bessarabov, D. G., Reactor technology options for distributed hydrogen generation via ammonia decomposition: A review. *Int J Hydrogen Energ* **2013**, *38* (35), 14968-14991.
87. Uribe, F. A.; Gottesfeld, S.; Zawodzinski, T. A., Effect of ammonia as potential fuel impurity on proton exchange membrane fuel cell performance. *J Electrochem Soc* **2002**, *149* (3), A293-A296.
88. Miyaoka, H.; Miyaoka, H.; Ichikawa, T.; Ichikawa, T.; Kojima, Y., Highly purified hydrogen production from ammonia for PEM fuel cell. *Int J Hydrogen Energ* **2018**, *43* (31), 14486-14492.
89. Vitse, F.; Cooper, M.; Botte, G. G., On the use of ammonia electrolysis for hydrogen production (vol 142, pg 18, 2005). *J Power Sources* **2005**, *152* (1), 311-312.
90. Modisha, P.; Bessarabov, D., Electrocatalytic Process for Ammonia Electrolysis: A Remediation Technique with Hydrogen Co-Generation. *Int J Electrochem Sc* **2016**, *11* (8), 6627-6635.
91. Yin, S. F.; Xu, B. Q.; Zhou, X. P.; Au, C. T., A mini-review on ammonia decomposition catalysts for on-site generation of hydrogen for fuel cell applications. *Appl Catal a-Gen* **2004**, *277* (1-2), 1-9.
92. Schuth, F.; Palkovits, R.; Schlögl, R.; Su, D. S., Ammonia as a possible element in an energy infrastructure: catalysts for ammonia decomposition. *Energy Environ Sci* **2012**, *5* (4), 6278-6289.
93. Bell, T. E.; Torrente-Murciano, L., H₂ Production via Ammonia Decomposition Using Non-Noble Metal Catalysts: A Review. *Top Catal* **2016**, *59* (15-16), 1438-1457.
94. Norskov, J. K.; Studt, F.; Abild-Pedersen, F.; Bligaard, T., The Potential Energy Diagram. *Fundamental Concepts in Heterogeneous Catalysis* **2014**, 6-25.
95. Bradford, M. C. J.; Fanning, P. E.; Vannice, M. A., Kinetics of NH₃ decomposition over well dispersed Ru. *J Catal* **1997**, *172* (2), 479-484.
96. Appl, M., Ammonia. In *Ullmann's Encyclopedia of Industrial Chemistry*, on-line edn ed.; Wiley-VCH: Weinheim, 2006.

97. Hansgen, D. A.; Vlachos, D. G.; Chen, J. G. G., Using first principles to predict bimetallic catalysts for the ammonia decomposition reaction. *Nat Chem* **2010**, *2* (6), 484-489.
98. Logadottir, A.; Rod, T. H.; Norskov, J. K.; Hammer, B.; Dahl, S.; Jacobsen, C. J. H., The Bronsted-Evans-Polanyi relation and the volcano plot for ammonia synthesis over transition metal catalysts. *J Catal* **2001**, *197* (2), 229-231.
99. Ganley, J. C.; Thomas, F. S.; Seebauer, E. G.; Masel, R. I., A priori catalytic activity correlations: the difficult case of hydrogen production from ammonia. *Catal Lett* **2004**, *96* (3-4), 117-122.
100. Aika, K.; Kubota, J.; Kadowaki, Y.; Niwa, Y.; Izumi, Y., Molecular sensing techniques for the characterization and design of new ammonia catalysts. *Appl Surf Sci* **1997**, *121*, 488-491.
101. Zhong, Z. H.; Aika, K., Effect of ruthenium precursor on hydrogen-treated active carbon supported ruthenium catalysts for ammonia synthesis. *Inorg Chim Acta* **1998**, *280* (1-2), 183-188.
102. Hager, T., *The Alchemy of Air: A Jewish Genius, a Doomed Tycoon, and the Scientific Discovery That Fed the World but Fueled the Rise of Hitler*. 1st ed.; Three Rivers Press: New York, 2008; p 316.
103. Wang, S. J.; Yin, S. F.; Li, L.; Xu, B. Q.; Ng, C. F.; Au, C. T., Investigation on modification of Ru/CNTs catalyst for the generation of CO_x-free hydrogen from ammonia. *Appl Catal B-Environ* **2004**, *52* (4), 287-299.
104. Dahl, S.; Logadottir, A.; Jacobsen, C. J. H.; Norskov, J. K., Electronic factors in catalysis: the volcano curve and the effect of promotion in catalytic ammonia synthesis. *Appl Catal a-Gen* **2001**, *222* (1-2), 19-29.
105. Vitse, F.; Cooper, M.; Botte, G. G., On the use of ammonia electrolysis for hydrogen production. *J Power Sources* **2005**, *142* (1-2), 18-26.
106. Hill, A. K.; Torrente-Murciano, L., Low temperature H₂ production from ammonia using ruthenium-based catalysts: Synergetic effect of promoter and support. *Appl Catal B-Environ* **2015**, *172*, 129-135.
107. ARPA-E Award No. DE-AR0000813 With SAFCell. In *DE-FOA-00001562, Renewable Energy to Fuels through Utilization of Energy-dense Liquids (REFUEL)*, ARPA-E: 2017; p 8.
108. Lim, D.-K.; Plymill, A. B.; Paik, H.; Qian, X.; Zecevic, S.; Chisholm, C. R. I.; Haile, S. M., Solid Acid Electrochemical Cell for the Production of Hydrogen from Ammonia. *Joule* **2020**.
109. Kurihara, L. K.; Chow, G. M.; Schoen, P. E., Nanocrystalline Metallic Powders and Films Produced by the Polyol Method. *Nanostruct Mater* **1995**, *5* (6), 607-613.
110. Hill, A. K.; Torrente-Murciano, L., In-situ H₂ production via low temperature decomposition of ammonia: Insights into the role of cesium as a promoter. *Int J Hydrogen Energy* **2014**, *39* (15), 7646-7654.
111. Li, J. P.; Wang, W. Y.; Chen, W. X.; Gong, Q. M.; Luo, J.; Lin, R. Q.; Xin, H. L.; Zhang, H.; Wang, D. S.; Peng, Q.; Zhu, W.; Chen, C.; Li, Y. D., Sub-nm ruthenium cluster as an efficient and robust catalyst for decomposition and synthesis of ammonia: Break the "size shackles". *Nano Res* **2018**, *11* (9), 4774-4785.
112. Yin, S. F.; Zhang, Q. H.; Xu, B. Q.; Zhu, W. X.; Ng, C. F.; Au, C. T., Investigation on the catalysis of CO_x-free hydrogen generation from ammonia. *J Catal* **2004**, *224* (2), 384-396.
113. Yin, S. F.; Xu, B. Q.; Wang, S. J.; Ng, C. F.; Au, C. T., Magnesia-carbon nanotubes (MgO-CNTs) nanocomposite: novel support of Ru catalyst for the generation of CO_x-free hydrogen from ammonia. *Catal Lett* **2004**, *96* (3-4), 113-116.
114. Zhang, H.; Alhamed, Y. A.; Al-Zahrani, A.; Daous, M.; Inokawa, H.; Kojima, Y.; Petrov, L. A., Tuning catalytic performances of cobalt catalysts for clean hydrogen generation via variation of the type of carbon support and catalyst post-treatment temperature. *Int J Hydrogen Energy* **2014**, *39* (31), 17573-17582.
115. Zhang, H.; Alhamed, Y. A.; Chu, W.; Ye, Z. B.; AlZahrani, A.; Petrov, L., Controlling Co-support interaction in Co/MWCNTs catalysts and catalytic performance for hydrogen production via NH₃ decomposition. *Appl Catal a-Gen* **2013**, *464*, 156-164.
116. Zhang, J.; Muller, J. O.; Zheng, W. Q.; Wang, D.; Su, D. S.; Schlogl, R., Individual Fe-Co alloy nanoparticles on carbon nanotubes: Structural and catalytic properties. *Nano Lett* **2008**, *8* (9), 2738-2743.
117. Nagaoka, K.; Eboshi, T.; Abe, N.; Miyahara, S.; Honda, K.; Sato, K., Influence of basic dopants on the activity of Ru/Pr₆O₁₁ for hydrogen production by ammonia decomposition. *Int J Hydrogen Energy* **2014**, *39* (35), 20731-20735.

118. Li, G.; Nagasawa, H.; Kanezashi, M.; Yoshioka, T.; Tsuru, T., Graphene nanosheets supporting Ru nanoparticles with controlled nanoarchitectures form a high-performance catalyst for CO_x-free hydrogen production from ammonia. *J Mater Chem A* **2014**, *2* (24), 9185-9192.
119. Huang, D. C.; Jiang, C. H.; Liu, F. J.; Cheng, Y. C.; Chen, Y. C.; Hsueh, K. L., Preparation of Ru-Cs catalyst and its application on hydrogen production by ammonia decomposition. *Int J Hydrogen Energ* **2013**, *38* (8), 3233-3240.
120. Duan, X. Z.; Qian, G.; Zhou, X. G.; Sui, Z. J.; Chen, D.; Yuan, W. K., Tuning the size and shape of Fe nanoparticles on carbon nanofibers for catalytic ammonia decomposition. *Appl Catal B-Environ* **2011**, *101* (3-4), 189-196.
121. Lorenzut, B.; Montini, T.; Pavel, C. C.; Comotti, M.; Vizza, F.; Bianchini, C.; Fornasiero, P., Embedded Ru@ZrO₂ Catalysts for H₂ Production by Ammonia Decomposition. *Chemcatchem* **2010**, *2* (9), 1096-1106.
122. Bale, C. W.; Belisle, E.; Chartrand, P.; Deckerov, S. A.; Eriksson, G.; Gheribi, A. E.; Hack, K.; Jung, I. H.; Kang, Y. B.; Melancon, J.; Pelton, A. D.; Petersen, S.; Robelin, C.; Sangster, J.; Spencer, P.; Van Ende, M. A., FactSage thermochemical software and databases, 2010-2016 (vol 54, pg 35, 2016). *Calphad* **2016**, *55*, 1-19.
123. Roki, F. Z.; Ohnet, M. N.; Fillet, S.; Chatillon, C.; Nuta, I., Improvements in the assessment of the thermodynamic properties of condensed and gaseous phases of the CsOH compound. *J Chem Thermodyn* **2015**, *80*, 147-160.
124. Cattaruzza, E.; Battaglin, G.; Cristofori, D.; Finotto, T.; Riello, P.; Glisenti, A., On the synthesis and thermal stability of RuN, an uncommon nitride. *Surf Coat Tech* **2016**, *295*, 93-98.
125. Lan, R.; Irvine, J. T. S.; Tao, S. W., Ammonia and related chemicals as potential indirect hydrogen storage materials. *Int J Hydrogen Energ* **2012**, *37* (2), 1482-1494.
126. Smith, C.; Hill, A. K.; Torrente-Murciano, L., Current and future role of Haber-Bosch ammonia in a carbon-free energy landscape. *Energy Environ Sci* **2020**, *13* (2), 331-344.
127. Cao, P. Y.; Lu, C. Q.; Yu, Z., Historical nitrogen fertilizer use in agricultural ecosystems of the contiguous United States during 1850-2015: application rate, timing, and fertilizer types. *Earth Syst Sci Data* **2018**, *10* (2), 969-984.
128. Wisner, R., Bolinger, M., Barbose, G., Darghouth, N., Hoen, B., Mills, A., Rand, J., Millstein, D., Jeong, S., Porter, K., Disanti, N., Oteri, F. *2018 Wind Technologies Market Report*, Office of Energy Efficiency and Renewable Energy: 2018; p 65.
129. Denholm, P., Mai, T. *Timescales of Energy Storage Needed for Reducing Renewable Energy Curtailment*, National Renewable Energy Laboratory: 2017; p 33.
130. Lawder, M. T. *EPAT: the Energy Price Analysis Tool*, 2016.
131. Zablocki, A. *Fact Sheet: Energy Storage (2019)*; Environmental and Energy Study Institute: 2019.
132. Annual Electric Generator Report. 2020.
133. Bartels, J. R. A feasibility study of implementing an Ammonia Economy. Iowa State University, Ames, Iowa, 2008.
134. Appl, M., *Ammonia: Principles and Industrial Practice*. Wiley: 1999; p 310.
135. *AMMONIA: ZERO-CARBON FERTILISER, FUEL AND ENERGY STORE*; The Royal Society: 2020; p 40.
136. *State of the Fertilizer Industry Report*, The Fertilizer Institute: 2016; p 58.
137. Hignett, T. P., *Fertilizer Manual*. 1 ed.; Springer Netherlands: 1985; p 363.
138. Amos, W. A. *Costs of Storing and Transporting Hydrogen*; National Renewable Energy Laboratory Golden, 1998; p 216.
139. Soloveichik, G., Ammonia as a Virtual Hydrogen Carrier. H₂@Scale Workshop, 2016; p 19.
140. Gillette, J. L., Kolpa, R. L. *Overview of Interstate Hydrogen Pipeline Systems*; Argonne National Laboratory: 2007; p 52.
141. Kim, J.; Park, K.; Yang, D. R.; Hong, S., A comprehensive review of energy consumption of seawater reverse osmosis desalination plants. *Appl Energy* **2019**, *254*.
142. Shen, S. Y., Wolsky, A. M. *Energy and Materials Flows in the Production of Liquid and Gaseous Oxygen*; Argonne National Laboratory: 1980; p 71.
143. *Renewable Energy to Fuels Through Utilization of EnergyDense Liquids (REFUEL) Program Overview*; ARPA-E: 2015; p 16.
144. Kyriakou, V.; Garagounis, I.; Vasileiou, E.; Vourros, A.; Stoukides, M., Progress in the Electrochemical Synthesis of Ammonia. *Catal Today* **2017**, *286*, 2-13.

145. Bosma, R. H.; Verdegem, M. C. J., Sustainable aquaculture in ponds: Principles, practices and limits. *Livest Sci* **2011**, 139 (1-2), 58-68.
146. *Current (2009) State-of-the-Art Hydrogen Production Cost Estimate Using Water Electrolysis*; National Renewable Energy Laboratory: Golden, 2009; p 51.
147. DOE Technical Targets for Hydrogen Production From Electrolysis. <https://www.energy.gov/eere/fuelcells/doe-technical-targets-hydrogen-production-electrolysis> (accessed 12/09/2020).
148. Mayyas, A., Ruth, M., Pivovar, B., Bender, G., Wipke, K. *Manufacturing Cost Analysis for Proton Exchange Membrane Water Electrolyzers*; National Renewable Energy Laboratory: Golden, 2019; p 65.
149. Bañares-Alcántara, R., Dericks, G., Fiaschetti, M., Grünewald, P., Lopez, J. M., Tsang, E., Yang, A., Ye, L., Zhao, S. *Analysis of Islanded Ammonia-based Energy Storage Systems*; University of Oxford: Oxford, 2015; p 158.
150. Saur, G. *Wind-To-Hydrogen Project: Electrolyzer Capital Cost Study*; National Renewable Energy Laboratory: Golden, 2008; p 48.
151. Dias, V., Pochet, M., Contino, F., Jeanmart, H., Energy and Economic Costs of Chemical Storage. *Frontiers in Mechanical Engineering* **2020**, 29, 17.
152. Leighty, B., Costs of Delivered Energy from Large-scale, Diverse, Stranded, Renewable Resources, Transmitted and Firmed as Electricity, Gaseous Hydrogen, and Ammonia. In *Ammonia: Key to US Energy Independence*, Denver, 2006; p 132.
153. Historical RTM Load Zone and Hub Prices. Electric Reliability Council of Texas: ercot.com, 2019.
154. Utility Scale Solar 2020 Data Update. Berkeley Lab: 2020.
155. *World Nuclear Performance Report 2018*; World Nuclear Association: 2018; p 36.
156. *Fact Book 2020*; Nutrien: 2020; p 51.
157. Svejkovsky, C. *Locally Owned Renewable Energy Facilities*; National Sustainable Agriculture Information Service: 2007.
158. Romain, F.; Novak, A., Raman-Study of the High-Temperature Phase-Transition in Csh2po4. *J Mol Struct* **1991**, 263, 69-74.
159. Bocchetta, P.; Ferraro, R.; Di Quarto, F., Advances in anodic alumina membranes thin film fuel cell: Csh2PO4 pore-filler as proton conductor at room temperature. *J Power Sources* **2009**, 187 (1), 49-56.
160. Moon, B. K.; Isobe, C.; Aoyama, J., Insulating properties of tantalum pentoxide capacitor films obtained by annealing in dry ozone. *J Appl Phys* **1999**, 85 (3), 1731-1738.
161. Lee, S.; Tang, A.; Aloni, S.; Wong, H. S. P., Statistical Study on the Schottky Barrier Reduction of Tunneling Contacts to CVD Synthesized MoS2. *Nano Lett* **2016**, 16 (1), 276-281.
162. Park, J. S.; Lee, M. J.; Lee, C. S.; Kang, S. W., Plasma-enhanced atomic layer deposition of tantalum nitrides using hydrogen radicals as a reducing agent. *Electrochem Solid St* **2001**, 4 (4), C17-C19.
163. Langereis, E.; Knoops, H. C. M.; Mackus, A. J. M.; Roozeboom, F.; van de Sanden, M. C. M.; Kessels, W. M. M., Synthesis and in situ characterization of low-resistivity TaNx films by remote plasma atomic layer deposition. *J Appl Phys* **2007**, 102 (8).
164. Burton, B. B.; Lavoie, A. R.; George, S. M., Tantalum nitride atomic layer deposition using (tert-butylimido) tris(diethylamido) tantalum and hydrazine. *J Electrochem Soc* **2008**, 155 (7), D508-D516.
165. Blanquart, T.; Longo, V.; Niinisto, J.; Heikkila, M.; Kukli, K.; Ritala, M.; Leskela, M., High-performance imido-amido precursor for the atomic layer deposition of Ta2O5. *Semicond Sci Tech* **2012**, 27 (7).
166. Ulissi, Z. W.; Medford, A. J.; Bligaard, T.; Norskov, J. K., To address surface reaction network complexity using scaling relations machine learning and DFT calculations. *Nat Commun* **2017**, 8.
167. Birdja, Y. Y.; Perez-Gallent, E.; Figueiredo, M. C.; Gottle, A. J.; Calle-Vallejo, F.; Koper, M. T. M., Advances and challenges in understanding the electrocatalytic conversion of carbon dioxide to fuels. *Nat Energy* **2019**, 4 (9), 732-745.
168. Zhu, D. D.; Liu, J. L.; Qiao, S. Z., Recent Advances in Inorganic Heterogeneous Electrocatalysts for Reduction of Carbon Dioxide. *Adv Mater* **2016**, 28 (18), 3423-3452.

169. Li, Y. C., Melenbrink, E. L., Cordonier, G. J., Boggs, C., Khan, A., Isaac, M. K., Nkhonjera, L. K., Bahati, D., Billinge, S. J., Haile, S. M., Kreuter, R. A., Crable, R. M., Mallouk, T. E., An Easily Fabricated Low-Cost Potentiostat Coupled with User-Friendly Software for Introducing Students to Electrochemical Reactions and Electroanalytical Techniques. *Journal of Chemical Education* **2018**, 95 (9), 1658-1661.

ProQuest Number:28318035

All rights reserved

INFORMATION TO ALL USERS

The quality of this reproduction is dependent on the quality of the copy submitted.

In the unlikely event that the author did not send a complete manuscript and there are missing pages, these will be noted. Also, if material had to be removed, a note will indicate the deletion.



ProQuest 28318035

Published by ProQuest LLC (2021). Copyright of the Dissertation is held by the Author.

All Rights Reserved.

This work is protected against unauthorized copying under Title 17, United States Code
Microform Edition © ProQuest LLC.

ProQuest LLC
789 East Eisenhower Parkway
P.O. Box 1346
Ann Arbor, MI 48106 - 1346